

FOR REFERENCE ONLY

✓
019 ✓
16/9/09

**The Nottingham Trent University
Library & Information Services
SHORT LOAN COLLECTION**

Date	Time	Date	Time
13	XXXXXXXXXX		
	2XXXXXX		

Please return this item to the issuing library.
Fines are payable for late return.

THIS ITEM MAY NOT BE RENEWED

Short Loan 03

09 JUL 2003

10354038

40 0736528 9



ProQuest Number: 10290247

All rights reserved

INFORMATION TO ALL USERS

The quality of this reproduction is dependent upon the quality of the copy submitted.

In the unlikely event that the author did not send a complete manuscript and there are missing pages, these will be noted. Also, if material had to be removed, a note will indicate the deletion.



ProQuest 10290247

Published by ProQuest LLC (2017). Copyright of the Dissertation is held by the Author.

All rights reserved.

This work is protected against unauthorized copying under Title 17, United States Code
Microform Edition © ProQuest LLC.

ProQuest LLC.
789 East Eisenhower Parkway
P.O. Box 1346
Ann Arbor, MI 48106 – 1346

SIMULATION OF TWO-PHASE BUBBLY FLOWS- AN INERT BUBBLE INTRODUCED INTO A HOT LIQUID

HUANXIN LAI

A thesis submitted in partial fulfilment of the
requirements of The Nottingham Trent University
for the degree of Doctor of Philosophy

This research programme was carried out in the
School of Engineering,
Faculty of Construction, Computing and Technology,
The Nottingham Trent University,
Burton Street, Nottingham NG1 4BU, UK.

January 2003

SIMULATION OF TWO-PHASE BUBBLY FLOWS- AN INERT BUBBLE INTRODUCED INTO A HOT LIQUID

By
Huanxin Lai

ABSTRACT

This thesis numerically studies the behaviour and heat and mass transfer relevant to an inert bubble introduced into a hot liquid. This study is a starting point of investigating the mechanism of transfer phenomena in two-phase bubbly flow based chemical reactors whose production capacity depends on the surface area of the bubbles and on the concentration gradients of species in each phase coupled with the local rate of reaction.

This entirely numerical and theoretical research starts with physical and mathematical modelling. The physical problem is modelled as unsteady conjugate heat and fluid flows around and inside a single rising inert bubble while full Navier-Stokes equations with well-posed boundary conditions are employed as the mathematical description of the problem.

Numerical algorithm for solving the mathematical model has been proposed and developed into Fortran codes. Firstly, a procedure for heat and flows in complex geometries with time-dependent moving boundaries is proposed. This procedure incorporates a multi-block iteration strategy with a moving mesh arrangement and is designed to calculate the heat and flows inside and around a single inert bubble; high order discretisation schemes are introduced and employed to obtain high resolution of the numerical results. Secondly, interfacial treatments are introduced and the algorithm is further developed to calculate gas-liquid interfacial flows in bubbles. Validations are widely carried out by available experiments and benchmark numerical data, robustness and potentials of the numerical algorithm and the codes are well shown.

Steady heat and fluid flows inside and around inert bubbles are carefully studied. Considering the importance of spherical bubble model, interfacial characteristics and flow structures of spherical bubbles are carried out. As the main work, detailed numerical studies are applied to moderately deformed bubbles in the ranges of $(Re^{(2)}, We) = [0, 200] \times [0, 6]$. Bubble shape, interfacial characteristics, flow structure, drag coefficient, and heat and mass transfer are carefully analysed to study the mechanism of interfacial transfer phenomena. The effects of bubble wake on the recovery of heat and mass transfer are identified and physically explained.

Based on some supplementations of the numerical procedure, time-accurate simulations on the rising-up of single inert bubbles are carried out to observe the unsteady heat and mass transfer and the relevant mechanisms. Full story of the bubble rising, evolution of bubble shape, development and propagation of temperature and concentration fields are numerically observed and analysed.

ACKNOWLEDGMENTS

At first, the author would like to thank the Nottingham Trent University for having offered me the three-year research studentship supported by EPSRC Grant under GR/M90207.

I am grateful to Dr Yuying Yan and professor Richard Gentle for great support and advice to me. Especially, Dr Yuying Yan had initiated the project and obtained EPSRC research grant; this should be specially appreciated.

I would like to thank professor John Smith at Surrey University for worthwhile advices.

I would like to extend a special thank-you to Mrs Doreen Corlett for maintaining to supply me with new relevant research information and materials.

My greatest thanks go to my family, and in particular my wife Hongbo Zhang who has been persistently supporting my research work.

PUBLICATIONS ARISING FROM THIS WORK

1. Lai, H and Yan, Y., 2001, "The effect of choosing dependent variables and cell-face velocities on convergence of the SIMPLE algorithm using non-orthogonal grids", *International Journal of Numerical Methods for Heat & Fluid Flow*, Vol.11, No.5, PP.524-546.
2. Lai, H., Yan, Y. and Smith, J., 2002, "A Calculation Procedure with Multi-Block Iteration and Moving Mesh for Heat and Fluid Flows in Complex Time-Dependent Geometries," *International Journal of Numerical Methods for Heat & Fluid Flow*, Vol.12, No.2, PP.106-125.
3. Yan, Y., Lai, H., Gentle, C. R. and Smith J. M., 2002, "Numerical Analysis of Fluid Flows inside and around A Liquid Drop Using An Incorporation of Multi-Block Iteration and Moving Mesh", *Transactions of The Institution of Chemical Engineers, Part A*, Vol.80, No.A3, PP. 325-331.
4. Lai, H., Yan, Y. and Gentle, C. R., 2003, "Calculation Procedure for Conjugate Viscous Flows About and Inside Single Bubbles", *Numerical Heat Transfer, Part B*, Vol.43, No.3, PP. 241-265.
5. Yan, Y., Lai, H., Gentle, C.R., and Smith, J.M., 2001, "Numerical Analysis of Fluid Flow and Heat Transfer in Complex Time-Dependent Geometries", *7th UK National Conference on Heat Transfer*, Sept. 2001, Nottingham.
6. Lai, H., Yan, Y., Gentle, C. R. and Smith, J. M., 2002, "Numerical Study of Conjugate Steady Viscous Flow About and Inside a Spherical Bubble", *12th International Heat Transfer Conference*, Aug.18-23, Grenoble, France.

TABLE OF CONTENTS

	Page
Abstract	i
Acknowledgments	ii
Publications arising from this work	iii
Table of contents	iv
Lists of Tables	ix
Lists of Figures	x
Nomenclature	xiv
Chapter 1: Introduction	1
1.1 Background	1
1.2 Aims and Objectives	2
1.3 Outline of the Work	3
Chapter 2: Literature Review	6
2.1 Introduction	6
2.2 Experimental Study on Single Rising Bubbles	7
2.2.1 Bubble Shape	7
2.2.2 Trajectory of Rising Bubble	9
2.2.3 Rising Velocity and Drag	9
2.2.4 Pressure Field and Wake	11
2.3 Analysing and Numerical Research on Single Rising Bubbles	14
2.3.1 Flow Models	15
2.3.2 CFD Algorithms for Studying Bubbles Using Full Navier-Stokes	19

2.3.3 Numerical Studies of Single Rising Bubbles	29
2.4 Summary	30
2.4.1 Investigations on physical phenomenon	30
2.4.2 Comparisons of numerical methods	31
Chapter 3: Physical and Mathematical Descriptions of the Problem	33
3.1 Introduction	33
3.2 Physical Model	33
3.3 Basic Governing Equations	34
3.4 Initial and Boundary Conditions	35
3.4.1 Initial Conditions	36
3.4.2 Boundary Conditions	36
3.5 Non-Inertial Coordinates and Normalisation of Equations	38
3.5.1 Non-Inertial Coordinate System	38
3.5.2 Transform of Equations	39
3.5.3 Normalisation of Basic Equations	41
3.6 Summary of the Chapter	44
Chapter 4: CFD Strategies for Moving Boundary Problems	45
4.1 Introduction	45
4.2 Eulerian-Lagrangian Transformation	45
4.3 FVM Discretisation on Moving Mesh	47
4.3.1 Finite Volume Integration	47

4.3.2 Space Conservation Law	51
4.3.3 High Order Schemes and Deferred Correction	53
4.3.4 Non-Staggered SIMPLE Method	63
4.3.5 Numerical Grid Generation	69
4.4 Multi-Block Computation	72
4.4.1 Uniqueness of Zonal Boundary	74
4.4.2 Zonal Boundary Variable Interpolation	75
4.5 Validations of the Numerical Methods	77
4.5.1 Lid-Driven Flow in a Squeezed Cavity	78
4.5.2 Laminar Flow Through Tubes with Constrictions	81
4.5.3 Separated Flow Over Backward-Facing Step	83
4.5.4 Natural Convection in Horizontal Annulus	86
4.5.5 Time-Dependent Moving Indentation Channel Flow	90
4.6 Summary	94
Chapter 5: Numerical Study of Gas-Liquid Interfacial Flows in Bubbles	95
5.1 Introduction	95
5.2 Gas-Liquid Interface Treatments	96
5.2.1 Expansion of Interfacial Boundary Conditions	96
5.2.2 Continuous Stress Method	98
5.2.3 Interface Deformation	101
5.3 Solution Approach	106
5.4 Results and Analysis	108

5.4.1 Spherical Drops	108
5.4.2 Deformable Liquid Drops	116
5.4.3 Deformable Bubbles: Validation by Experimental Data	118
5.5 Summary of Chapter	121
Chapter 6: Steady Heat and Fluid Flows Inside and Around Inert Bubbles	122
6.1 Introduction	122
6.2 Spherical Bubbles	123
6.2.1 Flow Structure of a Single Spherical Bubble	123
6.2.2 Interfacial Characteristics	124
6.3 Moderately Deformed Bubbles	127
6.3.1 Bubble Shape	127
6.3.2 Flow Structure	130
6.3.3 Drag Coefficient	134
6.3.4 Interfacial Characteristics	140
6.3.5 Heat and Mass Transfer	141
6.4 Summary of the Chapter	149
Chapter 7: Time-Accurate Simulations of an Inert Bubble Introduced into a Hot Liquid	150
7.1 Introduction	150
7.2 Rising Velocity and Acceleration	151
7.2.1 A Model Equation for Spherical Bubbles	151
7.2.2 A Full Analytical Model	153

7.3 Solution Approach for Time-Accurate Simulation	155
7.4 Results	156
7.4.1 Rising Velocity	157
7.4.2 Evolution of Bubble Shape and Flow Structure	159
7.4.3 Heat and Mass Transfer	178
7.5 Summary of Chapter	182
Chapter 8: Conclusions and Recommendations for Further Work	183
8.1 Physical and Mathematical Modelling	184
8.2 Development of Numerical Algorithm and CFD Codes	184
8.2.1 Finite Volume Method (FVM) with High Order Schemes	184
8.2.2 Multi-Block Iteration and Moving Mesh Arrangement	185
8.2.3 Gas-Liquid Interfacial Treatments	185
8.2.4 Supplementation for Time-Accurate Simulation	186
8.3 Numerical Simulation and Results	186
8.3.1 Dynamics of Single Spherical Bubbles	186
8.3.2 Dynamics of Single Deformable Bubbles	187
8.3.3 Unsteady Behaviour of Inert Bubble Introduced into Hot Liquid	188
8.4 Recommendation for Further Work	188
References	190
Appendix: Development of FORTRAN Codes for Solving the Inert Bubble Problem	206

LISTS OF TABLES

Tables

4.1 Model Geometries

4.2 Comparison of the present results with experiments

4.3 Reattachment points predicted by three meshes

5.1 Comparison of wake vortex length

5.2 Comparison between computed and measured aspect ratios

LISTS OF FIGURES

Figures

- 2.1 Shape regimes for bubbles and drops in unhindered gravitational motion through liquids
- 3.1 Non-inertial coordinates
- 4.1 Control volume for integration
- 4.2 Space conservation law
- 4.3 One-dimensional finite volume and associates nodal stencil
- 4.4 Range of boundness-preserving limiters for monotonic blend of Lax-Wendroff and Warming-Beam schemes
- 4.5 $\tilde{\phi}_f \sim \tilde{\phi}_c$ diagram (NVD)
- 4.6 Multi-block and zonal boundary
- 4.7 Notations used in two-block interface
- 4.8 Geometry and boundary conditions for squeezed lid-driven cavity flow
- 4.9a Centre line velocity profiles in the squeezed cavity, u component
- 4.9b Centre line velocity profiles in the squeezed cavity, v component
- 4.10 Convergent paths of different convection schemes
- 4.11 Geometric configuration of the pipe with a constriction
- 4.12 Flow pattern for Model M-3 at $Re=40$
- 4.13 Illustration of grids distribution for calculation of backward facing step
- 4.14 Positions of reattachment points in a step flow
- 4.15 Computational domain and grids for the natural convection in annulus
- 4.16 Convergent path for natural convection in annulus
- 4.17 Local equivalent conductivities at inner and outer walls
- 4.18 Temperature profiles
- 4.19 Distribution of angular velocity
- 4.20 Contour of non-dimensional temperature
- 4.21 Computational domain for moving indentation problem
- 4.22 Streamlines at various instants in a cycle

-
- 4.23 Positions of the crests and troughs of the eddies
 - 5.1 Zoned computational domain
 - 5.2 Zonal boundary and gas-liquid interface
 - 5.3 Determination of the new interface position
 - 5.4 Definition of curvature radii
 - 5.5 Flow structure inside and around a spherical droplet
 - 5.6 Topology of two wake-vortex types
 - 5.7a Tangential velocity at interface of a spherical droplet
 - 5.7b Pressure coefficient at interface of a spherical droplet
 - 5.7c Exterior Vorticity $\Omega^{(2)}$ at interface of a spherical droplet
 - 5.7d Interior Vorticity $\Omega^{(1)}$ at interface of a spherical droplet
 - 5.8 Wake flow structure and its change with $Re^{(2)}$
 - 5.9 Wake zone length and its change with $Re^{(2)}$
 - 5.10 Shapes of deformable drops $\Phi_\rho = 0.909$, $\Phi_\mu = 0.909$
 - 5.11 Convergent path of calculating deformable bubbles
 - 5.12 Comparison of bubble shapes
 - 6.1 Flow structure inside and around a spherical air bubble
 - 6.2a Interfacial tangential velocity of a spherical bubble
 - 6.2b Interfacial pressure of a spherical bubble
 - 6.2c Exterior Vorticity $\Omega^{(2)}$ of a spherical bubble
 - 6.2d Exterior Vorticity $\Omega^{(1)}$ of a spherical bubble
 - 6.3 Shapes of moderately deformed bubbles
 - 6.4 Influence of the Weber number on aspect ratio
 - 6.5 Influence of the Weber number on exchange surface coefficient
 - 6.6 Flow structures of moderately deformed bubbles
 - 6.7 Topology of vortex structure
 - 6.8 Comparison of flow structures with results of Ryskin and Leal (1984b)
 - 6.9 Drag force coefficients of moderately deformed bubbles
 - 6.10a Tangential velocity for “rear-flattening” bubbles ($Re^{(2)}=10$)

- 6.10b Interfacial pressure for “rear-flattening” bubbles ($Re^{(2)}=10$)
- 6.10c Exterior vorticity $\Omega^{(2)}$ for “rear-flattening” bubbles ($Re^{(2)}=10$)
- 6.11a Tangential velocity for “fore-aft symmetric” bubbles ($Re^{(2)}=50$)
- 6.11b Interfacial pressure for “fore-aft symmetric” bubbles ($Re^{(2)}=50$)
- 6.11c Exterior vorticity for “fore-aft symmetric” bubbles ($Re^{(2)}=50$)
- 6.12a Tangential velocity for “front-flattening” bubbles ($Re^{(2)}=200$)
- 6.12b Interfacial pressure for “front-flattening” bubbles ($Re^{(2)}=200$)
- 6.12c Exterior vorticity for “front-flattening” bubbles ($Re^{(2)}=200$)
- 6.13 Contour of temperature field
- 6.14 Contour of concentration field
- 6.15a Distribution of local Nusselt number for bubbles at $Re^{(2)}=10$
- 6.15b Distribution of local Sherwood number for bubbles at $Re^{(2)}=10$
- 6.16a Distribution of local Nusselt number for bubbles at $Re^{(2)}=50$
- 6.16b Distribution of local Sherwood number for bubbles at $Re^{(2)}=50$
- 6.17a Distribution of local Nusselt number for bubbles at $Re^{(2)}=200$
- 6.17b Distribution of local Sherwood number for bubbles at $Re^{(2)}=200$
- 6.18 Wake vortex structure and its effects on heat and mass transfer
- 7.1a Time history of bubble rising velocity at $Re^{(2)} = 10$
- 7.1b Time history of bubble rising velocity at $Re^{(2)} = 50$
- 7.1c Time history of bubble rising velocity at $Re^{(2)} = 200$
- 7.2a Evolution of bubble shape and flow structure at $Re^{(2)} = 10, We = 3$
- 7.2b Evolution of bubble shape and flow structure at $Re^{(2)} = 10, We = 5$
- 7.2c Evolution of bubble shape and flow structure at $Re^{(2)} = 50, We = 3$
- 7.2d Evolution of bubble shape and flow structure at $Re^{(2)} = 50, We = 5$
- 7.2e Evolution of bubble shape and flow structure at $Re^{(2)} = 200, We = 3$
- 7.2f Evolution of bubble shape and flow structure at $Re^{(2)} = 200, We = 5$
- 7.3a Development of temperature field, $Re^{(2)} = 10, We = 3$
- 7.3b Development of temperature field, $Re^{(2)} = 10, We = 5$
- 7.3c Development of temperature field, $Re^{(2)} = 50, We = 3$

-
- 7.3d Development of temperature field, $Re^{(2)} = 50$, $We = 5$
- 7.3e Development of temperature field, $Re^{(2)} = 200$, $We = 3$
- 7.3f Development of temperature field, $Re^{(2)} = 200$, $We = 5$
- 7.4a Development of concentration field, $Re^{(2)} = 10$, $We = 3$
- 7.4b Development of concentration field, $Re^{(2)} = 10$, $We = 5$
- 7.4c Development of concentration field, $Re^{(2)} = 50$, $We = 3$
- 7.4d Development of concentration field, $Re^{(2)} = 50$, $We = 5$
- 7.4e Development of concentration field, $Re^{(2)} = 200$, $We = 3$
- 7.4f Development of concentration field, $Re^{(2)} = 200$, $We = 5$
- 7.5a Time history of averaged Nusselt number at $Re^{(2)} = 10$
- 7.5b Time history of averaged Nusselt number at $Re^{(2)} = 50$
- 7.5c Time history of averaged Nusselt number at $Re^{(2)} = 200$
- 7.6a Time history of averaged Sherwood number at $Re^{(2)} = 10$
- 7.6b Time history of averaged Sherwood number at $Re^{(2)} = 50$
- 7.6c Time history of averaged Sherwood number at $Re^{(2)} = 200$

NOMENCLATURE

Symbol	Meaning	SI unites
a	acceleration	ms^{-2}
	thermal diffusivity	m^2s^{-1}
	coefficient in discretisation equation for variable ϕ	-
a_k	Fourier coefficient	-
a_l	grid controlling coefficient	-
b_k	Fourier coefficient	-
b_l	grid controlling coefficient	-
c_l	grid controlling coefficient	-
c	concentration	kgm^{-3}
C	coefficient of pressure correction equation	-
C_D	drag coefficient	-
d	bubble diameter	m
D	mass diffusivity	m^2s^{-1}
	diffusive conductivity	m^3s^{-1}
e_i, e_1, e_2	covariant coordinate base vector	-
E_2, ETN, ERZ, EVT	relative errors of calculation	-
Eo	Eotvos number	-
f_T, f_c	wake contribution factors	-
F	flow rate	m^3s^{-1}
F_D	drag force	N
F_g	gravity	N
Fr	Froude number	

g	acceleration due to gravity	ms^{-2}
G	contravariant related velocity component	-
Gr	Grashof number	-
h	height of bubble	m
J	Jacobian transformation number	—
\mathcal{J}	convection-diffusion flux	m^3s^{-1}
\mathcal{J}^C	convection flux	m^3s^{-1}
\mathcal{J}^D	diffusion flux	m^3s^{-1}
k	coefficient of convective mass transfer	ms^{-1}
L	length of wake vortex	m
	cavity boundary length	m
\dot{m}_p	imbalance of mass source	m^3s^{-1}
m_b	mass of bubble	kg
Mo	Morton number	-
n	magnitude of normal vector	m
p	pressure	Pa
Pe	Peclet number	-
Pr	Prandtl number	-
P_s	pressure coefficient	-
P_1, P_2	grid control functions	-
r	radius in axisymmetric coordinates system	m
R	position	-
R_a	curvature radial in azimuthal surface	m
R_m	curvature radial in meridional surface	m
s	arc length	m
	bubble surface area	m^2
$S, S', S'', S_1, S_2, S_{DC}$	source terms in general governing equations	-

Sc	Schmidt number	-
Sh	Sherwood number	-
T	temperature	[K]
t	time	s
	magnitude of tangential vector	m
u	velocity component in $x - (r -)$ direction	$m s^{-1}$
v	velocity component in $y -$ direction	$m s^{-1}$
V	absolute velocity	$m s^{-1}$
V	volume	m^3
w	width of bubble shape	m
W	relative velocity in non-inertial coordinates system	$m s^{-1}$
We	Weber number	-
x	horizontal coordinate	m
y	vertical coordinate	m

Greek symbols

α	metric parameter	-
α	coefficient of convective heat transfer	$W m^{-2} [K]^{-1}$
$\alpha_\phi, \alpha_{pro}, \alpha_{uz}$		
	relaxation factors	-
β	metric parameter	-
	inclination angle	-
β	coefficient of cubic expansion	$[K]^{-1}$
$\varepsilon_{\bar{n}}, \varepsilon_{pro}, \varepsilon_{ref}, \varepsilon_{\bar{i}1}, \varepsilon_{\bar{i}2}$		
	criteria of error	-
ϕ	general variable	-
	level set function	-
	volume fraction of fluid	-
γ	metric parameter	-

η	curvilinear coordinate	-
μ	dynamic viscosity	$\text{kg m}^{-1} \text{s}^{-1}$
ν	kinetic viscosity	$\text{m}^2 \text{s}^{-1}$
λ	coefficient of heat conductivity	$\text{Wm}^{-1}[\text{K}]^{-1}$
π	ratio of the circumference of a circle to its diameter	-
θ	circumferential angle (measured from front stagnant point)	-
ρ	density	kg m^{-3}
σ	surface tension coefficient	N m^{-1}
τ	tensor of stress	N m^{-2}
Ω	dimensionless vorticity	-
ξ	curvilinear coordinate	-
χ	ratio of variation	-
$\varphi(\chi)$	flux limiter	-
κ	numerical parameter	-
ζ	surface tension	Nm^{-2}
Φ_ρ	ratio of density (dispersed phase to continuous phase)	-
Φ_μ	ratio of viscosity (dispersed phase to continuous phase)	-
Γ	diffusion coefficient	-
	position of gas-liquid interface	-
Δ	finite difference operator	-
∇	gradient (Hamilton) operator	-
\mathfrak{R}	volume scaling factor	-

Subscripts

av	averaged value of a variable
e, w, n, s	four facets of control volume
E, W, N, S	nodes adjacent to P
eff	effective value
eq	equivalent values

g	pertaining to moving grids
\bar{n}	pertaining to normal direction of bubble profile
O	pertaining to origin of non-inertial coordinates system
P	nodal point to be solved in difference equation
r	relative to moving mesh
ref	referential value
sys	state of the system environment
\bar{t}	pertaining to tangential direction of bubble profile
Z	values at zonal boundary
$Z-1$	values on the first inner grid near zonal boundary
ξ, η	partial derivative with respect to ξ, η

Superscripts

1, 2	components in ξ and η directions respectively
(1), (2)	domain indexes for multi-block system
O	values at an old time level
*	initial value
'	correction
n	values at last time level
$n+1$	values at new time level
K	values at last iteration
$K+1$	values at new iteration
O	values at old time level

Top Scripts

–	normalised variables (omitted after chapter 3)
→	vector
^	tensor
~	intermediate value
	Leonard normalised variable

Dimensionless Parameters

$$C_D = \frac{8F_D}{\rho^{(2)}V_{ref}^2\pi d_{ref}^2} = \frac{4gd_{ref}}{3V_{ref}^2} = \frac{4Eo^{\frac{3}{2}}}{3(\text{Re}^{(2)})^2 Mo^{\frac{1}{2}}} = \frac{4}{3} \cdot \frac{1}{Fr}$$

Drag coefficient

$$Eo = \frac{gd_{ref}^2 \rho^{(2)}}{\sigma}$$

Eötvös number

$$Fr = \frac{V_{ref}^2}{gd_{ref}} = \frac{(\text{Re}^{(2)})^2 Mo^{\frac{1}{2}}}{Eo^{\frac{3}{2}}}$$

Froude number

$$Gr = \frac{g\beta(T_1 - T_{ref})d_{ref}^3}{(\mu/\rho)^2}$$

Grashof number

$$Mo = \frac{g(\mu^{(2)})^4}{\rho^{(2)}\sigma^3}$$

Morton number

$$Nu = \frac{\alpha d_{ref}}{\lambda} = \frac{\partial \bar{T}}{\partial \bar{R}} \Big|_{\bar{R}(\Gamma)}$$

Nusselt number

$$Pe^{(i)} = \frac{V_{ref}d_{ref}}{D^{(i)}} = Re^{(i)} Sc^{(i)}$$

Peclet number

$$Pr^{(i)} = \frac{\mu^{(i)}/\rho^{(i)}}{a^{(i)}}$$

Prandtl number

$$Re^{(i)} = \frac{\rho^{(i)}V_{ref}d_{ref}}{\mu^{(i)}}$$

Reynolds number

$$Sc^{(i)} = \frac{\mu^{(i)}/\rho^{(i)}}{D}$$

Schmidt number

$$Sh = \frac{kd_{ref}}{D} = \frac{\partial \bar{c}}{\partial \bar{R}} \Big|_{\bar{R}(\Gamma)}$$

Sherwood number

$$We = \frac{\rho^{(2)} V_{ref}^2 d_{ref}}{\sigma},$$

Weber number

$$\Phi_\rho = \rho^{(1)} / \rho^{(2)}$$

ratio of density

$$\Phi_\mu = \mu^{(1)} / \mu^{(2)}$$

ratio of viscosity

Chapter 1

Introduction

This chapter gives an introduction to the research work in this thesis. Based on an explanation of the background of the project, concise descriptions of the aims and the objectives of the research are presented.

1.1 Background

In chemical reactors based on gas-liquid reactions (oxidation, chlorination, hydrogenation, fluoridation etc.), heat and mass transfer occur between the gas and liquid phases. The rate of transfer, and hence the production capacity of the reactor, depends on the surface area of the bubbles and the concentration gradients in each phase coupled with the local rate of reaction. To analyse such a complex situation, we must firstly understand how the concentration field becomes established. The most important stage in the establishing of concentration field is the development of the flow fields within and around the bubbles, coupled with the accompanying increase of surface area and the evolution of bubble shape, immediately after the bubbles entered the vessel through the sparger. Although the attempt to numerically model two-phase bubbly flows has been made in a number of research papers, the mechanism of heat and mass transfer at gas-liquid interface is still unclear.

The nature of bubbly flows in chemical reactors is extremely complex. The behaviour of bubbles, which includes the interface trajectory, the evolution of bubble shape and bubble coalescence and etc., are three dimensional, heterogeneous and transient phenomena and reflect significant effects of the non-linear interactions of two phases. A recent EPSRC supported work at the University of Surrey (Smith, 1998) experimentally

studied the behaviour of a single bubble saturating in a hot volatile liquid. This study revealed that a large volume of vapour could pass into the gas phase as the bubbles were sparged into a hot liquid; the vapour dilutes the driving force for mass transfer and increases the bubble size greatly. The experimental also showed that a large bubble usually rises faster than small bubbles, so the contact time for mass transfer is shorter for large bubbles. In order to optimise sparger design and performance, a detailed understanding of the initial saturation dynamics is required: this provides the primary objective for the present research. In order to obtain such an understanding, it is beneficial to start with numerical simulation of an inert bubble introduced into a hot liquid and analysing the heat and mass transfer at the gas-liquid interface.

This EPSRC supported research (Yan and Smith, 1999), which will be entirely numerical and theoretical, will try to study the dynamics of an isolated inert bubble introduced into a hot liquid. The behaviours of the inert bubble, especially the heat and mass transfer at the gas-liquid interface, will be carefully studied. The research is of significant industrial benefit, as it will provide starting points for large-scale simulations of two-phase bubble related processes in reactors and for the improvement of related industrial processes. In particular, this study provides proofs for evaluating the importance of introducing of fresh gas and of maintaining small bubble sizes.

1.2 Aims and Objectives

Aims:

- (1). To contribute to the understanding of unsteady heat and mass transfer between bubble and liquid phases.
- (2). To improve the understanding of the development of the fields within and around the bubble, and the evolution of the bubble's surface area and shape.
- (3). To improve and develop the capabilities of CFD methods to simulate the bubble behaviour.

Objectives:

- (1). To establish the physical and mathematical models to describe a single inert bubble introduced into a hot liquid;
- (2). To develop numerical methods for moving boundary problems on the basis of the finite volume discretisation on general non-orthogonal moving mesh system. The moving boundary is designed to track a moving gas-liquid interface explicitly and accurately;
- (3). To further improve the numerical algorithm to be second-order accurate so that it can be used for studying the mechanism of mass transfer at the interface;
- (4). To develop Fortran codes using the proposed numerical algorithm;
- (5). To treat a gas-liquid interface and develop the codes to be capable of simulating gas-liquid interfacial flows;
- (6). To carry out simulations of conjugate flows inside a spherical bubble and its surrounding unbounded quiescent liquid;
- (7). To numerically study the momentum, heat and mass transfer and their relevant basic mechanisms for deformable bubbles at the terminal steady state;
- (8). To carry out time-accurate simulations for heat and mass transfer between a single inert bubble and a hot liquid, study the dynamic behaviour of the bubble and analyse the related transfer mechanism.

1.3 Outline of the Work

As stated earlier, this research is entirely theoretical and numerical. The main works are organised and presented in the following seven chapters.

Chapter 2 is a review of literatures. In this chapter, both the theoretical and experimental studies on the dynamics of single bubbles introduced into unbounded liquids are summarised. Considering the tasks of current work, special attentions have been given

to the analysis models and numerical methods for studying single bubbles.

Full physical model and mathematical description for the single inert bubble problem are presented in chapter 3. The complex unsteady heat and fluid flows inside and around the bubble are physically modelled and the gas-liquid interface is highlighted. Based on the physical model, full Navier-Stokes equations for incompressible heat and fluid flows and relevant well-posed initial and boundary conditions are presented.

Viewing from the computational fluid dynamics (CFD), the tracking of a gas-liquid interface is a moving boundary problem. Chapter 4 presents a complete numerical procedure for a general moving boundary problem. The procedure incorporates a moving non-orthogonal mesh arrangement with a multi-block iteration strategy to assist future simulations of heat and mass transfer in the inert bubble problem. The total variation diminishing (TVD) schemes are introduced to obtain high-order accuracy. The algorithm is developed into a Fortran code and is validated.

Chapter 5 deals with two challenging tasks in calculating the deformable gas-liquid interface. To decide the velocity components at the interface, a continuous stress method is proposed; In the meanwhile, a modified Ryskin-Leal method is introduced to decide the position of the interface. A complete solution approach for conjugate heat and fluid flows in the inert bubble problem is presented and employed to study gas-liquid interfacial flow problems in bubbles.

Steady heat and mass transfer in an inert bubble introduced into a hot liquid are carefully studied in chapter 6. Considering the importance of spherical bubble model, the conjugate flows inside and around spherical bubbles are simulated to study the flow structure and interfacial characteristics. As the main work, detailed numerical studies on the bubble shape, flow structure, drag coefficient and heat and mass transfer are carried out for moderately deformed bubbles. The effects of the wake vortex on heat and mass transfer are observed and analysed; a physical explanation for the recovery of Nusselt

and Sherwood numbers in the flow separation zone is proposed.

In order to study the time-dependent deformation and evolution of the inert bubble, chapter 7 carries out time-accurate simulations for the rear flattened, front flattened and fore-aft symmetric bubbles, based on the supplement of numerical methods and controlling equations for the rising velocity and acceleration derived from analysis of the forces acted on the bubble. Analysis on the evolution and propagation of temperature and concentration fields are presented.

The conclusions of the research and recommendations for further work are given in chapter 8.

Chapter 2

Literature Review

2.1 Introduction

A single bubble, which is recognised as the basic element of bubbly flows, can be employed as a starting point to study the mechanism of heat and mass transfer in bubbly flow based chemical reactors because rising bubbles play a decisive role in heat and mass transfer. The study of a single bubble embedded in liquid provides understanding the basic mechanism of heat and mass transfer between gaseous and liquid phases.

It can be traced back to 500 years ago when the behaviour of a rising bubble was observed and recorded (see the description of Krishna and Baten, 1999). Clift, Grace and Weber (1978) summarised a listing of 1200 contributions to the subject of the motion of bubbles, drops and particles. However, detailed studies on the dynamics behaviours such as the time-dependent characteristics of heat and mass transfer and relevant mechanisms are still relatively limited.

This chapter presents a brief review for the available research works on the study of the dynamics of single rising bubbles. Related to our study, the review will be only restricted to works of a general purpose on a single rising bubble embedded in an unbounded liquid. The researches about oscillatory motions (the fluctuation of the volume or shape of the bubble around some equilibrium value); formation, growth and departure from superheated walls; rising in electric or magnetic fields; effects of interfacial surfactant on heat and mass transfer; and any other special techniques which have special mechanisms on heat mass transfer enhancement, will not be included in this review because they are not the topics of current study; Good reviews in these

topics have been made by other researchers (Son, Dhir and Ramanujapu, 1999; Ueno, Nishita and Kamiyama, 1999; Takata, Shirakawa, Tanaka, Kuroki and Ito, 1996; Ponoth and McLaughlin, 2000).

The review is organised according to investigating methods applied such as experimental and numerical studies. As our research is entirely numerical and theoretical, attention will be mainly paid to numerical simulations.

2.2 Experimental Study on Single Rising Bubbles

Experimental verification is the most effective approach to provide the first hand results in real situations for bubble dynamics study. Especially with the advent of laser based velocity anemometers in 1970s, experimentalists have optical tools which now permits a more accurate measurement of refractive index effects and can provide them with a quantitative improvement in the quality of resolution of bubble dynamics.

Experimental studies of translational bubble motion are concerned almost completely with the kinematics aspects of motion. These studies have revealed that kinematics aspects of bubble motion, such as bubble shape, trajectory, rising velocity, drag and wake of a bubble, are dependent upon its size and upon the physical properties of the liquid.

2.2.1 Bubble Shape

The shape of rising bubbles can be observed by means of flow visualisation technique and have been studied by Haberman and Morton (1953, 1954), Saffman (1956), Hartunian and Sears (1957), Hnat and Buckmaster (1976), Hacker and Hussein (1978), Bhaga and Weber (1981), Vassallo, Symolon, Moore and Trabold (1995), Duineveld (1995), Maxworthy, Gnann, Kurten and Durst (1996) and Raymond and Rosant (2000).

According to Clift, Grace and Weber's (1978) summary, different shapes of bubbles are determined based on the balance of inertia, lift, viscous and surface tension force. For air bubbles in water, as bubble size increases, bubble shape changes sequentially from spherical (for $d_{ref} < 0.1$ cm), where the surface tension forces dominate, through ellipsoidal, to spherical cap (for $d_{ref} > 2.0$ cm). In low viscosity liquids, such as water, there is also a transition region between ellipsoidal and

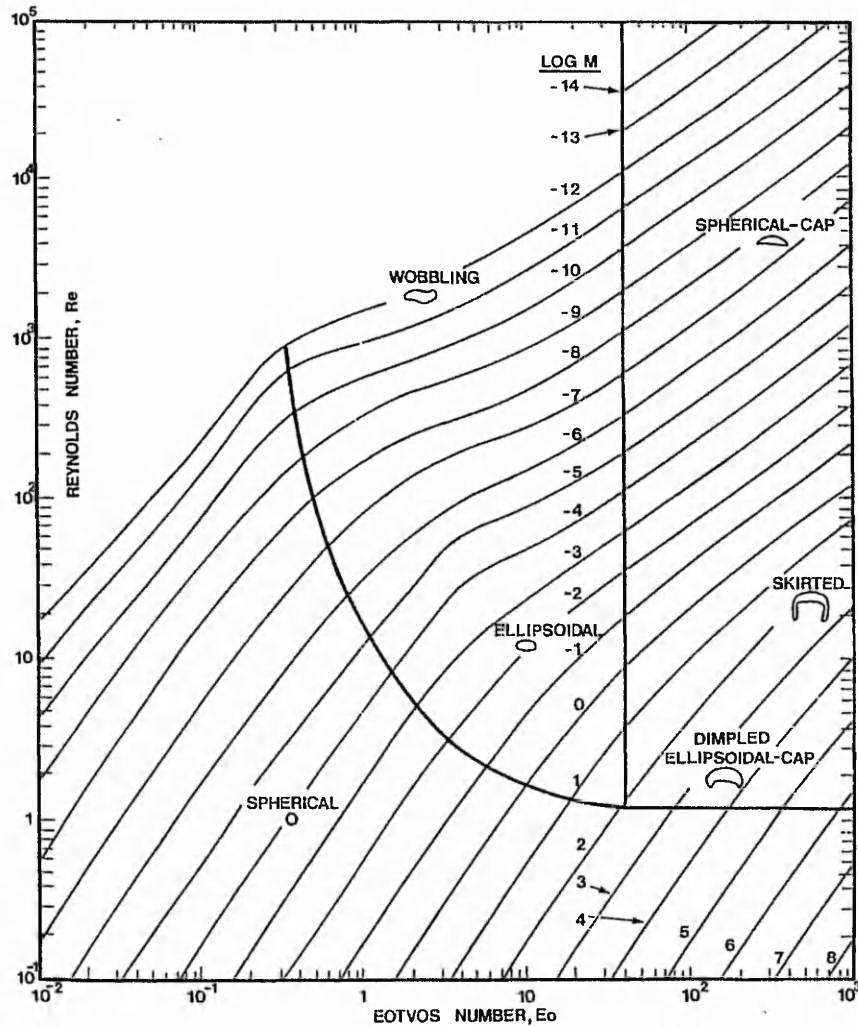


Figure 2.1 Shape regimes for bubbles and drops in unhindered gravitational motion through liquids

spherical cap shape regions ($1.0 \text{ cm} < d_{ref} < 2.0 \text{ cm}$), where bubble-shape is very irregular and unsteady. A complete map for bubble shape regimes in terms of Reynolds number, Morton number and Eotvos number was initially provided by Grace (1973) and is shown in figure 2.1. This map was further extended by Bhaga and Weber (1981) and by Maxworthy, Gnann, Kurten and Durst (1996). Shape regimes and terminal rise velocities have been correlated.

It should be mentioned that Duineveld (1995) studied the rise of slightly deformed bubbles in water. Based on the fact that in a liquid with a low Morton number, bubbles rising at large Reynolds number will have reasonably small deformation, “hyper clean” water was used as testing liquid to measure rise velocities and shapes of rising bubbles whose equivalent radius were varied between 0.33 and 1.00 mm. This experiment fills a gap concerning bubbles with high Reynolds and low Weber numbers.

2.2.2 Trajectory of Rising Bubble

Bubble trajectory was paid attention by Saffman (1956) and Hartunian and Sears (1957) both reported on experiments and theory dealing with path instability of a rising bubble. As summarised by Plesko and Leutheusser (1982), the bubble trajectory is generally rectilinear. However, ellipsoidal bubbles rising in clean liquids of low viscosity (such as filtered water) tend to follow a zigzagging or spiralling path. This phenomenon has been attributed to the periodic shedding of vortices behind the bubble, as vortex shedding has been observed experimentally to occur for rigid spheres at corresponding orders of magnitude of Reynolds number.

2.2.3 Rising Velocity and Drag

Terminal rising velocity is also an important parameter of bubble dynamics. In fact, almost nowadays' available experiments on bubble shape also provide results of bubble rising velocity, as bubble rising velocity is closely related to drag force, therefore,

bubble steady shape and terminal velocity are regarded as two main points of practical interests in engineering applications.

Haberman and Morton (1954) carried out extensive experiments, measuring rising velocities as a function of bubble size for various liquids. The results show that rising velocity is a steadily increasing function of the bubble size except for ellipsoidal bubbles in clean liquids of low viscosity. For these the velocity attains a maximum value at the upper limit of the ellipsoidal shape region, and then falls to a minimum as bubble size increases, before starting to rise again. Spherical cap rises at a velocity, which is independent of liquid properties and also confirmed by Komazawa, Otake and Kamojima (1980). Soo (1967) also reveals that the rise velocity of small bubbles is influenced by viscosity and surface tension of the fluid whereas that of large bubbles appears to depend on bubble size and its deformation.

Hacker and Hussein (1978) carried out the first application of a Laser-Schlieren technique to study of a single rising bubble dynamics. Two Newtonian fluids of widely differing properties were used as surrounding liquid. The results show that large volume ($> 3 \text{ cm}^3$) bubble takes a shape of stable spherical cap and move with a rectilinear path, surface tension is not an important parameter in influencing drag and rising velocity of these bubbles.

Miyahara and Takahashi (1985) studied previous data for the drag coefficient of a single bubble rising in a quiescent liquid are correlated with the Reynolds number on the basis of the major axis of the bubble. It was found that the drag coefficient is a function of Reynolds number only for Morton numbers above 10^{-7} , and also for Morton numbers below 10^{-7} provided the Reynolds number is below 10. Otherwise, the drag coefficient depends on Morton number. The drag coefficient is constant at high Reynolds numbers.

Vassallo, Symolon, Moore and Trabold (1995) measured freon bubble rising in a vertical rectangular duct, their results are used to obtain drag model for higher void fraction bubbly flow.

Raymond and Rosant (2000) presented some results for moderate deformed bubbles concerning the drag coefficient and deformation in the range of $(Re, We) = [1, 100] \times [0, 5]$. The experiments were made in tap water/glycerol mixtures. The experiment was made to compensate relations concerning the bubble aspect ratio in a large Morton number range $(9 \times 10^{-7} < Mo < 7)$.

The above measurements are mainly limited to time-averaged properties such as bubble shape and rising velocity. The temporal fluctuations in such properties have not been studied extensively to the date. Luewisutthichat, Tsutsumi and Yoshida (1997) carried out an attempt to characterise the time evolution of a single rising bubble motion in stationary liquids. In their study, time dependent dynamic changes in rising velocity, shape and orientation of bubbles were simultaneously measured using a flow visualisation method. Both deterministic chaos and stochastic analyses were used to diagnose bubble dynamics in gas-liquid two-phase systems. The bubbles were found to have chaotic fluctuations in shape and rising velocity. The Kolmogorov entropy and correlation dimension of the attractor reconstructed from time-series data of bubble-shape indices and velocity components by the embedding method were found to be positive and very high, indicating the chaotic-time evolution of bubble motion. On the other hand, the bubble inclined angle exhibited a periodic variation in bubble motion, reflecting the zigzag motion of rising bubbles. The fluctuation in bubble-rise velocity is considered to take place in streamwise direction due to the oscillation of drag force associated with the bubble-shape fluctuation.

2.2.4 Pressure Field and Wake

Pressure field measurements offer information of pressure fluctuations related to bubble

motion. Jezdinsky and Naudascher (1972) found through their experiments that, the magnitude of pressure fluctuations increases with air flow rate and bubble size, that the bubble shape is unsteady in the zone of separation, and that, no matter what size is originally, the bubble size beyond the zone of separation is similar to the size of turbulent eddies in the zone of separation. The investigators postulated that the pronounced increase in the magnitude of the pressure fluctuations (up to an order of magnitude greater than in flows containing no air) is due to the oscillatory behaviour of the bubbles which results from the deformation and break up of the bubbles.

Lazarek and Littman (1974) presented their results of pressure field due to a large circular capped air bubble rising in water. The result shows that pressure field extends axially as far as ten times of bubble half-widths below the bubble floor. Immediately below the floor the pressure is constant for about two-thirds of a bubble height. The wake is closed and contains symmetric pressure minima. Based on the pressure field, their further analysis also reveals that momentum and energy distributions in wake are controlled by turbulence and vorticity diffusion.

Plesko and Leutheusser (1982) focused their attention on the pressure associated with the motion of large, isolated spherical cap air bubbles rising either freely, or through a local constriction in a vertical cylindrical pipe filled with quiescent water. The pressure, measured at the pipe wall, was found to be as high as the dynamic bubble pressure for translational bubble motion.

During the free-rise of a single bubble through a liquid, an amount of the liquid is inevitably carried up behind the bubble, and this is known as the wake. It has been noticed that liquid carries dissolved gas from bubble and preferentially transfers it into the wake and an enhanced dissolved gas concentration can be observed in the wake (Schmidt, Nassar and Lubbert, 1992). Therefore, bubble wake can be regarded as having close relation with mass transfer, and this has been paid close attention by researchers.

Komasawa, Otake and Kamojima (1980) studied the wake dynamical behaviour of a single spherical-cap bubble by holding the bubble stationary using a downward liquid flow in a vertical channel. Through their study, three types of bubble wake were found. These are laminar wake ($10 < Re < 90$), transitional wake ($90 < Re < 500$), and turbulent wake ($Re > 500$). And it was found that laminar wakes are of a decisive effect on the rising velocity of the trailing bubbles, in which an additional velocity component caused by the wakes of the preceding bubbles was correlated well with wake velocities. The turbulent wakes have a limited effect on the acceleration of trailing bubbles and often cause bubble break.

Bessler and Littman (1987) experimentally investigated the wake behind a circularly capped bubble rising in fluids of different viscosity by using aspirin powder for flow visualisation and high-speed photography synchronised with pressure-time measurements to measure the pressure field. The bubble plus its primary wake with a cusped tail is observed to contain symmetric pressure minima within the primary wake. The details of wake structure such as a free shear layer contains large scale vortexes generated near bubble rim in the boundary wake, and the document for wake geometry change and transition to an ellipsoidal as fluid viscosity increases, were provided. Based on these, a wake model of circularly capped bubble and its primary wake was built.

Tsuchiya and Fan (1988) examined the fluid mechanic behaviour of the wake of a single bubble in a two-dimensional liquid-solid fluidised bed visually via a camera moving at the same speed as the bubble. The bubble wake was observed to consist of two regions: primary wake (near wake) and secondary wake. Wake formation-shedding mechanisms were illustrated for both symmetric and asymmetric shedding modes. In their study, the shedding frequency, expressed in terms of the Strouhal number, was shown to be a function of the bubble Reynolds number but independent of particle properties. It was also observed in their experiments that the primary wake size periodically varies in the form of a saw-tooth wave function, while the liquid wake exhibits no appreciable cyclic

variation in size. Based on their extensive study and research, Fan and Tsuchiya (1990) presented an excellent summary and review on bubble wake dynamics.

Schmidt, Nassar and Lubbert (1992) studied local dispersion in the liquid phase of gas-liquid reactors. Experiments on single bubbles was performed in order to demonstrate the key aspects and to estimate characteristic parameters of their physical model presented to describe the local mixing in liquid phase of gas-liquid flows agitated by rising bubbles. Local mixing mechanism and the high concentration of dissolved gas in the wake were explained.

Chen and Chou (1998) and Chen, Wang and Lin (1999) studied bubble wake dynamics of a single bubble rising in a two-dimensional column and a two-dimensional fluidised bed, respectively, using particle image analyser (PIA) system (based on the particle tracking technique). In these studies, fluid mechanic behaviour of wake is recorded by a high-frame-rate camera moving at the same speed as the bubble, PIA system and an interpolation are exerted to quantify the local microscopic flow properties. Through the topological characteristics of integrated streamline pattern, the formation-shedding mechanism of turbulent wake induced by a single rising bubble is illustrated. It is revealed that formation/shedding of a Strouhal vortex is dependent on the stability of free shear layer located on the side boundary of wake.

A study on the bubble wake dynamics behind a single bubble rising in stagnant water in a circular pipe is conducted by Hassan, Ortiz-Villafuerte and Schmidll (1999) using a whole volume three-dimensional particle image velocimetry flow measurement system. Transient investigations on the wake size and the wake decaying time were performed.

2.3 Analysing and Numerical Research on Single Rising Bubbles

Synchronal to experimental observations, analyses on the behaviours of single rising bubbles have also attracted attentions of researchers and been put in an amount of works. With the development and advances in computing technology and computational fluid dynamics (CFD), numerical studies on single rising bubbles are becoming more and more popular; and the effectiveness and excellent efficiency of numerical investigating methods have been shown.

2.3.1 Flow Models

The development of analysing models for flows in single bubbles is a procedure of from simplicity to completion. This can be explained by the facts that the shape of bubble was treated as spherical but now is deformable; the flow was regarded invicid but now is viscous; the transfer phenomena was analysed using external model but now using conjugate model; and the state of flow for analysing was only steady but now can be unsteady. Here we focus on reviewing researches on spherical bubbles and on development of conjugate flow models.

Analysis on spherical bubbles

The sphere (one-dimensional) model has always played an important role in the study of single bubble dynamics since Hadamard (1911) and Rybzyński (1911) obtained the analytical solution for creeping flow ($Re < 1$) inside and outside a fluid sphere. Indeed, this one-dimensional model is sometimes still used nowadays in qualitative analysis (Magnaudet, Rivero and Fabre, 1995).

The sphere model is mainly used to study bubble growth on a heated wall, which is a main topic of nucleate boiling. Rayleigh (1917), Plesset and Zwick (1954), Tong (1966), and Mikic, Rohsenow and Griffith (1970) all worked on obtaining a time-dependent formula for the radius of a sphere bubble. All these works are foundations for the study of nucleate boiling.

The first attempt to analyse the growth of a bubble in motion was made by Ruckenstein (1964). Later, Tokuda, Yang and Clark (1968), Ruckenstein and Davis (1971), Pinto and Davis (1971), Buyevich (1975), Shah and Sha (1978), Ida and Sugiya (1980) carried out analytical studies on the growth coupled with motion of a single spherical bubble.

The one-dimensional (spherical) bubble model has provided a simple and quick analysing method and some understanding of the bubble dynamics. However, for a real inert bubble embedded in an infinite liquid, it is impossible to keep the spherical shape and therefore its bubble dynamics, such as local heat and mass transfer, cannot be revealed by using this model and therefore, the determination of the shape of deformable bubbles has become an important topic in numerical study of interfacial flows which will be reviewed later.

External and conjugate flows

The phenomena of momentum, heat and mass transfer between a translating bubble or drop and its surrounding fluid is classified as “external” (if the transfer resistance is assumed negligible inside the dispersed phase as compared to that of continuous phase), “internal” (if the transfer resistance in the continuous phase is assumed negligible as compared to that inside the dispersed phase), and “conjugate” (if the transfer resistance in both phases is comparable to each other). For a single bubble rising in an unbounded liquid, its density and viscosity in gas side are generally smaller in magnitude order than those of liquid side, so the heat and fluid flows in the single rising bubble are often treated as an “external flow” problem, which means the flow and temperature fields inside the bubble are often regarded as uniform and constant (at the saturation points); and the gas-liquid interfacial flow can be treated as a “free boundary problem”, which indicates zero tangential stress at the interface. The external flow models of bubbles have been widely employed by researchers (Ryskin and Leal, 1984a, 1984b; Cao and Christensen, 2000; Raymond and Rosant, 2000; Yoon, Koshizuka and Oka, 2001; Li and Yan, 2002a, 2002b; Yan and Li, 2002).

Physically, the momentum, heat and mass transfer procedures through a gas-liquid interface are decisive to the production capacity of a device and are closely related to the conjugate flows inside and around the bubbles. In order to understand the mechanisms of these transfer phenomena, the conjugate heat and fluid flows at both sides of the interface should be carefully studied.

Bubble internal phenomena are also important facets of bubble dynamics. When an inert bubble is introduced into a hot liquid, heat and mass transfer take place at the interface and therefore the bubble is consisted of vapour and inert gas. With changing of surrounding pressure, the internal phenomena, such as thermal diffusion, diffusion between gases, possible formation of the mist due to bubble expanding and condensation, and heat and mass transfer through bubble wall, have a significant influence on bubble motion (Takemura and Matsumoto, 1994).

Chao (1962) made a first analysis, for the transient response behaviour of the thermal or concentrate boundary layers for a liquid droplet moving at a constant velocity, which has taken the effects of internal circulation included. Although this study was mainly on the relation between bubble growth and bubble moving, the importance of internal phenomena had come to be paid attention.

There were some studies where the internal phenomena inside the bubble were considered in the past two decades. Migmatulin, Khabeev and Nagiev (1981) and Kamath and Prospereti (1989) analysed the bubble motion numerically taking thermal diffusion into account. Matsumoto and Takemura (1992) simulated the bubble motion by integrating directly the full equations for mass, momentum and energy conservation inside and outside the bubble, and analysed the effects of internal phenomena on bubble motion. The results reveal that the bubble motion is affected by heat mass transfer inside and outside the bubble; and dimensionless heat conductivity influences the damping of bubble oscillation. They also show that the boundary layer of vapour

concentration is formed inside the bubble and diffusion affects the bubble motion. The distribution of concentration of vapour and the mass of vapour inside the bubble are correlated by the dimensionless diffusion coefficient.

An investigation of effects of internal phenomena on bubble motion when the surrounding pressure decreases stepwise was reported by Matsumoto (1986). Single bubble expanding process is studied, where a model of internal conditions during bubble motion on the assumption that temperature distribution is uniform except near bubble wall is proposed. The result reveals that gas mixture inside the bubble expands adiabatically and the temperature becomes low at the beginning of the expanding. Then mist appears inside the bubble due to homogeneous condensation and the temperature is restored to that of liquid. It is concluded that the gas mixture inside a bubble behaves almost isothermally.

The effects of internal transport phenomena on the motion of the single bubble, suffering from stepwise decreasing surrounding pressure, was numerically simulated by Takemura and Matsumoto (1994). In this simulation, the conservation equations for mass, momentum and energy are solved directly in order to estimate the effect of internal phenomena on bubble motion. At the same time, the mist formation in the gas phase and the diffusions of heat and non-condensable gas in the liquid phase are taken into account. The numerical results for several cases reveal that non-dimensional transport coefficients have large effects on the distributions of temperature, concentration of vapour and the mist formation. As the initial radius becomes smaller or depressurisation ratio becomes larger, bubble motion is less influenced by mist formation due to the heat penetration through the bubble wall by heat conduction.

Numerical study of solving full Navier-Stokes equations for conjugate heat and fluid flows in bubbles has been firstly carried out by Welch (1995, 1998). A conjugate heat and fluid flow model incorporated with an unstructured mesh were used in his calculation. However, the continuity of tangential stress at the interface was

unreasonably discarded in this work. Other conjugate numerical models can be found for a single drop falling at the terminal velocity in air, such as the works by LeClair, Hamielec, Pruppacher and Hall (1972); Rivkind and Ryskin (1976); Dandy and Leal (1989) and Juncu (1999).

2.3.2 CFD Algorithms for Studying Bubbles Using Full Navier-Stokes

In view point of CFD, a gas-liquid interface is a moving boundary problem, which is one of the most challenging problems to researchers (Shyy, Udaykumar, Rao and Smith, 1996). In order to study bubble behaviours, accurately modelling the interface and highlighting the fields in its vicinities are necessary. However, because of the discontinuity of physical-chemical properties across the interface, special technique is needed as the basic formula for fluid flows are based on the theory of continuous functions. Nowadays, three possible basic mathematical models for fluid flows are available; these are the well-established Navier-Stokes equations, the lattice-Boltzmann method (LBM) and molecular dynamics simulation (MDS) method. For the latter two models, they are newly developed and still in the developing stage although great potentials have been shown in developing them to simulate moving boundary flows (Yang, Dinh, Nourgaliev and Sehgal, 2000; Sankaranarayanan, Shan, Kevrekidis and Sundaresan, 1999; Kinjo, Ohguchi, Yasuoka and Matsumoto, 1999; Guo, Wang and Chen, 2000). For the time being, available robust algorithms for simulating gas-liquid bubble interface are still under the framework of Navier-Stokes equations, and a review will be made only for them in this paper; people have interest in LBM or MDS (Bird, 1995) can refer to the related literatures for details.

The Navier-Stokes equations based algorithms for the gas-liquid interfacial simulations can be classified in different categories. If according to the grid system employed, they can be put into Lagrangian methods and Eulerian methods. If according to the method of tracking a interface, they can be divided into the front tracking methods and the volume tracking methods. These algorithms can also be classified according to their

discretisation methods. Considering the key to solve a moving boundary problem being to track the moving boundary or interface that changes with time, this review catalogues the numerical techniques as:

- (a). surface tracking or predominantly Lagrangian methods (Harlow and Welch 1965; Vicelli, 1969; Chen, Garimella, Reizes and Leonardi, 1995);
- (b). volume tracking or Eulerian methods (Hirt and Nichols 1981).

Regardless the method employed, the following three essentials are needed to properly model an interfacial problem:

- (a). a scheme to describe the shape and location of a gas-liquid interface;
- (b). an algorithm to evolve the shape and location with time, and
- (c). interfacial boundary conditions applied at the surface.

In the following discussions we briefly review the types of numerical approaches and indicate the advantages and disadvantages of each method.

Arbitrary Lagrangian-Eulerian (ALE) method

Hirt, Amsden and Cook (1974) proposed an algorithm for solving invicid time-dependent flows. Ramaswamy (1990) developed this method for modelling unsteady viscous flows with free surfaces. According to Ramaswamy (1990), a physical time marching cycle, from the (n)th instant to the ($n+1$)th instant with a time increase Δt , can be divided into four sub-steps. These are Lagrangian calculation, rezoning, convective flux calculation, and scalars (temperature for example) calculation. In the Lagrangian calculation, the computational grid vertices are advected by a divergence-free flow velocity. This velocity is used to update the coordinates of the vertices (especially, to update the position of interface). For the rezoning, the interior grids (and therefore the whole mapping meshes) are regenerated using Thompson, Warsi and Mastin (1985)'s method, to conform the new boundary and eliminate the highly contorted deformation of internal grid lines by the Lagrangian advection, and the moving velocity of meshes are obtained. Thirdly, convective flux through the cells of updated

meshes (not Lagrangian meshes any more) are calculated and the velocity field is redistributed to the new meshes. Finally, the scalars such as temperature are obtained by solving their controlling equations on the moving meshes.

Fujita and Bai (1998) employed the ALE method to study the growth of an isolated bubble in nucleate boiling, quantitative description of the fluid and thermal fields surrounding the bubble was achieved. In order to improve the numerical accuracy of ALE, Li and Petzold (1997) tried to combine the moving mesh with high-order upwind schemes for the convection term, and good results were achieved in their simulation of discontinuous interface. Although the rearrangement of grid at every time step is needed, and the calculations maybe experience difficulties when the interface becomes multiple-valued (this corresponds to the topological changes of interface), the ALE moving mesh methods are still attractive because of their capability of highlighting the fields near interface, and the result of physical zero thickness of interface, which are always necessary to study the interface-related mechanism.

When the terminal steady state is calculate, the ALE moving mesh method becomes the body-fitted coordinates transformation method, proposed by Ryskin and Leal (1984a, 1984b). The moving mesh methods employed to track bubble surface and study bubble behaviour by Takagi and Matsumoto (1993, 1995) and Lee and Nydahl (1989) was the time-dependent form of Ryskin and Leal's (1984a, 1984b) method; it also belong to ALE in fact though implicit time-marching scheme was employed to replace the sub-step explicit time-marching.

The principal limitation of Lagrangian methods is that they cannot be used to track an interface which is changeable in topology. Even large amplitude surface motions are difficult to track without introducing regridding techniques.

Unstructured moving mesh method

The unstructured mesh finite volume method for gas-liquid two-phase flow by Welch

(1995, 1998) belonged to Lagrangian category because the mesh system was moving. In this method, the interface was embedded within control volumes defined on a moving triangular mesh and was tracked with nodes affixed on the liquid and vapour sides at the same spatial location. Using the moving mesh, a high grid resolution was kept near the interface to accurately represent the steep gradient attendant with the mass transfer problem. On finite volumes, mass, momentum and energy equations were solved using a semi-implicit procedure, in which thermodynamic equilibrium was assumed at the interface, and the state equations were extended smoothly into the saturation region allowing for the existence of metastable state. The interfacial motion was found from physics while the mesh motion in bulk regions was calculated by simple interpolation with neighbouring nodes.

Welch (1998) used this method to study heterogeneous vapour bubble growth and generally acceptable results were obtained in his investigation. The advantages of unstructured mesh are obvious; these include its excellent adaptability in grids generation and mapping complex geometries such as bubble shape. However, as compared with the algorithms using structured mesh, the unstructured mesh based algorithms are not easy to be vectorised and their accuracy, efficiency are worse although larger storage has been occupied because of the disorderliness of grid cells (Jameson and Mavriplis, 1985; Mavriplis and Jameson, 1987).

Front tracking method

Unverdi and Tryggvason(1992) put forward the front-tracking method, in which the interface itself is described by an additional Lagrangian computational element while the bulk flow (include the two phases) are computed with Eulerian meshes. In the front tracking method, an interface is explicitly tracked by an unstructured grid system. As the fluid properties, such as density and viscosity, are discontinuous across the interface, either excessive numerical diffusion or problems with oscillations around the jump are expected if no special treatment is used at the front. These problems are just unavoidable in the VOF methods. To solve these problems, the additional unstructured

Lagrangian meshes are introduced. However, these meshes are reduced in dimensions by 1 as compared with the bulk Eulerian meshes. That is, if the bubble is three-dimensional, the interface will be two-dimensional and the Lagrangian meshes are therefore in two dimensions. To avoid introducing disturbances of length scale equal to the mesh by having the properties jump abruptly from one grid point to the next, the interface is not kept sharp but given a small thickness of the order of mesh size. In this transition zone, the fluid properties change smoothly from value one side of the interface to the value on the other side. This artificial interface thickness is a function of mesh size used and does not change during the calculation.

The front tracking method is accurate because, firstly, no numerical diffusion or oscillation exists in the front tracking method; and secondly, the unphysical thickness of interface can be reduced as the unstructured mesh size is easy to be assigned. However, the weaknesses of front tracking method are also obvious, those are the complexities in both mathematics and programming; and in the physical, the surface-tension effects on the interface are simply distributed onto the fixed grid, the interface location still is not exactly specified.

Ervin and Tryggvason (1997) employed the front tracking method to simulate the rising bubble in a shear flow; Bunner and Tryggvason (1998) even developed this method into a parallel algorithm and used for the simulation of large three-dimensional bubble systems. Viewing from this, the front tracking method is still potential for bubble interface simulation if the local information about the bubble interface is not important.

Level-set methods

Level-Set Hamilton-Jacobi formulation (Osher and Sethian, 1988) was originally a notable new approach to solve the interfacial evolution problems such as morphological instability, Sussman, Smereka and Osher (1994) developed the algorithm to simulate incompressible flows with gas-liquid interfaces.

In the level-set method, a level set function ϕ , which is the distance from the interface in physical meaning, is used to track the interface. Assuming the interface is Γ , then the values for ϕ change in the following range:

$$\phi(\vec{R}, t) \begin{cases} > 0, & \vec{R} \in \text{liquid zone} \\ = 0, & \vec{R} \in \Gamma \\ < 0, & \vec{R} \in \text{gas zone} \end{cases}, \quad (2.1)$$

and the evolution of ϕ is controlled by the Halmilton-Jacobi equation as follows

$$\frac{\partial \phi}{\partial t} + \nabla \cdot (\vec{v} \phi) = 0. \quad (2.2)$$

The surface tension is expressed as a body force concentrated at the interface in the momentum equations, just like that of in the front tracking method by Unverdi and Tryggvason (1992). As ϕ is treated in a continuum approach, explicit reconstruction of the free surface (like that of VOF and front tracking method) from the level set function is then never needed, which also enable to calculate the surface tension and topological change of interface accurately. These are good virtues of level-set methods, and they are attractive in the simulation of gas-liquid interface. Sussman, Almgren, Bell, Colella, Howell and Welcome (1999) even tried to incorporate the single-grid method with adaptive mesh procedure to achieve higher resolution of free surface, results of fully three-dimensional air bubble and water drop can be found in their paper. However, although the interface can be remained sharp, it is still an artificially assigned finite thickness (Sussman, Almgren, Bell, Colella, Howell and Welcome 1999).

Although the level-set method is catalogued into the surface tracking (having good resolution at the interface), it uses a Eulerian mesh and therefore can be employed to cope with the difficulties associated with topological changes in the interface. However, the defect of mass conservation during the whole calculation (Son, 2001) still needs to be sorted out for the level-set method.

Marker-and-cell (MAC) method

Marker and cell (MAC) methods and volume of fluids (VOF) methods are the best-known volume tracking methods. The earliest numerical method devised for time-dependent, free-surface, flow problems was the Marker-and-Cell (MAC) method (Harlow and Welch 1965). This scheme is based on a fixed, Eulerian grid of control volumes. The location of fluid within the grid is determined by a set of marker particles that move with the fluid, but otherwise have no volume, mass or other properties.

Grid cells containing markers are considered occupied by fluid, while those without markers are empty (or void). An interface is defined to exist in any grid cell that contains particles and that also has at least one neighbouring grid cell that is void. The location and orientation of the surface within the cell was not part of the original MAC method.

Evolution of surfaces was computed by moving the markers with locally interpolated fluid velocities. Some special treatments were required to define the fluid properties in newly filled grid cells and to cancel values in cells that are emptied.

The application of free-surface boundary conditions consists of assigning the gas pressure to all surface cells. Also, velocity components were assigned to all locations on or immediately outside the surface in such a way as to approximate conditions of incompressibility and zero surface shear stress.

The extraordinary success of the MAC method in solving a wide range of complicated free-surface flow problems is well documented in numerous publications. One reason for this success is that the markers do not track surfaces directly, but instead track fluid volumes. Surfaces are simply the boundaries of the volumes, and in this sense surfaces may appear, merge or disappear as volumes break apart or coalesce.

A variety of improvements have contributed to an increase in the accuracy and applicability of the original MAC method. For example, applying gas pressures at interpolated surface locations within cells improves the accuracy in problems driven by hydrostatic forces, while the inclusion of surface tension forces extends the method to wider class of problems (Daly, 1969; Nichols and Hirt 1975).

In spite of its successes, the MAC method has been used primarily for two-dimensional simulations because it requires considerable memory and CPU time to accommodate the necessary number of marker particles. Typically, an average of about 16 markers in each grid cell is needed to insure an accurate tracking of surfaces undergoing large deformations.

Another limitation of marker particles is that they don't do a very good job of following flow processes in regions involving converging/diverging flows. Markers are usually interpreted as tracking the centroids of small fluid elements. However, when those fluid elements get pulled into long convoluted strands, the markers may no longer be good indicators of the fluid configuration. This can be seen, for example, at flow stagnation points where markers pile up in one direction, but are drawn apart in a perpendicular direction. If they are pulled apart enough (i.e., further than one grid cell width) unphysical voids may develop in the flow.

Volume of fluid (VOF) method

VOF (Volume of Fluid) method was initially proposed by Hirt and Nichols (1981). In VOF, a volume of fluid function with assigned values of 1 for cells contain one phase and 0 for those contain the other, is used to identify the location of interface as it is obvious that the interface lies in those cells take a function value in between. The VOF function ϕ , is a Lagrangian invariant of fluid, and its controlling equation (Hirt and Nichols, 1981) is an advection equation as follows

$$\frac{\partial \phi}{\partial t} + \nabla \cdot (\vec{v} \phi) = 0, \quad (2.3)$$

where

$$\phi(\vec{R}) = \begin{cases} 1, & \vec{R} \in \text{liquid zone} \\ 0, & \vec{R} \in \text{gas} \end{cases}, \quad (2.4)$$

is the void fraction. It is noticeable that equations (2.3) and (2.2) are completely the same in looking. However, equation (2.2) is as a Hamilton-Jacobi equation as ϕ is a continuous function which varies smoothly across the interface while equation (2.3) is an advection equation since the volume fraction ϕ is discontinuous there.

According to equation (2.3), which is based on concepts of continuous functions, the VOF function should vary continuously in spatial dimensions. In reality however, ϕ changes discretely from 1 to 0 over the interface whose physical thickness in space is zero, and therefore in computation, we expect the calculated thickness of interface is as infinitesimal as possible to get valid information of fields in the vicinity of interface. Consequently, special methods must be used to solve equation (2.3), which are the right tasks for CFD researchers.

Over the past years, more accurate schemes have been developed for equation (2.3) in VOF methods. For those calculations with direct difference of equation (2.3), Rudman (1997) employed a so-called flux-corrected transport (FCT) algorithm and put forward the FCT-VOF in which equation (2.3) is differenced using a combination of first-order upwind and downwind scheme, a comparison of this new scheme against other well-known schemes was undertaken in his work. Garrioch and Baliga (1998) developed a skewed subadvection scheme for multidimensional problems. However, the majority of VOF methods do not directly difference equation (2.3) but use a two-stage process, namely, free surface reconstruction and boundary flux integration. To recover the interface shape, piecewise constant schemes (SUFFER by Lafaurie, Nardone, Scardovelli, Zaleski and Zanetti, 1994) and piecewise linear schemes (Ashgriz and Poo

(FLAIR), 1991; Puckett, Almgren, Bell, Marcus and Rider, 1997; Rider and Kothe, 1998) of high resolutions, have been developed. Sou, Tomiyama, Zun and Yabushita (1997) compared the FLAIR with traditional “donor-acceptor” scheme (Hirt and Nichols, 1981) and found better accuracy for interface calculation can be achieved by the FLAIR. While to calculate the boundary cell flux accurately, Harvie and Fletcher (2000) developed a “Stream Scheme”, and a good review of VOF algorithms is available in their paper.

VOF methods have been widely employed in the simulations of gas-liquid bubble interface. Tomiyama, Sou, Minagawa and Sakaguchi (1993) analyse a bubble rising in stagnant liquid; Takata, Shirakawa, Tanaka, Kuroki and Ito (1996) simulated bubble growth under electric field; Krishna and Baten (1999) studied the rise characteristics of gas bubbles in a two-dimensional column; Bugg, Mack, and Rezkallah (1998) simulated the Taylor bubbles rising in vertical tubes. All of these investigations have employed the VOF methods and generally good results have been obtained.

However, the weaknesses of VOF methods are also obvious. Firstly, the stability of computation always arises from the varying of bubble volume when VOF is employed to simulate the bubble growth (Barkhudarov and Chin, 1994). In the second, a smeared interface is inevitable because of the numerical diffusion resulted from the “donor-acceptor” (Hirt and Nichols, 1981) or other schemes (for example, the FCT-VOF by Rudman, 1997), which are only first-ordered in accuracy. For higher ordered schemes, smearing can come from unphysical oscillations in the vicinity of interface. The thickness of interface is in a magnitude of 1.5 times of the mesh size. The uncertainties about interface shape and location have decided that VOF cannot be used for analysing the mechanisms of interface related phenomena. VOF is really not a method designed with intention to capture local physics near phase interfaces (Welch, 1998).

There are also some other methods available in the Eulerian algorithm family. We mentioned previously, in such methods, equation (2.3) also appears in their controlling

equations; these include the conserved-scalar method by Liu and Spalding (1988) and the method by Maronnier, Picasso and Rappaz (1999), both are volume tracking methods in which equation (2.3) is an advection equation.

2.3.3 Numerical Studies of Single Rising Bubbles

In earlier years, numerical studies of single bubble dynamics were carried out with Stokes equations. The inertial and viscous terms were neglected in the Navier-Stokes equations to reduce computational work (Youngren and Acrivos, 1976). With the fast development of computer sciences, the full Navier-Stokes equations have come to be widely used in numerical study of the behaviour of a single bubble, and many valuable studies have been carried out.

One of the most famous studies on a rising bubble by solving Navier-Stokes equations was presented by Ryskin and Leal (1984a, 1984b, 1984c). In their work, a gas-liquid interface was treated as a free boundary problem (tangential stress free for the interface). Navier-Stokes equations in terms of stream function and vorticity were solved to determine the flow field at the liquid side. Although the flow field was treated as steady, their strategies such as fitting the interface by grid line and determining the bubble shape by the normal stress balance, pioneered numerical simulations of a single bubble. Their results of wake vortexes, buoyancy-driven motion of a gas bubble through a quiescent liquid, and bubble deformation in an axisymmetric straining flow, showed quantitatively good agreement with experiments. This method was also used by McLaughlin (1996) to study bubbles in both pure water and contaminated water. Takagi and Matsumoto (1995) and Takagi, Matsumoto and Huang (1997) further developed Ryskin and Leal (1984a, 1984b, 1984c)'s method by using a moving mesh to study unsteady axisymmetric motion of a rising deformed bubble. Their results suggested that the growth of an axisymmetric shape oscillation causes three-dimensional motion of a rising bubble. In fact, this moving mesh method was just the arbitrary Lagrangian-Eulerian (ALE) calculating procedure that Yoon, Koshizuka and Oka (2001) employed

to simulate a gas bubble rising in viscous liquid. The shortcomings of these methods are the employment of an orthogonal BFC (Body Fitted Coordinate), which is difficult to construct for complex geometries, and the stream function-vorticity equations, which can not be used for a three-dimensional problem.

The employments of Eulerian type algorithms to study the dynamics of a single bubble are also largely presented. Tomiyama, Sou, Yoshikawa and Sakaguchi (1993, 1994) calculated bubble shapes and terminal velocities, using the VOF method, under wide ranges of Eotvos number and Morton numbers. Chen, Garimella, Reizes and Leonardi (1996) used a non-staggered SIMPLE method solving VOF controlling equations to study a bubble rising in a stationary liquid contained in a closed right vertical cylinder. Loth, Taeibi-Rahni and Tryggvason (1997) simulated a few cases of large deformable bubbles embedded in a non-linear free shear layer using a front tracking algorithm. Using a front tracking algorithm, Ervin and Tryggvason (1997) also studied the rise of a single bubble in a vertical shear flow. Krishna and Baten (1999) used commercial software, CFX4.1c, and employed VOF controlling equations, to study trajectories of bubbles of different diameters rising in a two-dimensional rectangular column filled with water. Li, Zhang and Fan (2000) studied the rising behaviour of a single bubble at elevated pressure in a bubble column using VOF method.

Numerical simulation has provided an economic and effective method to study bubble dynamics. Indeed, for fast transient dynamic behaviour such as bubble saturation where experimental methods seem completely impossible, numerical simulation is the only possibility.

2.4 Summary

2.4.1 Investigations on physical phenomenon

Based on the literature review in this chapter, it is found that little information is known in following aspects:

(a). Transport characteristics and flow structure for spherical bubbles

Clift, Grace and Weber (1978) stated that “for drops and bubbles rising or falling freely in systems of practical importance, significant deformations from spherical occur for all $Re^{(2)} > 600$ ” and “the shape of the drop or bubble remains spherical if the Weber number is small enough”. Recently, Juncu (1999) studied the structure of flow fields and interfacial characteristics of a drop for $Re^{(2)} < 500$. However, for a spherical bubble, the exterior Reynolds number $Re^{(2)} = 200$ appears to be the upper limit for which complete steady-state flow fields have been reliably determined so far.

(b). Effects of bubble internal heat and flows

Physically, the momentum, heat and mass transfer is a conjugate procedure between a gas bubble and a surrounding liquid; In order to study these mechanisms, both sides of the interface must be treated as real fluids although the fluid properties, such as density and viscosity, are different in magnitude order for gas and liquid.

(c). Heat and mass transfer in deformable inert bubbles

The mechanism of heat and mass transfer in an inert bubble introduced into a hot liquid is exactly the object of the current study.

2.4.2 Comparisons of numerical methods

In the Lagrangian methods, the grid is configured to conform the shape of the interface, and thus it adapts continually to it. The Eulerian methods usually employ a fixed grid formulation, and the interface between two phases is not explicitly tracked but is reconstructed from the properties of appropriate field variables, such as fluid fractions.

Based on these basic differences in approach of the two classes of methods, the following comparisons can be made:

(a). The Lagrangian methods maintain the interface as a discontinuity and explicitly can track its evolution. If detailed information regarding the interface location is desired, Eulerian methods may need elaborate procedures to deduce the interface location based on the volume fraction information, and uncertainty corresponding to one grid cell is unavoidable (Ashgriz and Poo 1991; Hirt and Nichols 1981; Lafaurie, Nardone, Scardovelli, Zaleski and Zanetti, 1994; Liang 1991). In the Lagrangian case, the interface can be tracked as an $(n-1)$ -dimensional entity for n -dimensional space (De Gregoria and Schwartz 1986; Glimm, Grove, Lindquist, McBryan and Tryggvason, 1988; Miyata 1986; Wang and McLay 1986). No modelling is necessary to define the interface or its effect on the flow field. In the cases of Eulerian schemes, modelling or solution of fractions or other functions yielding information in the two-phase regions.

(b). In Lagrangian method, boundary conditions can be applied at an exact location of the interface since the interface position is explicitly known at each instant. However, in an Eulerian method, the boundary conditions are manipulated to appear in the governing transport equations (Brackbill, Kothe and Zemach, 1992). This leads to smearing of a boundary condition.

(c). In a Lagrangian method, the grid adapts to the interface and hence the grid rearrangement and motion terms have to be incorporated. When the interface begins to distort, the grid needs to be regenerated each time, which may require the solution of another equation (Thompson, Warsi and Mastin, 1985). The resulting grid on which the field variables are computed may be skewed and unevenly distributed, thus influencing the accuracy of the field solver. The Eulerian methods have an advantage in this regard since the computations are performed on a fixed grid, hence obviating the need for grid rearrangement. However, when an interface is in an arbitrary shaped, it is difficult to obtain an improved resolution in desired regions, unless complicated local refinements are adopted.

Chapter 3

Physical and Mathematical Descriptions of the Problem

3.1 Introduction

According to the philosophy of CFD researches, an investigation on a certain problem is generally carried out in two steps:

- (a). based on a concrete physical phenomenon, propose a mathematical model which includes controlling equations and well-posed boundary conditions;
- (b). numerical solving of the mathematical model.

Our present study of the inert bubble problem is in line with this approach. As the first step, this chapter begins with the description of the physical problem, and then gives the governing equations and well-posed boundary conditions. The numerical method for solving the mathematical model will be presented in the next chapter.

3.2 Physical Model

Physically, the problem of an inert bubble introduced into a hot liquid can be summarised as “unsteady conjugate heat and fluid flows inside and around an inert bubble”. When the bubble is sparged into the hot liquid, it will rise up. The rising-up is an accelerating procedure during which the position of the gas-liquid interface $\vec{R}(\Gamma)$, flow velocity \vec{V} , acceleration \vec{a} , temperature T and concentration c are time-dependent, so the problem is unsteady; While in order to study the mechanism of the heat and mass transfer at the interface, flows in both sides of the bubble surface have to be taken into account, therefore, the problem contains conjugate heat and fluid flows.

Moreover, the gas-liquid interface is physically of zero-thickness where heat and mass transfer between the two phases take place. From the point of view of a chemical reaction, it is a procedure of changing electronics between ions; this procedure always happen in the liquid side where the dissolved gas can freely ionise, and the procedure may accompanied by heat transfer. Considering these facts of chemical reaction, and for simplicity as well, the heat and mass transfer could be regarded as procedures between bubble surface and the liquid in the current study.

In order to address a single inert bubble moving in a hot volatile liquid, the following assumptions are considered as valid:

- (a). both the gas and the liquid are Newtonian fluids and the physical properties of the two fluids are constants; Especially, the flows are incompressible;
- (b). the dissolving of the bubble is sufficiently slow and the concentration of dissolved mass is dilute enough so that the Stefan flow can be ignored. In the meanwhile, the dissolution of the dispersed-phase is not vice-versa and therefore can be regarded as a unidirectional diffusion from the dispersed phase at the interface;
- (c). there is no surface-active material;
- (d). the flows are laminar and axisymmetric;
- (e). the flow inside the bubble is isothermal.

3.3 Basic Governing Equations

The heat and fluid flows in both sides of the gas-liquid interface are mathematically described by a group of coupled equations. These include the continuity of fluids, momentum equation, energy equation and the transport equation of species. Considering that the fluids in both sides of the interface are different, we use superscripts (1) and (2) to denote the dispersed and the continuous phases, respectively; and for simplicity, these two superscripts are referred to as indexes (i) ($i = 1$ and 2) in this thesis but we should bear in mind that (i) is not a free index for summation law. The

basic governing equations of the current inert bubble problem are as follows:
continuity:

$$\nabla \cdot \vec{V} = 0, \quad (3.1)$$

momentum:

$$\frac{\partial \vec{V}}{\partial t} + (\vec{V} \cdot \nabla) \vec{V} = -\frac{1}{\rho^{(i)}} \nabla p^{(i)} + \frac{\mu^{(i)}}{\rho^{(i)}} \nabla^2 \vec{V} + \vec{g}, \quad (3.2)$$

energy:

$$\frac{\partial T}{\partial t} + \vec{V} \cdot \nabla T = a \nabla^2 T, \quad (3.3)$$

and species continuity:

$$\frac{\partial c}{\partial t} + \vec{V} \cdot \nabla c = D \nabla^2 c. \quad (3.4)$$

Equations (3.1)~ (3.4) are based on observing the bubbly flows on the Earth. We call a coordinates system fixed to the Earth the absolute coordinates, and a variable measured in the absolute coordinates system an absolute variable, then \vec{V} is the absolute velocity of fluid motion; ∇ is the Hamilton operator, t is absolute time; p , T , c are absolute pressure, temperature and concentration respectively; ρ , ν , a and D are fluid properties, namely, density, viscosity, thermal diffusivity and mass diffusivity, \vec{g} is the acceleration of gravity. In case of high-speed flows, \vec{g} is very small as compared with the inertial force and is omitted sometimes.

3.4 Initial and Boundary Conditions

As we mentioned before, well-posed equations must be implemented with well-posed

initial and boundary conditions so that unique numerical solutions can be obtained.

3.4.1 Initial Conditions

At the instant when an inert bubble is introduced into a hot liquid by a sparger, it can be regarded as spherical and motionless, so the initial conditions can be imposed as:

At $t = 0$,

$$\vec{V} = 0, \quad (3.5)$$

$$p^{(i)} = \text{constant } 1, \quad (3.6)$$

$$T^{(i)} = \text{constant } 2, \quad (3.7)$$

$$c^{(i)} = \text{constant } 3, \quad (3.8)$$

3.4.2 Boundary Conditions

In the range of incompressible regime, equations (3.1)~ (3.4) are elliptic in spatial dimensions, and therefore boundary conditions should be imposed at all spatial boundaries. For the current inert bubble problem, it has a far field boundary, gas-liquid interface and a geometric axis of the symmetric bubble.

The far field is the place where the blockage effects of the inert bubble can be neglected. In this case, the flow fields can be regarded as undisturbed and therefore the boundary conditions here is as following:

At far field,

$$\vec{V} = 0, \quad (3.9)$$

$$p^{(2)} = P_{\text{sys}}, \quad (3.10)$$

$$T^{(2)} = T_{sys}, \quad (3.11)$$

$$c^{(2)} = 0, \quad (3.12)$$

where the subscript “*sys*” denotes the state of the system environment.

The geometric axis of the symmetric bubble has relatively simple and straightforward boundary conditions:

At axis of the symmetry,

$$\vec{V} \cdot \vec{g} = \pm |\vec{V}| \times |\vec{g}|, \quad (3.13)$$

$$\frac{\partial p^{(i)}}{\partial x} = 0, \quad (3.14)$$

$$\frac{\partial T^{(i)}}{\partial x} = 0, \quad (3.15)$$

$$\frac{\partial c^{(i)}}{\partial x} = 0, \quad (3.16)$$

where $x-$ is the direction perpendicular to the gravity \vec{g} , ie, $x-$ is a horizontal coordinate.

The boundary condition at the gas-liquid interface is the most complex and its treatment will be a key issue in our future study. Here we only present the boundary conditions, these include the kinetic conditions and the dynamic conditions. The kinetic conditions are the continuity of tangential velocity and the conservation of mass; the dynamic conditions are the continuity of tangential stress and the balance of normal stress. Denote a bubble profile with a general function Γ , its tangential and normal unit

vectors are \vec{i} and \vec{n} respectively, and the stress tensor is $\hat{\tau}$, then the above mentioned boundary conditions are as follows:

At Γ (gas-liquid interface),

kinetic conditions:

$$(\rho^{(1)} - \rho^{(2)}) \left(\frac{\partial \Gamma}{\partial t} + \vec{V} \cdot \nabla \Gamma \right) = \frac{\partial m_b}{\partial t}, \quad (3.17)$$

$$V_{\vec{i}}^{(1)} = V_{\vec{i}}^{(2)}; \quad (3.18)$$

dynamic conditions:

$$\hat{\tau}_{\vec{i}}^{(1)} = \hat{\tau}_{\vec{i}}^{(2)}, \quad (3.19)$$

$$\hat{\tau}_{\vec{n}}^{(1)} + \vec{\zeta} = \hat{\tau}_{\vec{n}}^{(2)}, \quad (3.20)$$

where m_b is the total mass of the bubble, $\vec{\zeta}$ is the tension force.

Boundary conditions for temperature and concentration also posed at the interface,

$$T = T_{sat}, \quad (3.21)$$

$$c = c_{sat}. \quad (3.22)$$

3.5 Non-Inertial Coordinates and Normalisation of Equations

3.5.1 Non-Inertial Coordinate System

For the convenience of carrying out numerical study, it is beneficial to keep the bubble at the middle of the

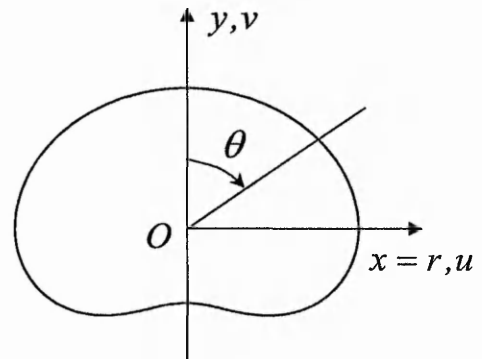


Figure 3.1 Non-inertial coordinates

computational domain. Based on this purpose, a coordinates system origin at the geometric centre of the bubble is selected.

Shown in figure 3.1, the coordinates system (x, y) is fixed to the bubble, the origin O moves in the absolute coordinates system at a velocity $\vec{V}_o(t)$ and acceleration $\vec{a}_o(t)$, and then we have

$$\frac{d\vec{V}_o(t)}{dt} = \vec{a}_o(t), \quad (3.23)$$

$$\vec{W} = \vec{V} - \vec{V}_o(t), \quad (3.24)$$

where \vec{W} is the velocity of flow in the non-inertial coordinates system (x, y) .

3.5.2 Transform of Equations

Denote the components of \vec{W} with u and v , in x - and y - directions respectively, the governing equations for present study, namely, equations (3.1)~ (3.5) can be rewritten in the non-inertial coordinates system (x, y) as follows:

continuity,

$$\frac{\partial(ru)}{\partial x} + \frac{\partial(rv)}{\partial y} = 0, \quad (3.25)$$

x - momentum:

$$\frac{\partial(ru)}{\partial t} + \frac{\partial(ruu)}{\partial x} + \frac{\partial(rvu)}{\partial y} = r \left(-\frac{1}{\rho^{(t)}} \frac{\partial p^{(t)}}{\partial x} \right) + \frac{\partial}{\partial x} \left(r\nu \frac{\partial u}{\partial x} \right) + \frac{\partial}{\partial y} \left(r\nu \frac{\partial u}{\partial y} \right) + \left[-\nu \frac{u}{r} \right], \quad (3.26)$$

y - momentum:

$$\frac{\partial(rv)}{\partial t} + \frac{\partial(ruv)}{\partial x} + \frac{\partial(rvv)}{\partial y} = r \left(-\frac{1}{\rho^{(i)}} \frac{\partial p^{(i)}}{\partial y} \right) + \frac{\partial}{\partial x} \left(rv \frac{\partial v}{\partial x} \right) + \frac{\partial}{\partial y} \left(rv \frac{\partial v}{\partial y} \right) - rg - ra_o(t), \quad (3.27)$$

energy:

$$\frac{\partial(rT)}{\partial t} + \frac{\partial(ruT)}{\partial x} + \frac{\partial(rvT)}{\partial y} = \frac{\partial}{\partial x} \left(ra \frac{\partial T}{\partial x} \right) + \frac{\partial}{\partial y} \left(ra \frac{\partial T}{\partial y} \right), \quad (3.28)$$

and species continuity:

$$\frac{\partial(rc)}{\partial t} + \frac{\partial(ruc)}{\partial x} + \frac{\partial(rvc)}{\partial y} = \frac{\partial}{\partial x} \left(rD \frac{\partial c}{\partial x} \right) + \frac{\partial}{\partial y} \left(rD \frac{\partial c}{\partial y} \right). \quad (3.29)$$

It should bear in mind that (x, y) can be either a Cartesian or an axisymmetric system. In case of Cartesian coordinates, the last term in the square bracket of equation (3.24), *ie*, $\left[-v \frac{u}{r} \right]$ will disappear; In the meanwhile, r is a constant in this time and is set to be $r = 1$. On the other hand, for the case of axisymmetric system, r becomes the horizontal coordinate in the meridional plane, that is, $r = x$.

In case of buoyancy-driven flows, namely, natural convections, a so-called Boussinesq approximation (Gray and Giorgin, 1976) is often introduced to consider the buoyancy effects on flows. This approximation is consisted of three parts as follows:

- (a). viscous dissipation is negligible;
- (b). except the density, all properties of the fluid are constants;
- (c). the variation of density has effects only in the momentum equation, and is presented in the term of buoyancy force.

According to the Boussinesq approximation, we have

$$\rho = \rho_{ref} [1 - \beta(T - T_{ref})], \quad (3.30)$$

where the subscript “ref” denotes reference values, β is the voluminal expansion coefficient of the fluid. Define an effective pressure, p_{eff} , as following:

$$p_{eff} = p + \rho_{ref} g y, \quad (3.31)$$

equation (3.27) can be changed into:

$$\begin{aligned} \frac{\partial(rv)}{\partial t} + \frac{\partial(ruv)}{\partial x} + \frac{\partial(rvv)}{\partial y} = r \left(-\frac{1}{\rho^{(i)}} \frac{\partial p_{eff}^{(i)}}{\partial y} \right) + \frac{\partial}{\partial x} \left(r v \frac{\partial v}{\partial x} \right) + \frac{\partial}{\partial y} \left(r v \frac{\partial v}{\partial y} \right) \\ + r g \beta [T - T_{ref}] - r a_o(t) \end{aligned} \quad (3.32)$$

3.5.3 Normalisation of Basic Equations

Dimensionless equations are often preferred by CFD researchers because field-parameters for different flows may be different in magnitude order while flows have similarities. For example, flows at a same Reynolds number may have quite different velocities. Based on the introduction of the dimensionless parameters describing the current problem, the flow fields can be non-dimensionalised by introducing some referencing parameters denoted by subscript “ref” as follows:

$$\left\{ \begin{array}{l} \bar{u} = \frac{u}{V_{ref}}, \quad \bar{v} = \frac{v}{V_{ref}}, \\ \bar{x} = \frac{x}{d_{ref}}, \quad \bar{y} = \frac{y}{d_{ref}}, \quad \bar{r} = \frac{r}{d_{ref}}, \\ \bar{t} = \frac{t}{d_{ref}/V_{ref}}, \\ \bar{p}^{(i)} = \frac{P_{eff}^{(i)}}{\rho^{(i)} V_{ref}^2}, \quad \bar{T} = \frac{T - T_{ref}}{T_1 - T_{ref}}, \quad \bar{c} = \frac{c - c_{ref}}{c_1 - c_{ref}} \end{array} \right. , \quad (3.33)$$

then equations (3.25)~ (3.29) can be changed into normalised and written in a general form as following:

$$\frac{\partial(\bar{r}\phi)}{\partial\bar{t}} + \frac{\partial}{\partial\bar{x}}(\bar{r}\bar{u}\phi) + \frac{\partial}{\partial\bar{y}}(\bar{r}\bar{v}\phi) = \frac{\partial}{\partial\bar{x}}\left(\bar{r}\Gamma\frac{\partial\phi}{\partial\bar{x}}\right) + \frac{\partial}{\partial\bar{y}}\left(\bar{r}\Gamma\frac{\partial\phi}{\partial\bar{y}}\right) + \bar{r}S, \quad (3.34)$$

where for Cartesian coordinates, ie, $\bar{r} = 1$,

$$\phi = \begin{bmatrix} 1 \\ \bar{u} \\ \bar{v} \\ \bar{T} \\ \bar{c} \end{bmatrix}, \quad \Gamma = \begin{bmatrix} 0 \\ \frac{1}{\text{Re}^{(i)}} \\ \frac{1}{\text{Re}^{(i)}} \\ \frac{1}{\text{Re}^{(i)} \text{Pr}^{(i)}} \\ \frac{1}{\text{Pe}^{(i)}} \end{bmatrix}, \quad \bar{r}S = \begin{bmatrix} 0 \\ -\frac{\partial\bar{p}_{eff}^{(i)}}{\partial\bar{x}} \\ -\frac{\partial\bar{p}_{eff}^{(i)}}{\partial\bar{y}} + \frac{Gr}{(\text{Re}^{(i)})^2}\bar{T} - \frac{d_{ref}}{V_{ref}^2}a_o(t) \\ 0 \\ 0 \end{bmatrix};$$

And for axisymmetric system, ie, $\bar{r} = \bar{x}$, we have

$$\phi = \begin{bmatrix} 1 \\ \bar{u} \\ \bar{v} \\ \bar{T} \\ \bar{c} \end{bmatrix}, \quad \Gamma = \begin{bmatrix} 0 \\ \frac{1}{\text{Re}^{(i)}} \\ \frac{1}{\text{Re}^{(i)}} \\ \frac{1}{\text{Re}^{(i)} \text{Pr}^{(i)}} \\ \frac{1}{\text{Pe}^{(i)}} \end{bmatrix}, \quad \bar{r}S = \begin{bmatrix} 0 \\ \left(-\frac{\partial\bar{p}_{eff}^{(i)}}{\partial\bar{x}} + \frac{1}{\text{Re}^{(i)}}\left(-\frac{\bar{u}}{\bar{x}^2}\right)\right)\bar{r} \\ \left(-\frac{\partial\bar{p}_{eff}^{(i)}}{\partial\bar{y}} + \frac{Gr}{(\text{Re}^{(i)})^2}\bar{T} - \frac{d_{ref}}{V_{ref}^2}a_o(t)\right)\bar{r} \\ 0 \\ 0 \end{bmatrix}.$$

Corresponding to the form changes in governing equations, modifications on the solution determining conditions have to be made as well,

At $\bar{t} = 0$,

$$\bar{u} = 0, \quad \bar{v} = -\bar{V}_o(0), \quad (3.35)$$

$$\bar{p}_{eff}^{(i)} = \text{constant } 1', \quad (3.36)$$

$$\bar{T}^{(i)} = \text{constant } 2', \quad (3.37)$$

$$\bar{c}^{(i)} = \text{constant } 3'; \quad (3.38)$$

At far field,

$$\bar{u} = 0, \quad \bar{v} = -\bar{V}_o(t), \quad (3.39)$$

$$\bar{p}_{eff}^{(2)} = 0, \quad (3.40)$$

$$\bar{T}^{(2)} = 0, \quad (3.41)$$

$$\bar{c}^{(2)} = 0; \quad (3.42)$$

At axis of the symmetry ($\bar{x} = 0$),

$$\bar{u} = 0, \quad \frac{\partial \bar{v}}{\partial \bar{x}} = 0 \quad (3.43)$$

$$\frac{\partial \bar{p}_{eff}^{(i)}}{\partial \bar{x}} = 0, \quad (3.44)$$

$$\frac{\partial \bar{T}^{(i)}}{\partial \bar{x}} = 0, \quad (3.45)$$

$$\frac{\partial \bar{c}^{(i)}}{\partial \bar{x}} = 0; \quad (3.46)$$

At the gas-liquid interface Γ , the kinetic and dynamic conditions still take their original form of equations (3.17)~ (3.20) and we will talk more details about these conditions when we calculate a real gas-liquid interface in chapter 5; For equations (3.21) and (3.22), their dimensionless forms are:

$$T = 1, \quad (3.47)$$

$$c = 1. \quad (3.48)$$

The normalised equation (3.34) and the solution determining conditions are the mathematical model for our inert bubble problem. For the convenience, the top bars for dimensionless flow field parameters will be omitted in the following chapters but we should bear in mind that all of these parameters are dimensionless except those specially declared.

3.6 Summary of the Chapter

Physical and mathematical models of an inert bubble introduced into a hot liquid have been presented. The problem is physically described as “unsteady conjugate heat and fluid flows inside and around an inert bubble” in this chapter. In order to highlight the “zero-thickness” of the gas-liquid interface and to study the mechanism of interfacial heat and mass transfer, appropriate assumptions on the flow regime are imposed.

Mathematical description of the problem is a coupled system of fluid continuity, momentum conservation, energy conservation and species’ conservation. Well-posed solution-determining conditions are presented.

Chapter 4

CFD Strategies for Moving Boundary Problems

4.1 Introduction

Based on the mathematical model established for the inert bubble problem, this chapter and the next are arranged to pursue numerical strategies for solving the mathematical model. Considering that the shape of the inert bubble is a time-dependent geometry and the gas-liquid interface is a moving boundary, it is natural and necessary to begin our numerical algorithm development for moving boundary problems.

This chapter presents a calculation procedure for heat and fluid flows in geometries with time-dependent moving boundaries. The procedure incorporates a moving mesh arrangement with a multi-block iteration strategy and has been developed to assist future simulations of heat and mass transfer in the inert bubble problem. The basic equations are discretised using a finite volume method (FVM) with high order total variation diminishing (TVD) schemes employed to obtain high numerical accuracy. The discretised equations are solved by the SIMPLE algorithm with a non-staggered grid arrangement. The space conservation law is invoked and applied for the explicit tracking of a moving boundary with a moving mesh. For mapping complex geometries a multi-block iteration strategy is employed.

4.2 Eulerian-Lagrangian Transformation

In order to calculate heat and fluid flows using moving mesh, a Eulerian-Lagrangian transform of basic equations must be carried out.

Consider a Lagrangian (time-dependent) non-orthogonal coordinates system (t, ξ, η) , where

$$\xi = \xi(t, x, y), \eta = \eta(t, x, y). \quad (4.1)$$

At a certain instant t , the inverse transformation of equation (4.1) exists

$$x = x(t, \xi, \eta), y = y(t, \xi, \eta), \quad (4.2)$$

provided equation (4.1) is a one-to-one transformation. In case both (x, y) and (ξ, η) are right hand systems, we have

$$J = \begin{vmatrix} x_\xi & y_\xi \\ x_\eta & y_\eta \end{vmatrix} = x_\xi y_\eta - y_\xi x_\eta > 0, \quad (4.3)$$

where the subscripts ξ and η denote partial derivatives with respect to ξ and η respectively, *ie*,

$$x_\xi = \frac{\partial x}{\partial \xi}, y_\xi = \frac{\partial y}{\partial \xi}, x_\eta = \frac{\partial x}{\partial \eta}, y_\eta = \frac{\partial y}{\partial \eta}. \quad (4.4)$$

For a general flows field parameter ϕ , its derivatives can be obtained by applying the chain rule of differentiation,

$$\frac{\partial \phi}{\partial x} = \frac{1}{J} \left(y_\eta \frac{\partial \phi}{\partial \xi} - y_\xi \frac{\partial \phi}{\partial \eta} \right), \quad \frac{\partial \phi}{\partial y} = \frac{1}{J} \left(-x_\eta \frac{\partial \phi}{\partial \xi} + x_\xi \frac{\partial \phi}{\partial \eta} \right), \quad (4.5)$$

$$\frac{\partial \phi}{\partial \xi} = x_\xi \frac{\partial \phi}{\partial x} + y_\xi \frac{\partial \phi}{\partial y}, \quad \frac{\partial \phi}{\partial \eta} = x_\eta \frac{\partial \phi}{\partial x} + y_\eta \frac{\partial \phi}{\partial y}. \quad (4.6)$$

The metrics of the Lagrangian system is calculated as follows:

$$\begin{cases} \alpha = x_\eta^2 + y_\eta^2 \\ \beta = x_\xi x_\eta - y_\xi y_\eta \\ \gamma = x_\xi^2 + y_\xi^2 \end{cases} \quad (4.7)$$

Equations (4.1)~(4.7) give a complete Eulerian-Lagrangian transformation.

Based on the Eulerian-Lagrangian transformation, the governing equations for the present study, given by equation (3.34), are re-written as follows:

$$\frac{\partial(rJ\phi)}{\partial t} + \frac{\partial}{\partial \xi} \left\{ r \left[G_r^1 \phi - \frac{\Gamma}{J} \left(\alpha \frac{\partial \phi}{\partial \xi} - \beta \frac{\partial \phi}{\partial \eta} \right) \right] \right\} + \frac{\partial}{\partial \eta} \left\{ r \left[G_r^2 \phi - \frac{\Gamma}{J} \left(-\beta \frac{\partial \phi}{\partial \xi} + \gamma \frac{\partial \phi}{\partial \eta} \right) \right] \right\} = rJS, \quad (4.8)$$

where ϕ , Γ and rS are the same as those in equation (3.34) and are omitted here. G_r^1 and G_r^2 are curvilinear components of the relative velocity \vec{W}_r , which is defined as the difference between physical and grid velocities, that is,

$$\begin{cases} \vec{W}_r = \vec{W} - \vec{W}_g \\ G_r^1 = G^1 - G_g^1 = (u - u_g)y_\eta - (v - v_g)x_\eta, \\ G_r^2 = G^2 - G_g^2 = (v - v_g)x_\xi - (u - u_g)y_\xi \end{cases} \quad (4.9)$$

u_g and v_g are components of grid velocity \vec{W}_g ,

$$\begin{cases} \vec{W}_g = \frac{d\vec{R}}{dt} \\ u_g = \frac{dx}{dt} \\ v_g = \frac{dy}{dt} \end{cases} \quad (4.10)$$

4.3 FVM Discretisation on Moving Mesh

4.3.1 Finite Volume Integration

Integrating equation (4.8) over the shaded control volume shown in figure 4.1, we have

$$\begin{aligned} & \frac{(Jr\phi)_P - (Jr\phi)_P^o}{\Delta t} \Delta\xi\Delta\eta + \left[r \left(G_r^1 \phi - \frac{\Gamma}{J} \alpha \frac{\partial\phi}{\partial\xi} \right) \Delta\eta \right]_n - \left[r \left(G_r^1 \phi - \frac{\Gamma}{J} \alpha \frac{\partial\phi}{\partial\xi} \right) \Delta\eta \right]_s \\ & \quad + \left[r \left(G_r^2 \phi - \frac{\Gamma}{J} \gamma \frac{\partial\phi}{\partial\eta} \right) \Delta\xi \right]_e - \left[r \left(G_r^2 \phi - \frac{\Gamma}{J} \gamma \frac{\partial\phi}{\partial\eta} \right) \Delta\xi \right]_w, \quad (4.11) \\ & = [JrS]_P \Delta\xi\Delta\eta + S' \\ & = S_1 \end{aligned}$$

where

$$\begin{aligned} S' = & \left[r \frac{\Gamma}{J} (-\beta) \frac{\partial\phi}{\partial\eta} \Delta\eta \right]_n - \left[r \frac{\Gamma}{J} (-\beta) \frac{\partial\phi}{\partial\eta} \Delta\eta \right]_s \\ & + \left[r \frac{\Gamma}{J} (-\beta) \frac{\partial\phi}{\partial\xi} \Delta\xi \right]_e - \left[r \frac{\Gamma}{J} (-\beta) \frac{\partial\phi}{\partial\xi} \Delta\xi \right]_w. \quad (4.12) \end{aligned}$$

Set

$$\left\{ \begin{aligned} \mathcal{F}_n &= F_n \phi_n - D_n (\Delta\phi)_n, \quad F_n = G_{r,n}^1 \Delta\eta, \quad D_n = \left(r \frac{\Gamma}{J} \alpha \right)_n \frac{\Delta\eta}{\xi_N - \xi_P} \\ \mathcal{F}_s &= F_s \phi_s - D_s (\Delta\phi)_s, \quad F_s = G_{r,s}^1 \Delta\eta, \quad D_s = \left(r \frac{\Gamma}{J} \alpha \right)_s \frac{\Delta\eta}{\xi_P - \xi_S} \\ \mathcal{F}_e &= F_e \phi_e - D_e (\Delta\phi)_e, \quad F_e = G_{r,e}^2 \Delta\xi, \quad D_e = \left(r \frac{\Gamma}{J} \gamma \right)_e \frac{\Delta\xi}{\eta_E - \eta_P} \\ \mathcal{F}_w &= F_w \phi_w - D_w (\Delta\phi)_w, \quad F_w = G_{r,w}^2 \Delta\xi, \quad D_w = \left(r \frac{\Gamma}{J} \gamma \right)_w \frac{\Delta\xi}{\eta_P - \eta_W} \end{aligned} \right., \quad (4.13)$$

equation (4.11) changes into:

$$\mathcal{F}_n - \mathcal{F}_s + \mathcal{F}_e - \mathcal{F}_w = S_1 + \frac{(Jr\phi)_P^o - (Jr\phi)_P}{\Delta t}. \quad (4.14)$$

In equation (4.13), cell-face fluxes \mathcal{F}_n , \mathcal{F}_s , \mathcal{F}_e and \mathcal{F}_w are always consisted of two parts. For convenience, denote a cell-face flux with \mathcal{F}_f ($f = n, s, e$ and w), then we have

$$\mathcal{F}_f = \mathcal{F}_f^C + \mathcal{F}_f^D, \quad (4.15)$$

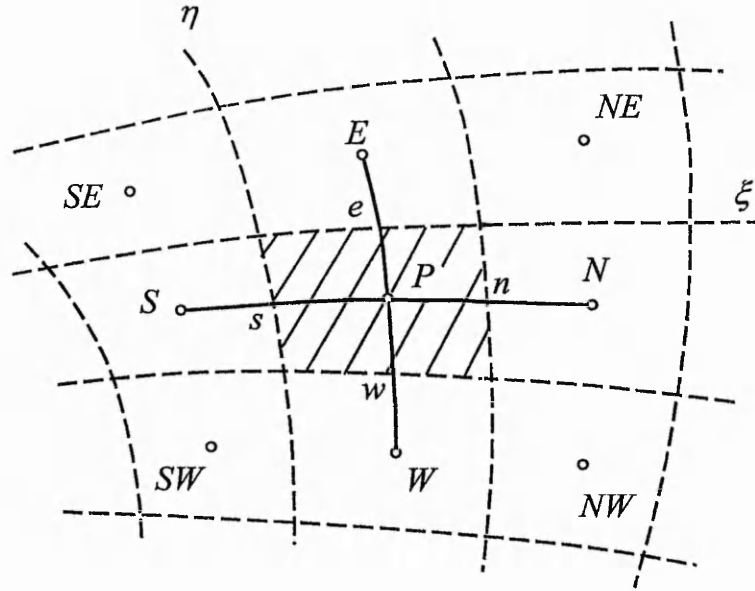


Figure 4.1 Control volume for integration

where \mathcal{F}_f^C and \mathcal{F}_f^D are convective and diffusive fluxes respectively,

$$\mathcal{F}_f^C = F_f \phi_f, \quad (4.16)$$

$$\mathcal{F}_f^D = -D_f (\Delta\phi)_f. \quad (4.17)$$

\mathcal{F}_f^D is often calculated using central-difference schemes in which second order accuracy can always be obtained. \mathcal{F}_f^C , however, is difficult to be calculated because there is a balance between accuracy and stability. For engineering calculations, the stability is often more important than the accuracy and therefore schemes with lower accuracy may be used. Here for convenience of description, we temporarily use the first order upwind

scheme, which is unconditionally stable and the simplest convective scheme, to discretise \mathcal{J}_f^C ; development of high order accurate schemes will be introduced later.

Based on the above understanding, we have

$$\left\{ \begin{array}{l} \mathcal{J}_n^C = \begin{cases} F_n \phi_P & , \text{ if } (G_{r,n}^1 \geq 0) \\ F_n \phi_N & , \text{ if } (G_{r,n}^1 < 0) \end{cases} , & \mathcal{J}_n^D = -D_n (\phi_N - \phi_P); \\ \mathcal{J}_s^C = \begin{cases} F_s \phi_S & , \text{ if } (G_{r,s}^1 \geq 0) \\ F_s \phi_P & , \text{ if } (G_{r,s}^1 < 0) \end{cases} , & \mathcal{J}_s^D = -D_s (\phi_P - \phi_S); \\ \mathcal{J}_e^C = \begin{cases} F_e \phi_P & , \text{ if } (G_{r,e}^2 \geq 0) \\ F_e \phi_E & , \text{ if } (G_{r,e}^2 < 0) \end{cases} , & \mathcal{J}_e^D = -D_e (\phi_E - \phi_P); \\ \mathcal{J}_w^C = \begin{cases} F_w \phi_W & , \text{ if } (G_{r,w}^2 \geq 0) \\ F_w \phi_P & , \text{ if } (G_{r,w}^2 < 0) \end{cases} , & \mathcal{J}_w^D = -D_w (\phi_P - \phi_W); \end{array} \right. , \quad (4.18)$$

and the discretised form of equation (4.8) is obtained as following:

$$a_P \phi_P = a_N \phi_N + a_S \phi_S + a_E \phi_E + a_W \phi_W + S_2, \quad (4.19)$$

where

$$\left\{ \begin{array}{l} a_N = D_n + \max(-F_n, 0) \\ a_S = D_s + \max(F_s, 0) \\ a_E = D_n + \max(-F_e, 0) \\ a_W = D_w + \max(F_w, 0) \\ a_P = (a_N + a_S + a_E + a_W + (Jr \Delta \xi \Delta \eta) / \Delta t) / \alpha_\phi \\ S_2 = S_1 + (Jr \phi)^o \Delta \xi \Delta \eta / \Delta t + a_P (1 - \alpha_\phi) \phi^* \end{array} \right. , \quad (4.20)$$

α_ϕ is an under-relaxation factor for iteration.

4.3.2 Space Conservation Law

The application of the space conservation law (SCL) is fundamental to heat and fluid flow calculations using a moving mesh. However, as pointed out by Demirdzic and Peric (1988), although the SCL was discovered by Trulio and Trigger (1961) and “rediscovered” by Thomas and Lombard (1979), its importance has not always been sufficiently realised by researchers. As a result problems have been encountered with oscillations and instabilities, the sensitivity to volume changes and difficulties in pressure iteration.

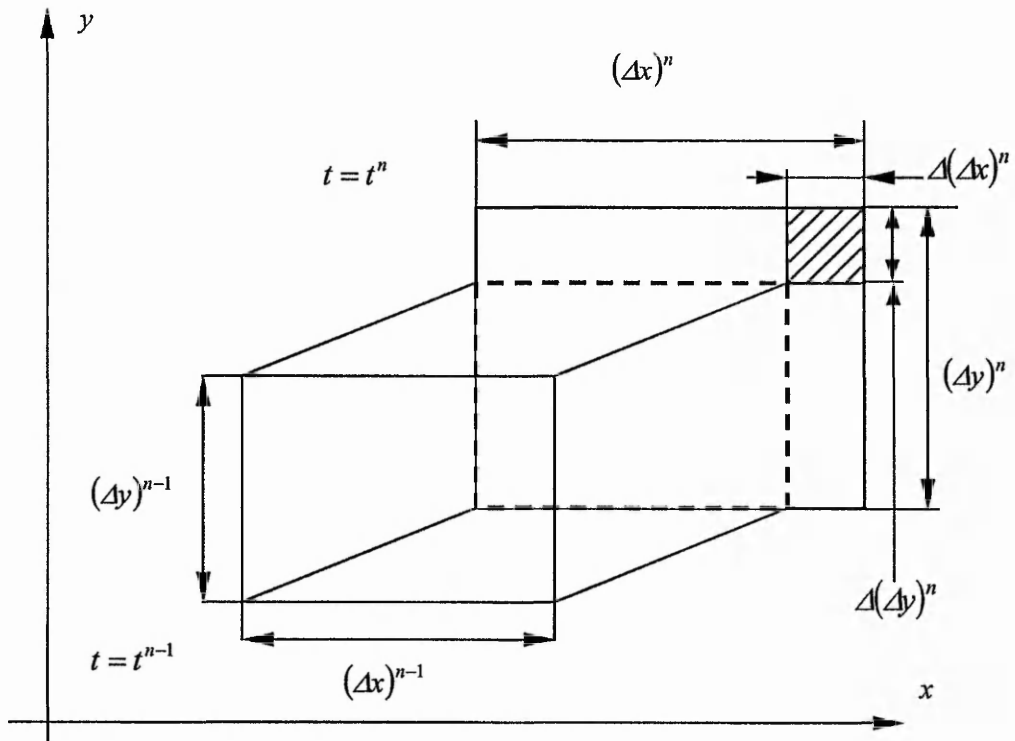


Figure 4.2 Space conservation law

The SCL is illustrated in figure 4.2. For simplicity, a Cartesian co-ordinate cell is employed. The volume of the cell, V , is calculated as

$$V = \Delta x \Delta y. \quad (4.21)$$

To calculate the time change rate of V using a differential scheme such as the first-order implicit scheme, we have

$$\frac{V^n - V^{n-1}}{\Delta t} = \frac{[\Delta(\Delta x)]^n \Delta y^n + [\Delta(\Delta y)]^n \Delta x^n}{\Delta t}. \quad (4.22)$$

It is easy to see that the shaded area in figure 4.2 has been used twice in calculating the area increase and that this will result in a computational error. The error cannot be avoided by choosing another differential scheme since a similar problem will always be encountered.

In mathematical terms the SCL can be obtained from equation (4.8) by setting $\phi = 1$, $\Gamma = 0$, $S = 0$, $r = 1$ and $\vec{W}_r = -\vec{W}_g$ ($\vec{W} = 0$), which results in:

$$\frac{\partial J}{\partial t} = \frac{\partial G_g^1}{\partial \xi} + \frac{\partial G_g^2}{\partial \eta}. \quad (4.23)$$

Equation (4.23) implies that the time derivative of the computational cell volume is closely related to the grid velocity. To satisfy the SCL, one method is to calculate the grid velocity using equation (4.10) and then update J through equation (4.23). An alternative approach, proposed by Demirdzic and Peric (1988), is to calculate the grid velocity from known grid positions in such a way that the SCL is satisfied. However, in Demirdzic and Peric (1988)'s "general formula" for grid velocity, the projection of the cell face, which might possibly be zero, is used as denominator, which would cause the calculation to fail. For this reason the former method of satisfying the SCL is employed in our paper.

4.3.3 High Order Schemes and Deferred Correction

Why high order schemes?

The accuracy with which transport processes are approximated numerically is of crucial importance in assessing the predictive realism of mathematical models which represent physical processes. Advection usually poses the biggest problems, since this process provokes or is associated with steep property gradients and thus raises the need for high-accuracy approximation schemes.

Because advection is represented by a first order derivative, its approximation by a first order numerical scheme can be argued to be both appropriate and consistent on physical as well as mathematical grounds. Indeed, the essential validity of this argument is reflected, among others, by unconditional boundedness of the first order upwind scheme which we used in equation (4.18), due to the absence of parasitic components in the resulting numerical solution. However, this scheme is generally unacceptable on grounds of accuracy, unless extremely fine grids are used, since it introduces a high level of artificial second order diffusions which tends to seriously erode property gradients in the same way as physical diffusion does.

The use of high order approximations is the route most frequently taken in efforts to increase accuracy. However, schemes of order two and above, particularly symmetric one, can provoke spurious oscillations when the Peclet number Pe is high in combination with steep gradients of the flow properties. Such oscillations are not only optical defects but can have seriously deleterious or even catastrophic effects on the iterative stability and convergence properties of coupled system.

The tendency towards oscillation may be counteracted, in principle, by adding an oscillatory scheme a component which introduces a bias towards upstream flow conditions or strengthens the bias which may already be an inherent feature of the scheme. This can be effected either explicitly, by the addition of an artificial diffusion

fragment to the advective flux returned by the basic scheme (for example, Jameson, Schmidt and Turkel, 1981), or implicitly, through an increase in the contribution or weight of values residing at the upstream nodes of the approximation stencil (Warming and Beam, 1976). If, as is usually the case, the strength of the oscillation-damping mechanism is decided upon by an a priori choice of weighting factors or coefficients, then the resulting composite scheme will not, in general, be monotonic. To achieve monotonicity, upstream biasing must be controlled by the oscillatory features of the solution, *ie*, the scheme must be non-linear.

Early proposals for using non-linear limiters, sensitised to the ratio of consecutive gradients of the numerical solution, were made by Boris and Book (1973, 1976) and van Leer (1974, 1977, 1979). It was not until Harten (1983) injected formal mathematical rigour into the subject by proposing the total variation diminishing (TVD) concept as the criterion for developing high resolution convection schemes which combine accuracy with monotonicity and entropy preservation.

Within the framework of an explicit time-marching solution, any second order accurate TVD scheme may be constructed by linearly blending the Lax and Wendrof (1960) and Warming and Beam (1976) schemes in conjunction with a smart slope limiter which switches off the antidiffusive flux when a local extremum (an oscillation) is detected. Different schemes arise through different limiter forms and Sweby (1984) has presented a general framework in terms of a TVD diagram. On the other hand, if interest is focused on steady state only, it is possible to re-interpret Sweby's TVD diagram in terms of the normalised variable diagram (NVD) and normalised variable formulation (NVF) proposed by Leonard (1988). Using this NVF methodology and following Sweby's rationale, Leonard (1988) and Gaskell and Lau (1988) have formulated the SHARP and SMART schemes, respectively, both being monotonic implementations of Leonard's (1979) QUICK scheme.

TVD and $\phi(\chi) \sim \chi$ diagram

The construction of any numerical scheme required to be monotonicity-preserving rest on two general principles:

- (a). No new local (spatial) extrema must be created;
- (b). The value of an existing local minimum must be non-decreasing and that of a local maximum must be non-increasing.

Consider a spatially one-dimensional scalar conservation law

$$\frac{\partial \phi}{\partial t} + u \frac{\partial \phi}{\partial x} = 0, \quad (4.24)$$

where ϕ is a bounded function defined on a zone $[a, b]$ (it is permitted for $[a, b] = (-\infty, +\infty)$), the numerical solution for ϕ is defined on discrete grid nodes: $a = x_0 < x_1 < \dots < x_m = b$, the total variation (TV) is defined as

$$TV(\phi) = \sum_{i=1}^m |\phi(x_i) - \phi(x_{i-1})|, \quad (4.25)$$

The solution is said to be TVD (Harten, 1983) if

$$TV(\phi^{n+1}) \leq TV(\phi^n). \quad (4.26)$$

Equation (4.26) is the so-called TVD constraint. This constraint ensures the scheme is stable while the numerical results are physically reasonable. Therefore, the TVD constraint actually places two limitations to a discrete scheme: one is on the length of time step, and another is on spatial accuracy. As a result, the TVD constraint given in equation (4.26) is often employed to construct numerical schemes of high spatial accuracy (second order).

Integrating equation (4.24) over the control volume shown in figure 4.3, and using first order explicit difference in temporal direction, we have

$$\phi_i^{n+1} = \phi_i^n - \nu(\phi_{i+0.5}^n - \phi_{i-0.5}^n), \quad (4.27)$$

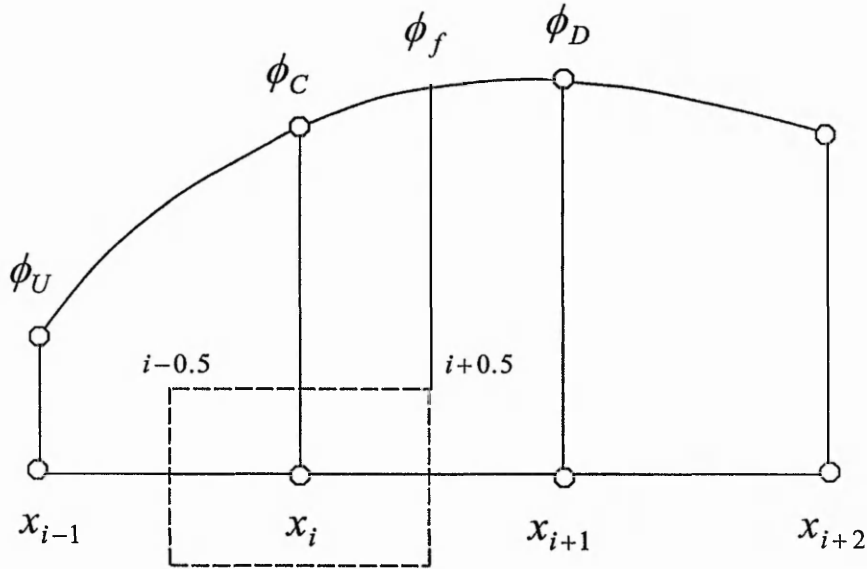


Figure 4.3 One-dimensional finite volume and associated nodal stencil

where $\nu = \frac{u\Delta t}{\Delta x}$. The key issue in equation (4.27) is how to calculate the cell-face values $\phi_{i-0.5}^n$ and $\phi_{i+0.5}^n$. A general form of the discrete approximation of equation (4.24) (and of equation (4.27) as well) is

$$\phi_i^{n+1} = \phi_i^n - C_i(\phi_i^n - \phi_{i-1}^n) + D_i(\phi_{i+1}^n - \phi_i^n), \quad (4.28)$$

where C and D are scheme-specific “influence coefficients”. In terms of equation (4.28), the conditions sufficient to secure the TVD constraint, *ie*, inequality (4.26) are

$$\begin{cases} C_i \geq 0 \\ D_i \geq 0 \\ C_i + D_i \leq 1 \end{cases} . \quad (4.29)$$

If we used the first order upwind scheme, as that used in equation (4.18), to calculate

$\phi_{i-0.5}^n$ and $\phi_{i+0.5}^n$, we have the upwind scheme for equation (4.24) as follows:

$$\phi_i^{n+1} = \phi_i^n - \lambda \left[\frac{1}{2}(u + |u|)(\phi_i^n - \phi_{i-1}^n) - \frac{1}{2}(u - |u|)(\phi_{i+1}^n - \phi_i^n) \right], \quad (4.30)$$

where $\lambda = \Delta t / \Delta x$. If we set $C_i = \frac{\lambda}{2}(u + |u|)$, $D_i = -\frac{\lambda}{2}(u - |u|)$ and $\lambda|u| \leq 1$, obviously equation (4.30) can satisfy equation (4.29) and therefore, the first order upwind scheme in equation (4.30) is a TVD scheme. The problem is that this scheme has only first order accuracy and the artificial viscosity is too big.

The Lax and Wendroff (1960) scheme for equation (4.24) is as follows:

$$\phi_i^{n+1} = \phi_i^n - \frac{1}{2}\nu [(\phi_{i+1}^n - \phi_i^n) + (\phi_i^n - \phi_{i-1}^n)] + \frac{1}{2}\nu^2 [(\phi_{i+1}^n - \phi_i^n) - (\phi_i^n - \phi_{i-1}^n)]. \quad (4.31)$$

This scheme has second-order accuracy but is not a TVD scheme if $|\nu| < 1$. Rearrange equation (4.31), we have

$$\begin{aligned} \phi_i^{n+1} = \phi_i^n - \frac{1}{2}(\nu + |\nu|)(\phi_i^n - \phi_{i-1}^n) - \frac{1}{2}(\nu - |\nu|)(\phi_{i+1}^n - \phi_i^n) \\ - \frac{1}{2}(1 - |\nu|)\nu [(\phi_{i+1}^n - \phi_i^n) + (\phi_i^n - \phi_{i-1}^n)] \end{aligned} \quad (4.32)$$

So, the Lax-Wendroff scheme is the first order upwind scheme plus the last term of equation (4.32). When $|\nu| < 1$, this plus term is a negative second order viscous dissipation which can cut down the artificial viscosity of the first order upwind scheme. Because of this, the last term of equation (4.32) is called as ‘‘anti-diffusive’’ term.

The above analysis indicates that a combination of the upwind and the Lax-Wendroff schemes may be of both TVD and second order accuracy. For simplicity and without losing generality, we set $u > 0$ and therefore $\nu > 0$. Based on the above indication, equation (4.32) is rewritten as follows:

$$\phi_i^{n+1} = \phi_i^n - C_i (\phi_i^n - \phi_{i-1}^n), \quad (4.33)$$

where

$$\begin{cases} C_i = \nu + \frac{1}{2}(1-\nu)\nu \left[\frac{\varphi(\chi_{i+0.5})}{\chi_{i+0.5}} - \varphi(\chi_{i-0.5}) \right] \\ \chi_{i+0.5} = \frac{\phi_i^n - \phi_{i-1}^n}{\phi_{i+1}^n - \phi_i^n} \end{cases},$$

$\varphi(\chi)$ is called a limiter. The choice of $\varphi(\chi)$ dictates the order of the scheme and its boundedness properties. Second order accuracy may, for example, can be obtained by the choice

$$\varphi(\chi) = (1-\theta) \times \underbrace{1}_{L-W} + \theta \times \underbrace{\chi}_{W-B}, \quad 0 \leq \theta \leq 1, \quad (4.34)$$

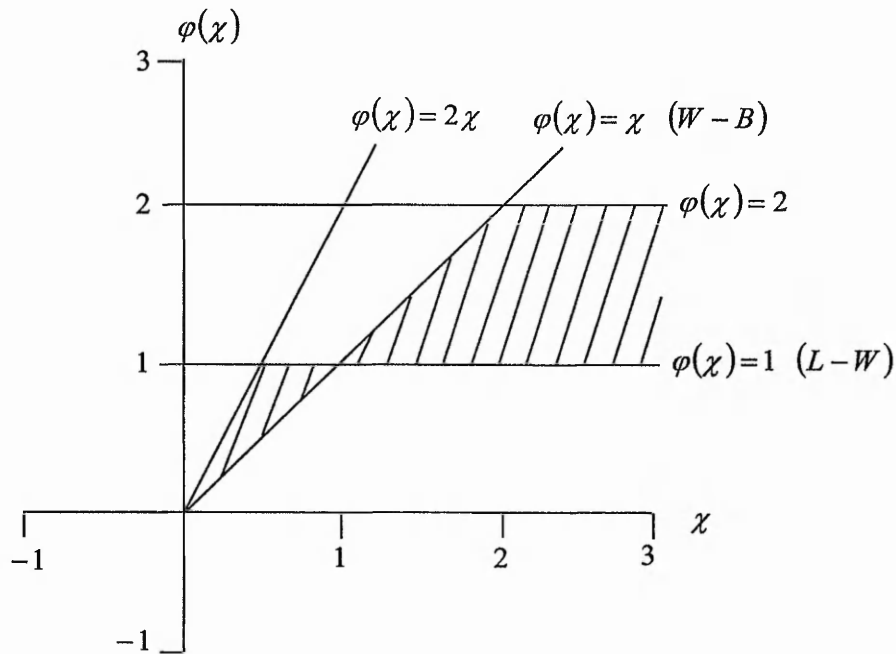


Figure 4.4 Range of boundness-preserving limiters for monotonic blend of Lax-Wendroff and Warming-Beam schemes

which represents a weighted linear average of the Lax and Wendroff (1960) scheme (“1”) and the Warming and Beam (1976) scheme (χ). While this approximation is only conditionally bounded (TVD), Sweby (1984) has shown that a TVD form arises from the constraint

$$\varphi(\chi) = \begin{cases} \min(2\chi, 2) & , \chi > 0 \\ 0 & , \chi \leq 0 \end{cases} . \quad (4.35)$$

Hence, any form of equation (4.33) for which $\varphi(\chi)$ lies in the shaded area of figure 4.4 is bounded and has second order accuracy.

MUSCAL method and $\tilde{\phi}_f \sim \tilde{\phi}_c$ diagram (NVD)

As we mentioned, in the context of an iterative solution for statistically steady flows within the finite volume framework, the essential task is to approximate the volume-face fluxes, combining accuracy with boundness. For a one-dimensional “volume” and positive velocity, schemes up to third order accuracy may be constructed by approximating the face value ϕ_f in figure 4.3 by the upwind value ϕ_U corrected by an “anti-diffusive” gradient involving ϕ_D , ϕ_C and ϕ_U . This is a key feature of van Leer’s (1979) Monotonic Upstream Scheme for Conservation Laws (MUSCAL) method. A general form of a MUSCAL scheme may be written as:

$$\phi_f = \phi_c + \frac{1}{4} [(1 + \kappa)(\phi_D - \phi_C) + (1 - \kappa)(\phi_C - \phi_U)], \quad (4.36)$$

where the numerical parameter κ controls the order of the scheme. Unbounded forms corresponding to the central differencing (CD), second order (linear) upwind differencing (LUDES) and Leonard’s (1979) quadratic upstream-weighted differencing (QUICK) arise by setting $\kappa = 1$, -1 and 0.5 respectively.

The approach to construct bounded forms leans on that outlined in the previous section

(TVD and $\varphi(\chi) \sim \chi$ diagram). Thus, to render equation (4.36) monotonic, while retaining a five-point stencil (for one dimensional), a slope limiter $\varphi(\chi_f)$ is introduced in a manner similar to that in equation (4.33):

$$\phi_f = \phi_C + \frac{1}{4} \left[(1 + \kappa) \varphi(\chi_f) (\phi_D - \phi_C) + (1 - \kappa) \varphi\left(\frac{1}{\chi_f}\right) (\phi_C - \phi_U) \right]. \quad (4.37)$$

For further consideration, it is expedient to replace the dimensional convected property ϕ by the normalised variable (NV) $\tilde{\phi}_f$, proposed by Leonard (1988) and defined as follows:

$$\tilde{\phi} = \frac{\phi - \phi_U}{\phi_D - \phi_U}. \quad (4.38)$$

With this definition, equation (4.37) may be written as

$$\tilde{\phi}_f = \tilde{\phi}_C + \frac{1}{4} \left[(1 + \kappa) \varphi(\chi_f) (1 - \tilde{\phi}_C) + (1 - \kappa) \varphi\left(\frac{1}{\chi_f}\right) \tilde{\phi}_C \right]. \quad (4.39)$$

Since

$$\chi_f = \frac{\tilde{\phi}_C}{1 - \tilde{\phi}_C}, \quad (4.40)$$

equation (4.39) can be simplified to

$$\tilde{\phi}_f = \tilde{\phi}_C + \frac{1}{4} \left[(1 + \kappa) \varphi(\chi_f) + (1 - \kappa) \chi_f \varphi\left(\frac{1}{\chi_f}\right) \right] (1 - \tilde{\phi}_C). \quad (4.41)$$

Introduce a symmetric limiter which satisfying the following condition:

$$\varphi(\chi_f) = \chi_f \varphi\left(\frac{1}{\chi_f}\right), \quad (4.42)$$

equation (4.41) becomes

$$\tilde{\phi}_f = \tilde{\phi}_C + \frac{1}{2}\varphi(\chi_f)(1 - \tilde{\phi}_C), \quad (4.43)$$

which is evidently independent of the parameter κ . Substituting equations (4.40) and (4.43) into equation (4.35) allows the TVD constraints to be expressed as:

$$\begin{cases} \tilde{\phi}_C \leq \tilde{\phi}_f \leq 2\tilde{\phi}_C & \text{and } \tilde{\phi}_f \leq 1, \text{ if } 0 < \tilde{\phi}_C < 1 \\ \tilde{\phi}_f = \tilde{\phi}_C & , \text{ if } \tilde{\phi}_C \leq 0 \text{ or } \tilde{\phi}_C \geq 1 \end{cases} \quad (4.44)$$

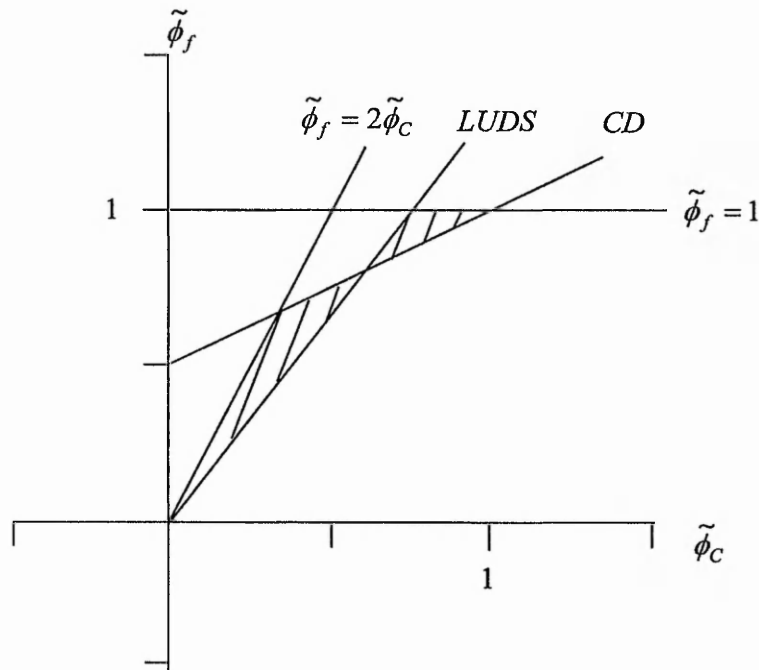


Figure 4.5 $\tilde{\phi}_f \sim \tilde{\phi}_C$ diagram (NVD)

Again, Sweby's TVD condition, taken in conjunction with the blending of Lax-Wendroff (Lax and Wendroff, 1960) and Warming-Beam (Warming and Beam, 1976), can be represented by the shaded area in figure 4.4. An analogous graphical representation can readily be derived using condition (4.44) together with form (4.36), the later written for

special of a weighted linear average of the central differencing scheme (CD, $\kappa=1$) and the second order upwind scheme (LU DS, $\kappa=-1$), ie,

$$\tilde{\phi}_f = (1-\theta) \underbrace{\frac{1}{2}(1+\tilde{\phi}_c)}_{CD} + \theta \underbrace{\frac{3}{2}\tilde{\phi}_c}_{LU DS}, \quad 0 \leq \theta \leq 1. \quad (4.45)$$

The graphical representation is given in figure 4.5, and the shaded area again is the range in which the composite second order scheme is fully bounded.

Deferred correction

With high order schemes, the evaluation of $\tilde{\phi}_f$ may involve a large number of neighbouring grid points. Therefore, in order to simplify the solution of the resulting system of algebraic equations, a compact procedure is usually used. In this thesis, Khosla and Rubin's (1974) deferred correction is employed. Ni, Tao and Wang's (1999) analysis shows that this procedure is also an effective method to stabilise numerical calculation when high order schemes are used.

In equations (4.18), we calculated the value of ϕ_f using the first-order upwind scheme and obtained the discretised equation (4.19). For the convenience of description, we denote the cell-face values of ϕ , calculated by the first order upwind scheme and a high order scheme respectively, as ϕ_f^U and ϕ_f . Therefore, the cell-face convective fluxes in equation (4.16) can be replaced by their equivalent fluxes:

$$\mathcal{F}_f^C = F_f \phi_f = F_f \phi_f^U - F_f (\phi_f^U - \phi_f), \quad (4.46)$$

equation (4.14) is transformed to

$$\begin{aligned} & (J_n^D + F_n \phi_n^U) - (J_s^D + F_s \phi_s^U) + (J_e^D + F_e \phi_e^U) - (J_w^D + F_w \phi_w^U) \\ & = S_1 + \frac{(Jr\phi)_P^o - (Jr\phi)_P}{\Delta t} + S_{DC} \end{aligned}, \quad (4.47)$$

where S_{DC} is the contribution due to the adopted deferred correction procedure,

$$S_{DC} = F_n(\phi_n^U - \phi_n) - F_s(\phi_s^U - \phi_s) + F_e(\phi_e^U - \phi_e) - F_w(\phi_w^U - \phi_w). \quad (4.48)$$

The final discretised governing equations take a general form as following:

$$a_P \phi_P = a_N \phi_N + a_S \phi_S + a_E \phi_E + a_W \phi_W + S_2 + S_{DC}, \quad (4.49)$$

where the discretisation coefficients, a_P , a_N , a_S , a_E , a_W and the source term S_2 are still calculated using equation (4.20). S_{DC} may have different expanded form when different high order schemes are used. For example, when Harten's (1983) minmod scheme is used, we have

$$\left\{ \begin{aligned} S_{DC} &= \frac{1}{2} \left\{ G_{r,n}^1 G_{r,n}^{1+} \min \text{mod}(\Delta_n, \Delta_n^-) - G_{r,n}^1 G_{r,n}^{1-} \min \text{mod}(\Delta_n, \Delta_n^+) \right. \\ &\quad - G_{r,s}^1 G_{r,s}^{1+} \min \text{mod}(\Delta_s, \Delta_s^-) + G_{r,s}^1 G_{r,s}^{1-} \min \text{mod}(\Delta_s, \Delta_s^+) \\ &\quad + G_{r,e}^2 G_{r,e}^{2+} \min \text{mod}(\Delta_e, \Delta_e^-) - G_{r,e}^2 G_{r,e}^{2-} \min \text{mod}(\Delta_e, \Delta_e^+) \\ &\quad \left. - G_{r,w}^2 G_{r,w}^{2+} \min \text{mod}(\Delta_w, \Delta_w^-) + G_{r,w}^2 G_{r,w}^{2-} \min \text{mod}(\Delta_w, \Delta_w^+) \right\} \\ \Delta_f^- &= \phi_P - \phi_{P-1}, \quad \Delta_f = \phi_{P+1} - \phi_P, \quad \Delta_f^+ = \phi_{P+2} - \phi_{P+1} \\ \min \text{mod}(x, y) &= \text{sgn}(x) \max\{0, \min[|x|, |y \text{sgn}(x)|]\} \\ G^\pm &= \frac{1 \pm \text{sgn}(G)}{2} \end{aligned} \right. \quad (4.50)$$

4.3.4 Non-Staggered SIMPLE Method

About the non-staggered SIMPLE method

The SIMPLE (semi-implicit method for pressure-linked equations) (Patankar and Spalding, 1972; Patankar, 1980) is one of the most sophisticated and successful numerical method for incompressible heat and fluid flows. Under the condition of

incompressibility, the continuity of fluids is only a constraint for velocity field and therefore the pressure-velocity coupling is very weak in the differential governing equations. This weak coupling is a difficulty for numerical methods and the central problem for calculation of incompressible flows is the pressure-velocity coupling. In a decoupled iterating method, this coupling has two meanings:

- (a). the pressure is an elliptic field and therefore, the gradient of pressure in the momentum equation shall be discretised by the central differencing (CD) scheme. However, CD may obtain a non-physical “chess-board” pressure field (Patankar, 1980) if there is no special strategy for remedy;
- (b). a decoupled iterating method obtains the correct pressure field by correcting the pressure step by step. So it is important to obtain the accurate pressure correction in each iteration step.

In the SIMPLE method, the staggered grid arrangement (Patankar and Spalding, 1972) and the non-staggered grid arrangement with a momentum interpolation technique (Rhie and Chow, 1983) are two methodologies to solve the “chess-board” pressure field problem; And the pressure correction equation is employed to obtain accurate pressure correction.

In the present study, the non-staggered grid algorithm is selected based on its advantages (Peric, Kessler and Scheuerer, 1988) as follows:

- (a). all variables share the same location; hence, only one set of control volume is needed;
- (b). in a discretisation equation, the convection contributions to the coefficients are same for all variables;
- (c). for a complex geometry, Cartesian velocity components can be used in conjunction with non-orthogonal coordinates, yielding simpler equations than when numerical coordinate-oriented velocity components are employed.

Momentum interpolation

The momentum interpolation and the pressure correction are two facets of the pressure-velocity coupling. As the first step, the momentum interpolation and relevant concepts should be introduced.

By setting $\phi = u$ and $\phi = v$ in equation (4.49) respectively, we have

$$\begin{cases} u = h_u + \left(\frac{Jr\Delta\xi\Delta\eta}{a_p} \right) \frac{\partial p}{\partial x} \\ v = h_v + \left(\frac{Jr\Delta\xi\Delta\eta}{a_p} \right) \frac{\partial p}{\partial y} \end{cases}, \quad (4.51)$$

where

$$h_u = \frac{\sum a_{NB} u_{NB} + S_u''}{a_p}, \quad \frac{\sum a_{NB} v_{NB} + S_v''}{a_p}, \quad (4.52)$$

S_u'' and S_v'' are the differences between $S_2 + S_{DC}$ in equation (4.49) and the pressure gradients for $\phi = u$ and $\phi = v$, respectively.

According to equation (4.5), we have

$$\frac{\partial p}{\partial x} = \frac{1}{J} \left(y_\eta \frac{\partial p}{\partial \xi} - y_\xi \frac{\partial p}{\partial \eta} \right), \quad \frac{\partial p}{\partial y} = \frac{1}{J} \left(-x_\eta \frac{\partial p}{\partial \xi} + x_\xi \frac{\partial p}{\partial \eta} \right). \quad (4.53)$$

Substituting equation (4.53) into equation (4.51) results in

$$\begin{cases} u = h_u + B_u \frac{\partial p}{\partial \xi} + C_u \frac{\partial p}{\partial \eta} \\ v = h_v + B_v \frac{\partial p}{\partial \xi} + C_v \frac{\partial p}{\partial \eta} \end{cases}, \quad (4.54)$$

where

$$\begin{cases} B_u = \left(-\frac{ry_\eta \Delta\xi \Delta\eta}{a_P} \right)_P, & C_u = \left(\frac{ry_\xi \Delta\xi \Delta\eta}{a_P} \right)_P \\ B_v = \left(\frac{rx_\eta \Delta\xi \Delta\eta}{a_P} \right)_P, & C_v = \left(-\frac{rx_\xi \Delta\xi \Delta\eta}{a_P} \right)_P \end{cases} \quad (4.55)$$

According to equation (4.9), the curvilinear velocities G_r^1 and G_r^2 become

$$\begin{cases} G_r^1 = H_1 + B_1 \frac{\partial p}{\partial \xi} + C_1 \frac{\partial p}{\partial \eta} \\ G_r^2 = H_2 + B_2 \frac{\partial p}{\partial \xi} + C_2 \frac{\partial p}{\partial \eta} \end{cases}, \quad (4.56)$$

where

$$\begin{cases} H_1 = (y_\eta h_u - x_\eta h_v) - G_g^1, & H_2 = (x_\xi h_v - y_\xi h_u) - G_g^2 \\ B_1 = B_u y_\eta - B_v x_\eta = \left(-\frac{r \Delta\xi \Delta\eta}{a_P} \right) \alpha, & C_1 = C_u y_\eta - C_v x_\eta = \left(\frac{r \Delta\xi \Delta\eta}{a_P} \right) \beta \\ B_2 = B_v x_\xi - B_u y_\xi = \left(\frac{r \Delta\xi \Delta\eta}{a_P} \right) \beta, & C_2 = C_v x_\xi - C_u y_\xi = \left(-\frac{r \Delta\xi \Delta\eta}{a_P} \right) \gamma \end{cases} \quad (4.57)$$

In order to eliminate the non-physical “chess-board” pressure field (Patankar, 1980), two methods, *ie*, Patankar and Spalding’s (1972) staggered grids arrangement method and Rhie and Chow’s (1983) momentum interpolation method, are available. For the non-staggered method used in the current study, Rhie and Chow’s (1983) momentum interpolation scheme, which is originally for fixed mesh system, is modified to calculate the relative curvilinear velocity components, G_r^1 and G_r^2 at cell faces of the control volume in our moving mesh arrangement. The derivation of the interpolation scheme is

straightforward and omitted for simplicity; here we directly give its final form as following:

$$\left\{ \begin{array}{l} G_{r,n}^1 = \overline{G_{r,n}^1} + B_{1,n} \left[\frac{p_N - p_P}{\xi_N - \xi_P} - \left(\frac{\partial p}{\partial \xi} \right)_n \right] \\ G_{r,s}^1 = \overline{G_{r,s}^1} + B_{1,s} \left[\frac{p_P - p_S}{\xi_P - \xi_S} - \left(\frac{\partial p}{\partial \xi} \right)_s \right] \\ G_{r,e}^2 = \overline{G_{r,e}^2} + C_{2,e} \left[\frac{p_E - p_P}{\eta_N - \eta_P} - \left(\frac{\partial p}{\partial \eta} \right)_e \right] \\ G_{r,w}^2 = \overline{G_{r,w}^2} + C_{2,w} \left[\frac{p_P - p_W}{\eta_P - \eta_W} - \left(\frac{\partial p}{\partial \eta} \right)_w \right] \end{array} \right. , \quad (4.58)$$

where the terms with top bars in $G_{r,n}^1$ are the linear interpolation between the corresponding parts of $G_{r,P}^1$ and $G_{r,N}^1$, and those in $G_{r,s}^1$, $G_{r,e}^2$ and $G_{r,w}^2$ are similar. The terms in square brackets have forth-order truncation error. When pressure oscillation occurs, the terms have big values; and when the pressure field is smooth (which is physically correct for incompressible flows), the terms are high order infinitesimalities. This procedure ensures strong velocity-pressure coupling and shows better convergence behaviour than the original SIMPLE, as reported by Rhie and Chow (1983) and Peric, Kessler and Scheuerer (1988).

Pressure correction equation and corrections of pressure and velocity

The second task for the pressure-velocity coupling is to obtain unknown pressure field by solving a pressure correction equation derived from the continuity of fluid.

By setting $\phi = 1$, $\Gamma_\phi = 0$ and $S(\phi) = 0$ in equation (4.11) and integrating over the control volume, the discretised continuity equation is obtained as:

$$\left(G_{r,n}^1 - G_{r,s}^1 \right) \Delta \eta + \left(G_{r,e}^2 - G_{r,w}^2 \right) \Delta \xi = \frac{(Jr)^O - (Jr)}{\Delta t} \Delta \xi \Delta \eta . \quad (4.59)$$

In the iteration procedure, the flow fields of u^* , v^* and p^* (the superscript asterisk denotes an intermediate iteration value) can not satisfy conservations of both continuity

and momentum, therefore the corrections should be applied as:

$$u = u^* + u', \quad v = v^* + v', \quad p = p^* + p', \quad (4.60)$$

and

$$G_r^1 = G_r^{1*} + G_r^{1'}, \quad G_r^2 = G_r^{2*} + G_r^{2'}, \quad (4.61)$$

where u' , v' , $G_r^{1'}$ and $G_r^{2'}$ are the corrections of velocity, and p' is the pressure correction. Assuming that the effects of pressure correction on h_u and h_v in equation (4.54) and on H_1 and H_2 in equation (4.56) are negligible, the relations between the corrections of velocity and pressure are obtained as following:

$$u' = B_u \frac{\partial p'}{\partial \xi} + C_u \frac{\partial p'}{\partial \eta}, \quad v' = B_v \frac{\partial p'}{\partial \xi} + C_v \frac{\partial p'}{\partial \eta}, \quad (4.62)$$

and

$$\begin{cases} G_{r,n}^{1'} = B_{1,n} \left(\frac{p'_N - p'_P}{\xi_N - \xi_P} \right), & G_{r,s}^{1'} = B_{1,s} \left(\frac{p'_P - p'_S}{\xi_P - \xi_S} \right) \\ G_{r,e}^{2'} = C_{2,e} \left(\frac{p'_E - p'_P}{\eta_E - \eta_P} \right), & G_{r,w}^{2'} = C_{2,w} \left(\frac{p'_P - p'_W}{\eta_P - \eta_W} \right) \end{cases} \quad (4.63)$$

Substituting equations (4.61) and (4.63) into equation (4.59) and rearranging the terms, we have the pressure correction equation as:

$$C_P p'_P = C_N p'_N + C_S p'_S + C_E p'_E + C_W p'_W + \dot{m}_P + \frac{(Jr)^o - (Jr)}{\Delta t} \Delta \xi \Delta \eta, \quad (4.64)$$

where

$$\left\{ \begin{array}{l}
 C_N = (-B_{1,n} \Delta \eta) / (\xi_N - \xi_P) \\
 C_S = (-B_{1,s} \Delta \eta) / (\xi_P - \xi_S) \\
 C_E = (-C_{2,e} \Delta \xi) / (\eta_E - \eta_P) \\
 C_W = (-C_{2,w} \Delta \xi) / (\eta_P - \eta_W) \\
 C_P = C_N + C_S + C_E + C_W \\
 \dot{m}_P = (G_{r,s}^{1*} - G_{r,n}^{1*}) \Delta \eta + (G_{r,w}^{2*} - G_{r,e}^{2*}) \Delta \xi
 \end{array} \right. \quad (4.65)$$

4.3.5 Numerical Grid Generation

In recent years, there has been considerable progress in developing computational methods to solve the Navier-Stokes equations in regions with irregularly shaped boundaries. For this purpose, finite-element methods (FEM) are considered as natural choice due to their intrinsic geometric flexibility. However, for calculations of heat and fluid flow problems, the computational theories and skills for finite-difference methods (FDM) are more mature than those for FEM. Therefore, many CFD researchers are working on the development of FDM for heat and fluid flows; and several successful methods, such as the extension of computational region (Patankar, 1980), combination of coordinates (Rastogi and Rodi, 1978), and the triangle network (Winslow, 1967) have been developed. For most of the engineering problems such as our present conjugate heat and fluid flows for a single bubble, the complex boundaries are basically impossible to be fitted by any of available simple coordinates systems. In these cases, body fitted coordinates (BFC) and nonorthogonal curvilinear grids are attractive choices and have been widely employed by CFD researchers. Our finite volume discretisation and the non-staggered SIMPLE method are just based on the moving body fitted coordinates system.

An excellent review on numerical method of grid generation was presented by Thompson, Warsi and Mastin (1982). Here we only introduce the grids generation differential equation method for body-fitted coordinates systems, ie, the so-called TTM method (Thompson, Thames and Mastin, 1974), where the TTM is a short form of Thompson, Thames and Mastin. This method was originally proposed by Winslow (1967) but systemically studied and developed by Thompson, Thames and Mastin (1974) and Thompson, Warsi and Mastin (1982, 1985). More general information about numerical grid generation can be found in relevant references.

The generation of body-fitted grids is a boundary value problem whose solution is a classic task for theory and study of partial differential equations. Second order elliptic equations are mathematical description of boundary value problems. The simplest elliptic equation is the Laplace equation. With well-posed boundary values, the solution of the Laplace equation has second order smoothness, which is a desired characteristic of numerical grids. According to the extremum principle and the uniqueness of the solution of Laplace equation, the curvilinear coordinates ξ and η can be regarded as the solutions of the following Laplace equations in the physically space:

$$\begin{cases} \nabla^2 \xi = \frac{\partial^2 \xi}{\partial x^2} + \frac{\partial^2 \xi}{\partial y^2} = 0 \\ \nabla^2 \eta = \frac{\partial^2 \eta}{\partial x^2} + \frac{\partial^2 \eta}{\partial y^2} = 0 \end{cases} \quad (4.66)$$

Setting the boundary values of $\xi(x, y)$ and $\eta(x, y)$ at all physical boundaries, equation (4.66) becomes a well-posed Laplace problem with the first kind- Dirichlet boundary conditions and can be solved numerically.

Although the solution methods for the Laplace equations are well studied, the irregular physical boundaries impose difficulties for solving equation (4.66) in the physical space. Because of this, equation (4.66) is always transformed into the computational

space where the computational domain can be set as regular. The transformed Laplace equations are as follows:

$$\begin{cases} \alpha \frac{\partial^2 x}{\partial \xi^2} - 2\beta \frac{\partial^2 x}{\partial \xi \partial \eta} + \gamma \frac{\partial^2 x}{\partial \eta^2} = 0 \\ \alpha \frac{\partial^2 x}{\partial \xi^2} - 2\beta \frac{\partial^2 x}{\partial \xi \partial \eta} + \gamma \frac{\partial^2 x}{\partial \eta^2} = 0 \end{cases}, \quad (4.67)$$

where the metrics α , β and γ are defined by equation (4.7). Again, setting the boundary values of $\xi(x, y)$ and $\eta(x, y)$ at all physical boundaries, equation (4.67) can be solved.

Although the non-staggered SIMPLE method can be theoretically applied to an arbitrarily non-orthogonal mesh, good orthogonality for numerical grids is still expected so as to obtain a smooth convergent path. It is well known that for a certain numerical method, the more non-orthogonal the mesh is, the convergent path is the rougher. Thomas and Middlecoff (1980) proposed a method of controlling the non-orthogonality and distribution by adding source terms to equation (4.67). Shieh (1984) proposed a more efficient grid-controlling function. In this paper, Shieh's (1984) method is used. With the added source term, equation (4.67) changes into the Poisson equation,

$$\begin{cases} \alpha \frac{\partial^2 x}{\partial \xi^2} - 2\beta \frac{\partial^2 x}{\partial \xi \partial \eta} + \gamma \frac{\partial^2 x}{\partial \eta^2} = -J^2 \left(P_1 \frac{\partial x}{\partial \xi} + P_2 \frac{\partial x}{\partial \eta} \right) \\ \alpha \frac{\partial^2 x}{\partial \xi^2} - 2\beta \frac{\partial^2 x}{\partial \xi \partial \eta} + \gamma \frac{\partial^2 x}{\partial \eta^2} = -J^2 \left(P_1 \frac{\partial y}{\partial \xi} + P_2 \frac{\partial y}{\partial \eta} \right) \end{cases}, \quad (4.68)$$

where P_1 and P_2 are the grid-controlling functions as follows (Shieh, 1984),

$$\left\{ \begin{array}{l} P_1(\eta) = -\sum_{i=1}^{m_1} a_i^1 \text{sign}(\eta - \eta_i) \exp(-b_i^1 L_i^1) \\ P_2(\xi) = -\sum_{i=1}^{m_2} a_i^2 \text{sign}(\xi - \xi_i) \exp(-b_i^2 L_i^2) \\ L_i^1 = \sqrt{c_i^1 (\eta - \eta_i)^2} \quad ; \quad L_i^2 = \sqrt{c_i^2 (\xi - \xi_i)^2} \end{array} \right. , \quad (4.69)$$

a_i^1 , a_i^2 , b_i^1 , b_i^2 , c_i^1 and c_i^2 are coefficients which are selected to control the distance between grid lines to specified points, lines or faces so that the distribution of grids can be controlled.

4.4 Multi-Block Computation

In application of numerical schemes to practical problems with complex geometries, despite the power and sophistication of present grid generation capabilities, the use of a single-grid system may cause difficulty in generating a reasonable single grid to cover the entire flow domain. For example, using a single grid system to map a spherical-cap or skirted gas bubble surrounded by liquid results in severely skewed grid lines which make calculation difficult. This challenging problem makes multi-block methods, also known as zonal approaches, more attractive. As the grids can be either patched (Rai, 1984) or overlapping (Steger, 1991), the flow domain of interest but with arbitrary geometry can be easily covered. Liu and Shyy (1996) summarised the advantages of multi-block methods as follows:

- (a). it can resolve the topological complexity of a complicated geometry by permitting grid components to be generated individually and more easily fitted with local boundary geometry;
- (b). grid lines need not be continuous across grid interfaces, and local grid refinement

- and adaptive redistribution can be conducted more easily to accommodate different physical length scales; and
- (c). it provides a natural route for parallel computation.

The most important point in a zonal approach is to properly treat the zonal boundaries so as to make good use of the above advantages of the methods. Because the grid lines may not be continuous across block interfaces, information between blocks has to be transferred with additional work. These information transformation methods should preferably be easy to implement while maintaining good efficiency and desirable accuracy. A major related issue is that, for many flow problems, it is often important to use conservative interface procedure to ensure that physical laws are satisfied. Such a consideration can impose serious constraints on the construction of an interface interpolation scheme; furthermore, in some cases, the above needs can conflict with one another. Simultaneous achievement of both conservation and accuracy can be a very difficult task. This difficulty has attracted the attention of scientists even since the appearance of multi-block methods and the following treatments have been proposed: the chimera scheme for interpolations on overlaid grids (Benek, Buning and Steger, 1985), Rai's scheme for a TVD (Total Variation Diminishing) finite difference formulation (Rai, 1984), Bush's (1985) scheme based on characteristic boundary conditions, and the FDM-FEM hybrid scheme (Nakahashi and Obayashi, 1987). Later than those, Furukawa, Yamasaki and Inoue (1991) proposed a zonal approach with non-overlapping structured grids, in which the requirements of uniquely defining the zone boundary satisfying flux conservation across the boundary were met; and more recently, Liu and Shyy (1996) devised an interpolation scheme based on the local conservative correction method for mass flux at the grid interfaces.

The multi-block method in this paper, which is employed to combine with the moving mesh method so as to calculate bubble deformation later, has two key issues for the treatment of the zonal boundaries. These are the uniquely defining the zonal boundary and an appropriate interpolation method.

4.4.1 Uniqueness of Zonal Boundary

In the present multi-block calculation method, we use a composite grid system. So the computational domain is divided into several zones, and grids are generated independently in each zone (block). The zone boundary is defined as the interface between the blocks.

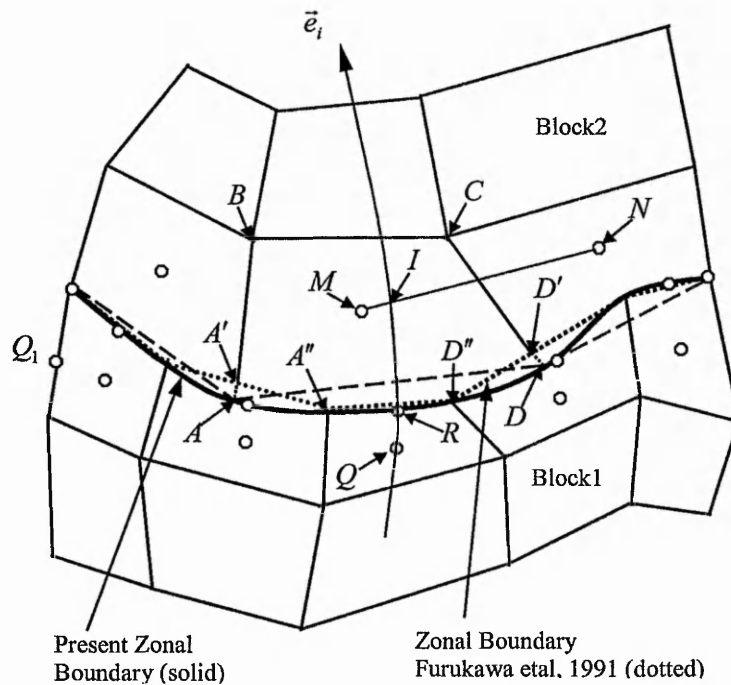


Figure 4.6 Multi-block and zonal boundary

Consider the composite multi-block grid system shown in figure 4.6. If the zonal boundary is not straight, the independent generation of the grids can cause gaps or overlaps where the boundaries of the two blocks do not coincide. In order to avoid this, Furukawa, Yamasaki and Inoue (1991) proposed defining the zonal boundary by the boundary of one block, block 1 in figure 4.6 for example. Consequently, the first cell in block 2 connected to the zone boundary is no longer a quadrilateral but a polygon. (That is, in figure 4.6, cell $ABCD$ is changed into $A'BCD'D''A''A'$). Furukawa, Yamasaki

and Inoue (1991) further developed an accurate method of high order for evaluating the flux across the zonal boundary. The numerical tests in their paper have demonstrated the potential of the method when applied to complex geometries.

However, altering the near boundary cells in block 2 from quadrilaterals to polygons also introduces extra calculation difficulties. Firstly, no single formula is available for the calculation of polygonal cell faces (or cell volumes in three-dimensional problems), and some means is required to identify the complex shape of each cell adjoining the boundary. Secondly, because with a moving mesh the grid speeds for different boundary points are different, there are extra computational difficulties in defining the topology of polygonal cells.

In this paper, the zone boundary is defined as one of the two blocks shown in figure 4.6. In the meantime, in order to guarantee the uniqueness of the boundary, the nodes of block 1, where the mesh has been generated first, are employed to interpolate the boundary nodes of block 2 using a cubic spline interpolation. The topology of the near boundary cells is retained as a “general” quadrilateral with curvilinear sections as the boundaries. In order to calculate the area of the cell, a cubic spline fit is also used to evaluate the determinant of the metric tensor, J ; while the cell area is calculated as $J\Delta\xi\Delta\eta$. The remainder of the near boundary cell is naturally and understandably treated as a “general” quadrilateral following the basic ideas of body fitted co-ordinates. This application of a cubic spline fit will compensate for the implicit error in the calculation of cell area.

4.4.2 Zonal Boundary Variable Interpolation

In order to solve incompressible flows described by equation (1), boundary values of ϕ are needed. The ϕ at the zone boundary for block 1 is calculated as follows (see figure 4.6):

$$\begin{cases} \phi_R^{(1)} = (s_I \phi_Q^{(1)} + s_Q \phi_I^{(1)}) / (s_I + s_Q) \\ \phi_I^{(1)} = (s_N \phi_M^{(2)} + s_M \phi_N^{(2)}) / (s_N + s_M) \end{cases}, \quad (4.70)$$

where the numbers in the bracket in the superscripts stand for the blocks, $s_N = \overline{IN}$ and $s_M = \overline{MI}$, $s_I = \overline{RI}$ and $s_Q = \overline{QR}$. The point I is defined as the intersection of the linear segment MN and the extended co-ordinate curve, which passes through point R and outwards from block 1 to block 2.

The $\phi_R^{(1)}$ is used as a boundary value for block 1, and also to evaluate the convection-diffusion flux through the zonal boundary. For block 2, the processing method is similar to that for block 1, and is omitted here.

In order to ensure the conservation of physical laws, a conservative treatment for mass flux should be carried out so that the interpolation scheme, ie, equation (4.70), can be regarded as appropriate.

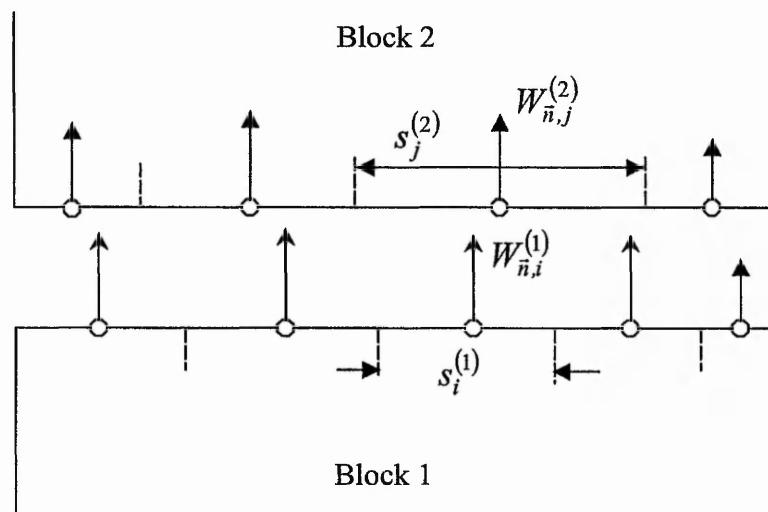


Figure 4.7 Notations used in two-block interface

Suppose the grids scenario of an interface schematically shown in figure 4.7, where the

grids on the side of block 1 are indexed from $i=1$ to $imax$, and from $j=1$ to $jmax$ for block 2; $s_i^{(1)}$ and $s_j^{(2)}$ are area of control volumes on blocks 1 and 2 sides, respectively; $W_{\bar{n},i}^{(1)}$ and $W_{\bar{n},j}^{(2)}$ are velocity components normal to $s_i^{(1)}$ and $s_j^{(2)}$ respectively. The conservation of mass flux is expressed as:

$$\sum_{i=1}^{imax} W_{\bar{n},i}^{(1)} \cdot s_i^{(1)} = \sum_{j=1}^{jmax} W_{\bar{n},j}^{(2)} \cdot s_j^{(2)} . \quad (4.71)$$

The interpolated velocity values obtained by equation (4.70) may not be able to satisfy equation (4.71) and therefore, a scaling procedure is carried out. For the convenience of description, we calculate the velocity $W_{\bar{n},j}^{(2)}$ firstly and denote its value obtained by equation (4.70) as $W_{\bar{n},j}^{(2)*}$. The scaling procedure is

$$W_{\bar{n},j}^{(2)} = W_{\bar{n},j}^{(2)*} \cdot \frac{\sum_{i=1}^{imax} W_{\bar{n},i}^{(1)} \cdot s_i^{(1)}}{\sum_{j=1}^{jmax} W_{\bar{n},j}^{(2)*} \cdot s_j^{(2)}} . \quad (4.72)$$

Equation (4.72) ensures the conservation of mass flux across the interface. The calculation of $W_{\bar{n},i}^{(1)}$ is similar and is omitted here for simplicity.

4.5 Validations of the Numerical Methods

Until now, a complete algorithm for moving boundary problems has been presented in this chapter. A series of validations are to be carried out so as to examine the calculating performance of the algorithm. The testing examples and the purpose of the validations are as follows:

- (a). lid-driven flow in a squeezed cavity, to validate the use of non-staggered non-orthogonal mesh and high order schemes;
- (b). laminar flow through tubes with constrictions, to validate the use of body-fitted coordinates in axisymmetric system;
- (c). flow over a backward-facing step, to validate the multi-block calculation for fluid flow;
- (d). natural convection in horizontal annulus, to validate the multi-block calculation of heat and fluid flows;
- (e). flow in channel with moving indentation, to validate the calculation of time-dependent moving boundary problems.

4.5.1 Lid-Driven Flow in A Squeezed Cavity

Demirdzic, Lilek and Peric (1992) proposed a lid-driven flow in a cavity with inclined sidewalls to test the use of non-orthogonal grids. The geometry and boundary conditions are shown in figure 4.8, in which the inclination angle $\beta = 45^\circ$, and $L = 1$, density $\rho = 1$ and lid velocity $U_L = 1$. The Reynolds number, defined using the lid velocity, U_L , and cavity length, L , is 1000 by setting the viscosity to be 0.001. Demirdzic, Lilek and Peric (1992) proved that it is impossible to obtain a grid dependent solution if the mesh is coarser than 80×80 . They provided a set of benchmark solutions on an extremely fine mesh, 320×320 , and a high order convection scheme was applied.

In the present calculation, a non-uniform mesh of 160×160 , which expands symmetrically towards the centrelines (CL1 and CL2 in figure 4.8) from all walls, is found to be fine enough to obtain the grid-independent solution and is therefore adopted. We have also tried to further refine the mesh to 320×320 , similar to what Demirdzic, Lilek and Peric (1992) did; however, no further accuracy improvement was achieved.

To check the effects of using high order schemes, following convection schemes, namely, the first-order upwind scheme, the power-law (which is also of first-order resolution), the second-order TVD scheme OSHER (Chakaravarthy and Osher, 1983), and the third-order scheme SMART (Gaskell and Lau, 1988), were employed. The computational results are presented in figures 4.9 and 4.10, respectively.

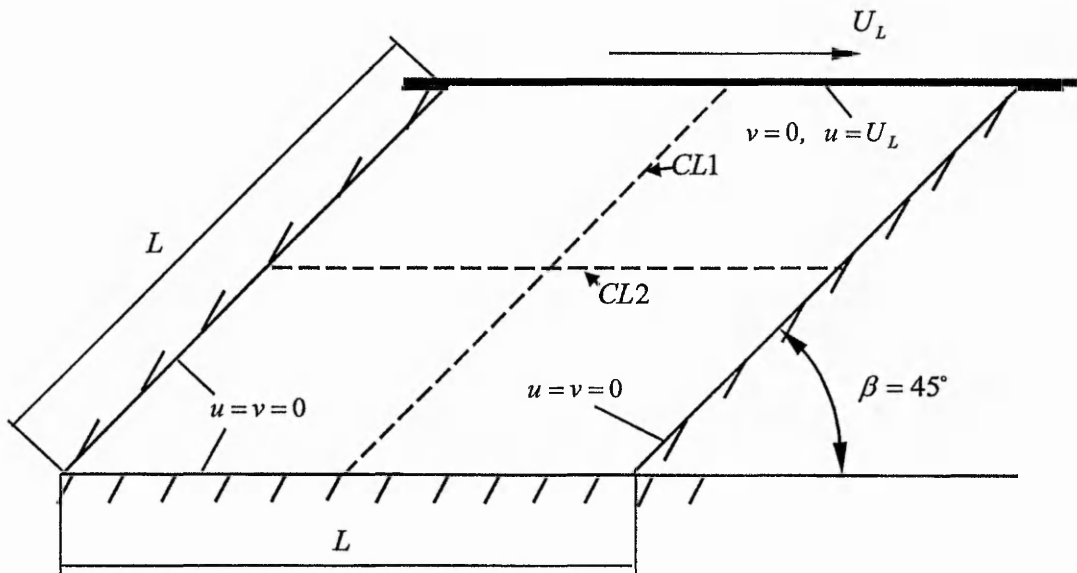


Figure 4.8 Geometry and boundary conditions for squeezed lid-driven cavity flow

The profiles of Cartesian velocity components, u in horizontal and v in vertical, along centrelines are shown in figures 4.9. The results for using different convection schemes are compared with the benchmark solutions (Demirdzic, Lilek and Peric, 1992). It is noted that, first-order schemes (the first-order upwind and the power-law) give worse results while high-order schemes (the OSHER and the SMART) offer excellent agreements with the benchmark solution.

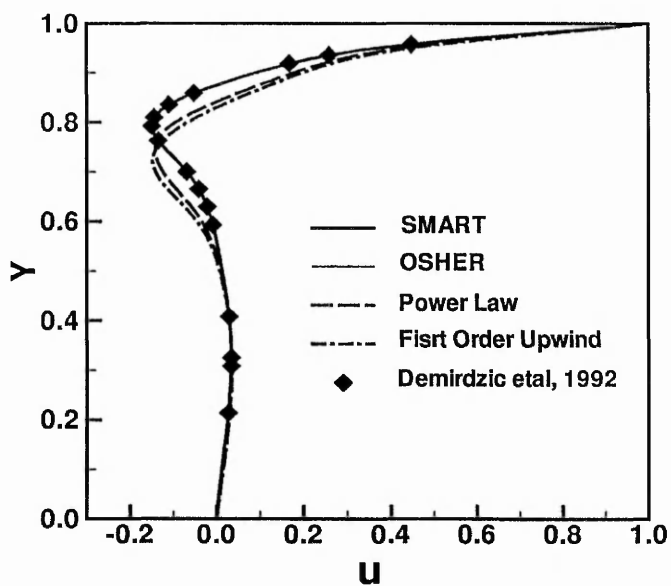


Figure 4.9a Centerline velocity profiles in the squeezed cavity
 u component

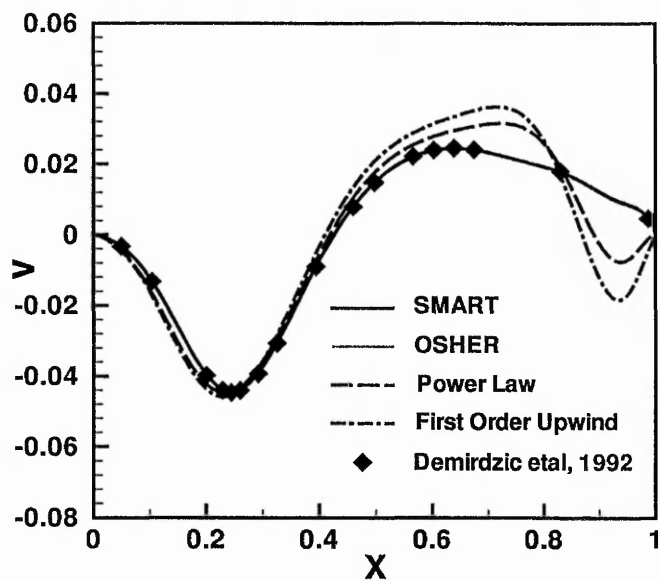


Figure 4.9b Centerline velocity profiles in the squeezed cavity
 v component

In figure 4.10, convergent paths of calculations using the above-mentioned first-order upwind and the third-order SMART schemes are described. Although the numerical accuracy for different schemes is different, the effect of deferred correction method is obvious as the convergent path for SMART is almost on the same level of roughness with that of the first-order upwind.

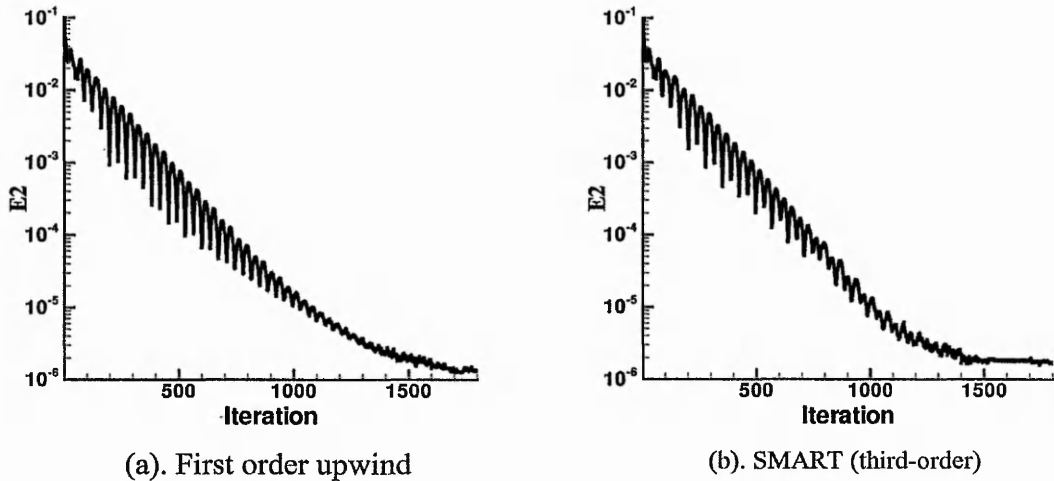


Figure 4.10 Convergent paths of different convection schemes

4.5.2 Laminar Flow Through Tubes with Constrictions

The laminar flow through a circular pipe with a sinusoidal constriction, experimentally studied by Young and Tsai (1973) and numerically studied by Rastogi (1984) and Karki and Patankar (1988), is selected to validate the using of body-fitted grids in axisymmetric coordinates system. The geometry is shown schematically in figure 4.11. Both the tube and the constriction are axisymmetric. The radius of the stenosis was specified as a cosine curve:

$$\frac{R}{R_0} = 1 - \frac{d}{2R_0} \left(1 + \cos \frac{\pi x}{X_0} \right) \quad -X_0 < x < X_0 . \quad (4.73)$$

The number of grid is taken as 82×30 in the $x-r$ coordinates. The density of grid points was higher near the wall and the grid was stretched in the axial direction with more grid points in the constricted region.

Table 4.1 Model Geometries

Model no.	R_0 (in.)	d/R_0	X_0/R_0	Stenosis (% reduction in area)
M-2	0.372	2/3	4	89
M-3	0.372	2/3	2	89

Results have been obtained for two geometries corresponding to models M-2 and M-3 of Young and Tsai (1973). The geometric characteristics of these stenoses are given in table 4.1. Computations were done at $Re=50$ and 100 for model M-2 and at $Re=40$ for model M-3.

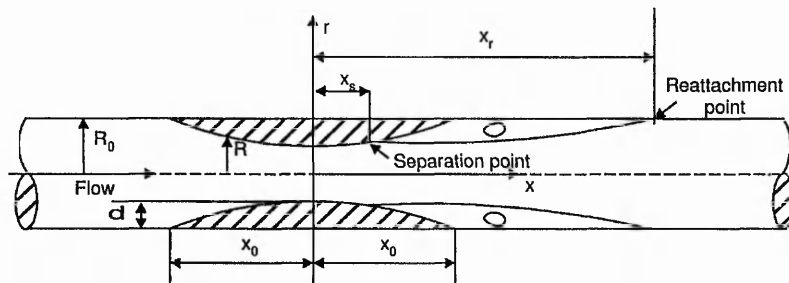


Figure 4.11 Geometric configuration of the pipe with a constriction

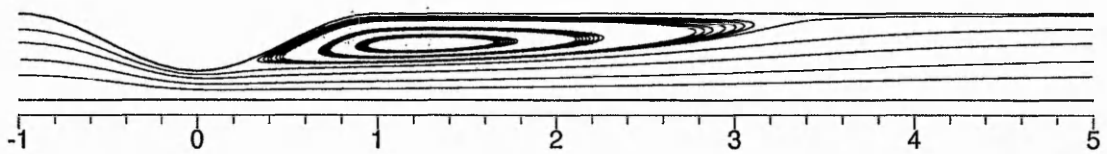
Figure 4.12 Flow pattern for Model M-3 at $Re=40$

Table 4.2 Comparison of the present results with experiments

Re	Model no.	Separation point (X_s/X_0)		Reattachment point (X_r/X_0)	
		Experiment	Present	Experiment	Present
50	M-2	0.37	0.37	2.2	2.1
100	M-2	0.37	0.37	4.1	4.1
40	M-3	0.37	0.37	2.9	3.1

The flow pattern for model M-3 for $Re=40$ is plotted in figure 4.12. Table 4.2 gives a comparison between the present results and the experimental results of Young and Tasi (1973). The agreement between the two sets of results is good. The error of X_r/X_0 is acceptable considering the experimental error at low Reynolds numbers.

4.5.3 Separated Flow Over Backward-Facing Step

The flow over a backward-facing step provides an excellent test case for the accuracy of a numerical method because of the dependence of the reattachment length on Reynolds number. Freitas (1995) recommended an experimental configuration which was used by Armaly, Durst, Pereira and Schonung (1983) as a benchmark problem for algorithm validation. Here we employ it to validate the potential of calculations using a multi-block mesh.

The inlet height of the channel is $h = 5.2$ mm, the step height $s = 4.9$ mm. In experiments, the upstream length of the step is nearly 40 inlet heights to ensure the flow is fully developed. Reynolds number is defined as $Re = u_{av} \times D / \nu$, where u_{av} is the averaged inlet velocity, $D = 2h$, $\nu = 1.5 \times 10^{-5}$ (air). In our calculation, the computational domain is divided into upstream and downstream blocks at the step. A fully developed parabolic velocity profile is imposed at 5 step heights upstream of the expansion, and the total length of the computational domain is set at 40 step heights.

Non-slip boundary conditions are applied at the top and bottom walls; a uniform static pressure is imposed at the exit boundary. At the zonal boundary, pressure is transmitted upstream from the downstream block, and velocity is transmitted in the opposite direction. Typical grids are illustrated in figure 4.13. For block 1, the grid size is 27×54 , horizontal \times vertical; For block 2, three mesh sizes, 177×103 (mesh 1), 352×103 (mesh 2) and 452×162 (mesh 3), have been used to evaluate the grid independence of the results for a flow at $Re = 450$. The computed results are given in figure 4.14 and table 4.3.

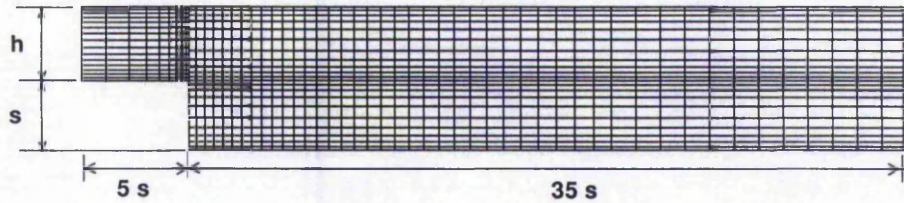


Figure 4.13 Illustration of grids distribution for calculation of backward facing step

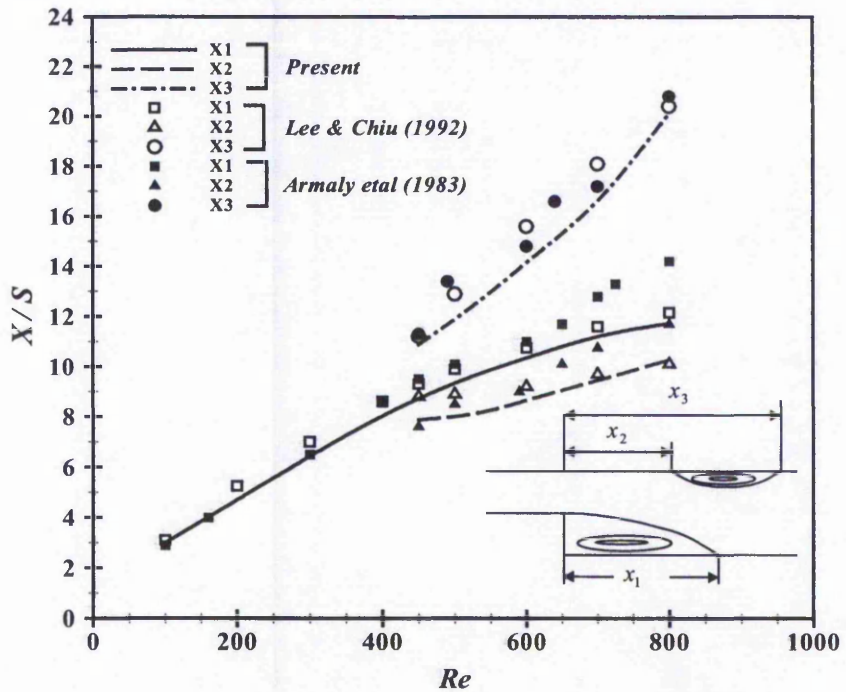


Figure 4.14 Positions of reattachment points in a step flow

Table 4.3 Reattachment points predicted by three meshes

	x_1	x_2	x_3
Mesh 1	7.69	6.53	10.67
Mesh 2	8.69	7.87	10.88
Mesh 3	8.72	7.89	10.88
Experiment	9.5	7.6	11.3

In Table 4.3, the size and location of the separation vortex at $Re = 450$, scaled by the lengths x_1 , x_2 and x_3 (see figure 4.14 for the definition), calculated by the present method with three different meshes are compared with experiments by Armaly, Durst, Pereira and Schonung (1983). It can be seen that the differences between calculation and experiment are reduced by increasing the grid number, from mesh 1 to mesh 2. For example, the error for x_1 has been reduced by 10.5% (the error for x_1 is 8.5% with mesh 2). This also implies that mesh 1 is not dense enough to get a grid-independent solution. However, further increasing grid density from mesh 2 to mesh 3, gives a reduction of only 0.3% in the error of x_1 . It is noted that with this change the error for x_2 even increases by 0.26%, which is about the same as the error reduction for x_1 and may result from experimental deviations will be mentioned later. It is therefore concluded that mesh 2 is fine enough to provide a grid independent solution. At the same time, we observe that the calculated x_1 , x_2 and x_3 , with mesh 2 or mesh 3, are smaller than their experimental values. Nevertheless these errors are generally smaller than those when commercial CFD codes are tested against the benchmarks as tabulated by Freitas (1995) and perhaps should be accepted.

Figure 4.14 compares the calculated distributions of x_1 , x_2 and x_3 , with experiments

(Armaly, Durst, Pereira and Schonung, 1983) as at different Reynolds number. In view of the results presented in table 1, only mesh 2 has been used in getting these distributions. Calculations for different Reynolds numbers are also available in Lee and Chiu (1992). The comparison between their results and the present prediction is also shown in figure 4.14, with satisfactory agreement up to $Re = 600$; as is also shown for the calculations by Lee and Chiu (1992). At still higher Reynolds numbers the deviation between calculation and experiment becomes steadily larger. As concluded by Kim and Moin (1985) and Freitas (1995), these deviations are not surprising and probably not a result of numerical error, but are more likely to be a result of the apparent three dimensionality and unsteadiness in the measured flow.

4.5.4 Natural Convection in Horizontal Annulus

The calculation of natural convection heat transfer in a horizontal annulus demonstrates the use of multi-block non-orthogonal meshes. The configuration employed here is that of the detailed experimental study by Kuehn and Goldstein (1976) also used for the numerical simulation using SIMPLE algorithm by Date (1986). The value of L/D_{in} (ratio of gap width/inner diameter) is 0.8, the Rayleigh number $Ra = \frac{g_a \beta \Delta T L^3}{\nu^2} Pr = 4.7 \times 10^4$ and the Prandtl number $Pr = 0.7$. Following the usual methods, as the heat and flow fields are symmetric, half of the concentric annulus, divided along the vertical symmetry line, is employed as the computational domain. In order to validate the robustness of the calculation procedure of using the multi-block body-fitted non-orthogonal mesh, the whole annulus is divided into two non-symmetric blocks as the computational domain (shown in figure 4.15). The mesh numbers for the two blocks are 82×52 and 74×42 , respectively. Convergence paths for the mass residuals are shown in figure 4.16. The computational results are compared with measurements and shown in figures 4.17- 4.20.

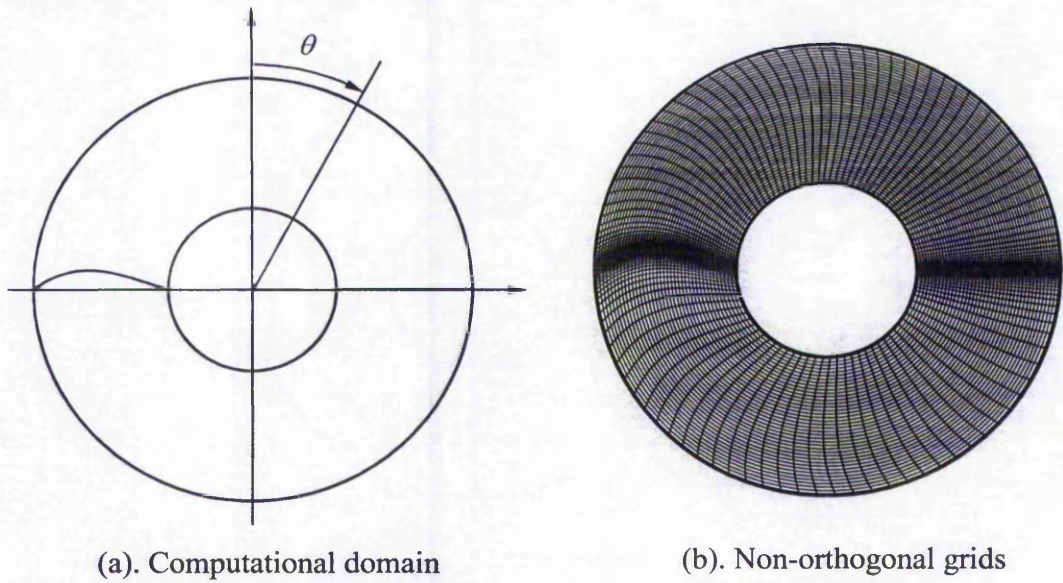


Figure 4.15 Computational domain and grids for the natural convection in annulus

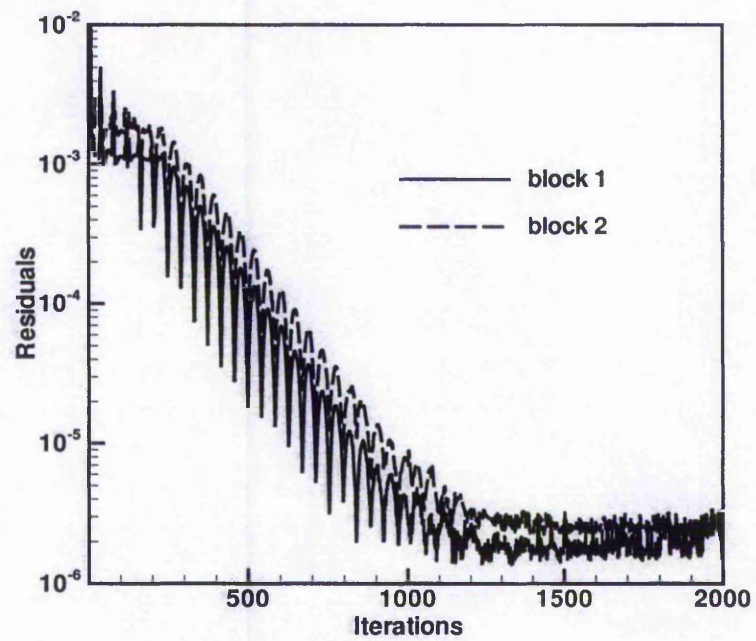


Figure 4.16 Convergent path for natural convection in annulus

Figure 4.17 shows the local thermal conductivities at the inner and outer cylinders, defined as follows:

$$K_{eq} = \frac{r \log(r_{out}/r_{in})}{T_{in} - T_{out}} \frac{\partial T}{\partial r}$$

Excellent agreement between calculation and experiment is achieved. Even at the near upper symmetry line ($\theta = 0^\circ$) of outer wall, where Date (1986) got a deviation of 10%.

The presently computed temperature and angular velocity profiles, also show good agreement with their respective measurements by Kuehn and Goldstein (1976), as shown in figure 4.18 and figure 4.19. Since the computational blocks are not symmetric,

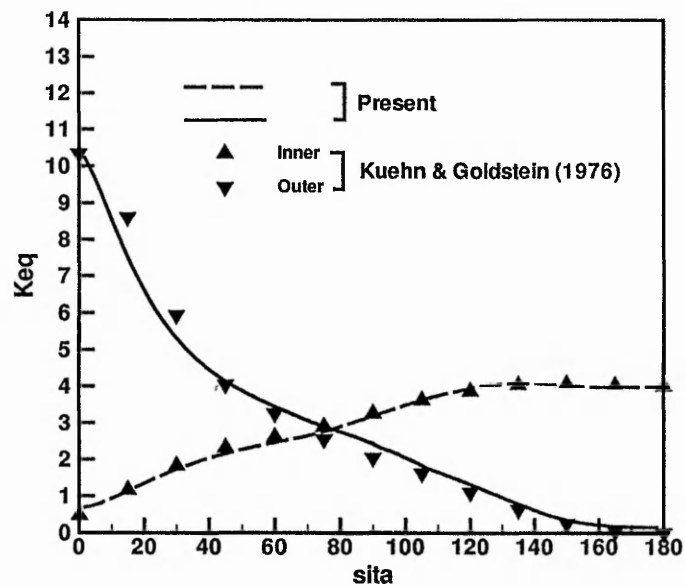


Figure 4.17 Local equivalent conductivities at inner and outer walls

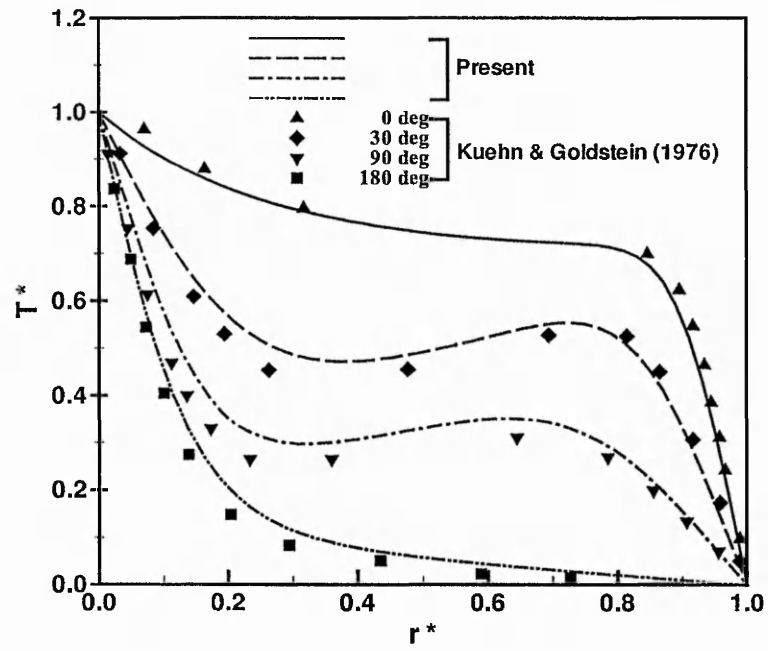


Figure 4.18 Temperature profiles

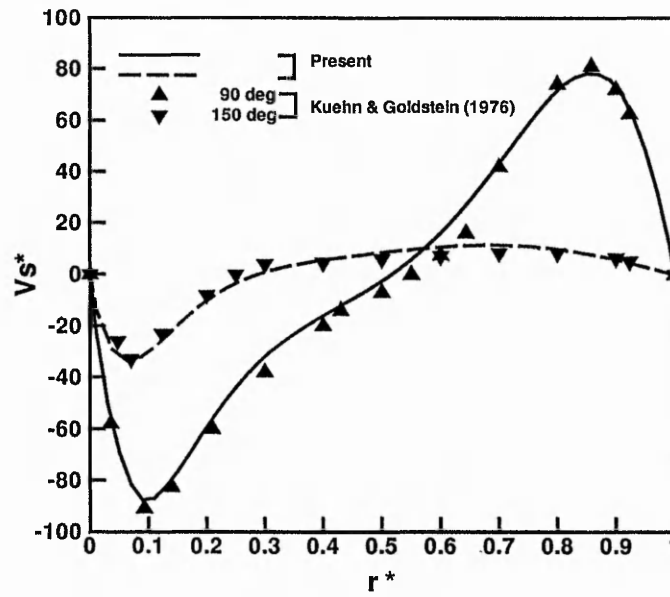


Figure 4.19 Distribution of angular velocity

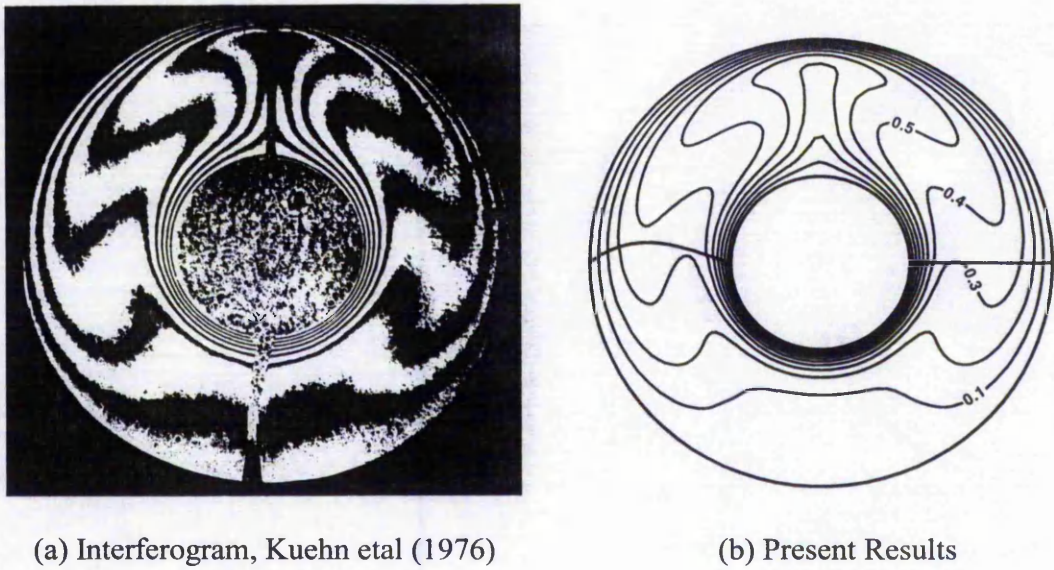


Figure 4.20 Contour of non-dimensional temperature

the results in these figures are mean values at the two sides of the geometric symmetry line. In fact, a maximum magnitude of 2 percent for the non-symmetric deviation, defined as the relative deviation of temperature at any two symmetric points, has resulted from the calculation, perhaps because the grids are still not fine enough. As can be seen from figure 11, very good symmetry for the temperature field and excellent agreement with Kuehn and Goldstein (1976)'s results are obtained in the present calculation.

4.5.5 Time-Dependent Moving Indentation Channel Flow

The unsteady channel flow with a time-dependent moving indentation in one wall, which Pedley and Stephanoff (1985) proposed as a benchmark experimental investigation, and to which Ralph and Pedley (1988), Rosenfeld and Kwak (1991) and Lee and Chiu (1992) have derived computed solutions, has been used here to assess the suitability of a multi-block moving mesh for calculation.

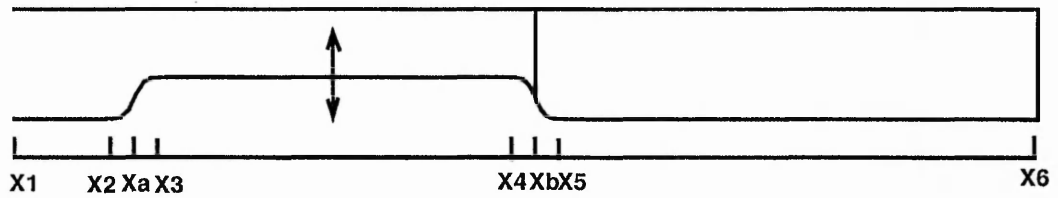


Figure 4.21 Computational domain for moving indentation problem

As shown in figure 4.21, the lower wall between x_2 and x_5 is moving periodically with the vertical co-ordinate $y(x, t)$ defined as following:

$$y(x, t^*) = f(x)h(t^*),$$

where $h(t^*) = 0.5(1 - \cos 2\pi t^*)$,

$$f(x) = \begin{cases} 0 & x_1 \leq x < x_2 \\ 0.5\varepsilon[1 + \tanh \gamma(x - x_a)] & x_2 \leq x < x_3 \\ \varepsilon & x_3 \leq x < x_4 \\ 0.5\varepsilon[1 - \tanh \gamma x] & x_4 \leq x < x_5 \\ 0 & x_5 \leq x < x_6 \end{cases},$$

$\varepsilon = 0.38$, $\gamma = 4.14$, $x_3 - x_2 = x_5 - x_4 = 2.5$, $x_4 - x_3 = 8$, $x_2 + x_3 = 2x_a$, and $x_4 + x_5 = x_b = 0$. Ralph and Pedley (1988) calculated how the downstream boundary can generally affect the solution up to $(x_6 - x) = 2$. Following their suggestion, $(x_2 - x_1) = 2$ and $(x_6 - x_5) = 12$ are taken as the computational domain in the present paper. In order to evaluate the multi-block calculation, the computational domain has been deliberately divided into two blocks along the vertical position $x = x_b = 0$, as shown in figure 4.21. The dimensionless time is defined by $t^* = \omega t$, where t is the dimensional time and ω is the frequency of indentation movement. The Reynolds

number based on the averaged inlet velocity u_{av} and the inlet height L is $Re = 507$, while the Strouhal number is $St = L\omega/u_{av} = 0.037$. No-slip boundary conditions are imposed on the top and bottom walls and a fully developed parabolic velocity profile at the inlet, uniform pressure and $\partial\phi/\partial x = 0$ for velocity at exit; The zone boundary is treated in the same way as the backward facing step in section 3.1. The grid number is 102×52 for block 1 and 177×60 for block 2 with a time step Δt of 0.01. The computational results are shown in figures 4.22 and 4.23.

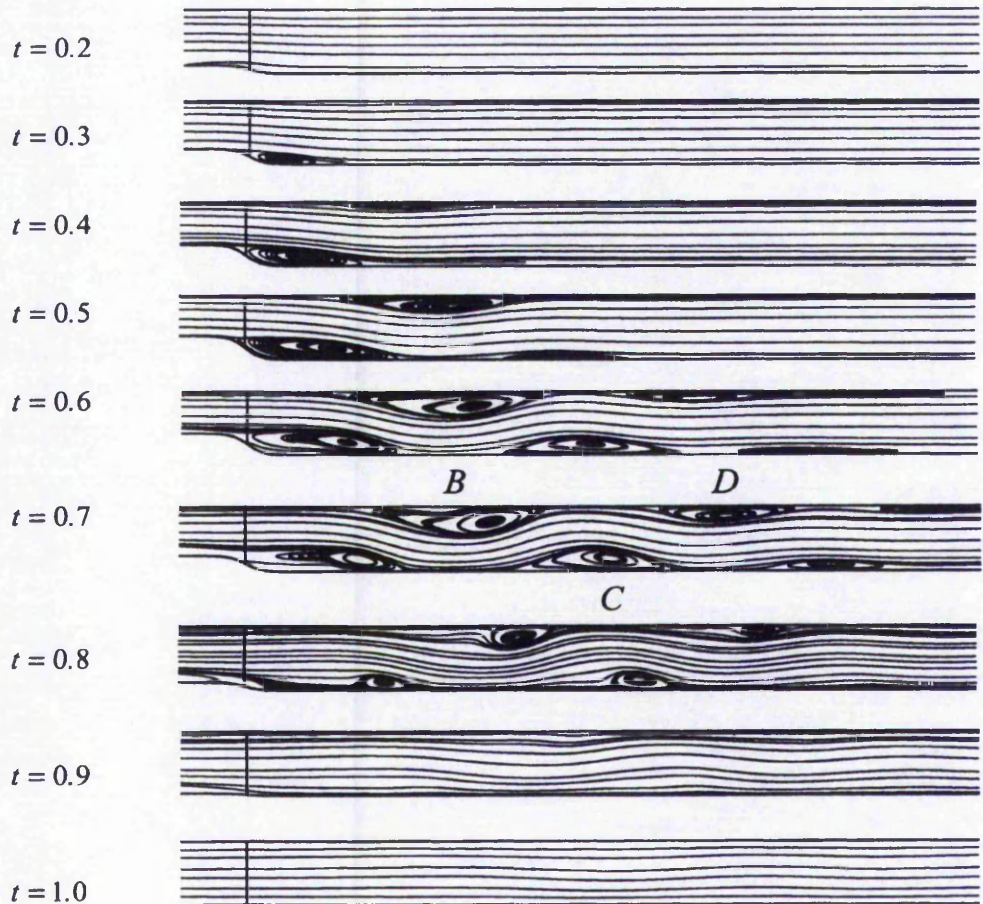


Figure 4.22 Streamlines at various instants in a cycle

Figure 4.22 shows the streamlines for a series of instants during one cycle of the indentation movement. The eddy doubling described by Pedley and Stephanoff (1985) is observed around $t^* = 0.6$, when the indentation has reached its top position and is moving downward. With this combination of Re and St numbers, no obvious vortex shedding is observed, which agrees with Lee and Chiu (1992)'s simulation.

The positions of crests and troughs of the eddies are compared to the experimental results by Pedley and Stephanoff (1985) in figure 14, where Lee and Chiu (1992)'s computed results are also given for comparison. Although noticeable differences can be found between the simulations of Lee and Chiu (1992) and the present, the overall agreement of both simulations with experiment is reasonable.

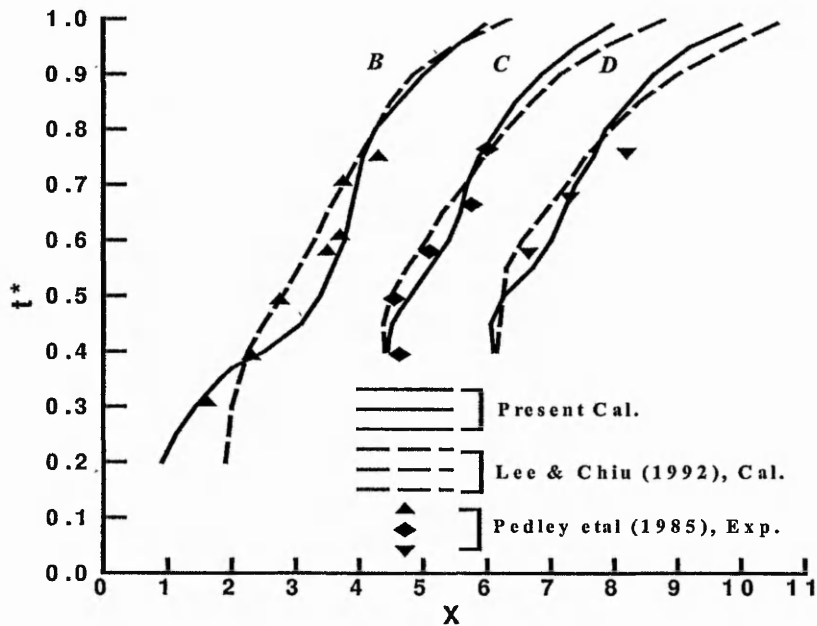


Figure 4.23 Position of the crests and troughs of the eddies

4.6 Summary

A calculation procedure for heat and fluid flows in geometries with time-dependent moving boundaries has been developed to assist future simulations of the inert bubble problem. The procedure, which is based on the non-staggered SIMPLE method with TVD treatment, incorporates a moving mesh arrangement with multi-block iteration to calculate moving boundary problems. The procedure is validated by a series of testing problems showing the robustness for further simulation of time-dependent inert bubble problem.

Chapter 5

Numerical Study of Gas-Liquid Interfacial Flows in Bubbles

5.1 Introduction

As described in chapter 3, the heat and fluid flows for the inert bubble problem are conjugate and unsteady. Compared with single-phase problems, the “conjugate flows” here have more specific meanings. It means the flows, separated by the zero-thickness gas-liquid interface, are conjugate and coupled by the interfacial boundary conditions (equations (3.17)~ (3.20)) though the fluids on both sides of the interface are different. Moreover, “unsteady” means the shape of the inert bubble is changeable; this imposes a new task of determining the bubble shape whose movement cannot be supposed to be externally decided but can only be decided by the interfacial conditions. Therefore, further to the numerical method for general moving boundary problems presented in chapter 4, special treatments on gas-liquid interfaces must be made.

This chapter presents a complete numerical study on gas-liquid interfacial flow problems. Treatments are applied to a gas-liquid surface so as to determine the bubble shape and the interfacial velocity. These treatments include a “continuous stress method” and a “modified Ryskin-Leal method”. Based on these, a full numerical algorithm for steady problems is presented and applied to the study of interfacial flows in deformable bubbles and drops with benchmark numerical solutions or experimental data.

5.2 Gas-Liquid Interface Treatments

5.2.1 Expansion of Interfacial Boundary Conditions

The interfacial boundary conditions given by equations (3.17)~ (3.20) are in general forms and should be expanded into the moving non-orthogonal coordinates system so as to carry out further treatments for determining the interfacial velocity and bubble shape.

Consider a two-block system shown in figure 5.1. The transform relation between the (x, y) and the (ξ, η) coordinates system has been given by equation (4.1). The coordinate lines $\eta = \eta_{max}$ in block 1 and $\eta = 0$ in block 2 are duplicated and describing the bubble profile. Therefore, unit vectors in the tangential and normal directions of the bubble face are as follows:

$$\begin{cases} \vec{t} = t_x \vec{i} + t_y \vec{j} = \frac{x_\xi \vec{i} + y_\xi \vec{j}}{\sqrt{x_\xi^2 + y_\xi^2}} \\ \vec{n} = n_x \vec{i} + n_y \vec{j} = \frac{-y_\xi \vec{i} + x_\xi \vec{j}}{\sqrt{x_\xi^2 + y_\xi^2}} \end{cases} \quad (5.1)$$

The velocity in tangential and normal directions:

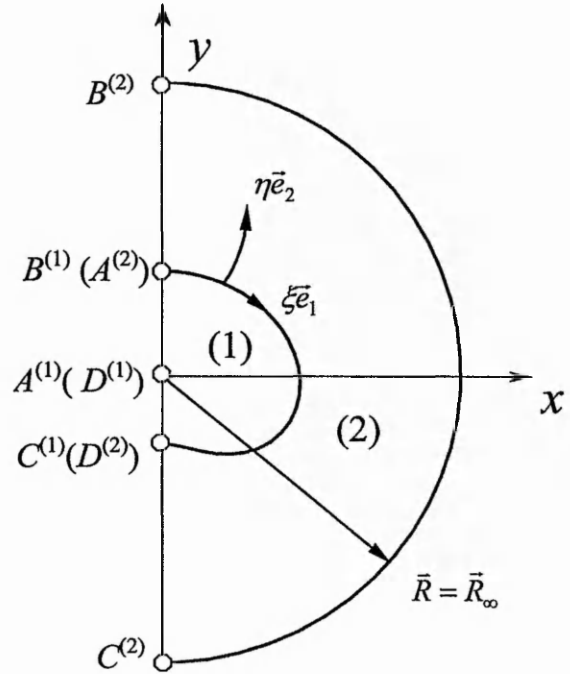


Figure 5.1 Zoned computational domain

$$\left\{ \begin{array}{l} W_{\bar{i}} = \frac{ux_{\xi} + vy_{\xi}}{\sqrt{x_{\xi}^2 + y_{\xi}^2}} \\ W_{\bar{n}} = \frac{-uy_{\xi} + vx_{\xi}}{\sqrt{x_{\xi}^2 + y_{\xi}^2}} \end{array} \right. ; \quad (5.2)$$

And the stresses of fluids

$$\tau_{\bar{i}}^{(i)} = \frac{1}{\text{Re}^{(i)} \gamma J} \left[x_{\xi} \gamma \frac{\partial u}{\partial \eta} + y_{\xi} \gamma \frac{\partial v}{\partial \eta} - (x_{\xi} \beta + y_{\xi} J) \frac{\partial u}{\partial \xi} + (x_{\xi} J - y_{\xi} \beta) \frac{\partial v}{\partial \xi} \right], \quad (5.3)$$

$$\tau_{\bar{n}}^{(i)} = -p^{(i)} + \frac{2}{\text{Re}^{(i)} \gamma J} \left[\beta \left(y_{\xi} \frac{\partial u}{\partial \xi} - x_{\xi} \frac{\partial v}{\partial \xi} \right) + \gamma \left(x_{\xi} \frac{\partial v}{\partial \eta} - y_{\xi} \frac{\partial u}{\partial \eta} \right) \right]. \quad (5.4)$$

Based on the above relations, the interfacial boundary conditions given by equations (3.17)~(3.20) can be expanded,

Kinetic conditions:

$$W_{\bar{n}}^{(1)} = W_{\bar{n}}^{(2)} = 0, \quad (5.5)$$

$$W_{\bar{i}}^{(1)} = W_{\bar{i}}^{(2)}; \quad (5.6)$$

dynamic conditions:

$$\tau_{\bar{i}}^{(1)} \Phi_{\rho} = \tau_{\bar{i}}^{(2)}, \quad (5.7)$$

$$\tau_{\bar{n}}^{(1)} \Phi_{\rho} + \frac{1}{We} \left(\frac{1}{R_m} + \frac{1}{R_a} \right) = \tau_{\bar{n}}^{(2)}, \quad (5.8)$$

where R_m and R_a are curvature radii in the meridional plane and the azimuthal surface respectively; and their calculating formula will be introduced in a lateral section in this chapter.

5.2.2 Continuous Stress Method

As we stated in section 5.1, there are two challenging tasks for calculating conjugate flows for a deformable single bubble. These are the determinations of the interfacial velocity and the bubble shape, respectively. The continuous stress method introduced here is for the first task.

Because a primitive variable based calculation requires explicit boundary values of u and v , which are implicitly given by the continuity of tangential stress in equation (5.7) and need to satisfy equations (5.5) and (5.6) as well, a special method to obtain the interfacial velocity must be found. This is the background for developing the “continuous stress method”.

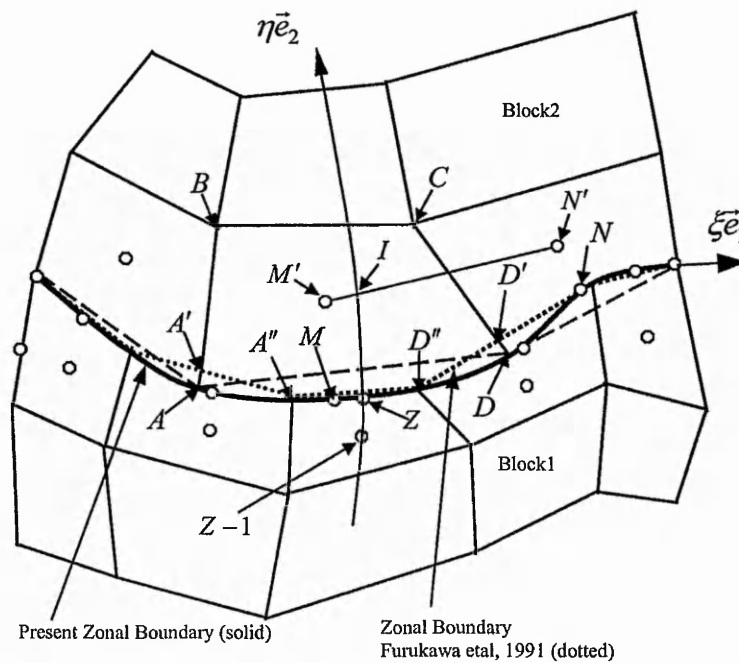


Figure 5.2 Zonal boundary and gas-liquid interface

Figure 5.2 is a two-block system separated by a gas-liquid interface. It has some slight

differences with figure 4.6 because the fluids in the two blocks here are different. In figure 4.6, the single-phase flow can penetrate the zonal boundary while the interpolation is to obtain the boundary values of dependent variables by inner grid nodes located on both sides of the zonal boundary; In figure 5.2, fluids are not supposed to penetrate the zonal boundary (which is a gas-liquid interface) directly, and the interpolation here is to transfer the values of functions (such as stresses and tangential velocity) from one side to the other of the zonal boundary.

Based on the above background and the clarification of concepts, we can consider the fact that equations (5.5), (5.6) and (5.7) are well-posed boundary conditions for a bubble of a specified shape. This means that the implicit equation (5.7) can be satisfied all the time during the iteration procedure if the tangential velocity remains discontinuous. Therefore, we can use the discontinuity of tangential velocity to correct the zonal boundary values of u and v until a numerical convergence is reached. In order to satisfy equation (5.7), the velocity at both nodes on the zonal boundary and on the first inner grid line are corrected at the same time so that the velocity gradient across the interface can remain unchanged. For the convenience of description, we denote the nodes on the zonal boundary and the first inner grid line with subscripts Z and $Z-1$ respectively and shown in figure 5.2, and we calculate $u_Z^{(1)}$ and $v_Z^{(1)}$ for example.

Rearranging equation (5.3), we have:

$$E \frac{\partial u}{\partial \eta} + G \frac{\partial v}{\partial \eta} = C, \quad (5.9)$$

where $E = x_\xi \gamma$, $G = y_\xi \gamma$, $C = \text{Re}^{(i)} \tau_i^{(i)} \gamma J + (x_\xi \beta + y_\xi J) \partial u / \partial \xi - (x_\xi J - y_\xi \beta) \partial v / \partial \xi$.

When we calculate the flow in block 1, the boundary values of block 2, $W_i^{(2)}$ and $\tau_i^{(2)}$ of a previous iteration step are used to determine the new boundary velocity values, $u_Z^{(1)*}$ and $v_Z^{(1)*}$. Firstly, $W_i^{(2)}$ and $\tau_i^{(2)}$ are interpolated to block 1, the results are $\tilde{W}_i^{(1)}$ and $\tilde{\tau}_i^{(1)}$ respectively. Then, $\tau_i^{(1)}$ in equation (5.9) is incorporated with $W_n^{(1)} = 0$, which results in:

$$\begin{cases} u_Z^{(1)*} = [Eu_{Z-1}^{(1)*} + Gv_{Z-1}^{(1)*} + C(\eta_Z^{(1)} - \eta_{Z-1}^{(1)})] / (E + G y_\xi / x_\xi) \\ v_Z^{(1)*} = u_Z^{(1)*} y_\xi / x_\xi \end{cases} \quad (5.10)$$

The tangential velocity corresponding to $u_Z^{(1)*}$ and $v_Z^{(1)*}$, $W_i^{(1)*}$, is not equal to $\tilde{W}_i^{(1)}$ and needs to be corrected. The discontinuity in the tangential velocity,

$$W_i^{(1)'} = \tilde{W}_i^{(1)} - W_i^{(1)*}, \quad (5.11)$$

can be incorporated with $W_{\bar{n}}^{(1)} = 0$ to obtain the corrections of the Cartesian velocity components. This results in

$$\begin{cases} u' = W_i^{(1)'} x_\xi / \gamma \\ v' = W_i^{(1)'} y_\xi / \gamma \end{cases} \quad (5.12)$$

The corrections of velocity are applied to both the zonal boundary and the first inner cell nodes,

$$\begin{cases} u_Z^{(1)} = u_Z^{(1)*} + \alpha_{uz} \cdot u' \\ v_Z^{(1)} = v_Z^{(1)*} + \alpha_{uz} \cdot v' \\ u_{Z-1}^{(1)} = u_{Z-1}^{(1)*} + \alpha_{uz} \cdot u' \\ v_{Z-1}^{(1)} = v_{Z-1}^{(1)*} + \alpha_{uz} \cdot v' \end{cases}, \quad (5.13)$$

where α_{uz} is an under-relaxation factor. Equation (5.13) ensures that the velocity gradient in η – direction does not change during the correcting procedure of tangential velocity and therefore the continuity of tangential stress is guaranteed. This method for obtaining interfacial velocity is therefore named as the “continuous stress method”.

5.2.3 Interface Deformation

Modified Ryskin-Leal method

Following the determination of interfacial velocity by the “conjugate stress method”, the second challenging task for calculation of deformable bubbles is to decide the bubble shape by the second interfacial dynamic condition, the balance of normal forces described by equation (5.8). More precisely, the second task is to use the local excess of normal forces to update the interface shape step by step during iteration procedures so that equation (5.8) can be satisfied. This is the essential of the method proposed by Ryskin and Leal (1984a, 1984b, 1984c).

Ryskin and Leal (1984a, 1984b, 1984c) reviewed possible routes of determining the interface shape by using equation (5.8). These possibilities include treating the equation as a non-homogeneous differential equation for boundary-shape coordinates x and y ; or treating the whole problem in a genuine transient mode and applying equations (5.7) and (5.8) as boundary conditions. Based on their reviewing, Ryskin and Leal (1984a) proposed a simple and indirect method, in which the shape of an interface is modified at each iteration step by moving the points of the surface in local normal direction by an amount proportional to the pressure difference. As introduced by Ryskin and Leal (1984a), due to the restraint of using orthogonal meshes, the interface updating had to be done indirectly by changing the scale factor, the Lamé metric coefficients (Ryskin and Leal, 1984a) of the coordinates system. Such changing of scale factor is possible to induce instability of numerical calculation. Moreover, the adoption of orthogonal meshes adds a troublesome requirement to the application of this method.

In order to sort out the problem, Salvador (1994) proposed to decide the interface shape by directly modifying the coordinates of the points. In this method, general non-orthogonal mesh can be used. Salvador (1994) studied the bubbles in the range of $(Re^{(2)}, We) = [0, 100] \times [0, 4]$ using this method while Raymond and Rosant (2000)

applied the method to $(Re^{(2)}, We) = [0, 100] \times [0, 5]$. Recently, Li and Yan (2002a, 2002b) have further applied the method to $(Re^{(2)}, We) = [0, 200] \times [0, 50]$. Although these applications are for studying bubbles using “external flow” models, their methods of determining the interface shape can be straightforwardly modified to our current study.

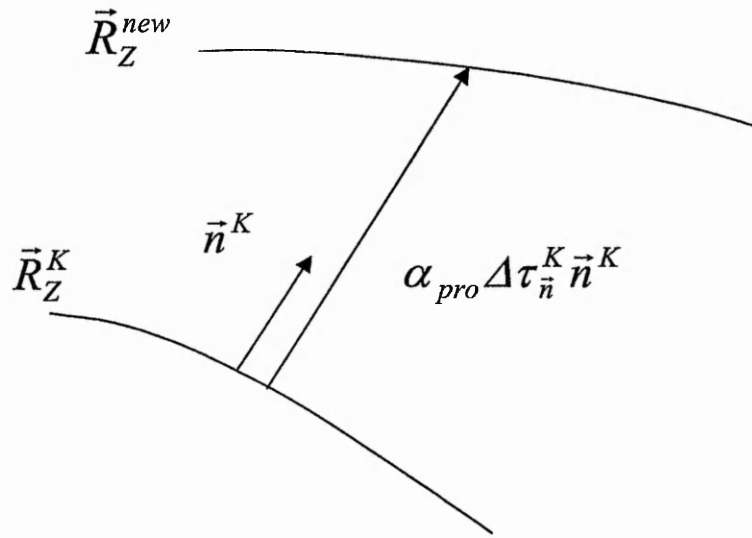


Figure 5.3 Determination of the new interface position

Consider an initial interface shape \vec{R}_Z^K shown in figure 5.3. It could be a result of an unconverged calculation where the dynamic condition, equation (5.8), has not been satisfied and therefore further iterations must be carried out. The imbalance of normal forces on the current iteration (denoted by script K),

$$\Delta \tau_{\vec{n}}^K = \tau_{\vec{n}}^{(2)K} - \left[\tau_{\vec{n}}^{(1)K} \Phi_{\rho} + \frac{1}{We} \left(\frac{1}{R_m} + \frac{1}{R_a} \right) \right]^K, \quad (5.14)$$

is used to predict the interface shape. That is,

$$\vec{R}_Z^{new} = \vec{R}_Z^K + \alpha_{pro} \Delta \tau_{\vec{n}}^K \vec{n}^K, \quad (5.15)$$

where \vec{n}^K is the unit normal vector of the interface given by equation (5.1), α_{pro} is an under-relaxation factor.

The new position of the interface, \vec{R}_Z^{new} determined by equation (5.15) is not an exact value. This is because magnitude of α_{pro} is only specified by numerical experiments. For a larger α_{pro} , the displacement of interface may be larger than actual values; while for a smaller α_{pro} , the displacement could be smaller. To determine exact position at the $K+1^{th}$ iteration, the conservation of the bubble volume must be controlled. The volume of bubble can be specified by

$$\mathcal{V} = \int_0^{\xi_{max}} \pi r^2 \frac{\partial y}{\partial \xi} d\xi. \quad (5.16)$$

The updated position of the interface is therefore decided as

$$\vec{R}_Z^{K+1} = \mathfrak{R} \cdot \vec{R}_Z^{new}, \quad (5.17)$$

where \mathfrak{R} is a scaling factor of the volume,

$$\mathfrak{R} = \left(\frac{\mathcal{V}^K}{\mathcal{V}^{new}} \right)^{\frac{1}{3}}. \quad (5.18)$$

The two-step method of determining interface shape by applying equations (5.15) and (5.17) is called as “modified Ryskin-Leal method”.

Curvature radii

The curvature radii, R_m and R_a appeared in equation (5.8), are in the meridional and azimuthal surfaces respectively. In space, the physical meanings of the curvature radii and of equation (5.8) can be illustrated in figure 5.4.

Consider an interface \bar{R}_Z determined by the modified Ryskin-Leal method. As the curvilinear η coordinates for the interface are constants, namely, $\eta = \eta_{max}^{(1)} = \eta_{min}^{(2)}$, so the Eulerian coordinates of \bar{R}_Z can be functions of ξ ,

$$\begin{cases} x_Z = x_Z(\xi) \\ y_Z = y_Z(\xi) \end{cases} \quad (5.19)$$

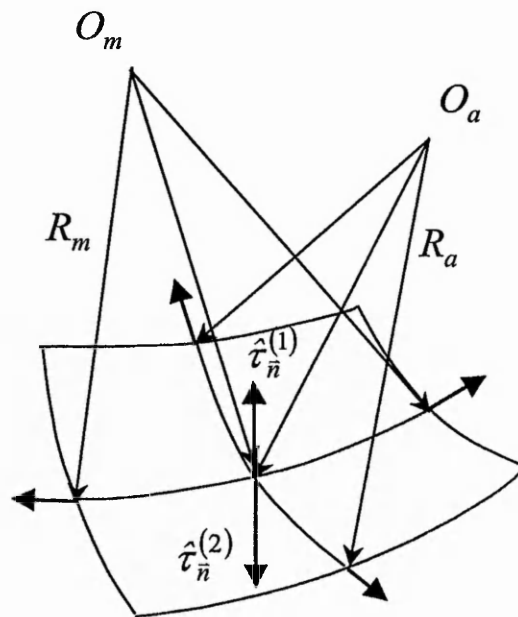


Figure 5.4 Definition of curvature radii

Therefore, the curvature in the meridional surface $x-y$ is

$$\frac{1}{R_m} = \frac{y_\xi x_{\xi\xi} - x_\xi y_{\xi\xi}}{(x_\xi^2 + y_\xi^2)^{3/2}} \quad (5.20)$$

The curvature in the azimuthal surface is determined by its definition,

$$\frac{1}{R_a} = -\frac{y_\xi}{x(x_\xi^2 + y_\xi^2)^{3/2}}. \quad (5.21)$$

It should be noticed that $y_\xi \leq 0$ in figure 5.1. In the meanwhile, due to the axisymmetric assumption, at the two ends of interfacial profile, we have

$$\frac{1}{R_a} = \frac{1}{R_m}. \quad (5.22)$$

Equation (5.22) is also applicable to the whole interfacial profile of spherical bubbles or drops.

Harmonious decomposition of normal constraints

As pointed out by Salvador (1994), the determination of interface by equations (5.15) and (5.17) is a highly unstable treatment and therefore extremely low values of the under-relaxation factor α_{pro} should be used in equation (5.15). This problem is genetic from the original Ryskin-Leal method, where the relaxation factor is reported to be on the magnitude of $O(10^{-3})$ while McLaughlin (1996) and Ponoth and McLaughlin (2000) even had to use relaxation factors of $O(10^{-4})$. In order to reduce instability, Salvador (1994) suggested to carry out a harmonious decomposition to the imbalance of normal stress given by equation (5.14) before the updating of interfacial profile is processed. This harmonious decomposition is adopted in our study and introduced in the following.

Consider the imbalance of normal forces, $\Delta\tau_{\bar{n}}$. It is a continuous function of ξ . Because of the axisymmetry assumption, $\Delta\tau_{\bar{n}}$ can be further treated as a periodical function in the zone of $[-\xi_{max}, \xi_{max}]$. A harmonious decomposition can be carried out by expanding $\Delta\tau_{\bar{n}}$ using the Fourier series as following:

$$\Delta\tau_{\bar{n}}(\xi) = \frac{a_0}{2} + \sum_{k=1}^{\infty} [a_k \cos(k\omega\xi) + b_k \sin(k\omega\xi)], \quad (5.23)$$

where $\omega = \frac{\pi}{\xi_{max}}$,

$$\begin{cases} a_k = \frac{1}{\xi_{max}} \int_{-\xi_{max}}^{\xi_{max}} \Delta\tau_{\bar{n}}(\xi) \cdot \cos(k\omega\xi) \cdot d\xi & , \quad k=0, \quad 1, \quad 2, \quad 3, \dots \\ b_k = \frac{1}{\xi_{max}} \int_{-\xi_{max}}^{\xi_{max}} \Delta\tau_{\bar{n}}(\xi) \cdot \sin(k\omega\xi) \cdot d\xi & , \quad k=1, \quad 2, \quad 3, \dots \end{cases}$$

For calculations based on discretisation,

$$\begin{cases} a_k = \frac{1}{\xi_{max}} \sum_{\xi=-\xi_{max}}^{\xi_{max}} \Delta\tau_{\bar{n}}(\xi_i) \cdot \cos(k\omega\xi_i) \cdot \Delta\xi_i & , \quad k=0, \quad 1, \quad 2, \quad 3, \dots \\ b_k = \frac{1}{\xi_{max}} \sum_{\xi=-\xi_{max}}^{\xi_{max}} \Delta\tau_{\bar{n}}(\xi_i) \cdot \sin(k\omega\xi_i) \cdot \Delta\xi_i & , \quad k=1, \quad 2, \quad 3, \dots \end{cases}$$

According to Salvador's (1994) suggestion, the maximum order of the Fourier series can be set as $k_{max} = 5 \sim 6$.

5.3 Solution Approach

The solution approach for the gas-liquid interfacial flows in the single inert bubble problem can be summarised as follows:

- (a). Define a far field boundary $\vec{R} = \vec{R}_{\infty}$ where the flow blockage effects due to the bubble can be neglected;
- (b). Give an initial field;

- (c). Determine a zoned computational domain separated by the bubble profile and generate a non-orthogonal mesh in it. The shape of the bubble is described by

$$\bar{R}_Z^K = (x_Z^K, y_Z^K), \quad (5.24)$$

where the superscript K denotes an iteration step;

- (d). Obtain an approximation to the velocity and pressure fields by carrying out several iterations on the equations for heat and flow using the SIMPLE algorithm presented in chapter 4, subject to boundary conditions (5.5) to (5.7) at the zonal boundary and conditions (3.39) to (3.46) at other boundaries. In an iterating step, the two blocks are calculated in sequence and the velocity values at the zonal boundary are calculated by equations (5.10) to (5.20). Carry on iterating until the following inequality is satisfied:

$$EVT = |W_i^{(1)*} - W_i^{(2)*}| \leq \varepsilon_{i1}; \quad (5.25)$$

- (f). Calculate the imbalance of normal-stress according to equation (5.14) and carry out a harmonious decomposition using equation (5.23);
- (g). Update the profile of the interface according to equations (5.15) and (5.17);
- (f). If all the following inequalities are satisfied,

$$ETN = |\Delta\tau_{\bar{n}}| \leq \varepsilon_{\bar{n}}, \quad (5.26)$$

$$ERZ = |R_Z^{K+1} - R_Z^K| \leq \varepsilon_{pro}, \quad (5.27)$$

$$EVT = |W_i^{(1)*} - W_i^{(2)*}| \leq \varepsilon_{i2}, \quad (5.28)$$

convergence can be declared; Otherwise, return to step (d), and carry on iterating until all the above convergent criteria are satisfied.

The relaxation factors can be valued as: $\alpha_{uz} = 0.01 \sim 0.5$ (this is up to Φ_μ , use a small value if $\Phi_\mu \ll 1$ or $\Phi_\mu \gg 1$), $\alpha_{pro} = (1 \sim 5) \times 10^{-3}$. The criteria of convergence: $\varepsilon_{r1} = 10^{-2}$, $\varepsilon_{r2} = 10^{-3}$, $\varepsilon_{\bar{n}} = 10^{-3}$ and $\varepsilon_{pro} = (1 \sim 5) \times 10^{-5}$. During the calculation, we found that the roles of equations (5.40) and (5.41) were equivalent, and if equations (5.41) and (5.42) were satisfied then all the governing equations and boundary conditions were also generally satisfied within acceptable tolerances. Specifically, the maximum norm of the residual for the pressure correction equation (*ie*, continuity of mass) was $O(10^{-6})$.

5.4 Results and Analysis

5.4.1 Spherical Drops

Two groups of results have been obtained. The first group are to examine the robustness of the numerical procedure and to observe the topology of two types of wake structure; the second group are to study the wake structure and its variation with exterior Reynolds number of a spherical drop at typical density and viscosity ratios which are used in industrial liquid spraying processes.

In the first group, three cases of a single liquid drop problem are studied and simulated. Case 1 is concerned with a water drop falling in air with the viscosity ratio (internal/external) $\Phi_\mu = 55$, and density ratio $\Phi_\rho = 790$, and at an external Reynolds number, $Re^{(2)} = 100$. The other two cases are respectively concerned with a liquid drop moving in an unbounded immiscible liquid with $\Phi_\mu = 3$, $\Phi_\rho = 1$ and at $Re^{(2)} = 100$ (case 2) and a drop flow with $\Phi_\mu = 5$, $\Phi_\rho = 0.1$ and at $Re^{(2)} = 300$ (case 3). Numerical calculations are carried out with a mesh arrangement as: block1 = 82×42 and block2 = 90×82 . The outer bound of computational domain is assigned at 50 times the equivalent drop radius, where a free stream condition is imposed. Meanwhile, comparisons have been made between the present numerical results and those obtained

by other researchers such as LeClair, Hamielec, Pruppacher and Hall (1972) and Juncu (1999).

Flow structure

Rivkind and Ryskin (1976) have suggested two types of returning flow which may arise at the rear of a spherical drop. One is the returning flow or vortex behind the drop without a separation; the other is the vortex attached to the drop surface. Juncu (1999) has named these two wakes as a fluid vortex and a solid vortex, respectively. In the presence of a fluid vortex, a “break-up” of the circulatory flow inside the drop is inevitable, this means that two vortex pairs will appear inside the drop.

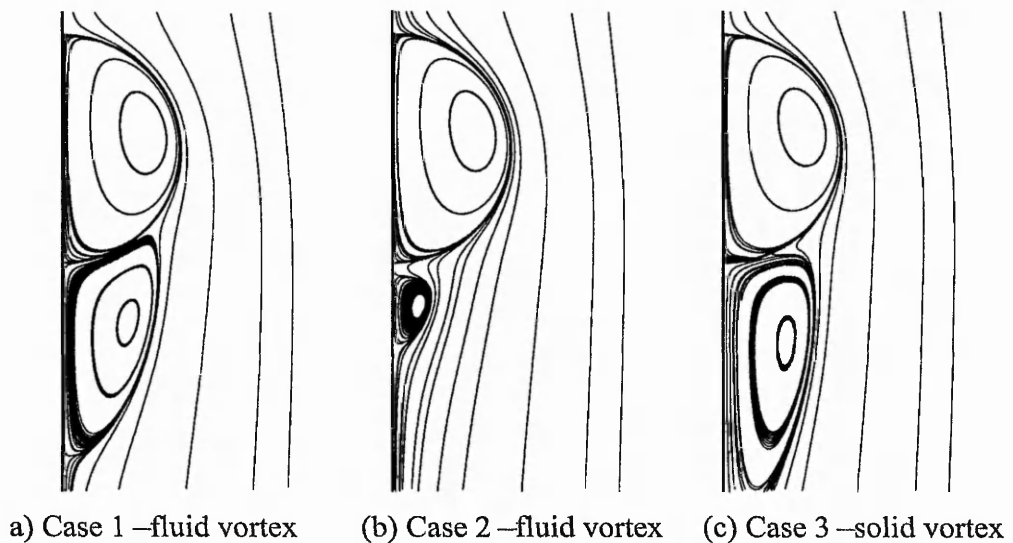


Figure 5.5 Flow structure inside and around a spherical droplet

Figure 5.5 shows the streamlines inside and outside a liquid drop for the three cases respectively. It can be seen from the figure that both two types of returning flow have been simulated. For case 1, as no “break-up” of internal flow can be identified, the vortex is therefore a fluid vortex. For case 2, the vortex identified is at a distance away

from the drop, it is also a fluid vortex. However, it is noted that, for case 3, two ring vortices (one with a larger size and the other with a smaller size near the rear stagnant point) exist inside the drop. This means that, for case 3, a “break-up” has taken place for the internal circulation of the drop and therefore the wake flow of the drop is in a form of solid vortex.

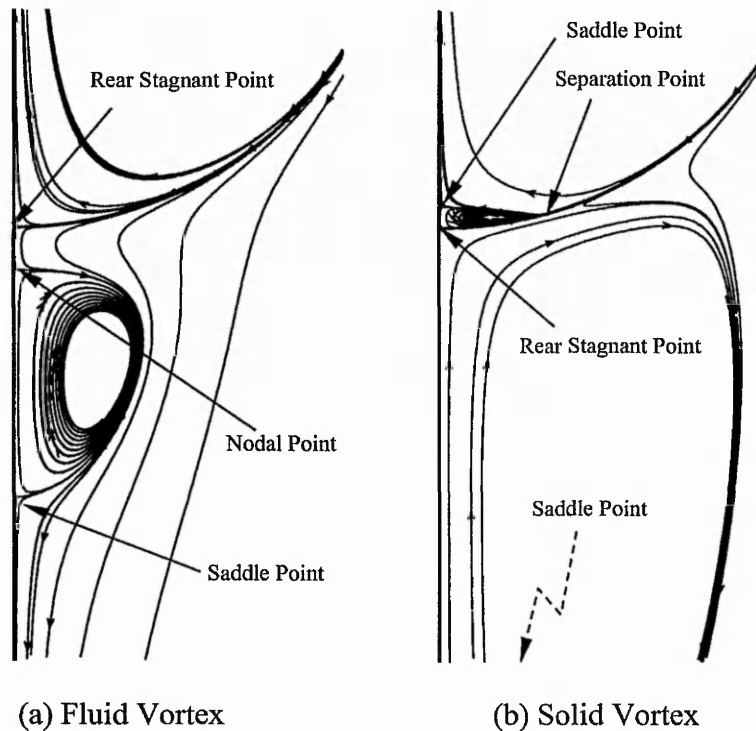


Figure 5.6 Topology of two wake-vortex types

The differences between the two types of wake vortex can be identified in a zoomed area of the rear stagnant point, as shown in figure 5.6. With a comparison of the topologies for the two types of wake, the fluid-vortex type has a smooth and unity internal circulation, while the flow inside a solid-vortex type is broken and a separation point can be identified. For case 2, as the wake vortex is not attached to the drop body

as seen in figure 5.6a, a nodal point of the streamlines between the rear stagnant point and the saddle point where is the end of wake vortex, can be observed. For the case of a solid-vortex type, the wake vortex is attached to the drop and therefore only a saddle point exists as shown in figure 5.6b.

Wake vortex length

The ratio of wake vortex length to the diameter of a drop is an important parameter for the study of mass transfer as the wake vortex is believed to have important effects on heat and mass transfer (Schmidt, Nassar and Lubbert, 1992). Therefore, it is necessary to calculate the ratio accurately. The results of calculation are obtained and compared with corresponding benchmark values showing good agreements; this is shown in Table 5.1.

Table 5.1 Comparison of wake vortex length

	Benchmark Value	Present	Error (%)
Case 1	0.85	0.86	1.18
Case 2	0.5	0.49	2
Case 3	2.3	2.25	2.17

Interfacial characteristics

Figure 5.7 shows the interfacial characteristics of the drop, where the tangential velocity W_t , interface pressure coefficient $P_s^{(2)}$, exterior interface vorticity $\Omega^{(2)}$ and interior interface vorticity $\Omega^{(1)}$. The definitions of these parameters are:

$$W_t = \frac{W_{\bar{t}}}{V_{ref}}, \quad (5.29)$$

$$P_s^{(2)} = \frac{P_{eff}^{(2)} - P_{eff,\infty}}{0.5\rho^{(2)}V_{ref}^2}, \quad (5.30)$$

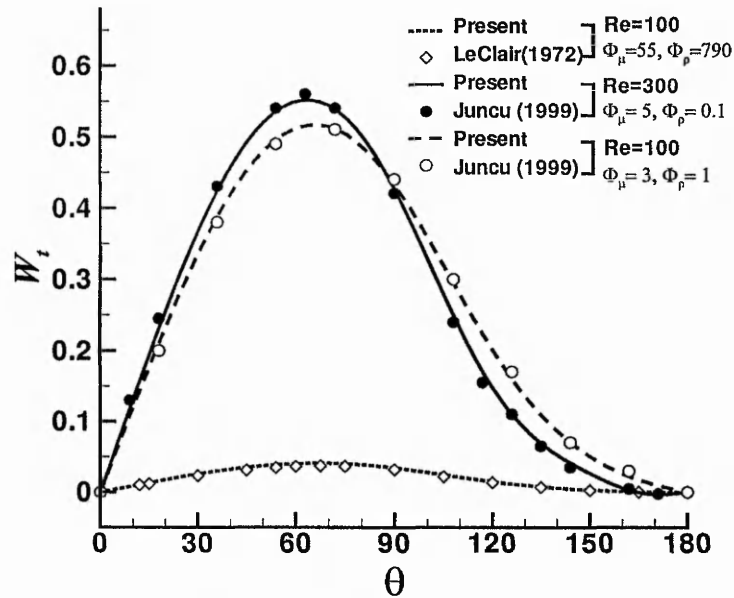


Figure 5.7a Tangential velocity at interface of a spherical droplet

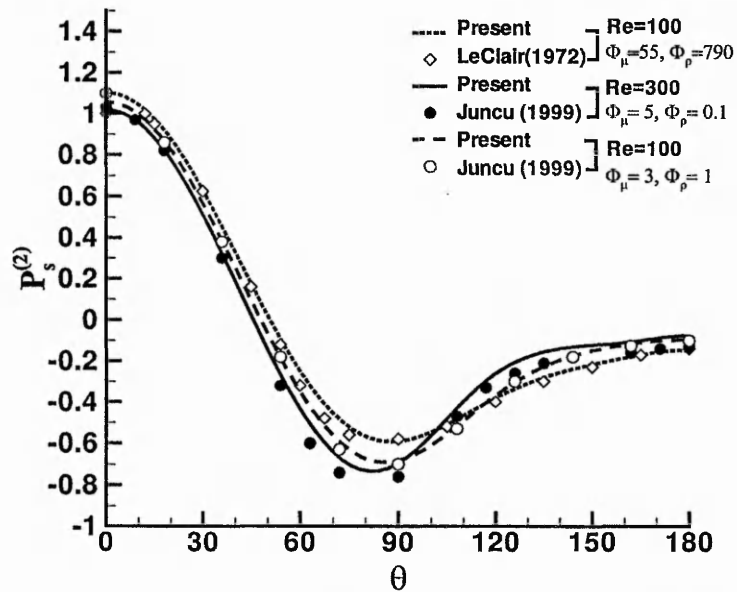
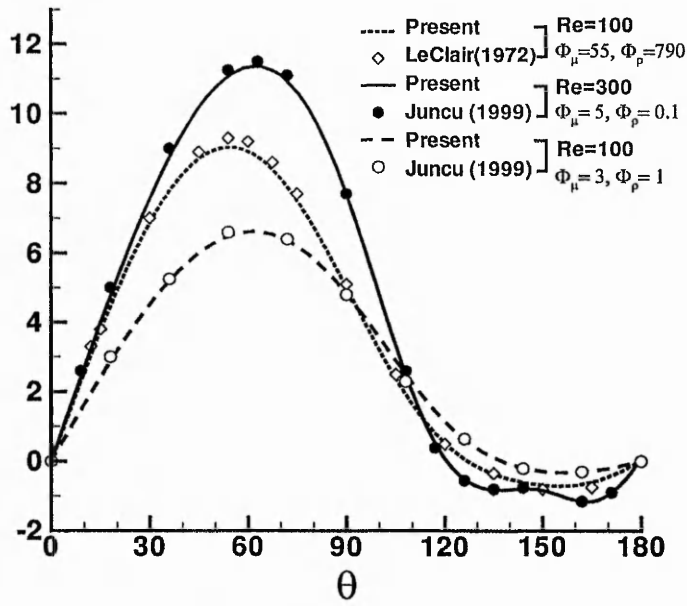
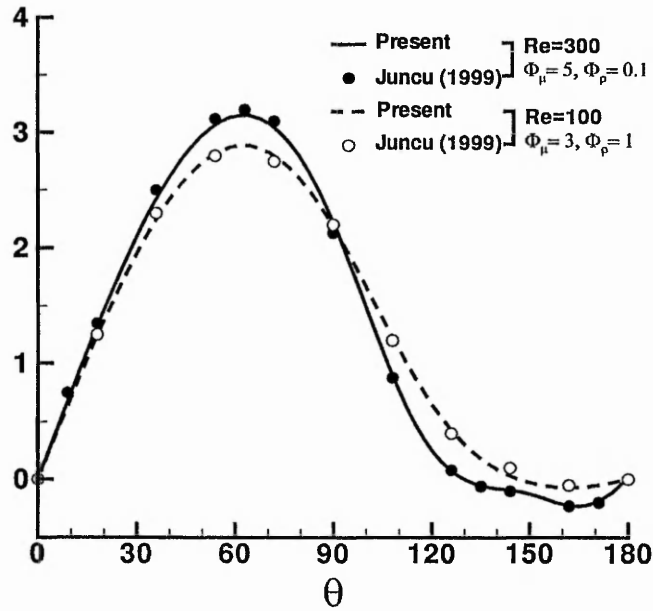


Figure 5.7b Pressure coefficient at interface of a spherical droplet

Figure 5.7c Exterior vorticity $\Omega^{(2)}$ at interface of a spherical dropletFigure 5.7d Interior vorticity $\Omega^{(1)}$ at interface of a spherical droplet

$$\Omega^{(i)} = \frac{1}{2} \nabla \times \vec{W}^{(i)}. \quad (5.31)$$

In general, good agreements between the present calculation and benchmark solutions have been obtained.

Wake structure and its variation with exterior Reynolds number

It is an interesting but very difficult topic to decide the wake type behind a drop as the ratio of viscosity Φ_μ , ratio of density Φ_ρ and the exterior $Re^{(2)}$ are all factors which influence wake type. In the present study, drops with fixed Φ_μ and Φ_ρ values in liquid spraying processes are considered. In an industrial spraying procedure, the density and

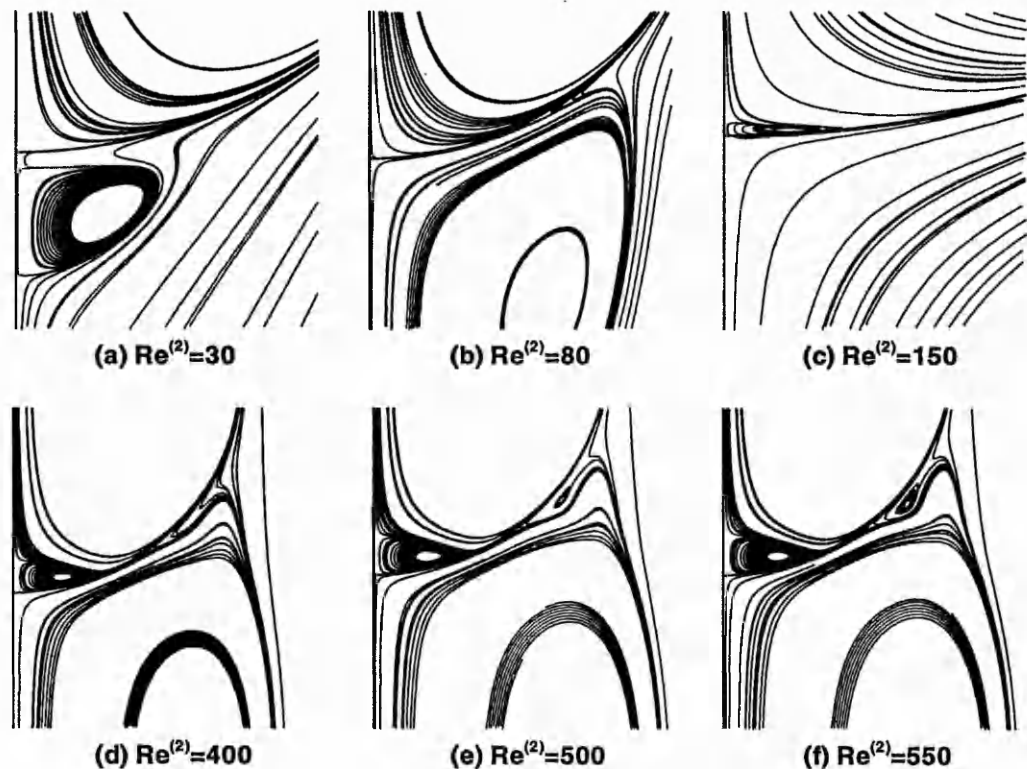


Figure 5.8 Wake flow structure and its change with $Re^{(2)}$

viscosity of the liquid (such as water) are often at a magnitude level larger than that of the surrounding fluid (generally air), so values of Φ_μ and Φ_ρ are selected as: $\Phi_\mu=55$ and $\Phi_\rho=790$, which are values of water to air, to represent a liquid spraying procedure. The exterior Reynolds number $Re^{(2)}=10, 20, 25, 30, 40, 50, 80, 100, 120, 150, 300, 400, 500$ and 550 are calculated to study the variation of wake structure. The mesh for simulation is the same as that of group 1. The results are shown in figures 5.8 and 5.9, respectively.

Figure 5.8 shows the zoomed wake zone at $Re^{(2)}=30, 80, 150, 400, 500$ and 550 respectively. Two changes of wake topology can be found when $Re^{(2)}$ increases from 10 to 550. The first change takes place at about $Re^{(2)}=27$ and the second takes place at about $Re^{(2)}=100$. In the calculation, no wake vortex was observed at $Re^{(2)}=25$, but a fluid vortex can be clearly identified at $Re^{(2)}=30$; as shown in figure 5.8, it appears at the rear stagnant point. As $Re^{(2)}$ increases, the vortex moves towards the drop and the distance between the vortex and the drop body becomes smaller and smaller. $Re^{(2)}=100$ is a critical value as the fluid vortex has already attached to the drop at the rear stagnant point. Our calculation for $Re^{(2)}=120$ reveals that the internal circulation of the drop has broken up, this means the second change of wake topology has taken place and the wake has become a solid vortex. At $Re^{(2)}=150$, the two-vortex structure of the internal circulation can be clearly identified; this is shown in figure 5.8. This topology of the wake (solid vortex type) is remained up to $Re^{(2)}=400$. As shown in figure 5.9, the wake length increases quickly with $Re^{(2)}$ after the wake vortex is formed while this length is almost the same in the range of $Re^{(2)} > 400$. A third change of wake structure is the appearance of another vortex at about $\theta=140^\circ$ outside the drop when $Re^{(2)} > 450$. This vortex can be identified at $Re^{(2)}=500$ in figure 5.8 and seen stronger at $Re^{(2)}=550$. However, this vortex should not be regarded as a change of topology as no additional nodal or saddle point is introduced.

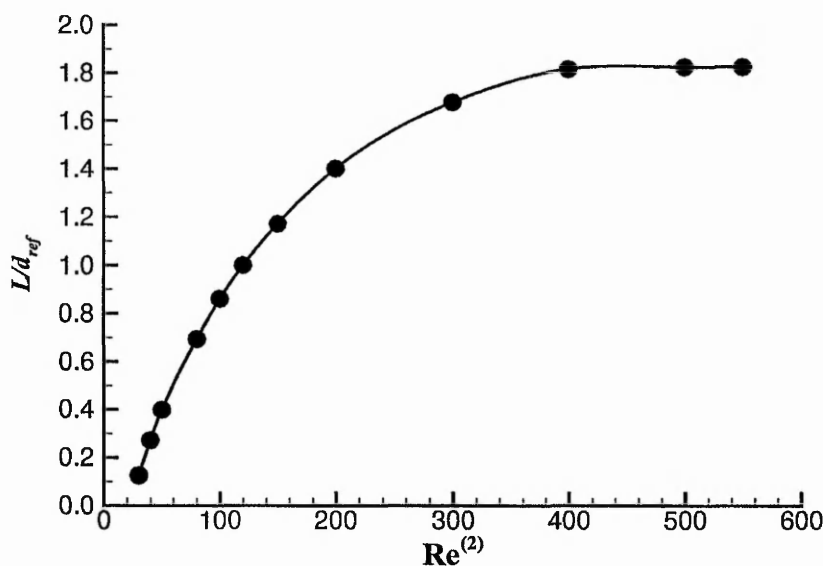


Figure 5.9 Wake zone length and its change with $Re^{(2)}$

5.4.2 Deformable Liquid Drops

The numerical procedure is further employed to calculate deformable drops. For convenience of discussion, the results for the deformation of droplets and bubbles are presented and discussed in terms of $Re^{(2)}$ and Weber number.

Dandy and Leal (1989) presented a numerical study of a buoyancy-driven deformable drop moving through a quiescent liquid. Here we use their results to validate the calculation of deformable interfaces. The ratios of fluid properties are $\Phi_\rho = 0.909$ and $\Phi_\mu = 4$, which are chosen as big values to expose interesting flow behaviour in the recirculating wake (Dandy and Leal, 1989). The settings of computational domain and mesh are the same as those for calculating spherical drops. The results of streamlines in the present calculation are compared with those of Dandy and Leal's (1989) in figure 5.10, where good agreement is demonstrated.

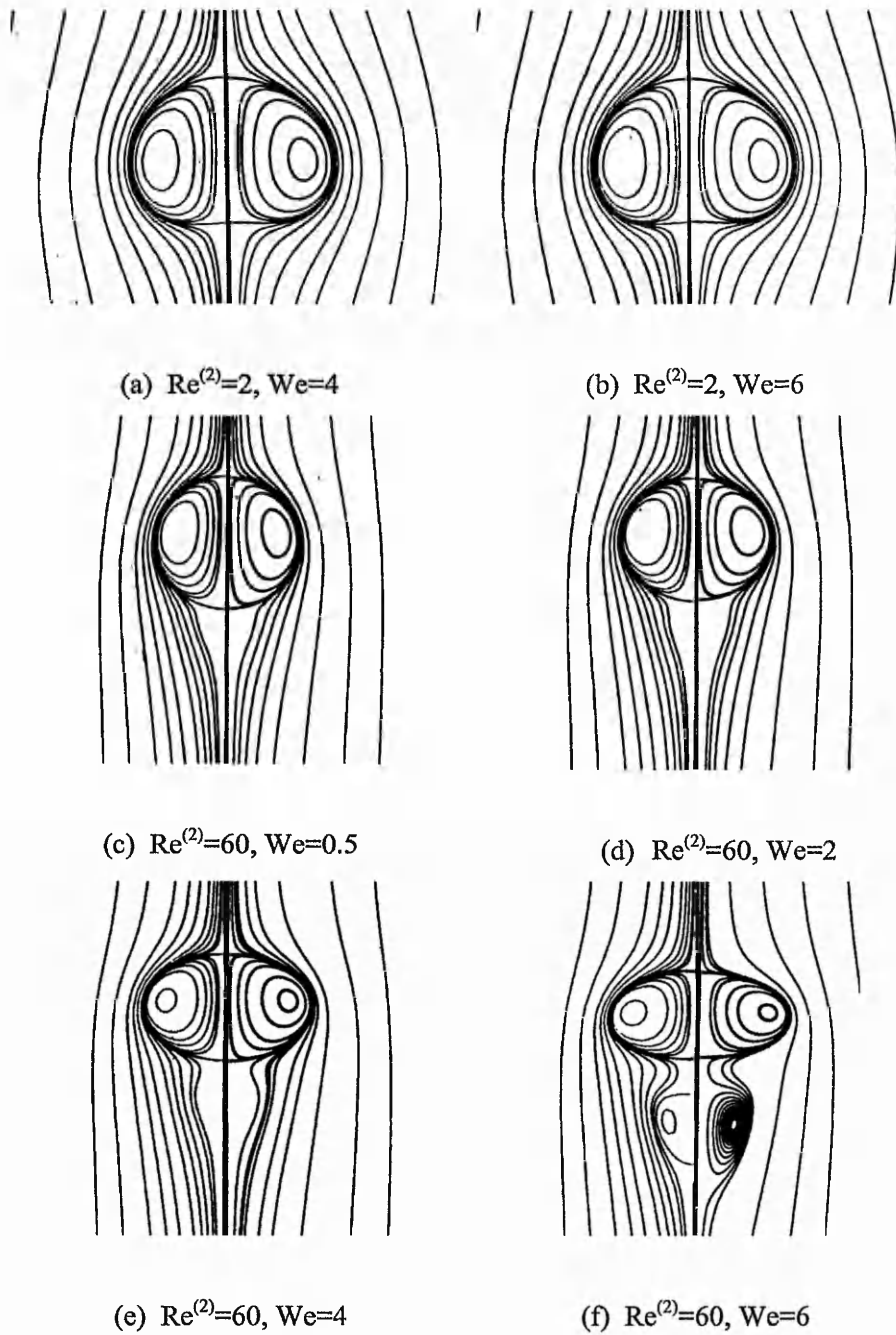


Figure 5.10 Shapes of deformable drops $\Phi_p = 0.909$, $\Phi_\mu = 0.909$,
 left hand side of axis: Dandy and Leal (1989), right hand side of axis: present calculation

5.4.3 Deformable Bubbles: Validation by Experimental Data

Raymond and Rosant (2000) carried out an extensive study of moderately deformed bubbles in the range of $(Re^{(2)}, We) = [1, 100] \times [0, 5]$. Corresponding to their experimental conditions (at room temperature, 20 °C, and in atmosphere), the ratios of fluid properties are set as $\Phi_\rho = 1:800$ and $\Phi_\mu = 1:100$.

Six cases with the Reynolds and Weber numbers given in table 5.2 are calculated. Figure 5.11 shows the convergent paths when $(Re^{(2)}, We) = (28, 3.7)$ and $(Re^{(2)}, We) = (9.3, 4)$, respectively, in terms of EVT and ERZ which are defined by equations (5.27) and (5.28). The error EVT is shown to reduce quickly for a given bubble shape. The profile error ERZ , however, reduces at a slower rate because of the extreme under-relaxation. Our calculations reveal that for the larger Reynolds and Weber numbers, a lower relaxation factor should be used and therefore a slower convergent rate is obtained.

Table 5.2 Comparison between computed and measured aspect ratios

$(Re^{(2)}, We)$	h/w	
	Raymond and Rosant (2000)	Present calculation
(0.5, 0.15)	0.98	0.975
(3.7, 1.00)	0.87	0.877
(28., 3.70)	0.64	0.640
(1.9, 1.30)	0.84	0.836
(9.3, 4.00)	0.57	0.601
(48, 7.7)	0.24	0.488

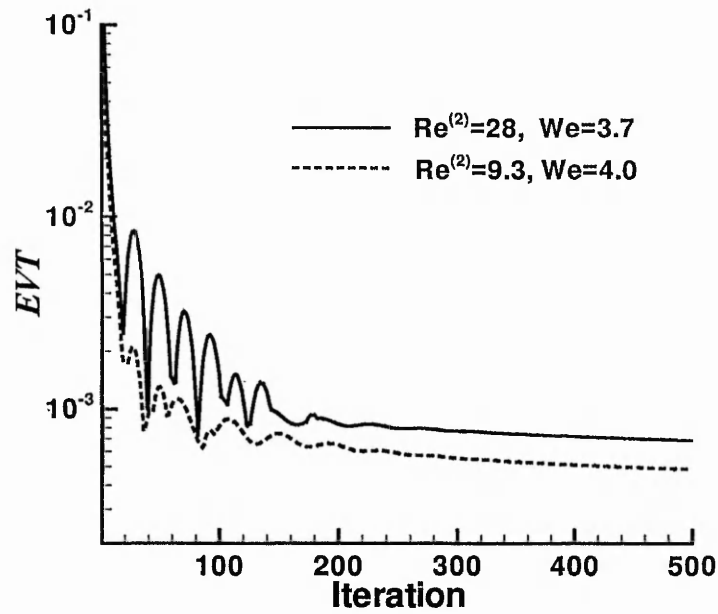
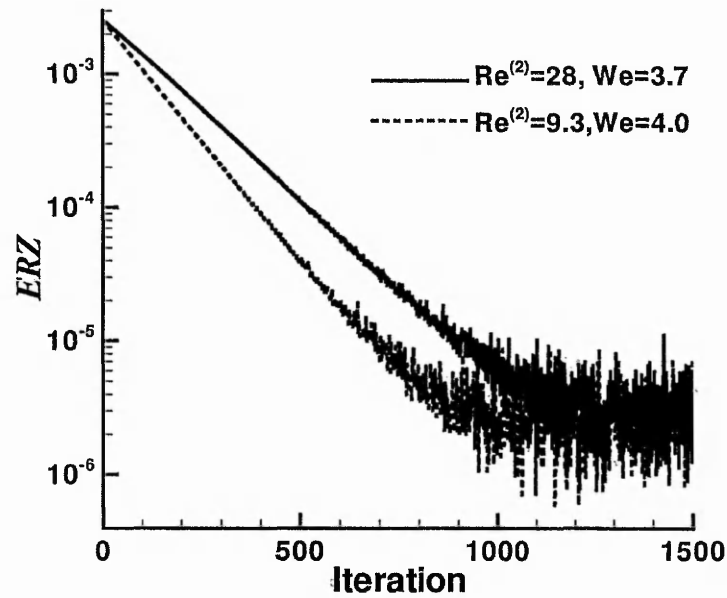
(a) Convergent path of *EVT*(b) Convergent path of *ERZ*

Figure 5.11 Convergent path of calculating deformable bubbles

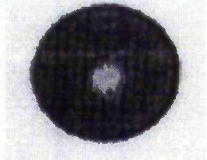
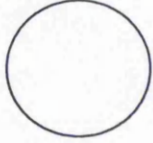

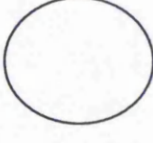


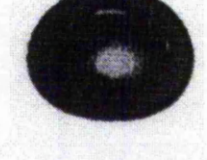
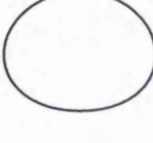




$(Re^{(2)}, We)$	Raymond and Rosant (2000)	Present Result
(0.5, 0.15)		
(3.7, 1.0)		
(28, 3.7)		
(1.9, 1.3)		
(9.3, 4.0)		
(48, 7.7)		

Figure 5.12 Comparison of bubble shapes

Figure 5.12 compares the calculated bubble shapes with the photographs given by Raymond and Rosant (2000) and shows good agreements between them. The aspect ratios of the bubbles h/w , where h and w are the height and width of the bubble respectively, are also calculated and compared with their measured values in table 5.2. The agreements between them are again very good for bubbles of moderate deformation; the last case, $(Re^{(2)}, We) = (48, 7.7)$, is more challenging because of the large bubble deformation ($h/w = 0.24$). This case is presented for the sake of completeness. It should be noticed that the experimentally observed bubble shape is not axisymmetric and that the assumptions used in the numerical model may therefore not be applicable here.

5.5 Summary of Chapter

A complete numerical study on gas-liquid interfacial flow problems of bubbles has been presented in this chapter. A “continuous stress method” and a “modified Ryskin-Leal method” are proposed and applied to a gas-liquid interface so as to determine the bubble shape and the interfacial velocity.

Numerical calculations of interfacial flows in single spherical and deformable drops and deformable bubbles. The robustness of the algorithm is shown in the calculations. These prove that the algorithm and codes are capable of calculating interfacial conjugate heat and fluid flows and can be used for further study on bubbles. The calculation also shows that for bubbles with the Weber number valued greater than 7.7, which was experimentally observed to be asymmetric, the calculation is physically meaningless.

Chapter 6

Steady Heat and Fluid Flows Inside and Around Inert Bubbles

6.1 Introduction

In chapter 3, the inert bubble problem is physically modelled as unsteady conjugate heat and fluid flows. When the bubble is introduced into the unbounded hot liquid, it rises up quickly and reaches a steady terminal state. For a slowly dissolving inert bubble, the rates of heat and mass transfer also reach their peak values at the terminal state and therefore, the flow phenomena at the interface are the clearest. However, even at this stage, many flow phenomena of the bubbles are still unknown. For example, the structure of flow fields and the interfacial characteristics are unclear for a spherical bubble in the range of $Re^{(2)} > 200$. Clift, Grace and Weber (1978) stated that “for drops and bubbles rising or falling freely in systems of practical importance, significant deformations from spherical occur for all $Re^{(2)} > 600$ ” and “the shape of the drop or bubble remains spherical if the Weber number is small enough”. Recently, Juncu (1999) studied the structure of flow fields and interfacial characteristics of a drop for $Re^{(2)} < 500$. However, for a spherical bubble, the exterior Reynolds number $Re^{(2)} = 200$ appears to be the upper limit for which complete steady-state flow fields have been reliably determined so far.

In the meanwhile, our review in chapter 2 shows that a conjugate flow model has never been applied to study the interfacial flows of bubbles, although this model has found its application in calculating single drops. Indeed, the momentum, heat and mass transfer is a conjugate procedure between a gas bubble and a surrounding liquid; In order to study these mechanisms, both sides of the interface must be treated as real fluids although $\Phi_\rho \ll 1$ and $\Phi_\mu \ll 1$.

This chapter studies the steady conjugate heat and fluid flows in single inert bubbles. The calculations are carried out for both spherical and moderately deformed bubbles. For spherical bubbles, the flow structure and interfacial characteristics at $10 \leq Re^{(2)} \leq 550$ is studied. Simulation on deformable bubbles is the main work of this chapter. Studies on the shape, flow structure and drag coefficient are carried out for moderately deformed bubbles; a comparison between the present conjugate model and Ryskin and Leal's (1984a, 1984b) "external flow model" is made. Detailed heat and mass transfer characteristics at the gas-liquid interface are studied.

6.2 Spherical Bubbles

In order to study the general bubble dynamics of single bubbles, an air bubble rising in an unbounded quiescent water is considered. The parameters are $\Phi_\rho=1:790$ and $\Phi_\mu=1:55$. Exterior Reynolds number $Re^{(2)}$ varies from 50, 100, 200, 300, 400, 500 and 550. The numerical grids are the same as that of calculating the drops, ie, block 1= 82×42 and block 2= 90×82 ; The outer boundary is assigned at 50 times of the equivalent bubble radius. The results presented and analysed are the flow structure (topology of streamlines) inside and around a spherical bubble and the interfacial characteristics.

6.2.1 Flow Structure of a Single Spherical Bubble

Figure 6.1 shows the streamlines inside and around the single air bubbles. Unlike a falling drop, the flows around the air bubbles are not separating from the spheres and no circulation "break-up" is observed throughout the Reynolds number range from 50 to 550. Moreover, no wake zone behind the bubble is observed.

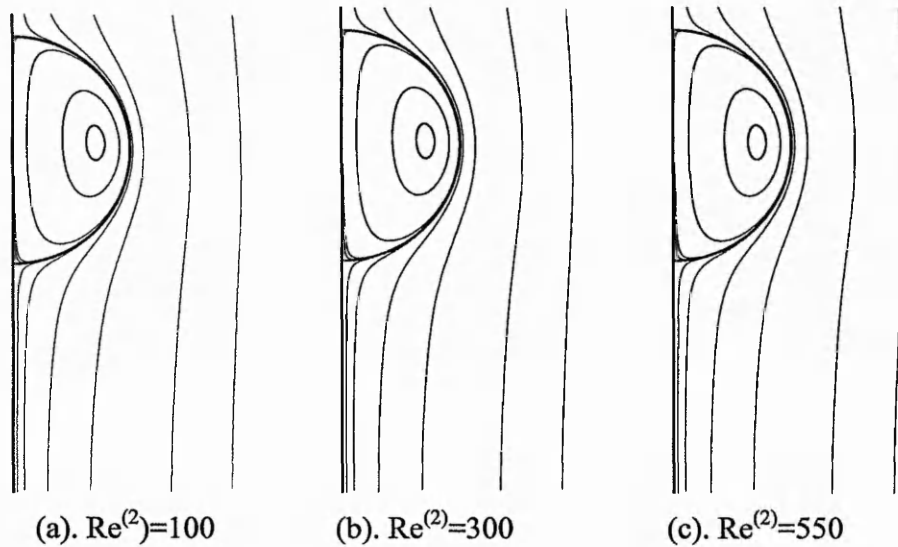


Figure 6.1 Flow structure inside and around a spherical air bubble

6.2.2 Interfacial Characteristics

Figure 6.2 shows the results of interfacial parameters such as tangential velocity W_t , pressure $P_s^{(2)}$, exterior vorticity $\Omega^{(2)}$ and interior vorticity $\Omega^{(1)}$, which are defined by equations (5.29) to (5.31). It is found that the tangential gradients of all these parameters increase with exterior Reynolds number. The vortices, $\Omega^{(1)}$ and $\Omega^{(2)}$, have the same strength level although differences of density and viscosity are very large between the two sides of the interface. Based on these results of rotational flows, it is seen that the one-side calculating method for a bubble (liquid side) and the corresponding treatments of “free surface” or “inviscid bubble” are not proper and therefore a conjugate study is necessary.

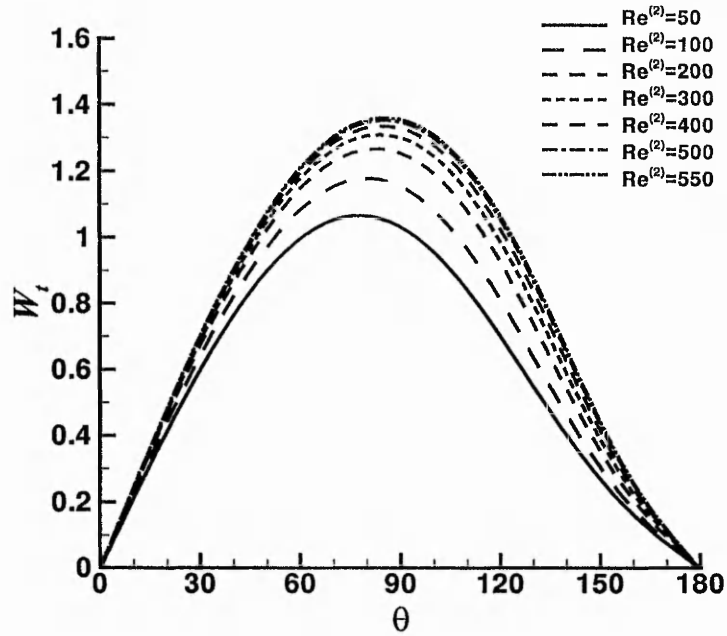


Figure 6.2a Interfacial tangential velocity of a spherical bubble

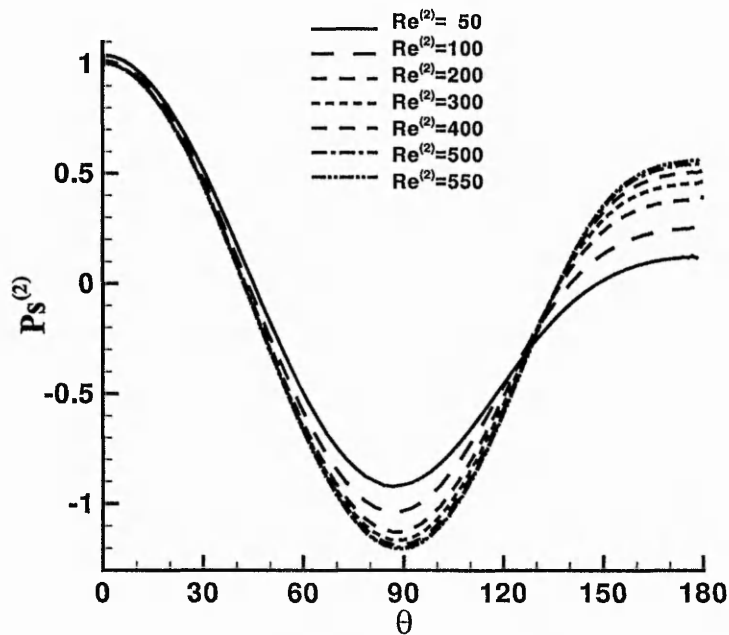
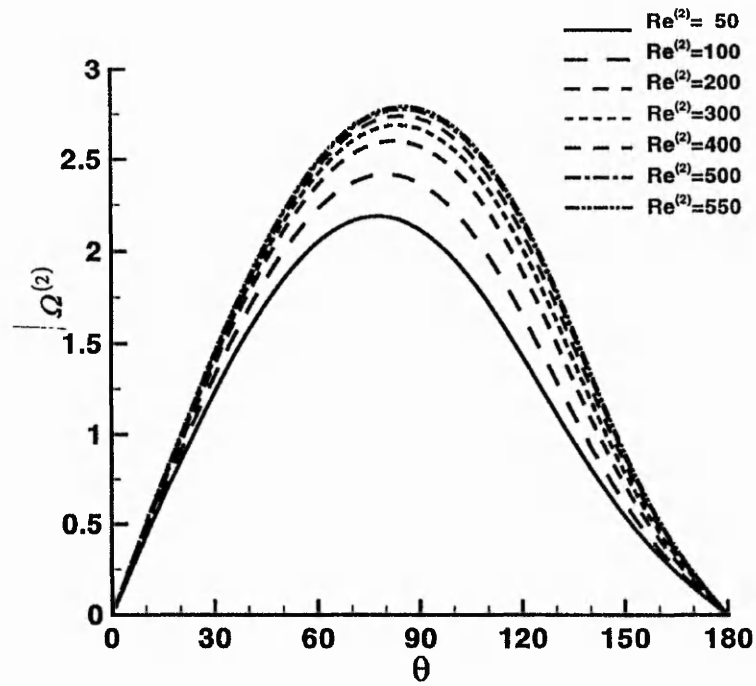
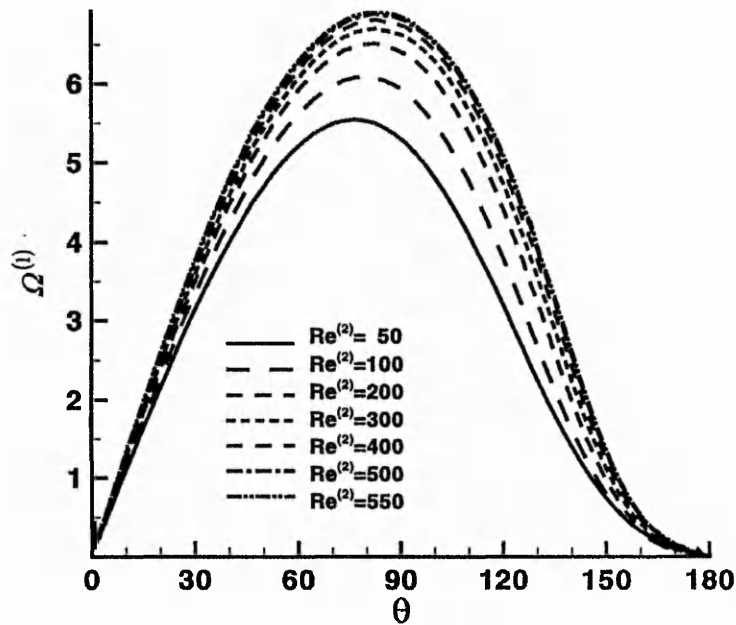


Figure 6.2b Interfacial pressure of a spherical bubble

Figure 6.2c Exterior Vorticity $\Omega^{(2)}$ of a spherical bubbleFigure 6.2d Exterior Vorticity $\Omega^{(1)}$ of a spherical bubble

6.3 Moderately Deformed Bubbles

The deformation of a single bubble is a very complex problem. The shape of a bubble rising at its terminal state could be spherical, ellipsoidal, spherical-capped or dimpled; this is decided by the properties of the fluids and the rising velocity. For a rising bubble that can physically arrive at a terminal steady state in experimental studies, the exterior Reynolds number is up to $Re^{(2)} = O(100 \sim 200)$ or even higher, depending on the Weber number. Based on the validations in chapter 5, we restrict our current calculations to bubbles of $(Re^{(2)}, We) = [0, 200] \times [0, 6]$ so that the results are with physical meaning.

6.3.1 Bubble Shape

Figure 6.3 presents the computed bubble shapes for all cases considered. For $Re^{(2)} \leq 20$, the progression of bubble shape with increase of We is in accord with qualitative “expectations” based on the most commonly reported experimental observations, namely, spherical to oblate-ellipsoid, and to more complicated “oblate” shapes with flattening at the rear. On the other hand, when $Re^{(2)} \geq 50$, the front stagnation pressure becomes dominant and the bubble initially flattens more at the front than at the back. The case of $Re^{(2)} = 50$ lies approximately on the border between the two types of deformation: one characteristic of lower $Re^{(2)}$, with stronger deformation at the rear, and the other characteristic of higher $Re^{(2)}$, with stronger deformation in the front. Consequently, at $Re^{(2)} = 50$ the bubbles almost preserve fore-aft symmetric. The change of bubble shape is described in figure 6.4 in terms of aspect ratio, h/w . The progression is also in accord with the experimental observation of Raymond and Rosant (2000), where h/w decreases with We for a certain $Re^{(2)}$ while it also tends to decrease with the increase of $Re^{(2)}$ for a given We value except at $We = 1$.

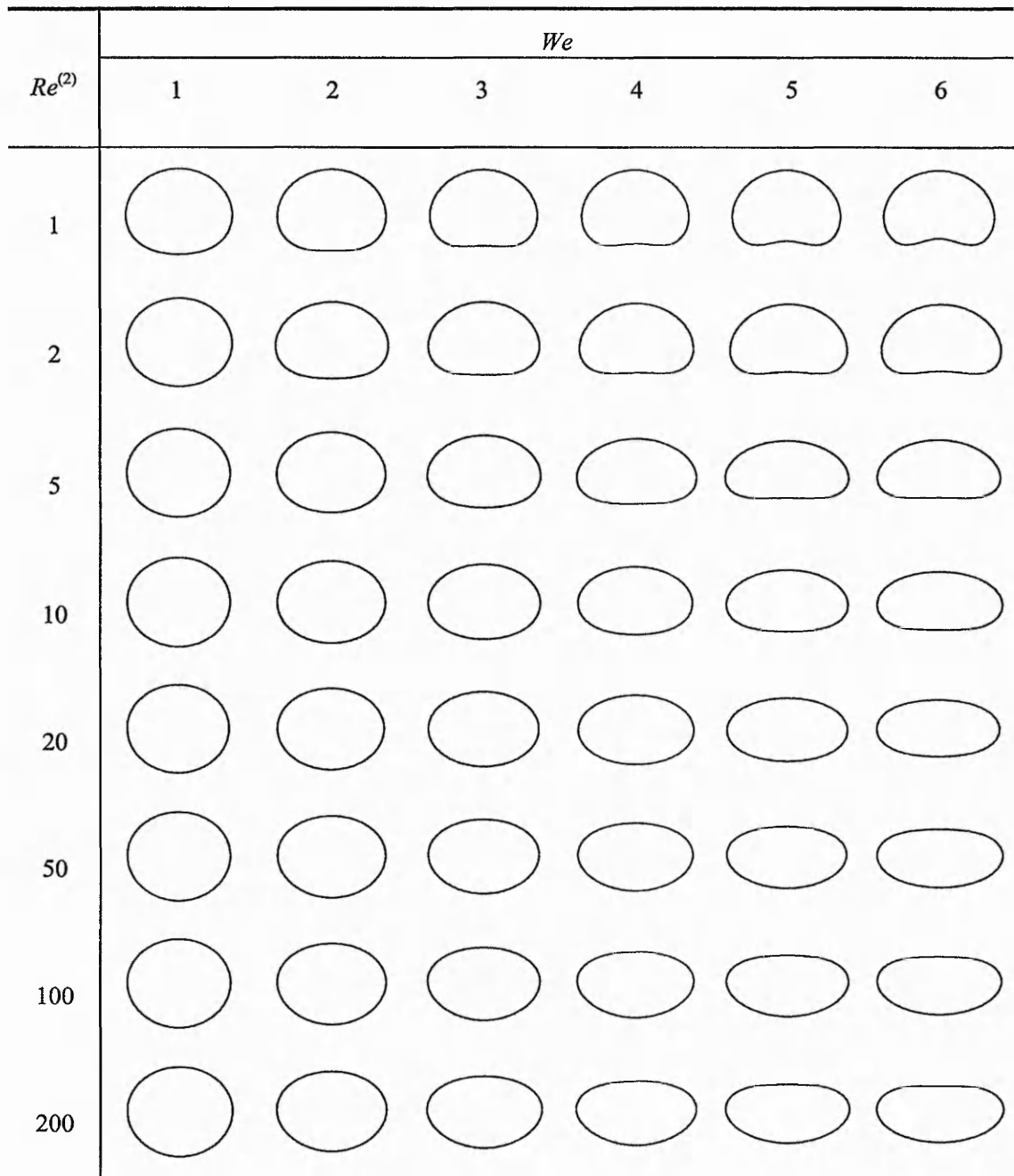


Figure 6.3 Shapes of moderately deformed bubbles

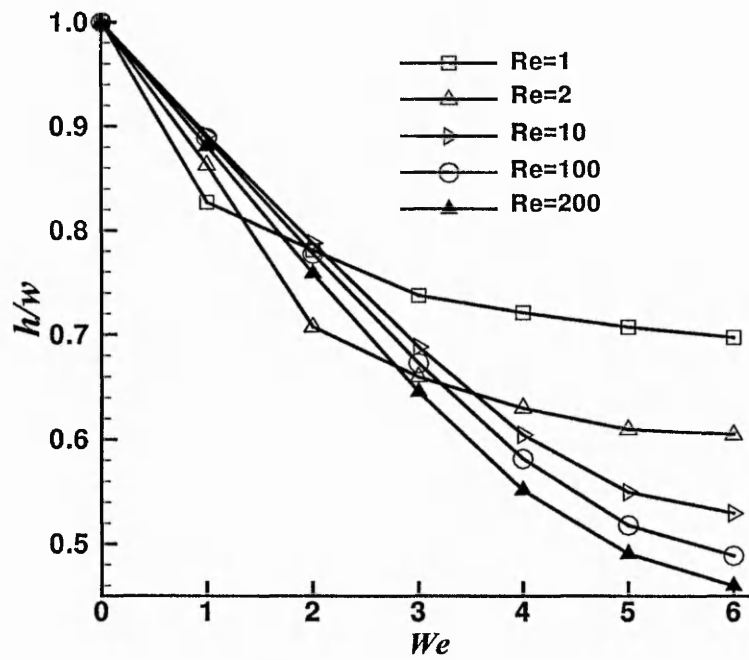


Figure 6.4 Influence of the Weber number on aspect ratio

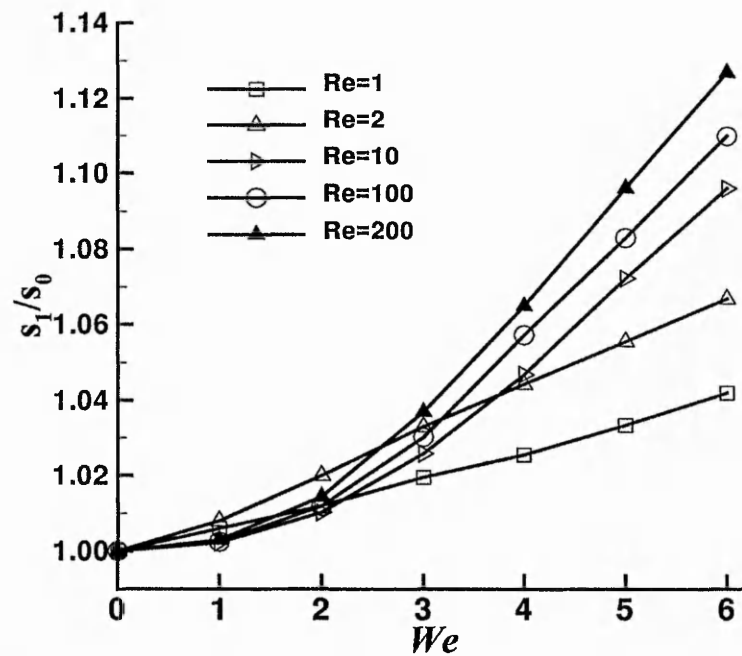


Figure 6.5 Influence of the Weber number on exchange surface coefficient

Figure 6.5 shows the influence of Weber number on the exchange surface coefficient s_1/s_0 , where s_1 and s_0 are surface of a deformed bubble at the actual Weber number and the same bubble at $We=0$. Due to the moderate value of the maximum Weber number considered ($We=6$), the variations of the coefficient are quite small. The maximum deviation from the bubble surface at $We=0$ is smaller than 4% at $Re^{(2)}=1$ (10% for $Re^{(2)}=10$ and 11% for $Re^{(2)}=100$, respectively). However, this increase of the surface area can have a significant impact on the efficiency of systems involving a large number of bubbles.

6.3.2 Flow Structure

As shown in previous sections, flow separation can take place for both spherical and deformed drops but doesn't occur for spherical bubbles. This phenomenon has also been noticed by Magnaudet, Rivero and Fabre (1995). An immediate question is whether flow separation can take place at the surface of a deformed bubble. The answer to this problem is definitely positive as such phenomena have been demonstrated by numerical simulations using "external flow models", such as by Ryskin and Leal (1984b) and Li and Yan (2002a, 2002b). However, it is an argument that an "external flow model" which treats the bubble surface as a "free surface" has only one mechanism for producing vorticity: the curvature; while a conjugate flow model has two mechanisms: both the curvature and the no-slip condition (Dandy and Leal, 1989). The generated vorticity can be brought to the rear of the bubble by convection and accumulates there and, as a result, flow separation takes place. Therefore it is necessary to find the differences between flow fields around a deformed bubble calculated by the current conjugate model and those calculated by "external flow models". In addition, as observed by Rivkind and Ryskin (1976), LeClair, Hamielec, Prupacher and Hall (1972) and Juncu (1999) and also revealed in our previous preliminary tests, both a "fluid vortex" and a "solid vortex" may occur as a wake vortex behind a drop calculated by a

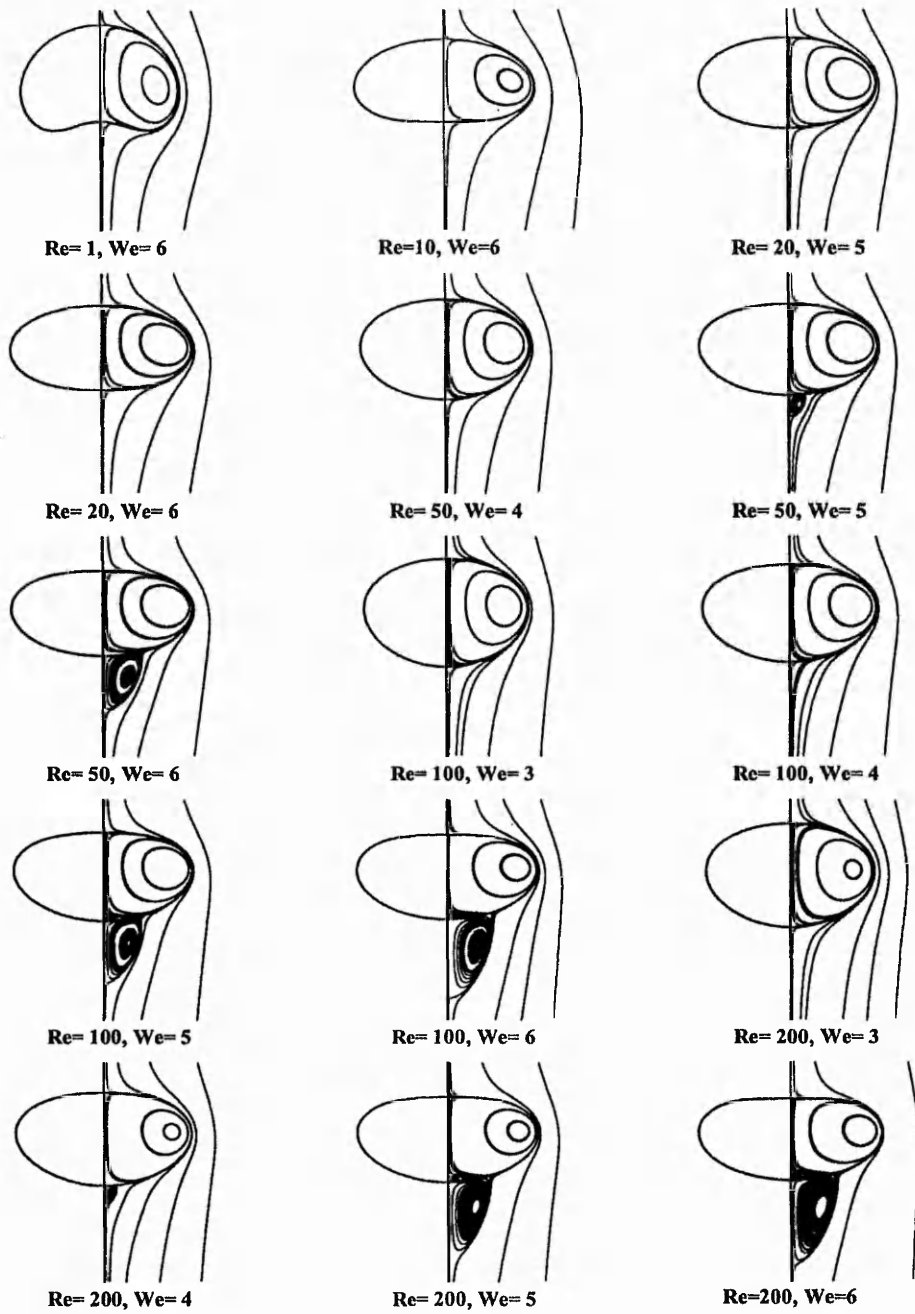


Figure 6.6 Flow structures of moderately deformed bubbles

conjugate model, it is also necessary to find whether these flow structures can possibly happen behind a bubble.

Figure 6.6 shows the flow separation for deformed bubbles. In the ranges of Reynolds and Weber numbers considered in this paper, a standing-vortex structure is observed to begin at $4 < We < 5$ for $Re^{(2)} = 50$, at $4 < We < 5$ for $Re^{(2)} = 100$, and at $3 < We < 4$ for $Re^{(2)} = 200$. These rough ranges are in agreement with those of Ryskin and Leal's (1984a, 1984b) "external flow model". Moreover, according to the suggestions by Hartunian and Sears (1957), two distinct criteria for the change of bubble rising path from rectilinear to zigzag or helical are:

- (a). a critical Reynolds number $Re^{(2)} \approx 200$ for impure liquids;
- (b). a critical Weber number $We \approx 3.2$ for pure liquids.

Our numerical solutions show that for $Re^{(2)} = 200$, the Weber number required for the separation is a value of $O(3-4)$. This agrees quite well with Hartunian and Sears's (1957) experimental value of $We \approx 3.2$ providing the separation will result in a zigzag rising path.

The topology of flow structure with the appearance of flow separation is illustrated in figure 6.7 where the internal flow "breaks up" and a pair of counter-rotating ring-vortices, one smaller-sized separation vortex and the other larger-sized main vortex, can be observed. Because of this counter-rotating vortex pair, a saddle point exists on the axis. Outside the bubble, only a separation ring vortex is observed and therefore a saddle point also exists on the axis where the end of the wake is. This wake flow structure is a typical "solid vortex" that we have mentioned before. In the present paper, we have only observed the occurrence of solid vortices attached to deformed bubbles; no fluid vortex behind a bubble has been observed though there is no obvious reason for its disappearance.

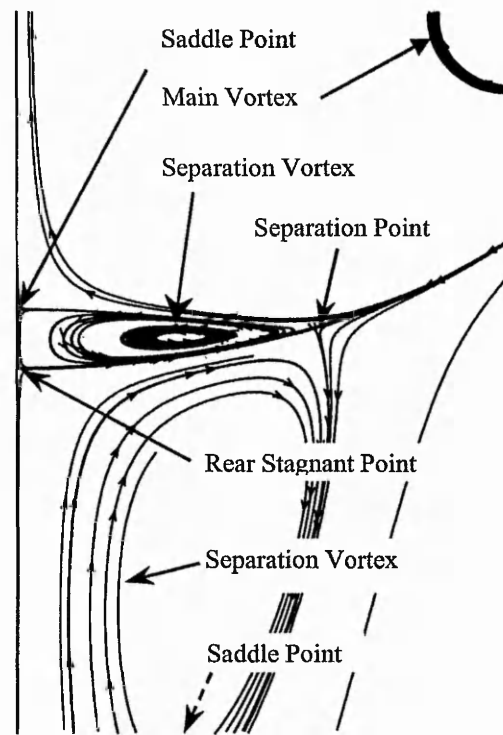


Figure 6.7 Topology of vortex structure

A comparison of the flow structures calculated by the present conjugate model with those calculated by Ryskin and Leal's (1984a, 1984b) "external flow model" is carried out and presented in figure 6.8. Ignoring the vortices inside the bubbles, which are impossible to be obtained with an "external flow model", a perceivable difference between the results is that the separation vortices predicted by the conjugate model are smaller than those by the external flow model of Ryskin and Leal (1984a, 1984b). As separation is a phenomenon occurring in viscous flows, it could be concluded from this difference that an "external flow model" may have over predicted the viscous effect when separation occurs behind a bubble.

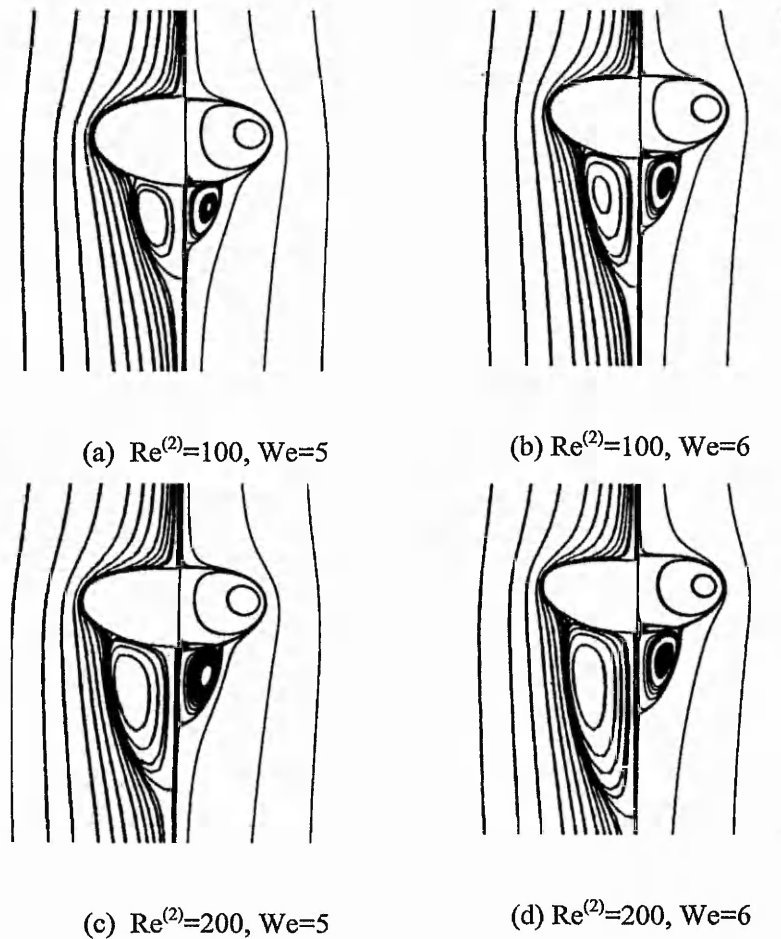


Figure 6.8 Comparison of flow structures with results of Ryskin and Leal (1984b).

Left of axis: Ryskin and Leal; right of axis: present calculation

6.3.3 Drag Coefficient

The definition of drag force coefficient given in the nomenclature is the same as that of Ryskin and Leal (1984a, 1984b) to allow a direct comparison of our results with their data. However, when we integrate the local forces computed by our conjugate flow model, the tangential stress has also to be counted, as described by equation (5.33). Therefore, the extended form of C_D is:

$$C_D = \frac{8F_D}{\rho^{(2)}V_{ref}^2 \pi d_{ref}^2} = 16 \int_0^{\xi_{max}} (-\tau_n^{(2)} x_\xi - \tau_t^{(2)} y_\xi) r \cdot d\xi. \quad (6.1)$$

The results of C_D are presented in figure 6.9, where Ryskin and Leal's (1984a) data are also plotted for comparison. In the range of $(Re^{(2)}, We) = [5, 50] \times [0, 6]$, our results are basically in agreement with those of Ryskin and Leal (1984a). Even in the case of $Re^{(2)} = 100$, the agreement is acceptable until $We \leq 4$; after which flow separation is observed to occur. Our calculated C_D values for $(Re^{(2)}, We) = 100 \times [4, 6]$ and for $(Re^{(2)}, We) = 200 \times [3, 6]$ are considerably lower than the corresponding results of Ryskin and Leal (1984a). This deviation agrees with our previous observation that the external flow model over predicts the viscous effect in cases where separation occurs. In the range of $(Re^{(2)}, We) = [0, 5] \times [0, 6]$, however, the viscous forces are important compared with the inertia. An "external flow model" treats the bubble surface as "tangential stress free" and therefore could under predict the viscous effect. Based on this understanding, it is no surprise that our C_D values in this range are higher than those given by Ryskin and Leal (1984a).

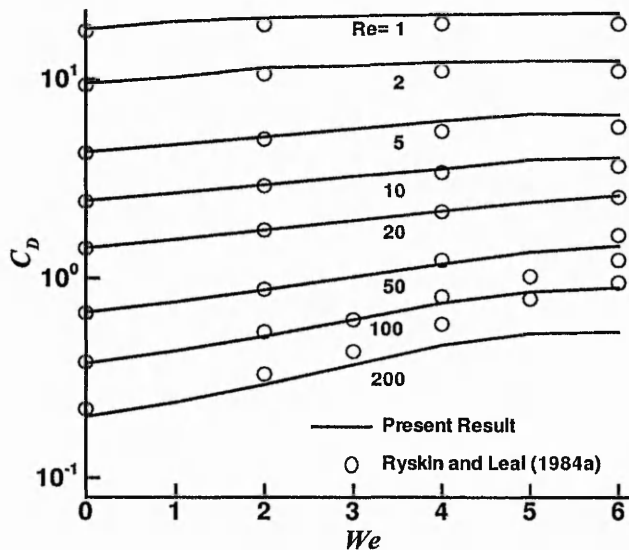
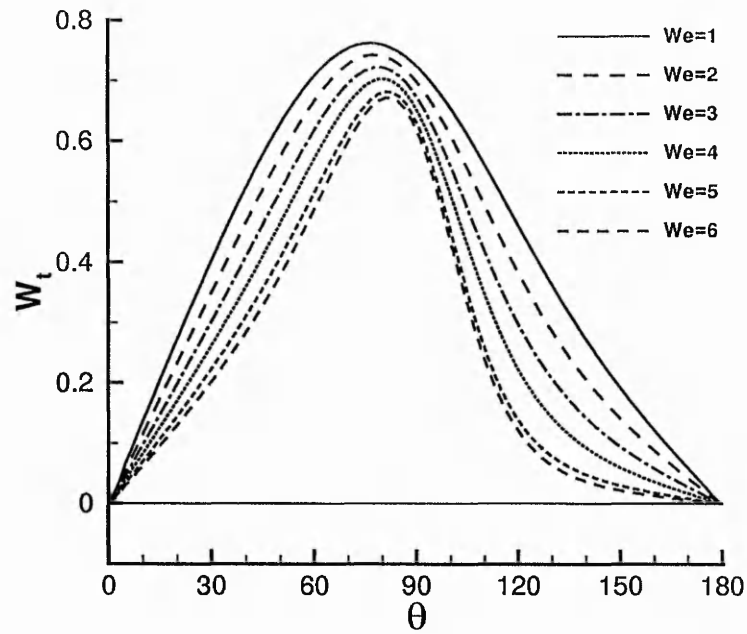
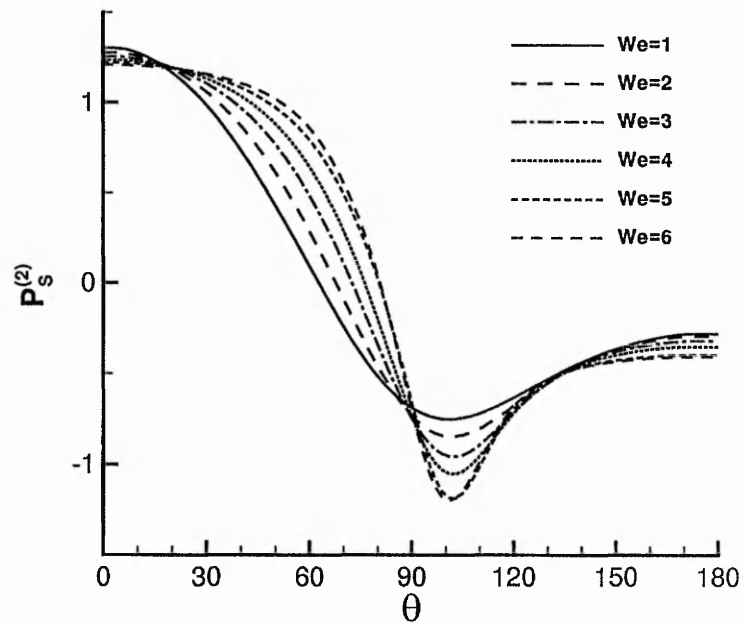


Figure 6.9 Drag force coefficients of moderately deformed bubbles

Figure 6.10a Tangential velocity for “rear-flattening” bubbles ($Re^{(2)}=10$)Figure 6.10b Interfacial pressure for “rear-flattening” bubbles ($Re^{(2)}=10$)

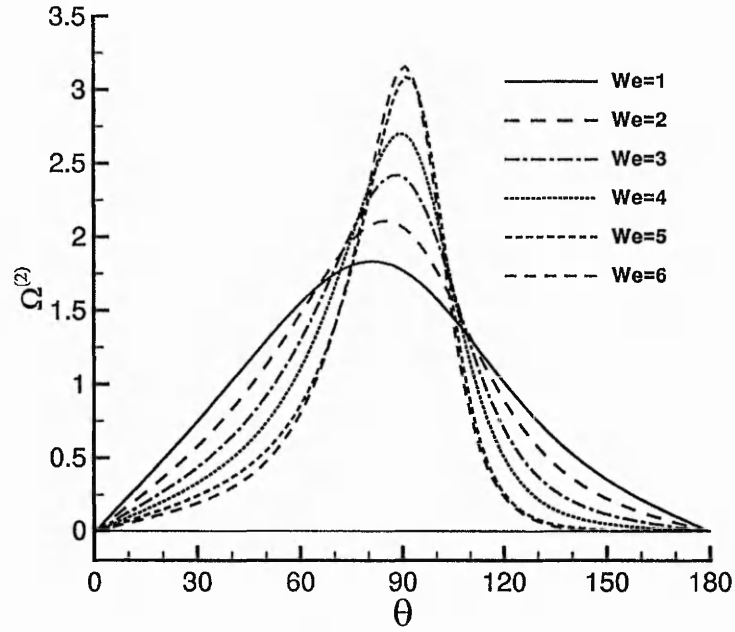


Figure 6.10c Exterior vorticity $\Omega^{(2)}$ for "rear-flattening" bubbles ($Re^{(2)}=10$)

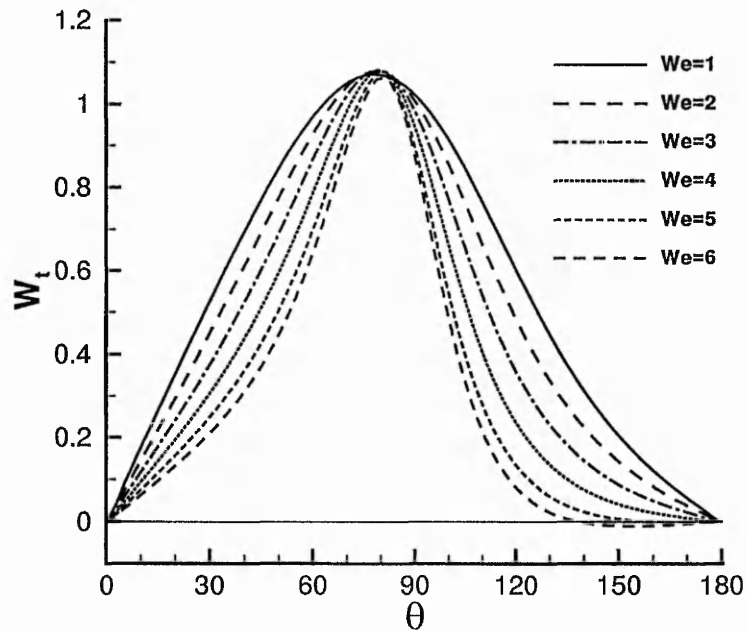


Figure 6.11a Tangential velocity for "fore-aft symmetric" bubbles ($Re^{(2)}=50$)

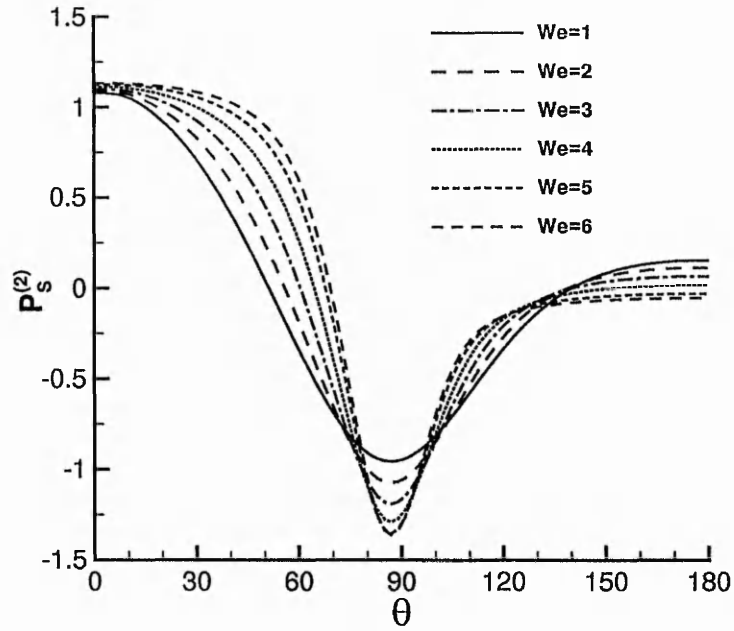


Figure 6.11b Interfacial pressure for “fore-aft symmetric” bubbles ($Re^{(2)}=50$)

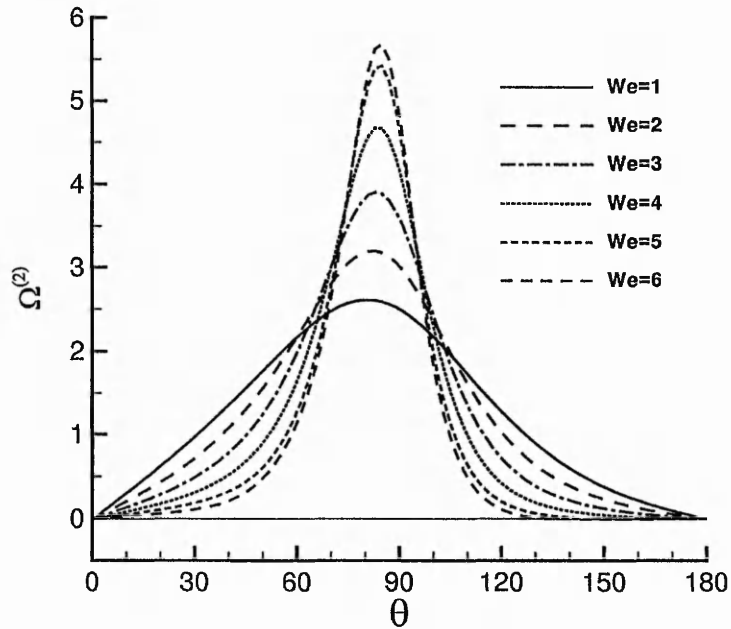


Figure 6.11c Exterior vorticity for “fore-aft symmetric” bubbles ($Re^{(2)}=50$)

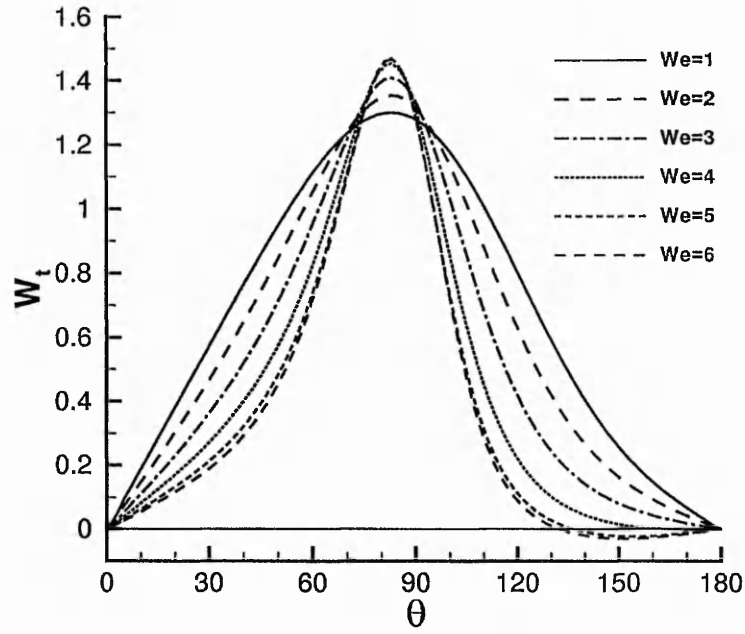


Figure 6.12a Tangential velocity for “front-flattening” bubbles ($Re^{(2)}=200$)

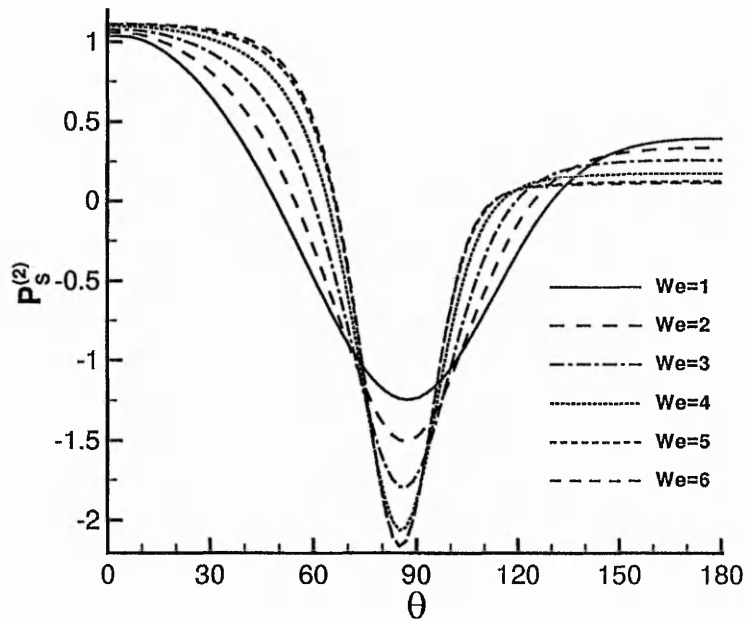


Figure 6.12b Interfacial pressure for “front-flattening” bubbles ($Re^{(2)}=200$)

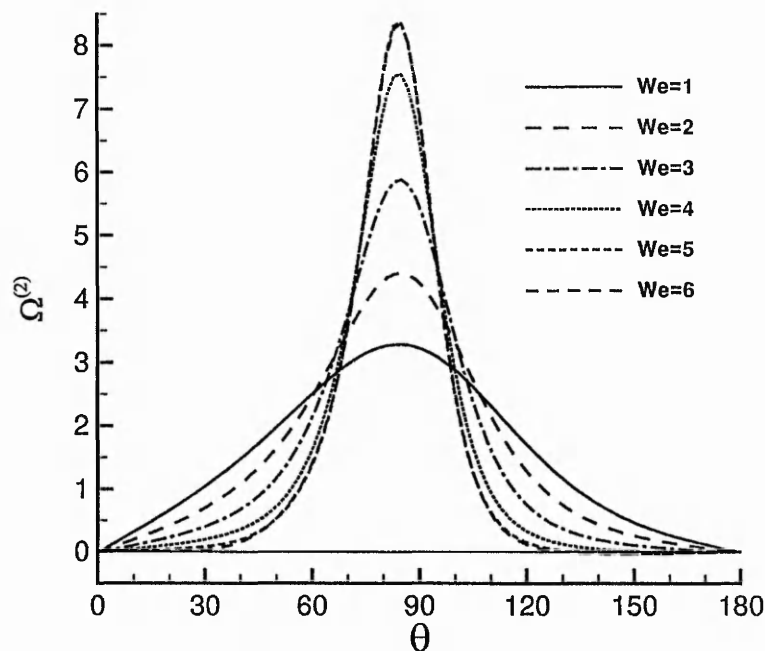


Figure 6.12c Exterior vorticity for “front-flattening” bubbles ($Re^{(2)}=200$)

6.3.4 Interfacial Characteristics

Based on the bubble deformations given in figure 6.3, three types of bubbles at $Re^{(2)}=10$, 50 and 200 are selected as representatives of “rear flattening”, “fore-aft symmetric” and “front flattening” bubbles respectively. The interfacial characteristics, tangential velocity W_t , interfacial pressure $P_s^{(2)}$ and exterior interface vorticity $\Omega^{(2)}$ for three types of bubbles are presented in figures 6.10, 6.11 and 6.12. Because the bubbles are only moderately deformed, the interfacial parameters of the bubbles are only different in magnitude; the tendencies of the distributions along the bubble profiles are similar to each other. For example, $P_s^{(2)}$ has two peak values, appearing at the front and rear stagnant points respectively; and a trough located in between of the two peaks, and

it is almost at the same θ angle where peak values for $\Omega^{(2)}$ and W_t . This tendency shows that the shear strength reaches its peak value at this point. The θ angle here is denoted as θ_A .

6.3.5 Heat and Mass Transfer

Based on the slow dissolution and unidirectional diffusion assumptions presented in chapter 3, the heat and mass transfer in the continuous phase are considered. For an inert bubble dissolving slowly when it is rising in an unbounded liquid, without losing generality, we use the fluid properties of hot water, namely, $Pr^{(2)} = 2$ and $Sc^{(2)} = 500$.

The contours of dimensionless temperature and concentration are shown in figures 6.13 and 6.14. It can be seen that the thermal field has stronger diffusion while the concentration is more dominantly controlled by convection. As a result, the wake zone of concentration field is long and its diameter is small while this of the temperature field is short but big.

The local Nusselt and Sherwood numbers Nu and Sh respectively, are shown in figures 6.15, 6.16 and 6.17 for three types of deformed bubbles. The distributions of Nu and Sh along the bubble profile have a good similarity, which indicates that although the equivalence for Nu and Sh is not available, the heat and mass transfer still have a formal analogy. In the meanwhile, the curves for the three types of bubbles are similar in shape but are different in magnitude. For a given Reynolds number, at $Re^{(2)} = 10$ for example, the curve of $Nu \sim \theta$ is monotonic with the maximum and minimum values occurred at the front and stagnant points respectively for the case of $We = 1$. In this case, the thermal or concentration boundary layer has its minimum and maximum thickness at the front and rear stagnant points, respectively. With the increase of Weber number, the $Nu \sim \theta$ curve becomes non-monotonic. A peak value of Nu , which corresponds to the minimum thickness of

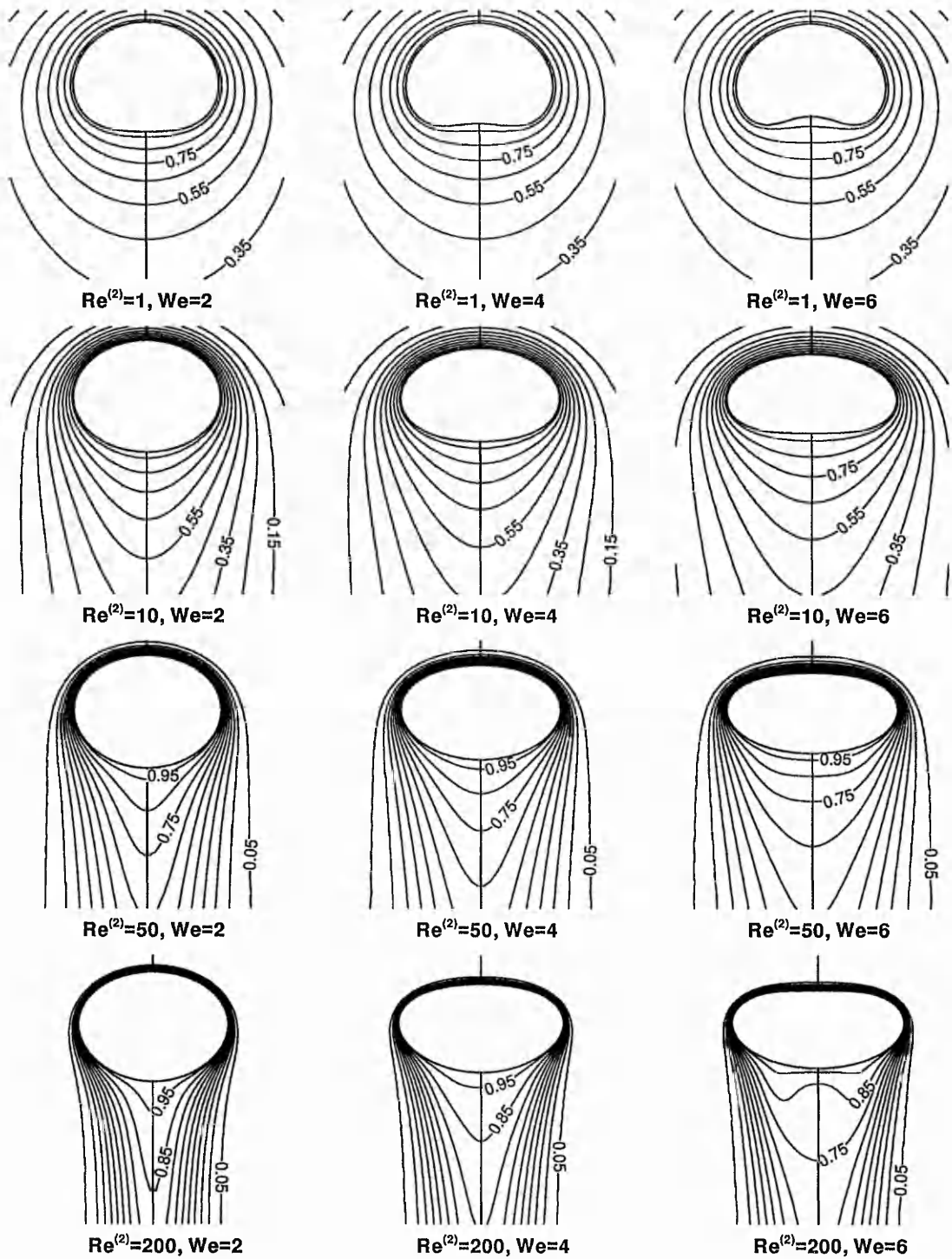


Figure 6.13 Contour of temperature field

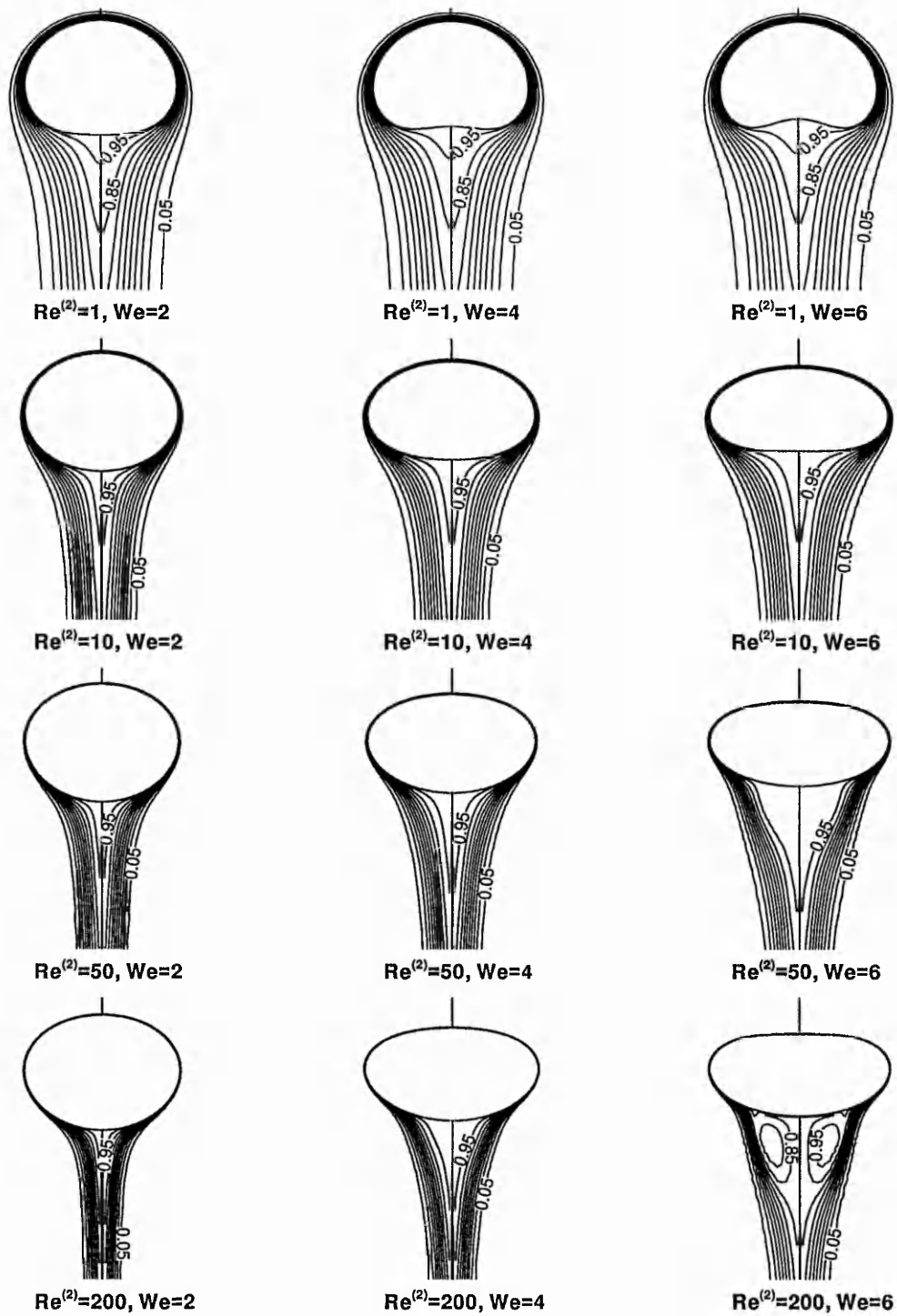


Figure 6.14 Contour of concentration field

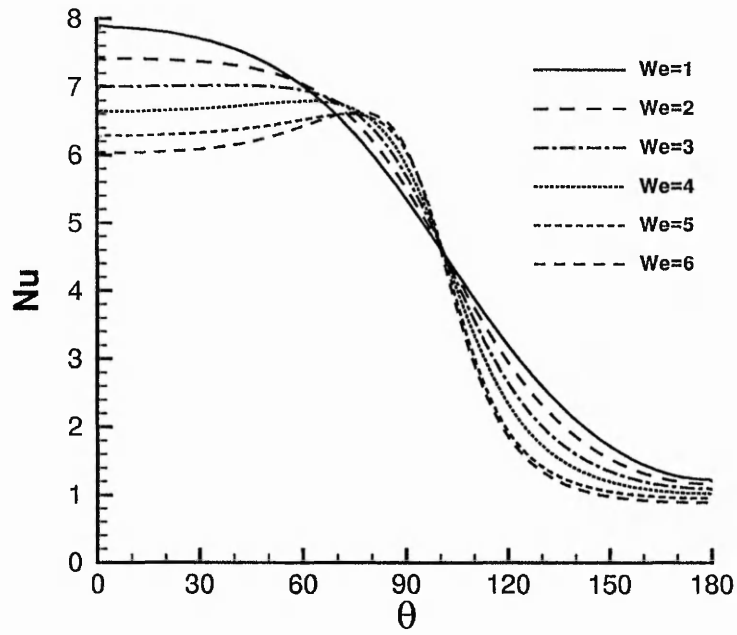


Figure 6.15a Distribution of local Nusselt number for bubbles at $Re^{(2)}=10$

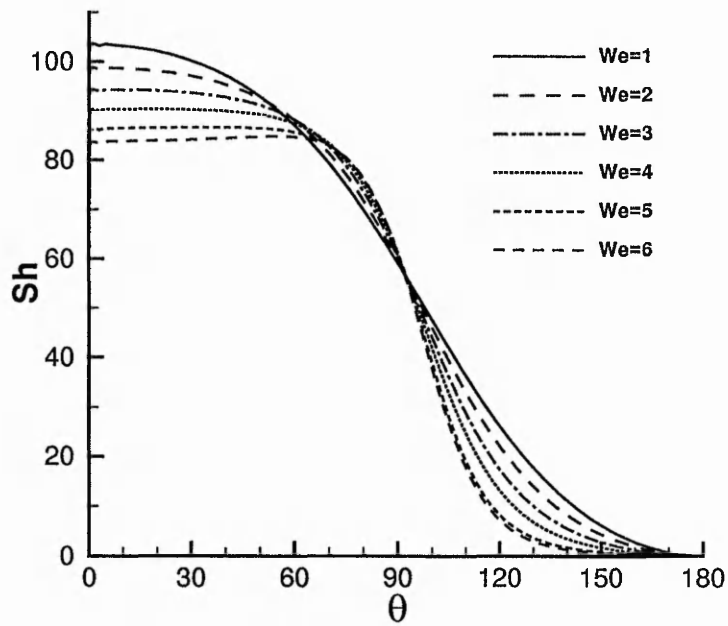


Figure 6.15b Distribution of local Sherwood number for bubbles at $Re^{(2)}=10$

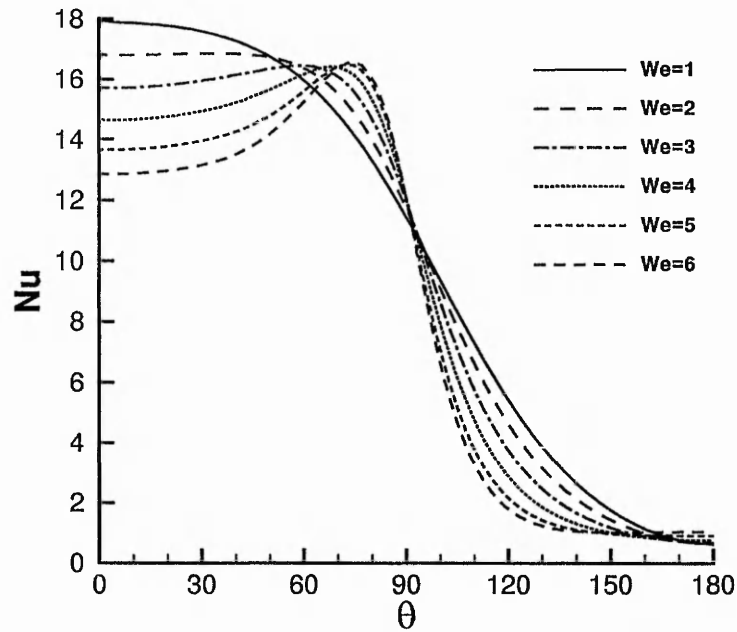


Figure 6.16a Distribution of local Nusselt number for bubbles at $Re^{(2)}=50$

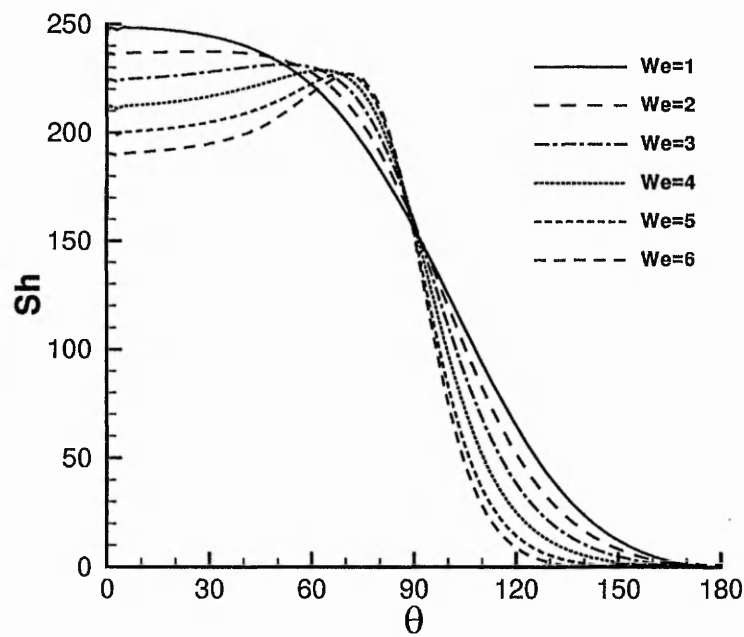


Figure 6.16b Distribution of local Sherwood number for bubbles at $Re^{(2)}=50$

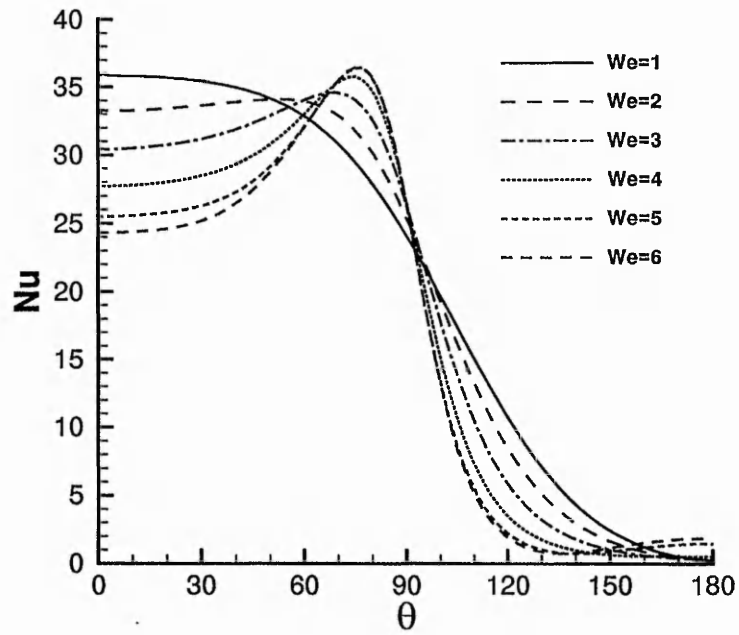


Figure 6.17a Distribution of local Nusselt number for bubbles at $Re^{(2)}=200$

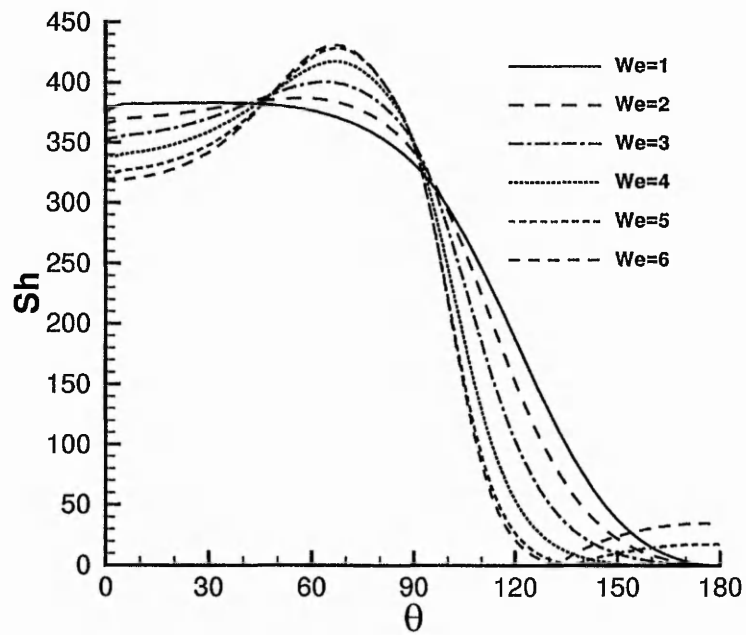


Figure 6.17b Distribution of local Sherwood number for bubbles at $Re^{(2)}=200$

thermal layer, moves backwardly. Denote θ for the peak Nu as θ_B . It can be seen that,

$$\theta_B \neq \theta_A, \quad (6.2)$$

which means the minimum thickness of the thermal or concentration layer doesn't occur at the same position where the strongest shear flow occurs.

In order to study the effects of wake vortex, wake contribution factors for heat and mass transfer, f_T and f_c , are defined as following:

$$f_T = \frac{\int_{\theta_s}^{180^\circ} \frac{\partial T}{\partial n} \cdot r \sqrt{x_\xi^2 + y_\xi^2} \cdot d\xi}{\int_0^{180^\circ} \frac{\partial T}{\partial n} \cdot r \sqrt{x_\xi^2 + y_\xi^2} \cdot d\xi}, \quad (6.3)$$

$$f_c = \frac{\int_{\theta_s}^{180^\circ} \frac{\partial c}{\partial n} \cdot r \sqrt{x_\xi^2 + y_\xi^2} \cdot d\xi}{\int_0^{180^\circ} \frac{\partial c}{\partial n} \cdot r \sqrt{x_\xi^2 + y_\xi^2} \cdot d\xi}, \quad (6.4)$$

where θ_s is the θ angle of separation point. For the case of $(Re^{(2)}, We) = (200, 6)$, which has the biggest separation zone ($\theta_s = 131^\circ$) in the ranges of Reynolds and Weber numbers considered in this paper, we have $f_T = 0.0049$ and $f_c = 0.0774$. These values are quite small as compared with the area ratio of the separation zone to the bubble. Therefore, viewing from the contribution factors only, wake and separation are not obviously beneficial to heat and mass transfer.

However, a notable phenomenon in figures 6.15-6.17, the recovery of Nu and Sh in the wake region, can be clearly identified. For the case of $(Re^{(2)}, We) = (200, 6)$, flow separation occurs at $\theta = \theta_s = 131^\circ$ (this can be identified in figure 6.12a), and a solid-type wake vortex attaches to the bubble body. As shown in figure 6.17, perceivable

recovery of Nu and Sh takes place in the range of $131^\circ \leq \theta \leq 180^\circ$. This recovery is a contribution of the wake vortex. In the zoomed-in wake zone shown in figure 6.18, the circulating flow takes in dissolved gas from the bubble body at the separation point, which results in the Sherwood number arrives at its minimum value. However, because of the steep concentration gradient, the circulating flow is “refreshed” before it arrives at the saddle point. That is, mass transfer occurs quickly when the concentrated liquid on its way from the separation point to the saddle point because of the mass diffusion induced by the steep gradient. Therefore, the returning flow from the saddle point to the rear stagnant point and then to the separation point has low gas concentration (“refreshed”) and a recovery of the Sherwood number is obtained.

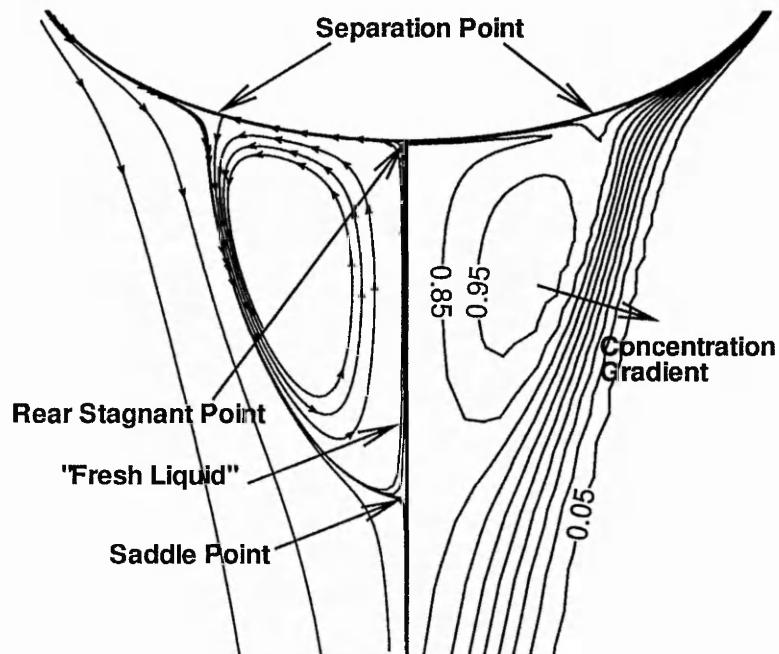


Figure 6.18 Wake vortex structure and its effects on heat and mass transfer

6.4 Summary of the Chapter

Steady heat and fluid flows inside and around inert spherical and deformable bubbles are studied in details. It is revealed that in nearly the whole range of exterior Reynolds number for a single bubble possibly to remain a spherical shape, namely, in the range of $10 \leq Re^{(2)} \leq 550$, flow separation behind a spherical bubble doesn't take place. Study on deformable bubbles is the main object of this chapter. The dynamics of bubbles, including the bubble shape, flow structure, interfacial characteristics, drag coefficients and heat and mass transfer are studied and carefully analysed. The following concluding remarks can be drawn from the study:

- (a). In the ranges of $(Re^{(2)}, We) = [0, 200] \times [0, 6]$, $Re^{(2)} = 50$ is the border of two types of deformation of a bubble: stronger in the rear at $Re^{(2)} \leq 50$ and stronger in the front at $Re^{(2)} \geq 50$.
- (b). For a single air bubble rising in unbounded water, at room temperature and atmospheric pressure, flow separation from the bubble body is observed to onset at $4 < We < 5$ for $Re^{(2)} = 50$, at $4 < We < 5$ for $Re^{(2)} = 100$, and at $3 < We < 4$ for $Re^{(2)} = 200$. In all these cases, the flow structure is a typical solid vortex type with a pair of counter-rotating ring vortices inside and a single separation ring vortex outside the bubble;
- (c). The conventional external flow model of the bubble, which treats the gas-liquid interface as a "free boundary" (a slip boundary free of tangential stress), can over predict the viscous effect on the separation which has occurred, and under predict the viscous effect at $Re^{(2)} \leq 5$.
- (d). The minimum thickness of the thermal or concentration layer doesn't occur at the same position where the strongest shear flow occurs, this shows a non-linear relationship between the flow, thermal and concentration fields.
- (e). A recovery of Sherwood and Nusselt numbers in the separation zone is observed and a physical explanation to this is proposed.

Chapter 7

Time-Accurate Simulations of an Inert Bubble Introduced into a Hot Liquid

7.1 Introduction

In order to study the mechanisms of heat and mass transfer in bubbly flows, a close observation of the time-dependent behaviour of the bubble-rise is crucial. Before the inert bubble reaches its terminal state, which has been carefully studied in chapter 6, the rising is an accelerating procedure during which the shape, rising velocity, thermal and concentration fields change with time. This procedure is short in time but important to the heat and mass transfer because the bubble deformation and mainly happened during this period as it will be shown later in this chapter.

Time-accurate simulation of the bubble-rise is a complete application of the algorithm and CFD codes developed in this thesis. In order to solve the full mathematical model presented in chapter 3, the unknown time-dependent velocity and acceleration, $V_o(t)$ and $a_o(t)$ in equations (3.27), (3.32) and (3.34) must be decided and additional independent equations must be derived and coupled with the mathematical model in chapter 3 so as to obtain the unique solution of an interfacial problem.

This chapter derives the controlling equations for $V_o(t)$ and $a_o(t)$ by analysing the forces acting on the dispersed phase. A supplementation to the numerical method presented in chapter 5 for steady calculations is presented for time-accurate simulation in this chapter. Based on these, study on the unsteady flows and heat and mass transfer in an inert bubble introduced into a hot liquid is carried out.

7.2 Rising Velocity and Acceleration

7.2.1 A Model Equation for Spherical Bubbles

As reviewed in chapter 2, the spherical model has important roles in analysing the dynamics of single bubbles. Indeed, many works have been done for the analysis of forces acting on a bubble by using a spherical model to establish the constitutive equation for the mathematical model of the single bubble problem. A summary of these models has been given by Clift, Grace and Weber (1978). Even in the recent years, spherical models were still being used by some researchers to calculate the translating velocity (Mei, 1994; Takagi and Matsumoto, 1995); this also shows the importance of the spherical model.

In the spherical models, the time-dependent rising velocity $V_o(t)$ is modelled and calculated using the dynamic parameters of the steady state. In order to model the time-dependent effects, a so-called “added mass term” and a “history force” are induced (Clift, Grace and Weber, 1978), and the balance of the forces is written as

$$\left(\rho^{(l)} + \frac{\rho^{(2)}}{2} \right) \frac{dV_o(t)}{dt} = g(\rho^{(2)} - \rho^{(l)}) - F_D - F_h, \quad (7.1)$$

where the $\frac{\rho^{(2)}}{2}$ is the “added mass” whose volume equal to a half of that of the bubble. On the right-hand side of the equation, the first term stands for buoyancy force, the second is the drag force and the final term is called the Basset history force which is induced by the contribution of a past acceleration. According to the suggestions by Clift, Grace and Weber (1978) and Takagi and Matsumoto (1995), the history term can be completely ignored. In the meanwhile, as the ration of gas-liquid density is generally very small, the contribution of the mass of the bubble is negligible on the left side.

Therefore, equation (7.1) is reduced to

$$\frac{\rho^{(2)}}{2} V \frac{dV_o(t)}{dt} = g\rho^{(2)}V - F_D. \quad (7.2)$$

In a dimensionless form, equation (7.2) changes to

$$\frac{1}{2} \frac{dV_o(t)}{dt} = \frac{1}{Fr} - \frac{F_D d_{ref}}{\rho^{(2)} V_{ref}^2 V}, \quad (7.3)$$

According to the definition of drag coefficient, the time-dependent drag force can be calculated as follows,

$$F_D = \frac{1}{8} C_D \pi \rho^{(2)} d_{ref}^2 [V_o(t)]^2 = \frac{1}{6} \frac{Eo^{\frac{3}{2}}}{(Re^{(2)})^2 Mo^{\frac{1}{2}}} \pi \rho^{(2)} d_{ref}^2 [V_o(t)]^2, \quad (7.4)$$

Equation (7.3) becomes

$$\frac{dV_o(t)}{dt} = \frac{2Eo^{\frac{3}{2}}}{(Re^{(2)})^2 Mo^{\frac{1}{2}}} [1 - (V_o(t))^2] = \frac{3}{2} C_D [1 - (V_o(t))^2]. \quad (7.5)$$

According to spherical models, the drag coefficient C_D can be approximately evaluated as (Mei, 1994):

$$C_D = \frac{24}{Re^{(2)}} \left\{ \frac{2}{3} + \left[\frac{12}{Re^{(2)}} + 0.75 \left(1 + \frac{3.315}{(Re^{(2)})^{0.5}} \right) \right]^{-1} \right\}. \quad (7.6)$$

Equation (7.6) is an ordinary differential equation. With a given initial value, this equation is solved using a second-order accurate scheme in this thesis,

$$\begin{cases} \tilde{V}_o(t^{n+1}) = V_o(t^n) + \Delta t \cdot \frac{3}{2} C_D [1 - (V_o(t^n))^2] \\ V_o(t^{n+1}) = V_o(t^n) + \frac{\Delta t}{2} \left\{ \frac{3}{2} C_D [1 - (V_o(t^n))^2] + \frac{3}{2} C_D [1 - (\tilde{V}_o(t^{n+1}))^2] \right\} \end{cases} \quad (7.7)$$

7.2.2 A Full Analytical Model

In the spherical model methods, the rising velocity is unreasonably decoupled from the full mathematical description of the problem and is treated as independent of the flow fields. This treatment is unacceptable for deformable bubbles. In the meanwhile, the drag coefficient of a deformable bubble defined in the nomenclature cannot be simply evaluated by using equation (7.6) as the drag force is time-dependent. In order to sort out this problem, a full analysis on the forces is needed.

Consider a single bubble rising in an unbounded liquid. The normal and tangential forces act on the body of the bubble through the surface. According to the axisymmetric assumption, the cooperation of these surface forces, obtained by integrating over the outer face of the bubble, is in the vertical direction and is the vectorial summation of the buoyancy and drag forces. That is,

$$\begin{aligned} F_y = F_B - F_D &= \oint_S (\tau_{\bar{n}}^{(2)} \bar{n} + \tau_{\bar{i}}^{(2)} \bar{i}) \cdot \bar{j} \, dS \\ &= \int_0^{\xi_{max}} 2\pi r (x_{\xi} \cdot \tau_{\bar{n}}^{(2)} + y_{\xi} \cdot \tau_{\bar{i}}^{(2)}) \cdot d\xi \end{aligned} \quad (7.8)$$

where S is the surface of the bubble whose volume is \mathcal{V} , F_B and F_D are the buoyancy

and drag forces respectively. It should be recalled that in the normal stress, as shown in equation (5.4), the pressure term is the static pressure of fluid, p ; not the effective pressure p_{eff} defined by equation (3.31) whose dimensionless form is

$$p_{eff} = p + \frac{1}{Fr} y. \quad (7.9)$$

If the gravity of the fluid surrounding the bubble is negligible, equation (7.8) becomes

$$\begin{cases} F_B = 0 \\ F_y = -F_D = \int_0^{\xi_{max}} 2\pi r (x_\xi \cdot \tau_{\bar{n}}^{(2)} + y_\xi \cdot \tau_{\bar{i}}^{(2)}) \cdot d\xi \end{cases}; \quad (7.10)$$

while equation (7.10) results in

$$\begin{cases} p_{eff} = p \\ Fr = \infty \end{cases}. \quad (7.11)$$

This is exactly the case of the water head having been neglected. This treatment is widely used to analyse the steady external flows over fluid particles.

Except the facial forces, the gravity is acting on the bubble in the form of a body force,

$$F_g = \rho^{(1)} V g. \quad (7.12)$$

Therefore, the acceleration of the bubble satisfies the following equation:

$$\rho^{(1)} V \cdot a_o(t) = F_y - F_g = F_B - (F_D + F_g). \quad (7.13)$$

The rising velocity of the bubble can be given by the integration of $a_o(t)$,

$$V_o(t) = V_o(t_0) + \int_0^t a_o(t) \cdot dt. \quad (7.14)$$

Give the initial value of $V_o(t_0)$ and proper initial fields, the mathematical model of the

current problem becomes well posed and can be solved.

7.3 Solution Approach for Time-Accurate Simulation

Based on the solution approach presented in section 5.3, supplementations are carried out for time-accurate simulations. A full numerical procedure for calculating the time-dependent rising of a single bubble introduced into an unbounded liquid is summarised as follows:

- (a). Define a far field boundary $\bar{R} = \bar{R}_\infty$ where the flow blockage effects due to the bubble can be neglected;
- (b). Give an initial field and a time step Δt ;
- (c). In time level $t^{n+1} = t^n + \Delta t$, determine $a_o(t^{n+1})$ and $V_o(t^{n+1})$ according to equations (7.13) and (7.14) respectively;
- (d). Solve the heat and fluid flows in steps similar to those for steady problem in section 5.3, but the temporal derivative terms in the controlling equations must be included and therefore the so-called space conservation law (section 4.3.2) should be applied;
- (e). Update the bubble profile step by step;
- (f). Return to step (c) to update $a_o(t^{n+1})$ and $V_o(t^{n+1})$ if they are still changing with the updating of bubble profile for t^{n+1} ; Otherwise, check the criteria ETN , ERZ and EVT , defined by inequalities (5.26)~(5.28), if they are satisfied, convergence can be declared for the time-level $t = t^{n+1}$ and go to step (h);
- (g). Otherwise, return to step (d) and repeat carrying out internal iterations until all the above convergent criteria are satisfied and $a_o(t^{n+1})$ and $V_o(t^{n+1})$ are not changing with the updating of bubble profile for t^{n+1} ;
- (h). Check the variation,

$$|V_o(t^{n+1}) - V_o(t^n)| \leq \varepsilon_{ref}; \quad (7.15)$$

If inequality (7.15) is satisfied, the rising bubble has arrived at its terminal state and the calculation can be stopped; Otherwise, return to step (b) to calculate the next time-level.

The criterion ε_{ref} defined by inequality (7.15) is important for the calculation and must be valued on the magnitude of $O(10^{-3})$ or even higher. It should be noted that even in a same time level, the calculation is only similar to that for a steady problem but different from it because $a_o(t)$ and $V_o(t)$ are time dependent. So the time-accurate calculation is not simply a series of steady problems; it is much more complicated and much more CPU-time consuming. The flow chart of the above calculation procedure is given in the appendix.

7.4 Results

Because the calculation is extremely time-consuming, calculations are carried out for the three types of deformations at terminal states observed in chapter 6. Nine cases are included, their terminal Reynolds and Weber numbers are $(Re^{(2)}, We) = [10, 50, 200] \times [1, 3, 5]$. The computational domain and mesh are the same as that used for previous calculations, i.e., the outer bound of computational domain is assigned at 50 times the equivalent bubble radius; mesh arrangement is: block1 = 82×42 and block2 = 90×82 . The fluid properties are set to those of air bubble rising in hot water ($100^\circ C$ and 1atm), namely, $\Phi_\rho = 1:800$, $\Phi_\mu = 1:100$, $Pr^{(2)} = 2$ and $Sc^{(2)} = 500$. These are typical values selected to expose the flow and transfer phenomena in rising bubbles, and the selection is considered for not losing generality.

7.4.1 Rising Velocity

The time histories of dimensionless rising velocity for three kinds of bubbles are shown in figure 7.1. For comparison, Mei's (1994) decoupled rising velocity model is employed. It can be seen that the decoupled model gives results close to those of lower Weber number cases calculated by the full analytical model. This may be because the Mei's (1994) model is for spherical bubbles. For results obtained by the full analytical model, at a given exterior Reynolds number, the bigger Weber number, the shorter dimensionless time is needed to reach the terminal state. The unsteady oscillatory rising velocity observed by Takagi, Matusmoto and Huang (1997), Krishna and Van Baten (1999) and Sato, Jung and Abe (2000) has not been found in our calculation. This could be because the Weber number used here is small and the flow around the bubble is laminar and with only very weak flow separation in some cases.

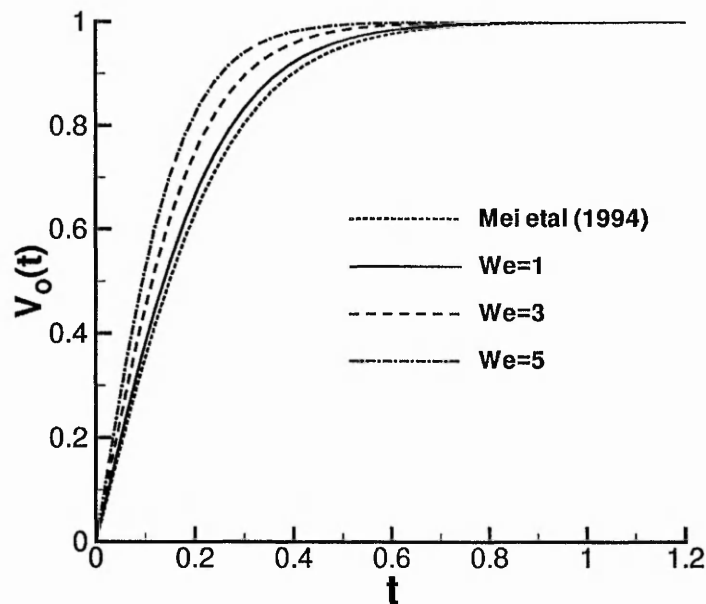


Figure 7.1a Time history of bubble rising velocity at $Re^{(2)} = 10$

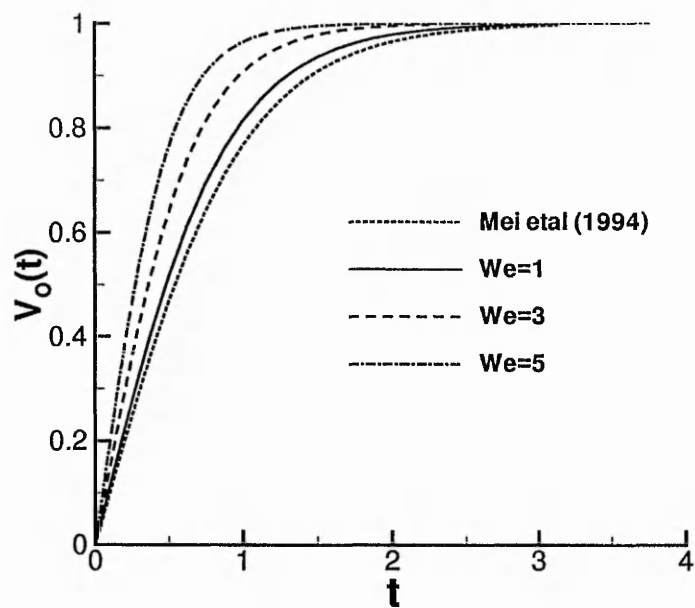


Figure 7.1b Time history of bubble rising velocity at $Re^{(2)} = 50$

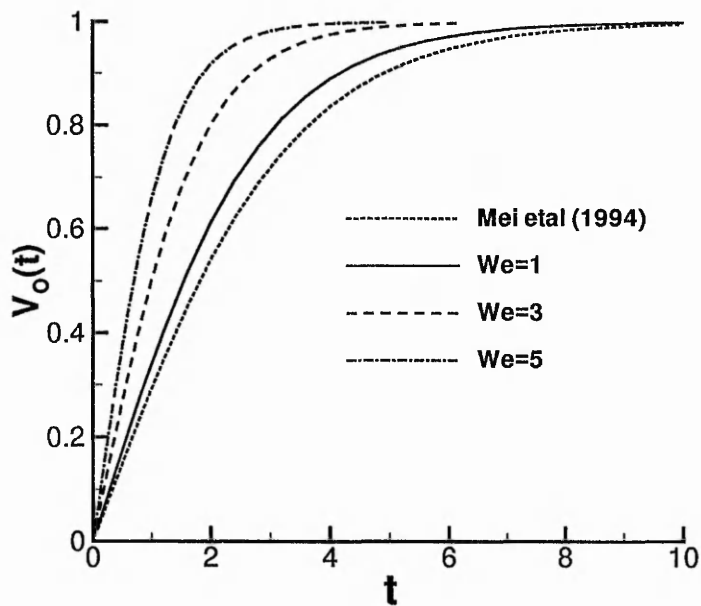


Figure 7.1c Time history of bubble rising velocity at $Re^{(2)} = 200$

7.4.2 Evolution of Bubble Shape and Flow Structure

The evolution of bubble shape and flow structure for cases at $(\text{Re}^{(2)}, \text{We}) = [10, 50, 200] \times [3, 5]$ are shown in figure 7.2. It should be noticed that the velocity used to show flow structure here is the relative velocity \vec{W} , because the flow is unsteady. For cases at $(\text{Re}^{(2)}, \text{We}) = [10, 50, 200] \times [1]$, the deformation is very slight and therefore omitted here for simplicity. As shown in figure 7.2, the deformation of a bubble mainly occurs at the early stage of the acceleration, namely, before $V_o(t)$ arrives at about 80 percents of its value at terminal state. In the later stage of acceleration, the deformation is very slow. However, for the cases with separations, the onset of separation is only at the late stage of acceleration. There are two such cases: $(\text{Re}^{(2)}, \text{We}) = (50, 5)$ and $(\text{Re}^{(2)}, \text{We}) = (200, 5)$. For $(\text{Re}^{(2)}, \text{We}) = (200, 5)$, the onset of separation happens at $t = 2.2$, when $V_o(t)$ is already nearly 95 percents of its terminal value; For $(\text{Re}^{(2)}, \text{We}) = (50, 5)$, the separation takes place even later, at $t = 1.575$ when $V_o(t)$ equal to 99.6 percents of its terminal value. This phenomenon further proves that separation is the accumulation of vortices, which has been concluded in chapter 6. Because of the curvature and no-slip boundary at the gas-liquid interface, vorticity is generated and be convected to the rear of the bubble and results in flow separation. This procedure takes time so the wake vortex can only be observed at the late stage of acceleration.

In the meanwhile, the late onset of separation raises a requirement for the convergent criterion ε_{ref} defined by inequality (7.15), just like what we mentioned previously. For case of $(\text{Re}^{(2)}, \text{We}) = (50, 5)$, the separation is impossible to be observed if $\varepsilon_{ref} = 5 \times 10^{-3}$. In our calculation, this criterion is set at $\varepsilon_{ref} = 1 \times 10^{-4}$ so as to expose all the possible details of flow phenomena.

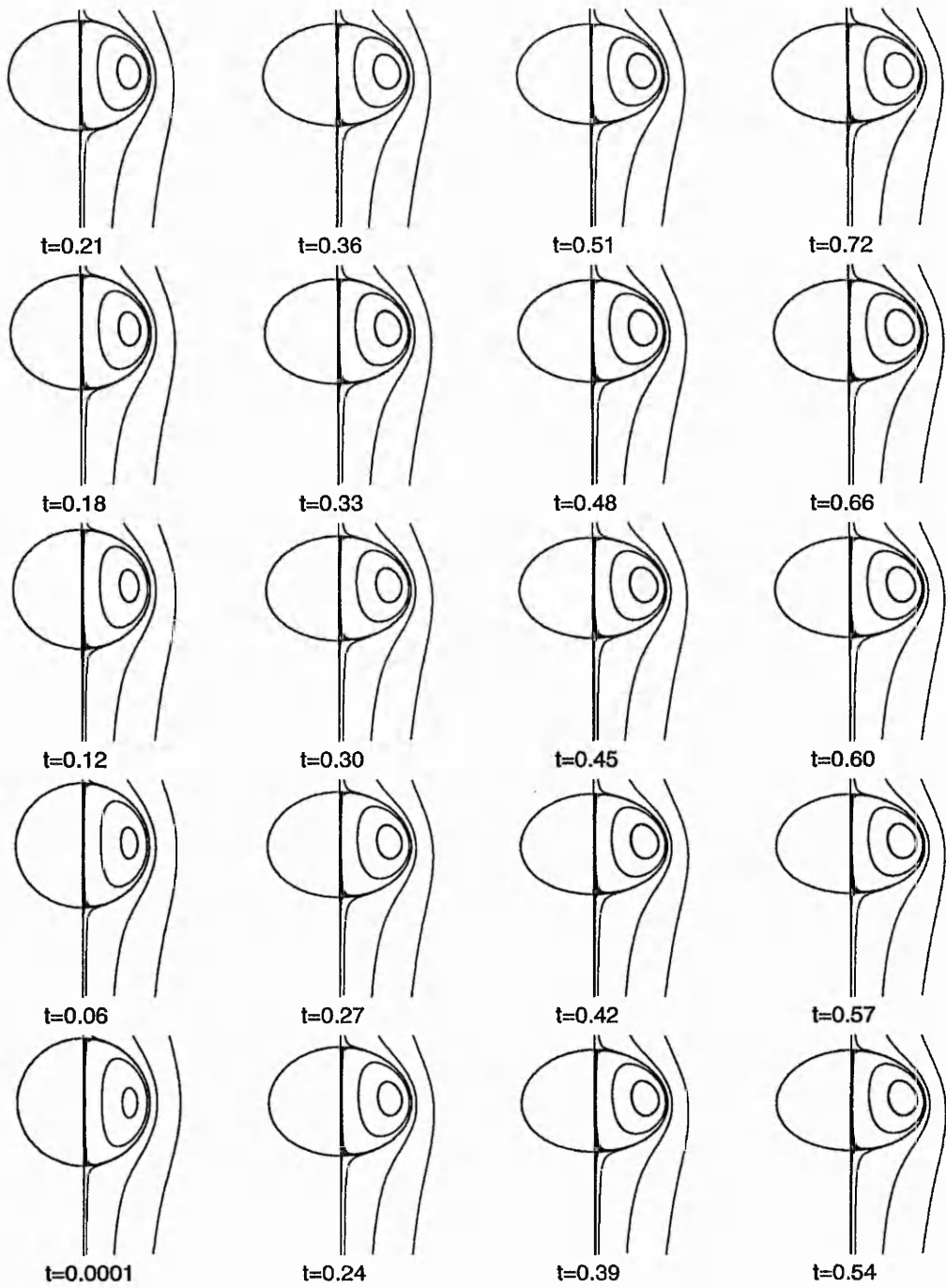


Figure 7.2a Evolution of bubble shape and flow structure at $Re^{(2)} = 10$, $We = 3$

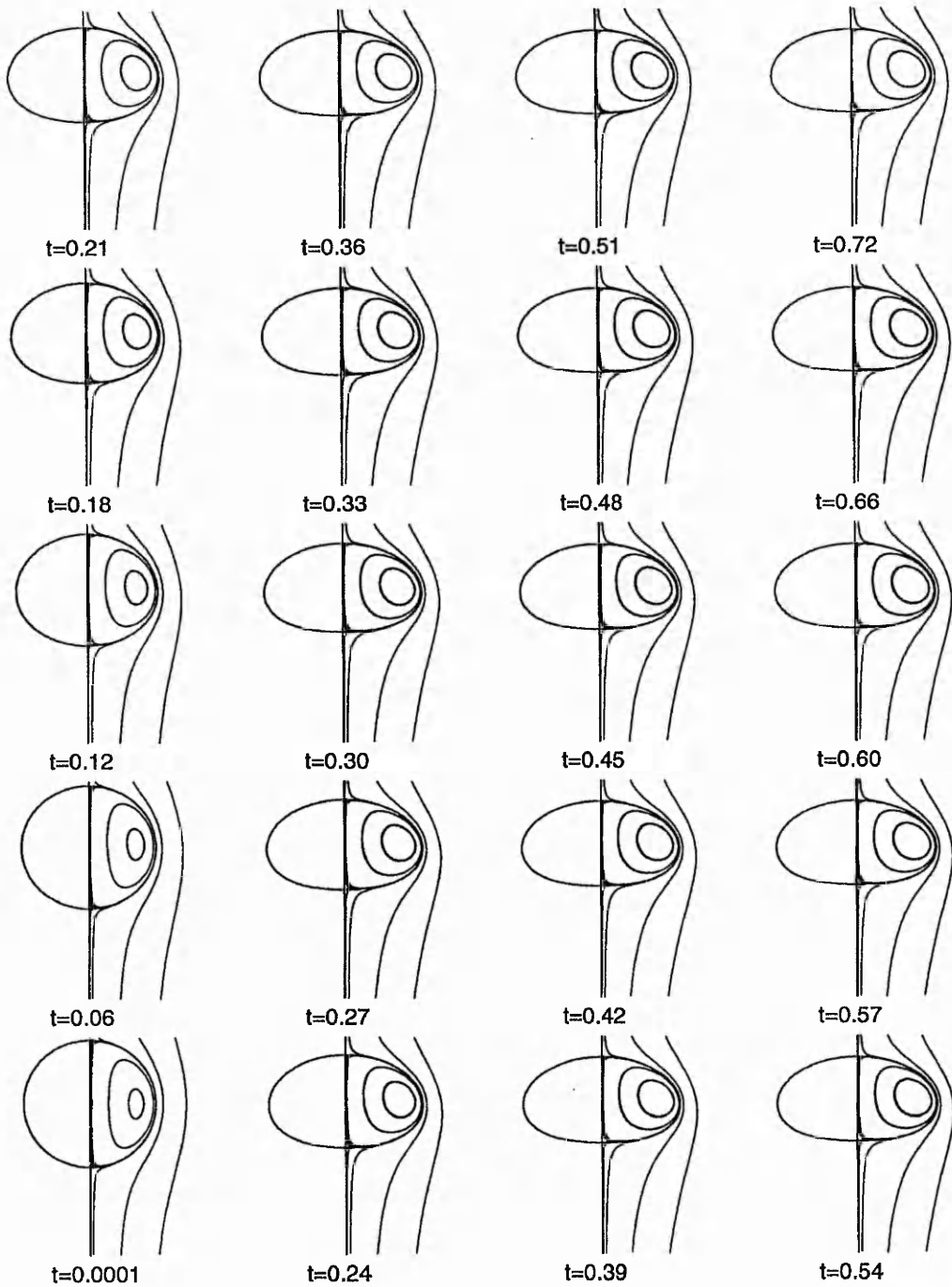


Figure 7.2b Evolution of bubble shape and flow structure at $Re^{(2)} = 10$, $We = 5$

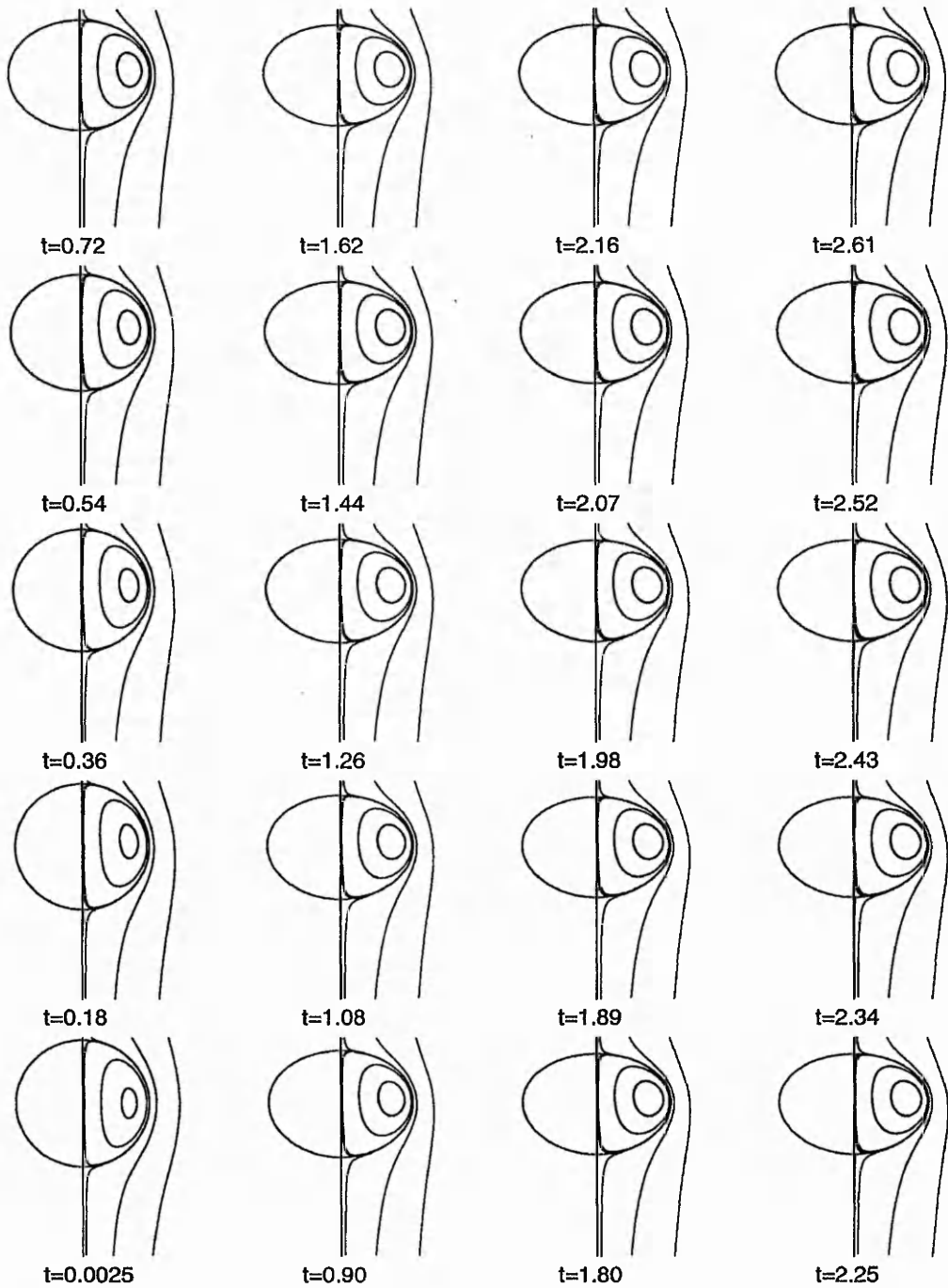


Figure 7.2c Evolution of bubble shape and flow structure at $Re^{(2)} = 50$, $We = 3$

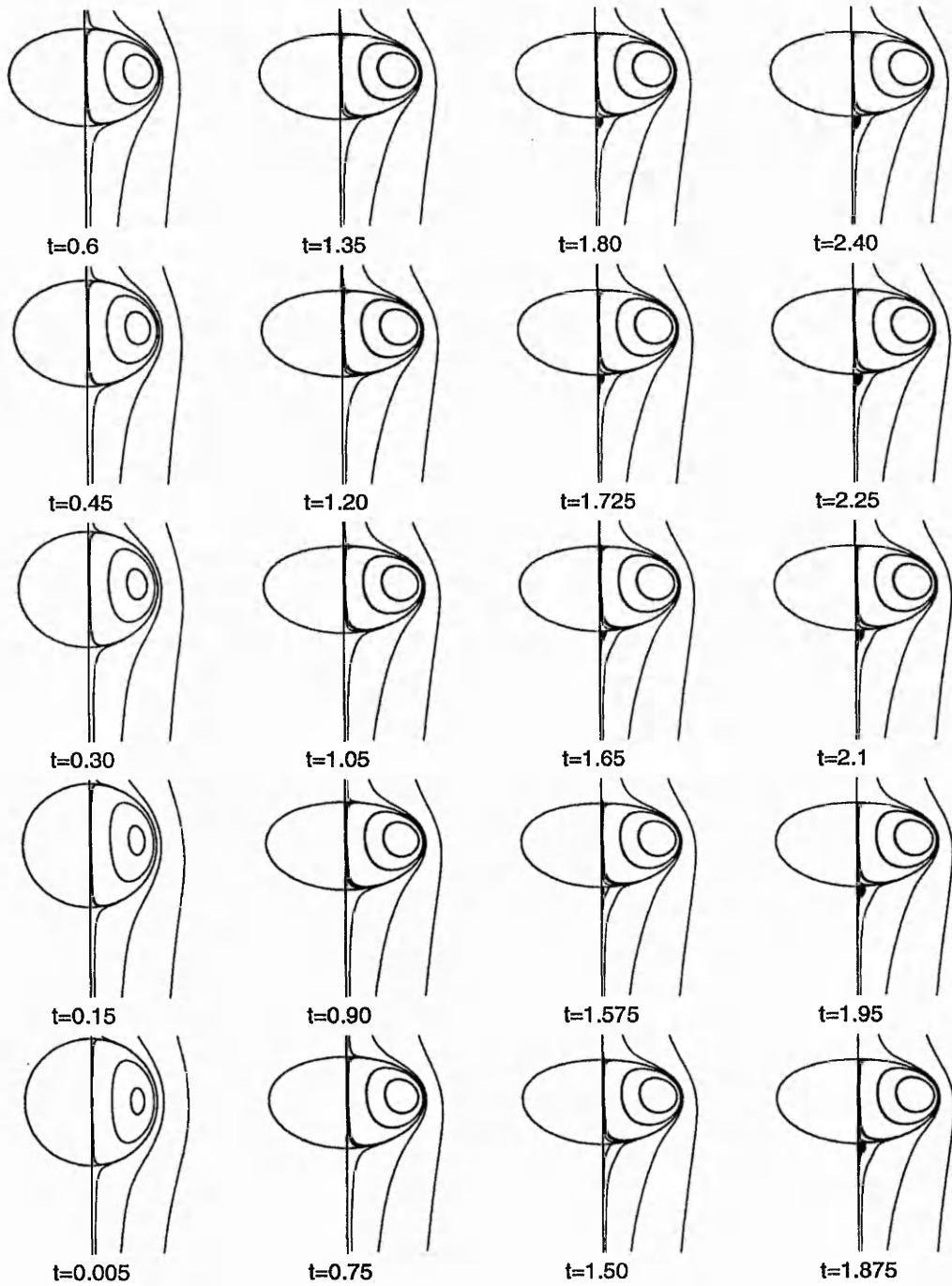


Figure 7.2d Evolution of bubble shape and flow structure at $Re^{(2)} = 50$, $We = 5$

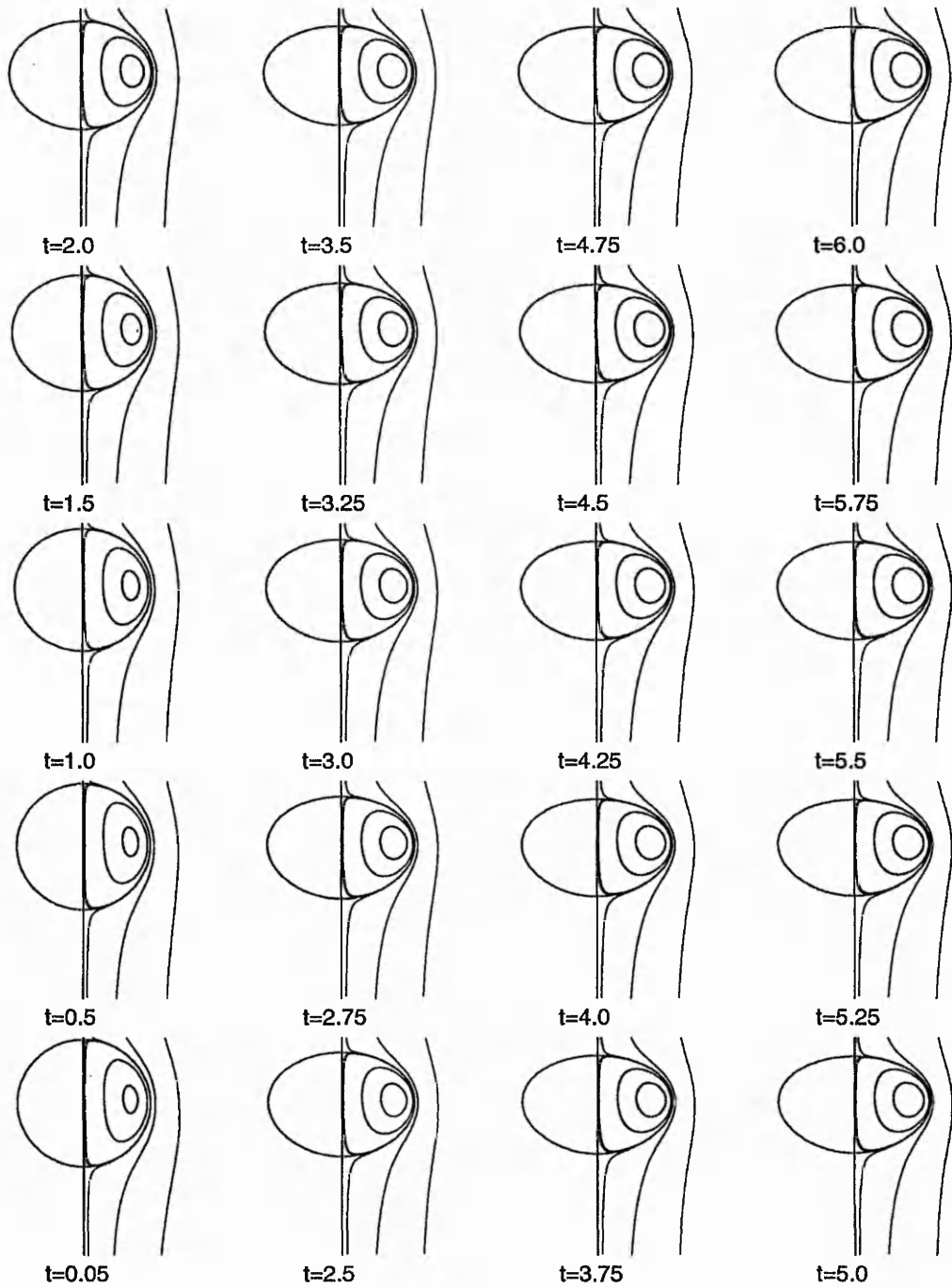


Figure 7.2e Evolution of bubble shape and flow structure at $Re^{(2)} = 200$, $We = 3$

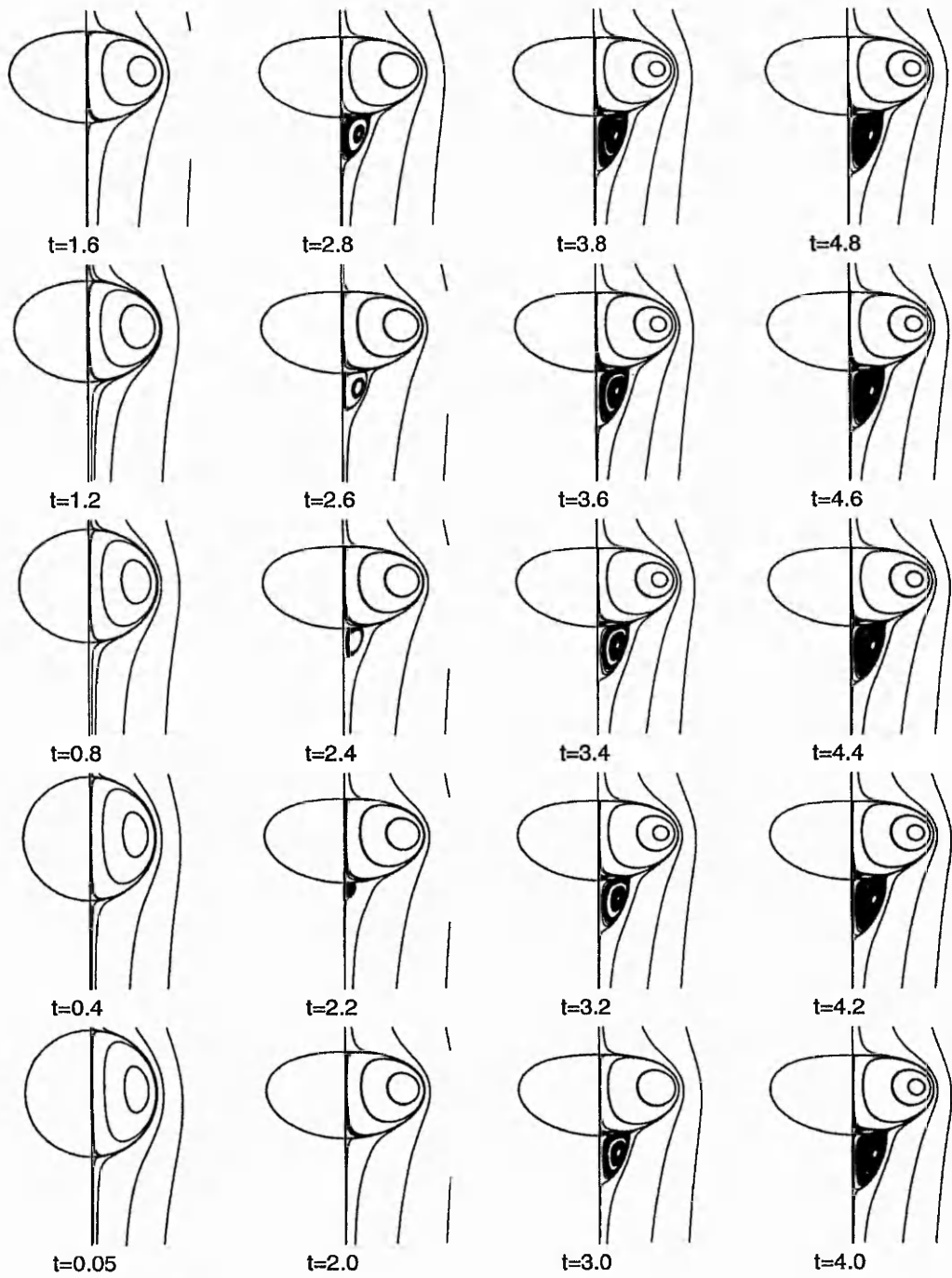


Figure 7.2f Evolution of bubble shape and flow structure at $Re^{(2)} = 200$, $We = 5$

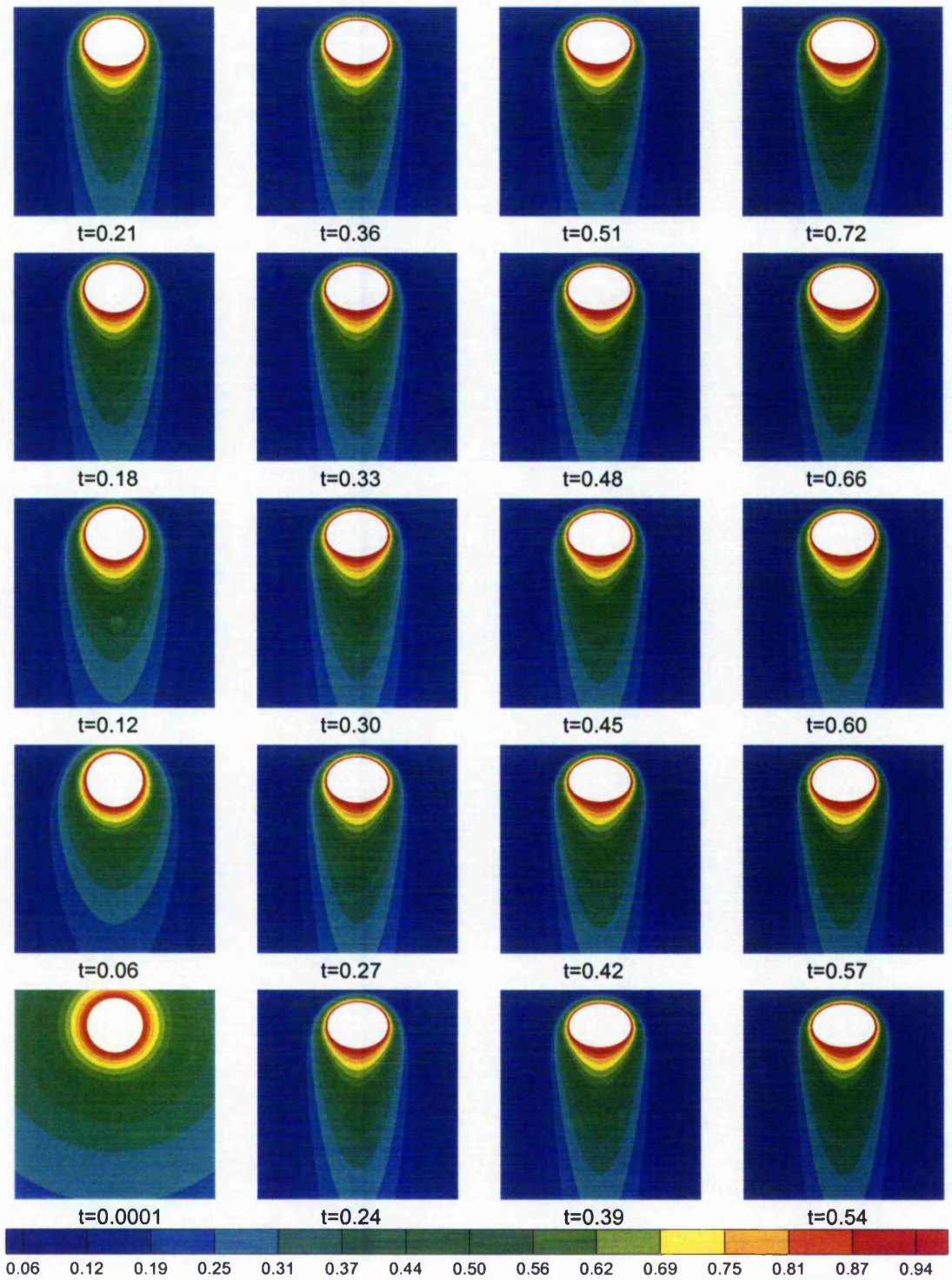


Figure 7.3a Development of temperature field, $Re^{(2)} = 10$, $We = 3$

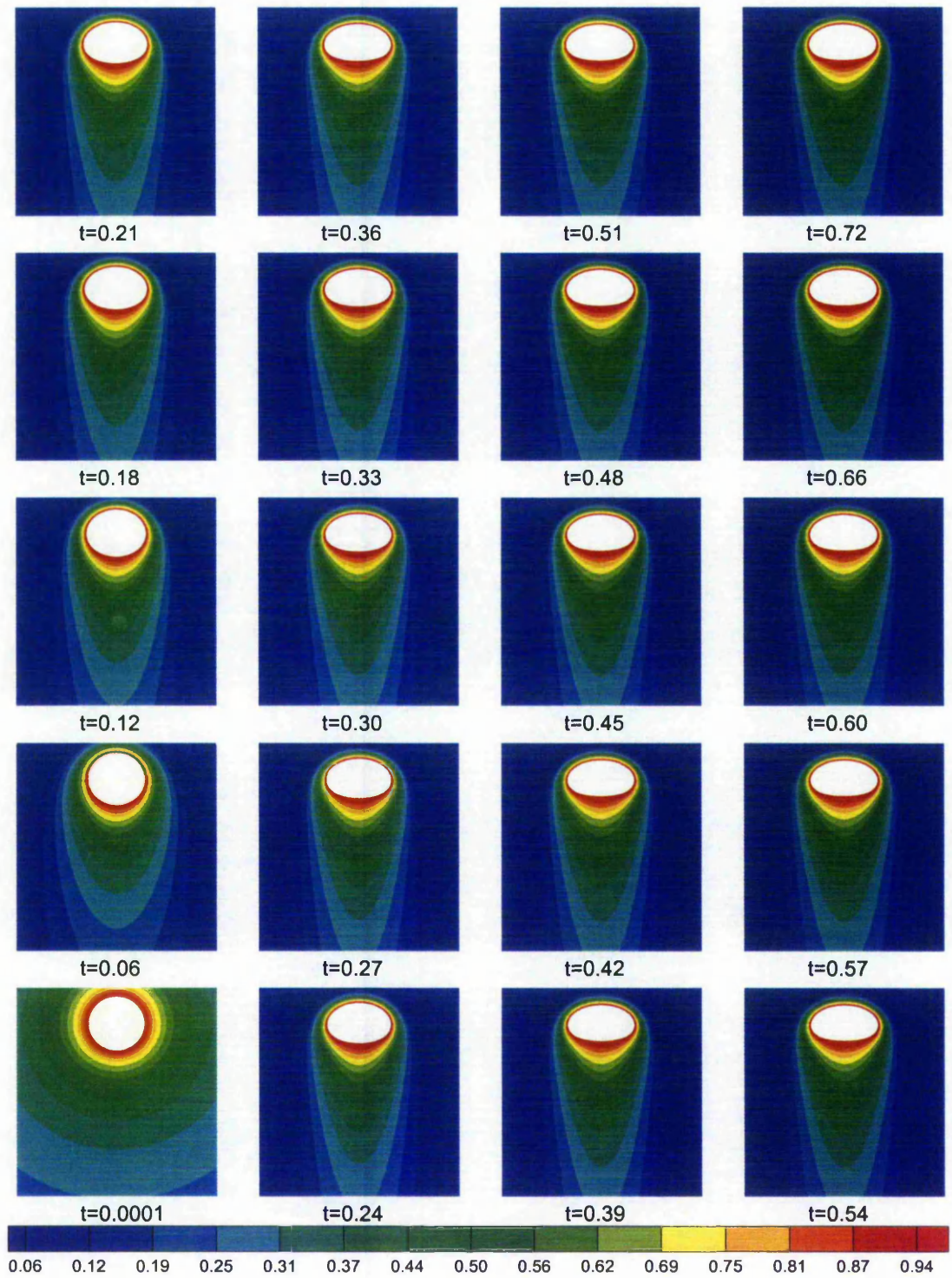
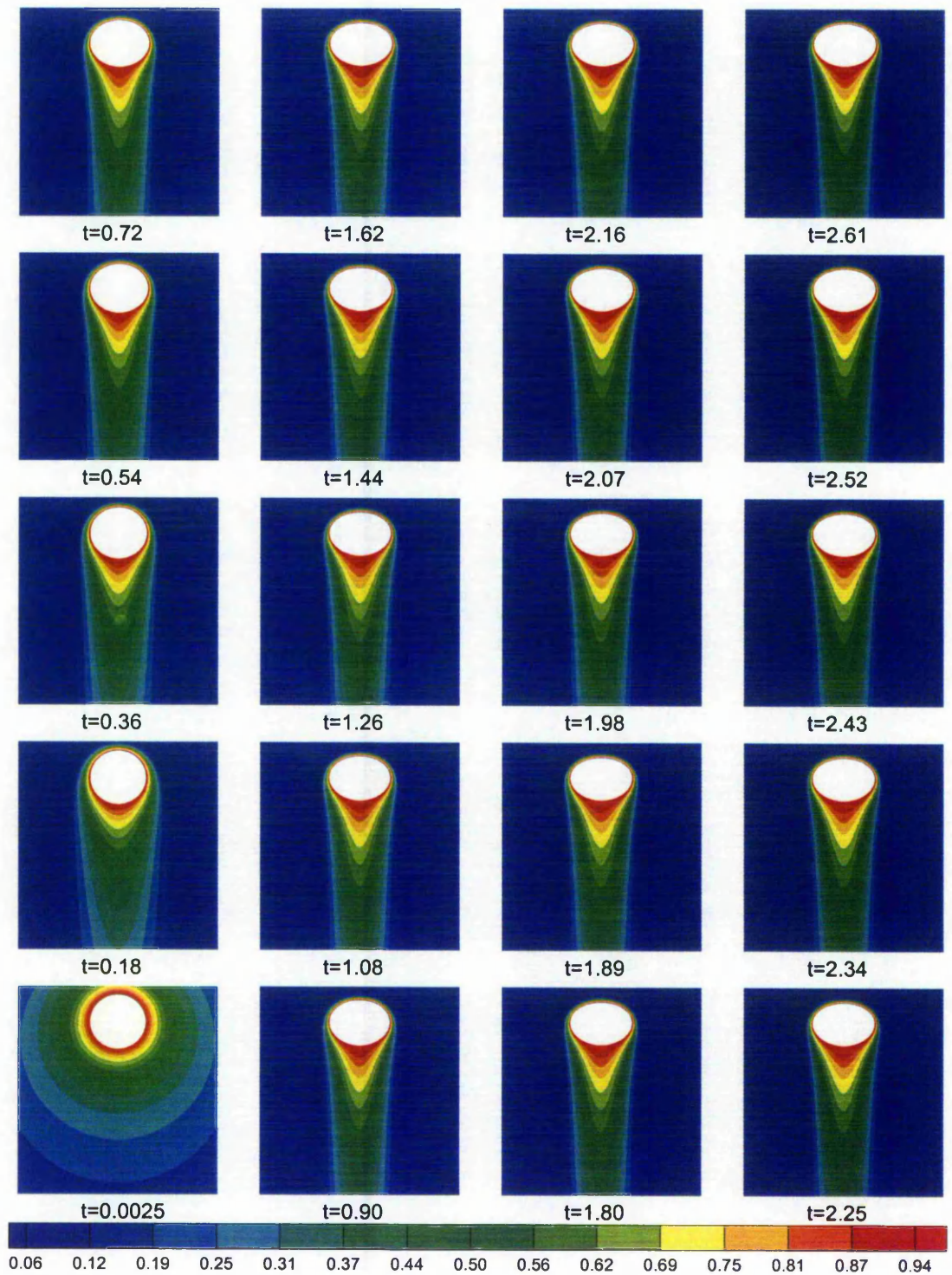
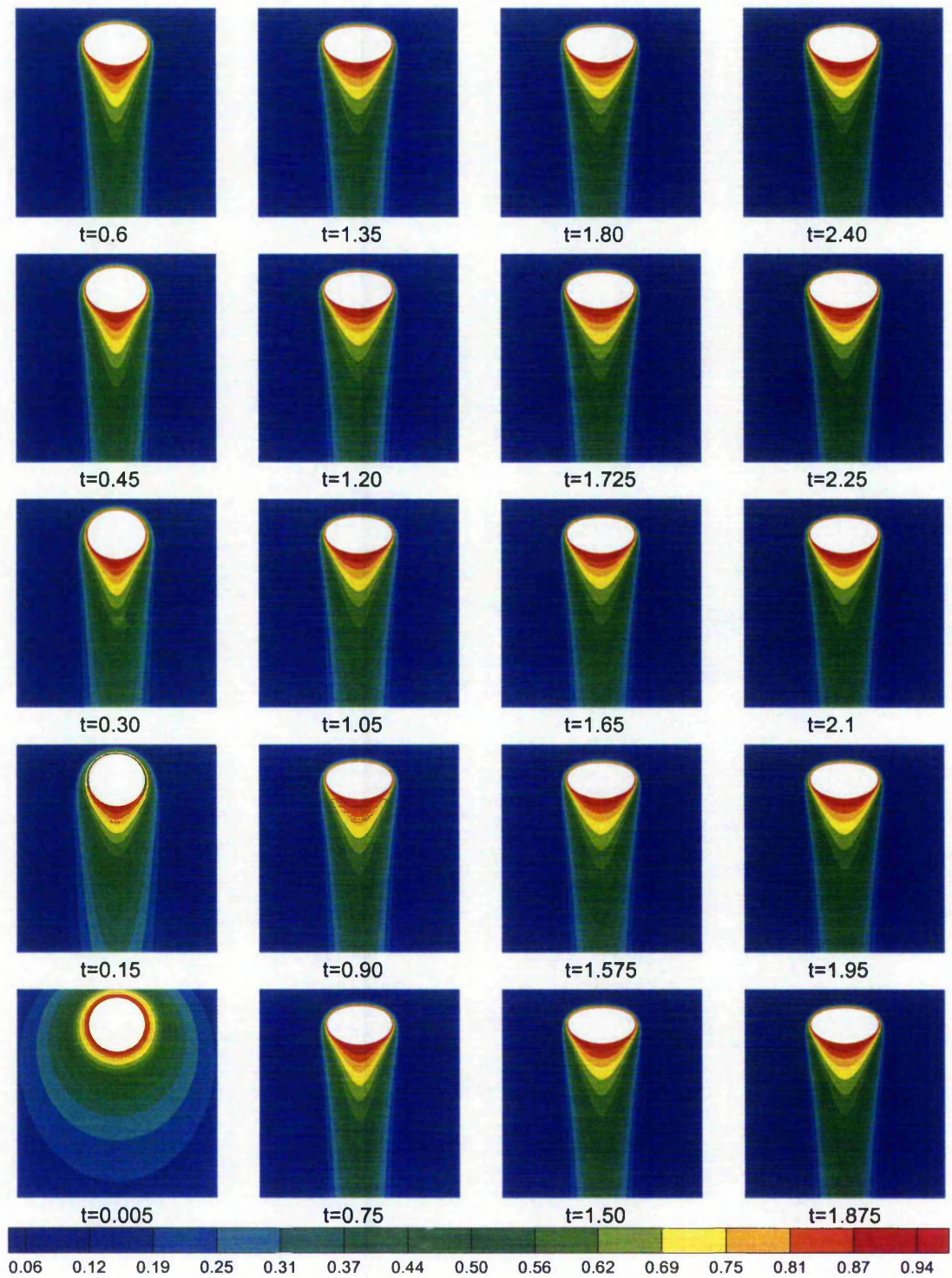


Figure 7.3b Development of temperature field, $Re^{(2)} = 10$, $We = 5$

Figure 7.3c Development of temperature field, $Re^{(2)} = 50$, $We = 3$

Figure 7.3d Development of temperature field, $Re^{(2)} = 50$, $We = 5$

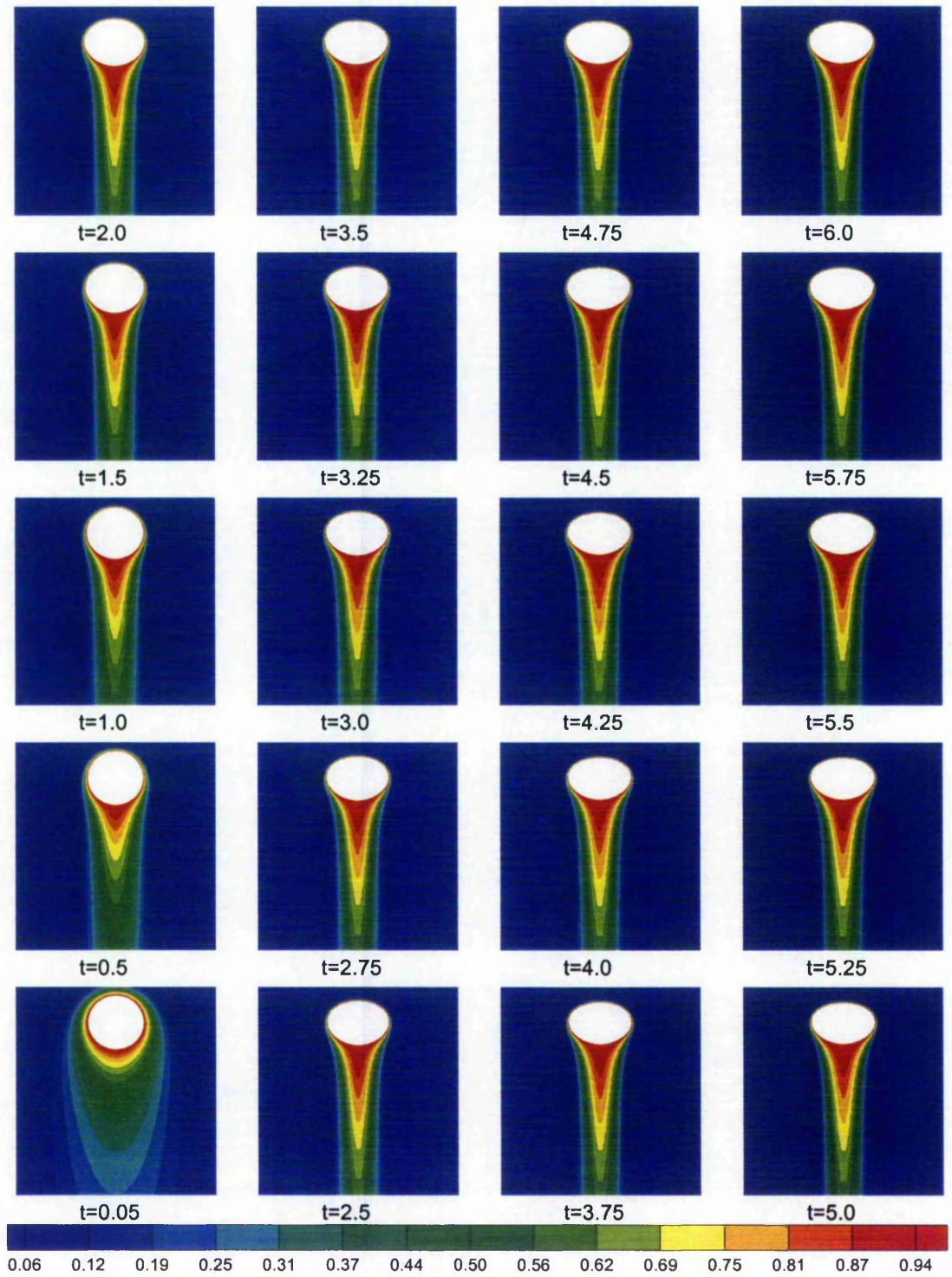


Figure 7.3e Development of temperature field, $Re^{(2)} = 200$, $We = 3$

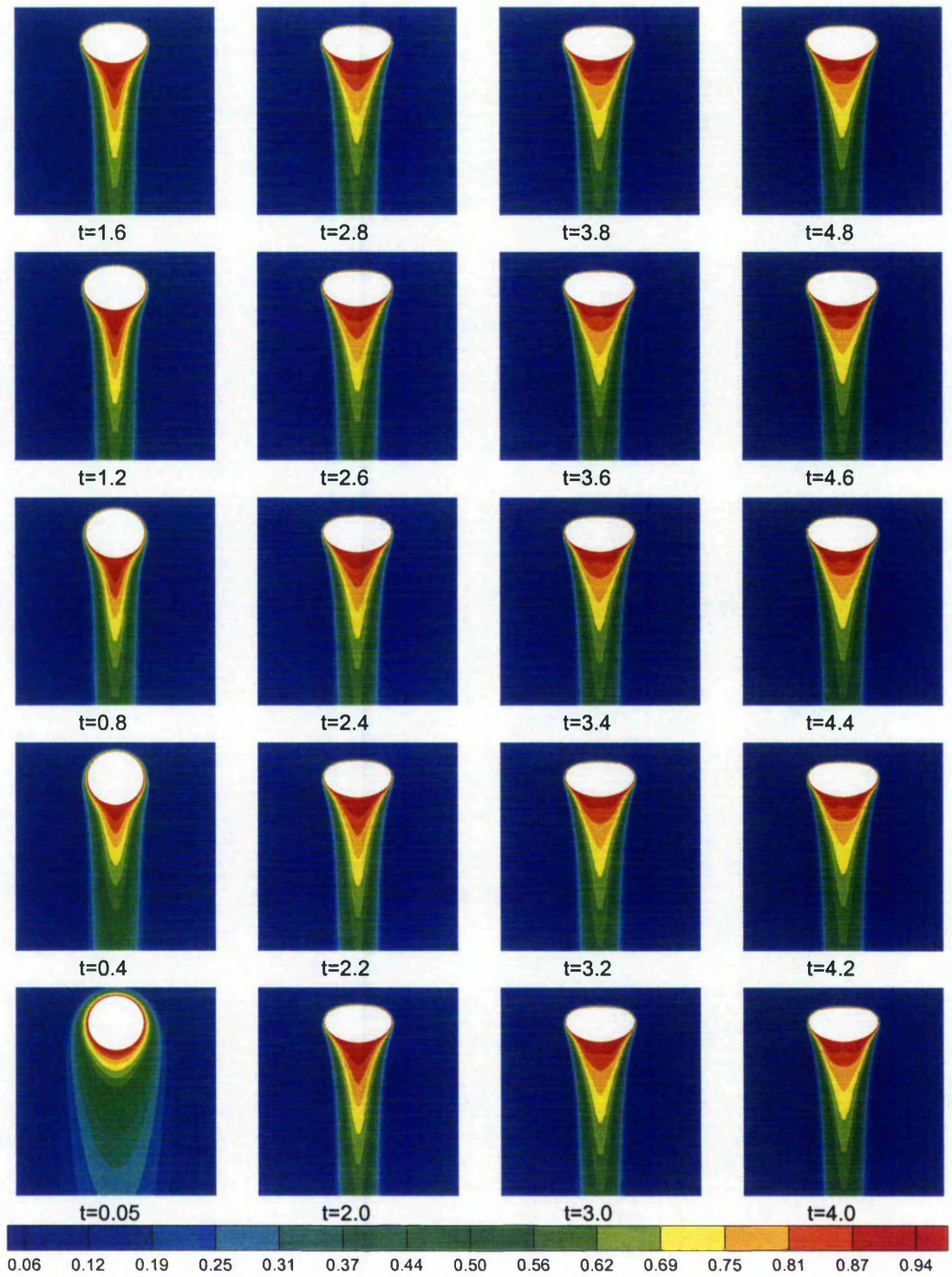


Figure 7.3f Development of temperature field, $Re^{(2)} = 200$, $We = 5$

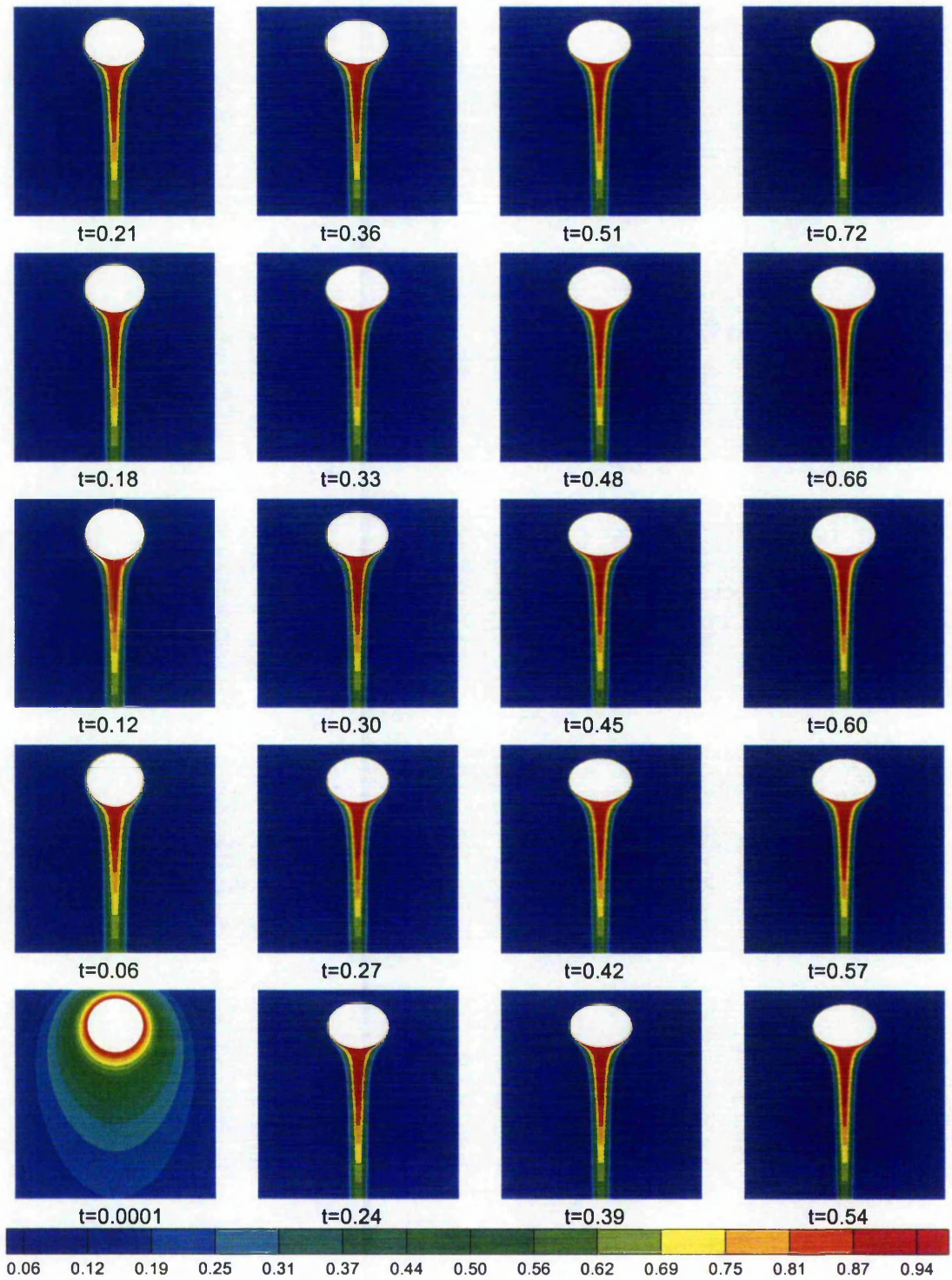


Figure 7.4a Development of concentration field, $Re^{(2)} = 10$, $We = 3$

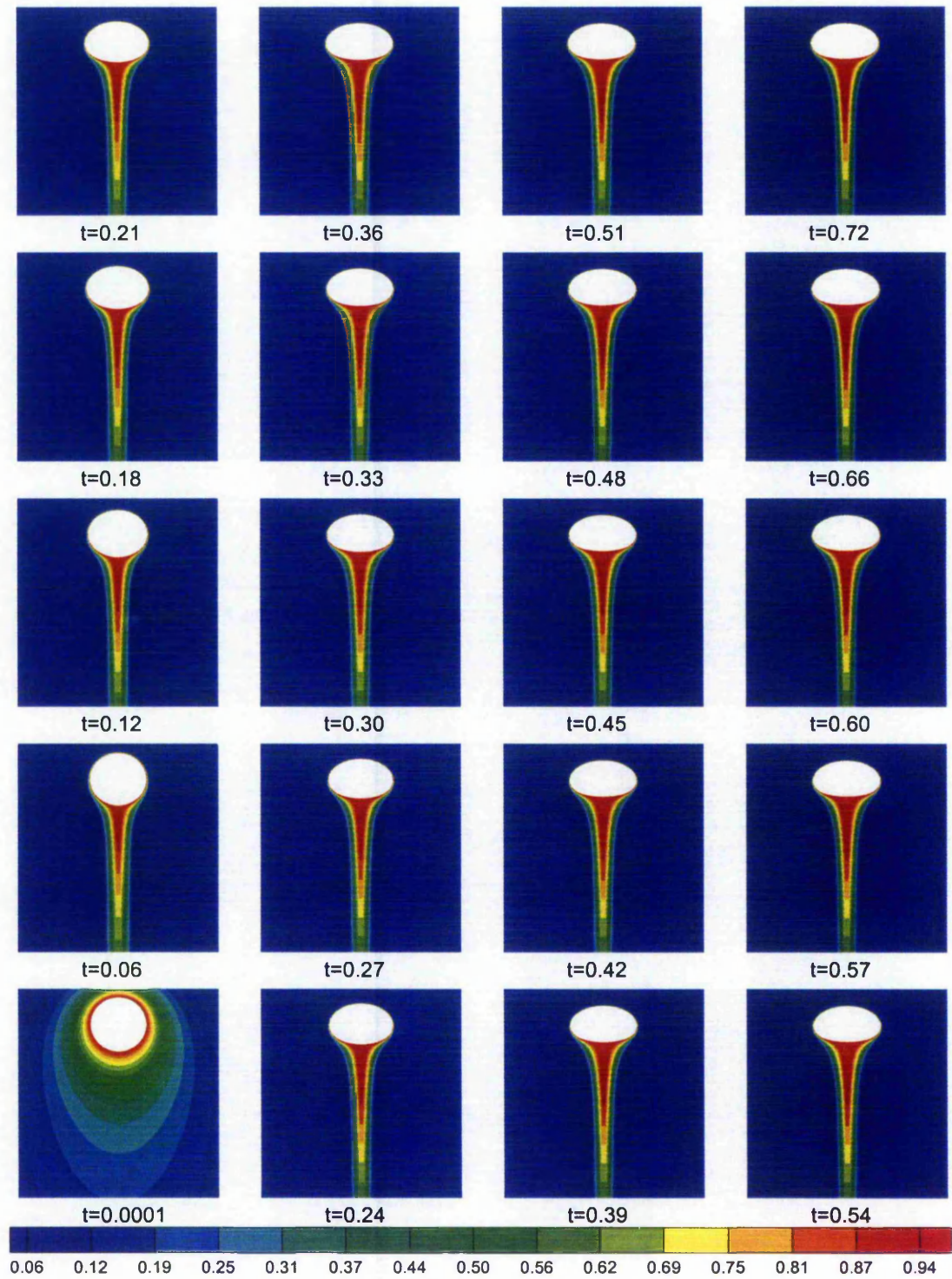


Figure 7.4b Development of concentration field, $Re^{(2)} = 10$, $We = 5$

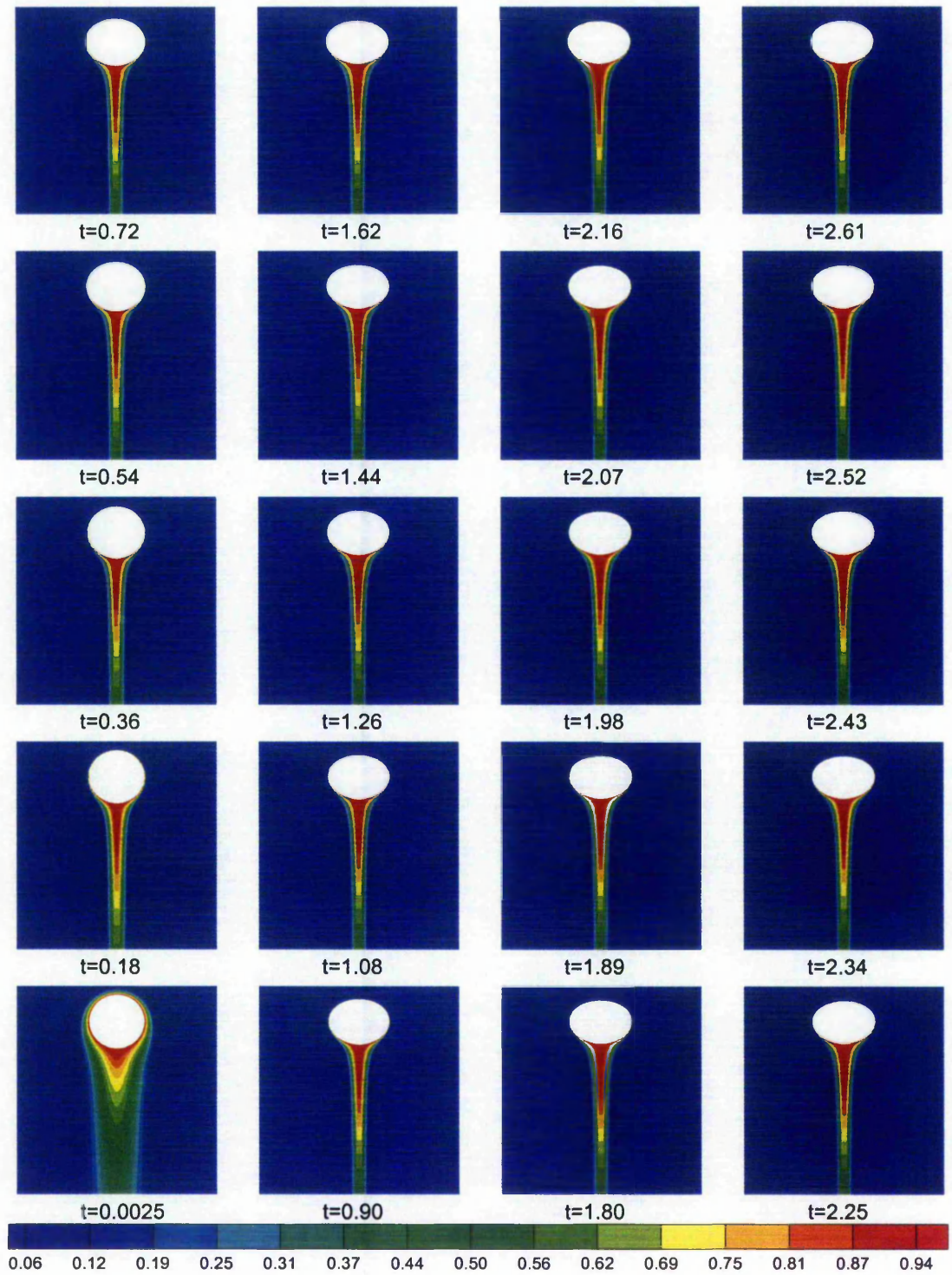


Figure 7.4c Development of concentration field, $Re^{(2)} = 50$, $We = 3$

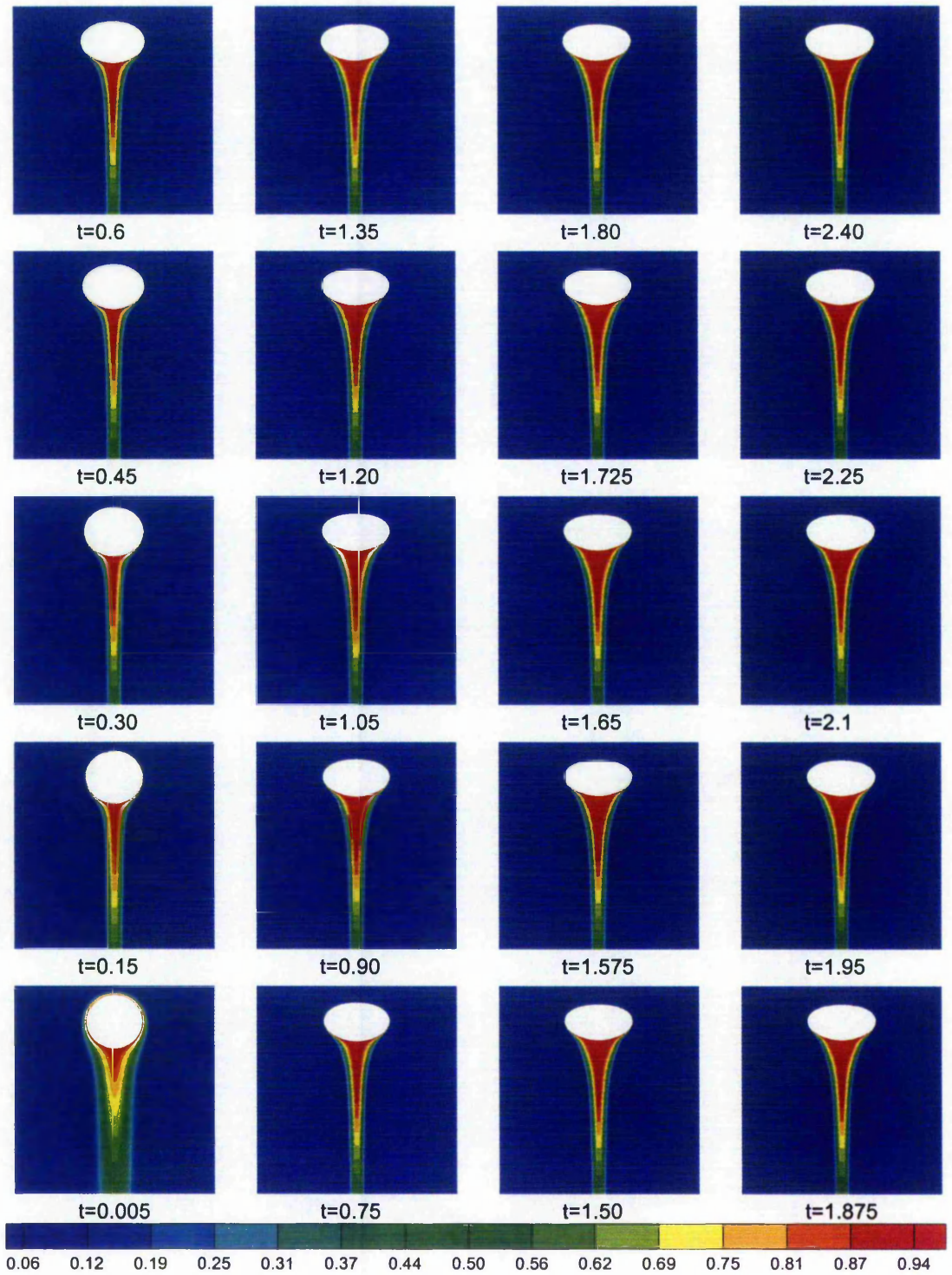


Figure 7.4d Development of concentration field, $Re^{(2)} = 50$, $We = 5$

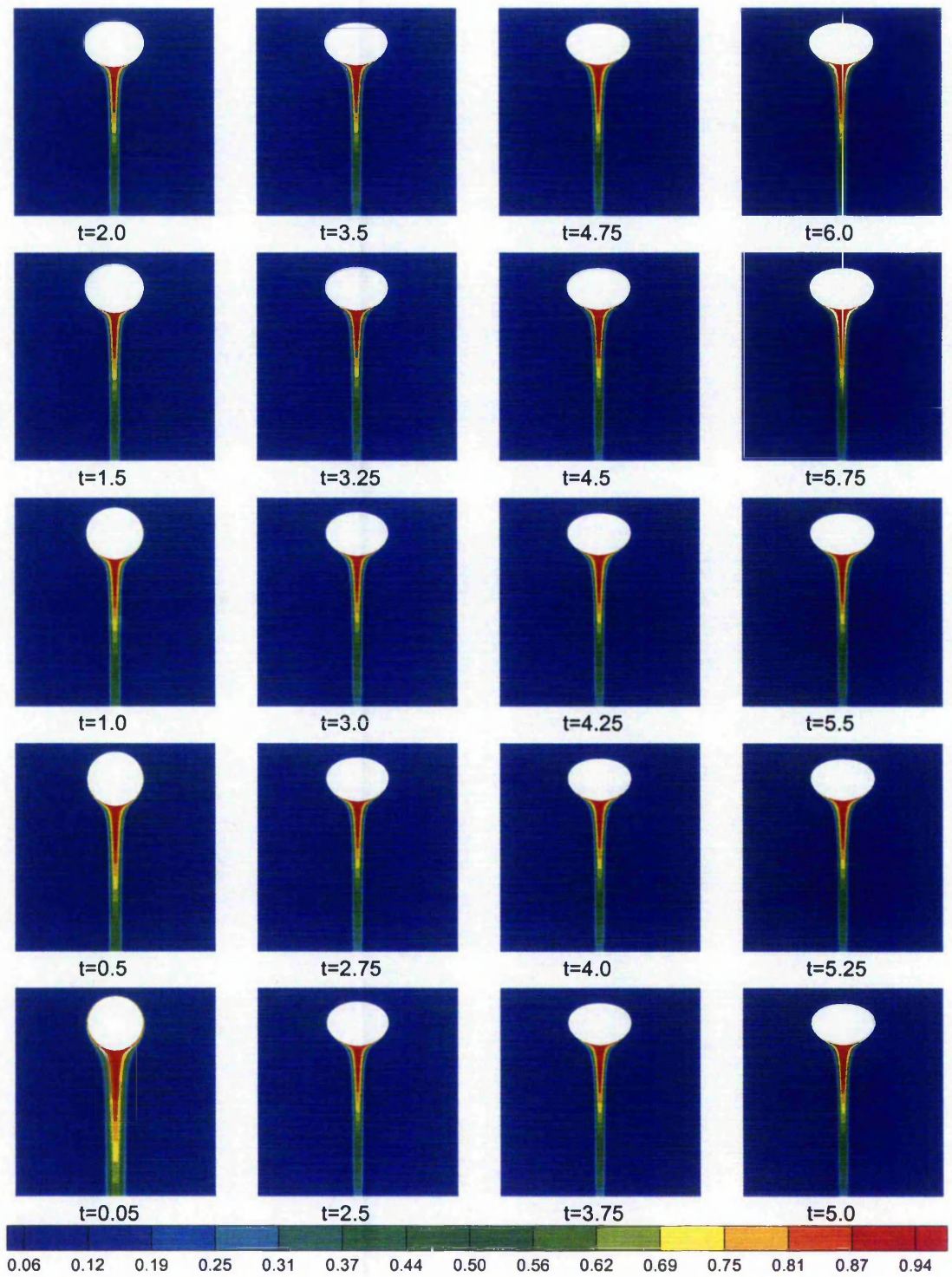


Figure 7.4e Development of concentration field, $Re^{(2)} = 200$, $We = 3$

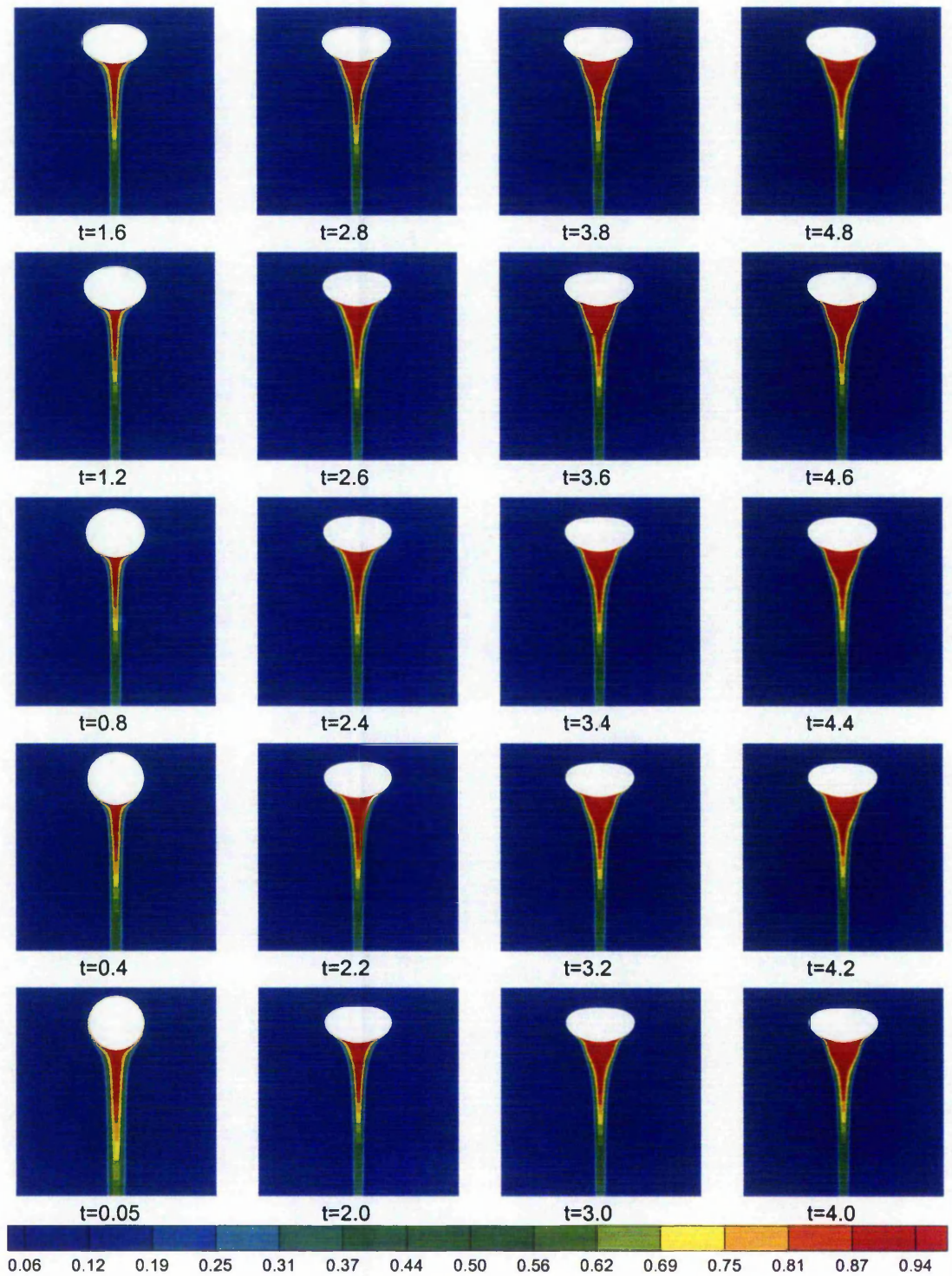


Figure 7.4f Development of concentration field, $Re^{(2)} = 200$, $We = 5$

As already shown in figure 7.1, the time scale for a rising bubble to arrive at its terminal state is dependent on the exterior Reynolds number. At a higher Reynolds number, the dimensionless time for the bubble to reach its terminal state is longer. Again, the oscillation of bubble profile is not found in figure 7.2 because the deformation is moderate and the separation is weak.

7.4.3 Heat and Mass Transfer

Figures 7.3 and 7.4 show the time-dependent development of dimensionless temperature and concentration fields. In these figures, the propagation of the temperature and concentration, which is seen closely related to the deformation of bubbles, happens at the early stage of bubble rising, when deformation quickly occurs. And again, the thermal field has stronger diffusion while the concentration is more dominantly controlled by convection. This can be clearly observed at the very beginning of bubble-rise, where the contours of temperature are almost fore-aft symmetric while the concentration fields are obviously asymmetric. In the meanwhile, the concentration wake zone behind the bubble is narrow and long while that of temperature is wide and short. These phenomena are similar to those of steady state discussed in chapter 6.

The time-dependent histories of averaged Nusselt and Sherwood numbers, defined as:

$$Nu_{av} = \frac{\int_0^{180^\circ} Nu \cdot r \cdot \sqrt{x_\xi^2 + y_\xi^2} \cdot d\xi}{\int_0^{180^\circ} r \cdot \sqrt{x_\xi^2 + y_\xi^2} \cdot d\xi}, \quad Sh_{av} = \frac{\int_0^{180^\circ} Sh \cdot r \cdot \sqrt{x_\xi^2 + y_\xi^2} \cdot d\xi}{\int_0^{180^\circ} r \cdot \sqrt{x_\xi^2 + y_\xi^2} \cdot d\xi}, \quad (7.16)$$

are shown in figures 7.5 and 7.6. These parameters have a same story with the time-dependent rising velocity, that is, the parameters increase quickly at the early stage of bubble acceleration while the increase for late stage is very slow. This agrees well with the observation of the time-dependent propagation of dimensionless temperature and

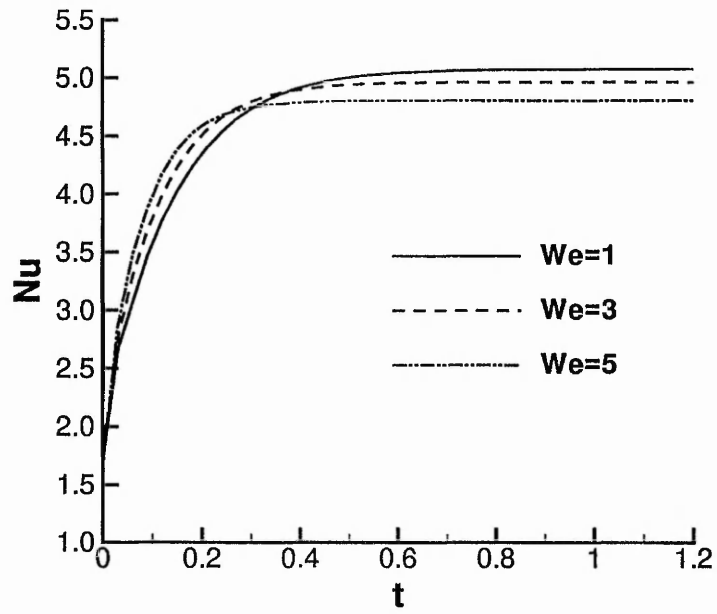


Figure 7.5a Time history of averaged Nusselt number at $Re^{(2)} = 10$

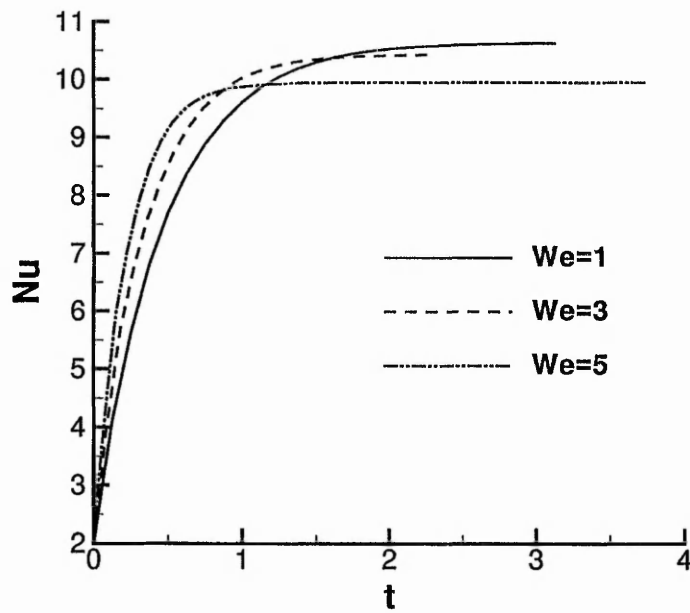


Figure 7.5b Time history of averaged Nusselt number at $Re^{(2)} = 50$

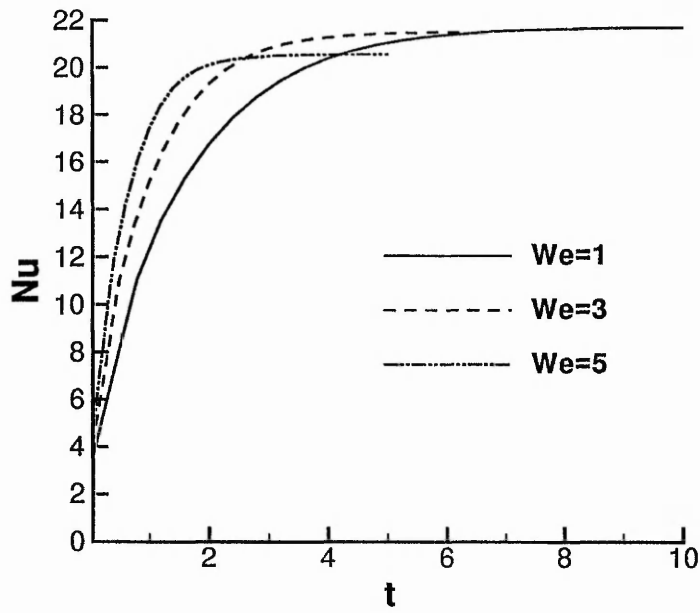


Figure 7.5c Time history of averaged Nusselt number at $Re^{(2)} = 200$

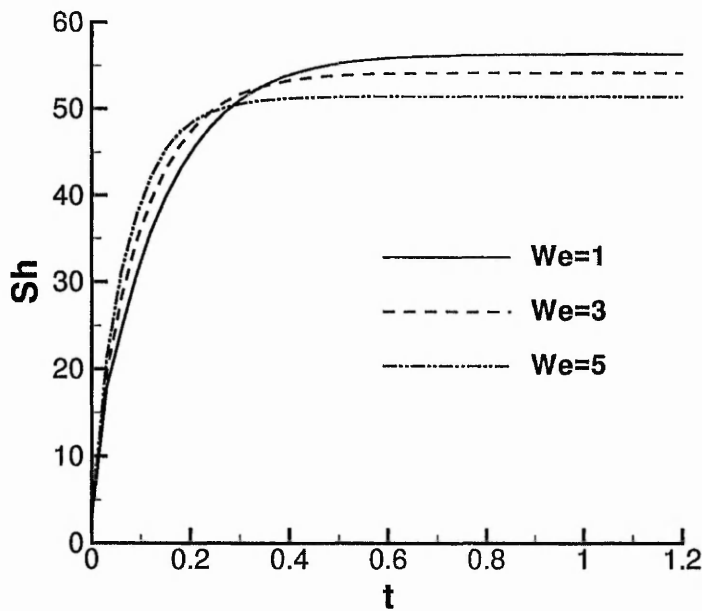


Figure 7.6a Time history of averaged Sherwood number at $Re^{(2)} = 10$

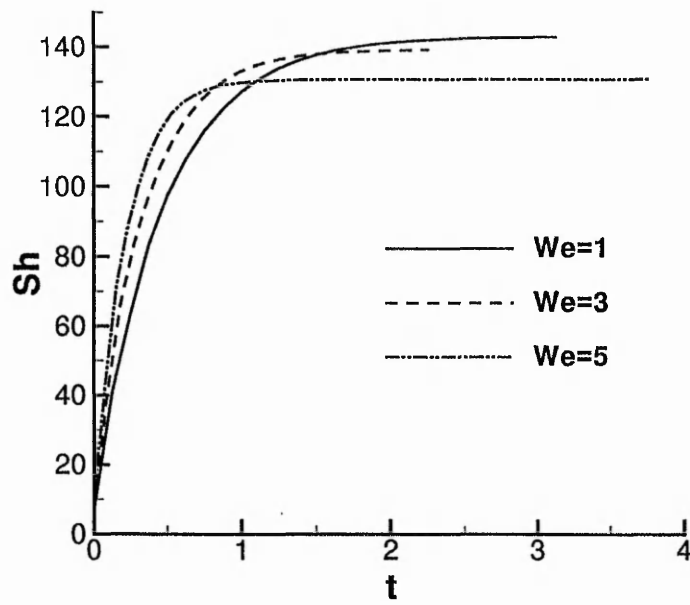


Figure 7.6b Time history of averaged Sherwood number at $Re^{(2)} = 50$

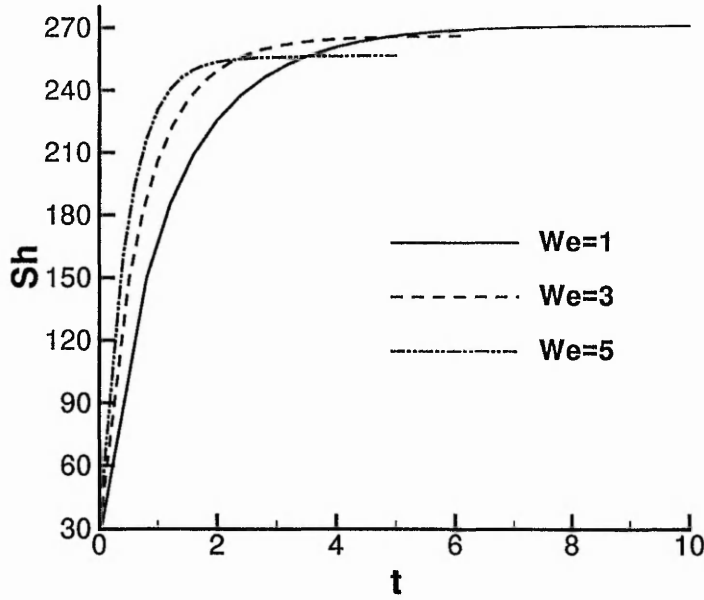


Figure 7.6c Time history of averaged Sherwood number at $Re^{(2)} = 200$

concentration. It should be noted that even at the instant when the bubble is introduced in the hot liquid, the averaged Nusselt and Sherwood numbers are not zero because of the diffusion effects.

7.5 Summary of Chapter

Time-accurate simulations of an inert bubble introduced into a hot liquid are presented. The numerical method for steady gas-liquid interfacial flows is supplemented and developed to do time-accurate simulations. Independent equations for bubble rising velocity and acceleration are derived and a full analytical model is presented. The conclusions of this chapter can be summarised as follows:

- (a). The rising velocity and acceleration of bubble-rise can be achieved by analysing the forces acting on the bubble; A full analytical model is presented in this chapter;
- (b). Time-dependent simulations are extremely time-consuming, they are not simply a series of steady calculations but a multi-level iteration procedure;
- (c). The rising velocity, bubble deformation and development of temperature and concentration fields share a same time history: fast change at the early stage of acceleration and slowing down later;
- (d). Temperature field has stronger diffusion while mass transfer is more dominantly controlled by convection. Because of diffusion, the Nusselt and Sherwood numbers are not zero even at the instant when the bubble is introduced into the hot liquid;
- (e). The onset of separation occurs at the nearly end of the acceleration stage. It proves that flow separation is a result of vorticity accumulation.

Chapter 8

Conclusions and Recommendations for Further Work

With the financial support provided by the British Engineering and Physical Sciences Research Council (EPSRC), numerical simulations of an inert bubble introduced into a hot liquid are carried out to study the mechanisms of heat and mass transfer at a gas-liquid interface in two-phase bubbly flows. As the research is entirely numerical and theoretical, three main parts of the work are included as: (1) modelling of physical phenomena, (2) development of numerical algorithm and (3) numerical simulations and analyses. Attentions have been paid to the details of heat and fluid flows at the gas-liquid interface of the inert bubble.

The study begins with a physical and mathematical modelling of the phenomena; the physical and mathematical models are established and presented in chapter 3. The inert bubble introduced into a hot liquid is physically modelled as an “unsteady conjugate heat and fluid flows inside and around a deformable gas-liquid interface”; basic governing equations and well-posed solution-determining conditions are given. In order to solve the mathematical model, the unsteady bubble deformation is treated as a moving boundary problem; and a numerical procedure with multi-block iteration and a moving mesh arrangement is proposed and presented in chapter 4. Especially, this procedure employs high order numerical schemes so as to highlight the flow phenomena at the moving boundary. Further to this procedure, chapter 5 introduces gas-liquid interface treatments to challenge the determinations of bubble profile and interfacial velocity by the complex dynamic boundary conditions. The algorithm presented in chapters 4 and 5 are validated. Moreover, the calculation of gas-liquid interfacial flows in chapter 5 gives a range for obtaining physical solutions for numerical simulation of bubbles. With all these preparation, detailed numerical studies

on the dynamics of the inert bubble introduced into the hot liquid are carried out. These studies are on the bubble shape, flow structure, drag force, rising velocity, interfacial characteristics and heat and mass transfer; the results are presented in chapters 6 and 7, for steady and unsteady states respectively. For the convenience of description, the conclusions are summarised according to the three parts of the research work.

8.1 Physical and Mathematical Modelling

In order to study the transfer phenomena and relevant mechanisms, both sides of a gas-liquid interface must be considered although the density and viscosity of the gas are smaller in magnitude order than those of the liquid. When both sides are considered, the heat and fluid flows are conjugate rather than those of “free surface problem” in “external flow model” of bubbles. Because the bubble-rise has an accelerating procedure, it is therefore physically modelled as “unsteady conjugate heat and fluid flows inside and around a deformable gas-liquid interface”.

Full Navier-Stokes equations and well-posed solution-determining conditions are employed as the mathematical description of the physical problem. Especially, kinetic and dynamic conditions are posed on the moving gas-liquid interfacial boundary. The mathematical model, in a dimensionless form, is presented in a non-inertial coordinates system for the convenience of studying the flows and transfer phenomena at the interface.

8.2 Development of Numerical Algorithm and CFD codes

8.2.1 Finite Volume Method (FVM) with High Order Schemes

It is a basic requirement to obtain high-resolution numerical results for studying the

mechanism of transfer phenomena. The SIMPLE method for incompressible heat and fluid flows is employed to develop a basic flow solver. In order to improve the numerical accuracy and resolution of results, high order total variation diminishing (TVD) schemes in finite volume integrating form are introduced and employed for discretisation of basic equations.

8.2.2 Multi-Block Iteration and Moving Mesh Arrangement

A numerical procedure with multi-block iteration is incorporated with a moving mesh arrangement to calculate heat and fluid flows in complex geometries separated by a time-dependent gas-liquid interface. The key issues of the multi-block iteration are the zonal boundary treatments; these include the uniqueness of the zonal boundary guaranteed by a spline-fitting and a zonal boundary interpolation method proposed by the present study. The moving mesh arrangement is employed to track the gas-liquid interface; and the spatial conservation law is applied to damp the discretisation error for moving mesh arrangement.

The reliability, good accuracy and robustness of this numerical procedure for studying complex heat and fluid flows in complex geometries with time-dependent moving boundaries are well examined and validated.

8.2.3 Gas-Liquid Interfacial Treatments

The numerical method for moving boundary problems is supplemented with gas-liquid interfacial treatments. These treatments include a “continuous stress method” for obtaining the explicit interfacial velocity which is implicitly given by the continuity of tangential stress; and a modified Ryskin-Leal method for determining the bubble shape by the balance of normal forces. Based on a comparison with the traditional “external flow model”, widely used by researchers for studying single bubbles, the “conjugate flow model” and the relevant interfacial treatments proposed in this paper and their

importance on revealing the mechanism of transfer phenomena are highlighted.

8.2.4 Supplementation for Time-Accurate Simulation

Based on the analysis of forces acting on the gas-liquid interface, independent controlling equations are derived to obtain the velocity and acceleration of the rising bubble. These equations are supplemented to the numerical procedure to carry out time-accurate simulation of an inert bubble introduced into hot liquid.

8.3 Numerical Simulations and Results

With the numerical methods and the CFD codes developed in this study, investigations on the heat and fluid flows and relevant transfer mechanisms in an inert bubble introduced into a hot liquid are carefully studied. Contributions of this thesis include:

- (a). A detailed study on the dynamics of spherical bubbles;
- (b). Results and analysis's on the dynamics of deformable bubbles at steady state. These detailed results are on bubble shape, flow structure, drag coefficient, interfacial characteristics, and heat and mass transfer phenomena.
- (c). Understanding of unsteady behaviours of an inert bubble introduced into a hot liquid based on time-accurate simulations. The behaviours include the time-dependent rising velocity, evolution of bubble shape and flow structure, development of thermal and concentration fields and time history of Nusselt and Sherwood numbers.

8.3.1 Dynamics of Single Spherical Bubbles

The interfacial characteristics and flow structures of a single spherical bubble rising in an unbounded quiescent liquid are studied and compared with those of falling spherical droplets. In nearly the whole range of exterior Reynolds number for a single bubble

possibly to remain a spherical shape, namely, in the range of $10 \leq \text{Re}^{(2)} \leq 550$, flow separation behind a spherical bubble doesn't take place while the interfacial vortices are found to have the same strength level although density and viscosity on both sides are different in magnitude order. The rotational flow results show that the one-side (liquid side) calculating method ("external flow model") of single bubbles and the corresponding treatments of "free surface" or "inviscid bubble" may not be proper, the conjugate flow model and the treatments are more practical and reasonable.

8.3.2 Dynamics of Single Deformable Bubbles

Calculations of deformable bubbles are carried out based on validation by available experimental results, which shows the range of Weber numbers for obtaining physical solutions must be $We < 7.7$ so that axisymmetric assumption is valid. Therefore, only the moderately deformed bubbles in the ranges of $(\text{Re}^{(2)}, We) = [0, 200] \times [0, 6]$ are numerically studied. The conclusions for these results and analysis's are:

- (a). In the ranges of $(\text{Re}^{(2)}, We) = [0, 200] \times [0, 6]$, $\text{Re}^{(2)} = 50$ is the border of two types of deformation of a bubble: stronger in the rear at $\text{Re}^{(2)} \leq 50$ and stronger in the front at $\text{Re}^{(2)} \geq 50$;
- (b). For a single air bubble rising in unbounded water, at room temperature and atmospheric pressure, flow separation from the bubble body has been observed to onset at $4 < We < 5$ for $\text{Re}^{(2)} = 50$, at $4 < We < 5$ for $\text{Re}^{(2)} = 100$, and at $3 < We < 4$ for $\text{Re}^{(2)} = 200$. In all these cases, the flow structure is a typical solid vortex type with a pair of counter-rotating ring vortices inside and a single separation ring vortex outside the bubble;
- (c). The conventional external flow model of the bubble, which treats the gas-liquid interface as a "free boundary" (a slip boundary free of tangential stress), can over predict the viscous effect where the flow separation has occurred, and under predict the viscous effect at $\text{Re}^{(2)} \leq 5$;

- (d). The minimum thickness of the thermal or concentration layer doesn't occur at the same position where the strongest shear flow occurs, this shows a non-linear relationship between the flow, thermal and concentration fields.
- (e). A recovery of Sherwood and Nusselt numbers in the separation zone is observed; this recovery can be physically explained by the flow structure and heat and mass transfer in the separated wake vortex.

8.3.3 Unsteady Behaviour of Inert Bubble Introduced into Hot Liquid

Time-accurate simulations of an inert bubble introduced into a hot liquid are carried out with the numerical method for gas-liquid interfacial flows, supplemented by independent equations for bubble rising velocity and acceleration. The conclusions of this study are summarised as follows:

- (a). The rising velocity and acceleration of bubble-rise can be achieved by analysing the forces acting on the bubble; a full analytical model is developed;
- (b). Time-dependent simulations are not simply a series of steady calculations but an extremely time-consuming multi-level iteration procedure;
- (c). The rising velocity, bubble deformation and the development of temperature and concentration fields share a same time-history: fast change at the early stage of acceleration and slowing down later;
- (d). Temperature field has stronger diffusion while mass transfer is more dominantly controlled by convection. Because of diffusion, the Nusselt and Sherwood numbers are not zero even at the instant when the bubble is introduced into the hot liquid;
- (e). The onset of separation occurs at the nearly end of the acceleration stage, therefore, flow separation is a result of vorticity accumulation.

8.4 Recommendations for Further Work

A famous CFD scientist has ever commented that excellent results could be obtained for

CFD studies based on good understanding of physical problems by researchers. Applying this saying to the current entirely numerical and theoretical study, good understanding of bubble physics is the most important point.

Firstly, my study has tried the best to obtain support from available experiments. Because of the expenses, experimental studies are relatively rare in literatures, as reviewed in the beginning of the present paper. For study the mechanism of interfacial transfer phenomena so far, our current numerical study seems in an outstripped position than experimental investigations. As a further work, detailed and careful experimental study on the heat and flow fields is the first choice to investigate the interfacial transfer phenomena and relevant mechanisms.

In the second, we still have a lot of works need to be done even for numerical simulations. For example, the current study is only on moderately deformed bubbles. In order to study the mechanism of interfacial transfer phenomena, bubbles at higher exterior Reynolds and Weber numbers should be studied as we found the wake vortex has special effects on heat and mass transfer in chapter 6. At a higher Reynolds number, the vortex shedding and local flow mixing may have important effects on heat and mass transfer and should be an important work needs to be done.

Meanwhile, numerical methods developed in the present study are not perfect for study more complex problem. For time-accurate simulations, the current method has high-order spatial accuracy; but the temporal accuracy is only first-order. How to improve the temporal accuracy of the numerical method could be a further work.

References

- ARMALY, B. F., DURST, F., PEREIRA, J. C. F. and SCHONUNG, B.** 1983 Experimental and Theoretical Investigation of Backward-Facing Step Flow, *Journal of Fluid Mechanics*, Vol.127, PP.473-496.
- ASHGRIZ, N. and POO, J.Y.** 1991 FLAIR: Flux Line-Segment Model for Advection and Interface Reconstruction, *Journal of Computational Physics*, Vol.93, PP.449.
- BARKHUDAROV, M.R. and CHIN, S.B.** 1994 Stability of a Numerical Algorithm for Gas Bubble Modelling, *International Journal for Numerical Methods in Fluids*, Vol.19, PP.415-437.
- BEAM, R. M. and WARMING, R. F.** 1976 An Implicit Finite Difference Algorithm for Hyperbolic Systems in Conservation Law, *Journal of Computational Physics*, Vol.22, PP.87-100.
- BENEK, J. A., BUNING, P. G. and STEGER, J. L.** 1985 A 3-D Chimera Grid Embedding Technique, AIAA Paper No. 85-1523.
- BESSLER, W. F. and LITTMAN, H.** 1987 Experimental Studies of Wake Behind Circularly Capped Bubbles, *Journal of Fluid Mechanics*, Vol.185, PP.137-151.
- BHAGA, D. and WEBER, M. E.** 1981 Bubbles in Viscous Liquids: Shapes, Wakes and Velocities, *Journal of Fluid Mechanics*, Vol.105, PP. 61-85.
- BIRD, G.A.** 1995 *Molecular Gas Dynamics and the Direct Simulation on Gas Flows*, Clarendon Press, Oxford.
- BORIS, J. P. and BOOK, D. L.** 1973 Flux Corrected Transport: I. SHATA, a Fluid Transport Algorithm That Works, *Journal of Computational Physics*, Vol.16, PP.85.
- BRACKBILL, J.U., KOTHE, D.B. and ZEMACH, C.** 1992 A Continuum Method for Modelling Surface Tension," *Journal of Computational Physics*, Vol.100, PP.335-354.

- BUGG, J.D., MACK, K. and REZKALLAH, K.S.** 1998 A Numerical Model of Taylor Bubbles Rising Through Stagnant Liquid in Vertical Tubes, *International Journal of Multiphase Flow*, Vol.24, No.2, PP.271-281.
- BUNNER, B. and TRYGGVASON, G.** 1998 Direct Numerical Simulation of Large Three-Dimensional Bubble Systems, ASME paper, FEDSM98-5214.
- BUSH, R. H.** 1985 External Compression Inlet Predictions Using an Implicit Upwind, Multiple Zone Approach, AIAA Paper No. 85-1521.
- BUYEVICH, Y. A.** 1975 Model of bubbles Rising in a Fluidised Bed, *Int J Multiphase Flow*, Vol. 2, No. 3, PP. 337-351.
- CAO, J. and CHRISTENSEN, R. N.** 2000 Analysis of moving boundary problem for bubble collapse in binary solutions, *Numerical Heat Transfer, Part A*, Vol. 38, PP. 681-699.
- CHAKRAVARVARTHY, S. R. and OSHER, S.** 1983 High Resolution Applications of OSHER Upwind Scheme for Euler Equations, AIAA Paper 83-1943.
- CHAO, B. T.** 1962 Motion of Spherical Gas Bubbles in a Viscous Liquid at Large Reynolds Numbers, *Physics of Fluids*, Vol.5, PP. 69-79.
- CHEN, R. C., and CHOW, I. S.** 1998 Wake Structure of a Single Bubble Rising in a Two-Dimensional Column, *Experimental Thermal and Fluid Science*, Vol.17, PP.165-178.
- CHEN, L., GARIMELLA, S. V., REIZES, J. A. and LEONARDI, E.** 1996 Analysis of Bubble Rise Using the VOF Method, Part 1: Isolated Bubbles, ASME National Heat Transfer Conference, HTD-Vol.326, PP.161-173.
- CHEN, R. C., WANG, F. M. and LIN, T. J.** 1999 Bubble Wake Dynamics of a Single Bubble Rising in the Freeboard of a Two-Dimensional Liquid-Solid Fluidised Bed, *Chemical Engineering Science*, Vol.54, PP.4831-4838.
- CLIFT, R., GRACE, J. R. and WEBER, M. E.** 1978, *Bubbles, Drops and Particles*, Academic Press, New York- San Francisco- London.
- DALY, B. J.** 1969 Numerical Study of the Effect of Surface Tension on Interface Instability. *Phys. Fluids*, Vol.12, PP.1340.

DANDY, D. and LEAL, L.G. 1989 Buoyancy-Driven Motion of a Deformable Drop Through a Quiescent Liquid at Intermediate Reynolds Numbers, *Journal of Fluid Mechanics*, Vol. 208, PP. 161-192.

DATE, A. W. 1986 Numerical Prediction of Natural Convection Heat Transfer in Horizontal Annulus, *International Journal of Heat and Mass Transfer*, Vol.29, No.10, PP.1457-1464.

DeGREGORIA, A. J. and SCHWARTZ, L. W. 1986 A Finger Break-up in Hele-Shaw cells, *Journal of Fluid Mechanics*, Vol. 164, pp. 384-400.

DEMIRDZIC, I. and PERIC, M. 1988 Space Conservation Law in Finite Volume Calculations of Fluid Flow, *International Journal for Numerical Methods in Fluids*, Vol.8, PP.1037-1050.

DEMIRDZIC, I., LILEK, Z. and PERIC, M. 1992 Fluid Flow and Heat Transfer Test Problems for Non-Orthogonal Grids: Benchmark Solutions, *International Journal for Numerical Methods in Fluids*, Vol. 15, PP. 329-354.

DUINEVELD, P. C. 1995 The Rise Velocity and Shape of Bubbles in Pure Water at High Reynolds Number, *Journal of Fluid Mechanics*, Vol.292, PP.325-332.

ERVIN, E. A. and TRYGGVASON, G. 1997 The Rise of Bubbles in a Vertical Shear Flow, *ASME Journal of Fluids Engineering*, Vol.119, No.2, PP.443-449.

FAN, S. and TSUCHIYA, K. 1990, Bubble Wake Dynamics in Liquids and Liquid-Solid Suspensions, Butterworth-Heinemann.

FREITAS, C. J. 1995 Perspective: Selected Benchmarks From Commercial CFD Codes, *ASME Journal of Fluids Engineering*, Vol.117, PP. 208-218.

FUJITA, Y. and BAI, Q. 1998 Numerical Simulation of the Growth for an Isolated Bubble in Nucleate Boiling, *Proceedings of the 11th IHTC*, Vol.2, August 23-28, 1998, Kyongju, Korea.

FURUKAWA, M., YAMSAKI, M. and INOUSE, M. 1991 A Zonal Approach for Navier-Stokes Computations of Compressible Cascade Flow Fields Using TVD Finite Volume Method, *ASME Journal of Turbomachinery*, Vol.113, PP.573-582.

GARRIOCH, S.H. and BALIGA, B.R. 1998 Interface Tracking Using a Multi-Dimensional Advection Techniques Based on Skewed Subadvections, ASME paper

FEDSM98-5207.

GASKELL, P. H. and **LAU, A. K. C.** 1988 Curvature-Compensated Convective Transport: SMART, a New Boundedness-Preserving Transport Algorithm, *International Journal of Numerical Methods in Fluids*, Vol.8, PP. 617-641.

GLIMM, J., GROVE, J., LINDQUIST, B., McBRYAN, O. A. and **TRYGGVASON, G.** 1988 The bifurcation of tracked scalar waves, *SIAM J Sci. Stat. Comput.*, Vol. 9 pp. 61-79.

GRACE, J. R. 1973 Shapes and Velocities of Bubbles Rising in Infinite Liquids, *Transaction of Institution of Chemical Engineers*, Vol.51, PP. 116-120.

GRAY, D. D. and **GIORGIN, A.** 1976 The Validity of the Boussinesq Approximation for Liquids and Gases, *International Journal of Heat and Mass Transfer*, Vol.19, PP. 545-551.

GUO, Z., WANG, Z. and **CHEN, M.** 2000 Molecular Dynamics Study on Interface Properties and Interphase Transport, *Heat Transfer Sciences and Technology 2000*, Beijing: Higher Education Press, ISBN 7-04-008955-6, PP.70-89.

HABERMAN, W. L. and **MORTON, R. K.** 1953 An Experimental Investigation of Drag and Shape of Air Bubble Rising in Various Liquids, *The David W. Taylor Model Basin*, Washington D. C., Report 802, NS 715-102, pp.55.

HARBERMAN, W. L. and **MORTON, R. K.** 1954 An Experimental Study of Bubbles Moving in Liquids, *Transactions of the American Society of Civil Engineeris*, Vol. 121, PP.227-252.

HACKER, D. S. and **HUSSEIN, F. D.** 1978 The Application of a Laser-Schlieren Techique to the Study of Single Bubble Dynamics, *Ind. Eng. Chem. Fundam.*, Vol.17, No.4, PP.277-283.

HADAMARD, J. 1911, Mouvement Permanent Lent d'une Sphere Liquide et Visqueuse Dans un Liquide Visqueux, *Compt. Rend.*, Vol.152, No.25, PP.1735-1738.

HARTEN, A. 1983 High Resolution Schemes for Hyperbolic Conservation Laws, *Journal of Computational Physics*, Vol.49, PP.357-393.

HARLOW, F.H. and **WELCH, J.E.** 1965 Numerical Calculation of Time-Dependent Viscous Incompressible Flow of Fluid with Free Surface, *Physics of Fluids*,

Vol.8, PP.2182-2189.

HARTUNIAN, R. A. and SEAR, W. R. 1957 On the Instability of Small Bubbles Moving Uniformly in Various Liquids, *Journal of Fluid Mechanics*, Vol.3, PP.27-47.

HARVIE, D.J.E. and FLETCHER, D.F. 2000 A New Volume of Fluid Advection Algorithm: The Stream Scheme, *Journal of Computational Physics*, Vol.162, PP.1-32.

HASSAN, Y. A., ORTIZ-VILLAFUERTE J. and SCHMIDL, W. D. 1999 Measurements of a Rising Single Bubble in Stagnant Liquid, *Journal of Flow Visualisation and Image Processing*, Vol.6, PP.129-137.

HIRT, C.W., AMSDEN, A.A. and COOK, J.L. 1974 An Arbitrary Lagrangian-Eulerian Computing Method for All Flow Speeds, *Journal of Computational Physics*, Vol.14, PP.227-253.

HIRT, C.W. and NICHOLS, B. D. 1981 Volume of Fluid (VOF) Method for the Dynamics of Free Boundaries, *Journal of Computational Physics*, Vol.39, PP.201-225.

HNAT, J. G. and BUCKMASTER, J. D. 1976 Spherical Cap Bubbles and Skirt Formation, *Physics of Fluids*, Vol.19, PP.182-194.

IDA, T. and SUGIYA, T. 1980 Motion of air bubbles in Mineral Oils Subject to Sudden Change in Chamber Pressure- 1. Experimental Analysis of Single Spherical Bubbles, *Bulletin of the JSME*, Vol. 23, No. 181, PP. 1132-1139.

JAMESON, A. and MAVRILIS, D. 1985 Finite Volume Solution of the Two Dimensional Euler Equation on a Regular Triangular Mesh, AIAA Paper 85-0435.

JAMESON, A., SCHMIDT, W. and TURKEL, E. 1981 Numerical Simulation of the Euler Equations by Finite Volume Methods Using Runge-Kutta Time-Stepping Schemes, AIAA Paper 81-1259.

JEZDINSKY, V. and NAUDASCHER, E. 1972 Effect of Entrained Gas on Pressure Fluctuations in Separated Liquid Flow, *Institut fur Hydromechanik der Universitat Karlsruhe*, Germany, Bericht Nr. 510, PP.116.

JUNCU, G. 1999 A Numerical Study of Steady Viscous Flow Past a Fluid

Sphere, *International Journal of Heat and Fluid Flow*, Vol. 20, pp.414-421.

KAMATH, V. and PROSPERETTI, A. 1989 Numerical Investigation Methods in Gas-Bubble Dynamics, *Journal of Acoust. Soc. Am.*, Vol.85, PP.1538.

KARKI, K. C. and PATANKAR, S. V. 1988 Solution of Some Two-Dimensional Incompressible Flow Problems Using a Curvilinear Coordinate System Based Calculation Procedure, *Numerical Heat Transfer, part B*, Vol.14, PP.309-321.

KHOSLA, P. K. and RUBIN, S. G. 1974 A Diagonal Dominant Second-Order Accurate Implicit Scheme, *Computers and Fluids*, Vol.2, PP.207-209.

KIM, J. and MOIN, P. 1985 Application of a Fractional-Step Method to Incompressible Navier-Stokes Equations, *Journal of Computational Physics*, Vol.59, PP.308-323.

KINJO, T., OHGUCHI, K., YASUOKA, K. and MATSUMOTO, M. 1999 Computer Simulation of Fluid Phase Change: Vapour Nucleation and Bubble Formation Dynamics, *Computational Materials Science*, Vol.14, PP.138-141.

KOMASAWA, I., OTAKE, T. and KAMOJIMA, M. 1980 Wake Behaviour and Its Effect on Interaction Between Spherical Cap Bubbles, *Journal of Chemical Engineering of Japan*, Vol.13, No.2, PP.103-109.

KRISHNA, R. and BATEN, J. M. 1999 Rise Characteristics of Gas Bubbles in a 2D Rectangular Column: VOF Simulations vs Experiments, *Int. Comm. Heat Mass Transfer*, Vol.26, No.7, PP.965-974.

KUEHN, T. H. and GOLDSTEIN, R. J. 1976 An Experimental and Theoretical Study of Natural Convection in the Annulus between Horizontal Concentric Cylinders, *Journal of Fluid Mechanics*, Vol.74, Part 4, PP.695-719.

LAFABURIE, B., NARDONE, C., SCARDOVELLI, R., ZALESKI, S. and ZANETTIN, G. 1994 Modelling Merging and Fragmentation in Multiphase Flows with SURFER, *Journal of Computational Physics*, Vol.113, pp.134.

LAX, P. D. and WENDROFF, B. 1960, Systems of Conservation Laws, *Communication of Pure Application Mathematics*, Vol.13, PP.217.

LAZAREK, G. M. and LITTMAN, H. 1974 The Pressure Field Due to a Large Circular Capped Air Bubble Rising in Water, *Journal of Fluid Mechanics*, Vol.66, PP.673-687.

LeCLAIR, B. P., HAMIELEC, A. E., PRUPPACHER, H. R. and HALL, W. D. 1972 A Theoretical and Experimental Study of the Internal Circulation in Water Drops Falling at Terminal Velocity in Air, *Journal of The Atmospheric Sciences*, Vol.29, pp.728- 740.

LEE, D. and CHIU, J. J. 1992 Covariant Velocity-Based Calculation Procedure with Non-Staggered Grids for Computation of Pulsatile Flows, *Numerical Heat Transfer, Part B*, Vol.21, PP.269-286.

LEE, R.C. and NYDAHL, J.E. 1989 Numerical Calculation of Bubble Growth in Nucleate Boiling from Inception through Departure, *ASME Journal of Heat Transfer*, Vol.111, PP74-479.

LEONARD, P. 1979 A Stable and Accurate Convective Modelling Procedure Based on Quadratic Upstream Interpolation, *Computer Methods in Applied Mechanics and Engineering*, Vol. 19, PP. 59-98.

LEONARD, B. P. 1988 Simple High-Accuracy Resolution Programme for Conservative Modelling of Continuities, *International Journal for Numerical Methods in Fluids*, Vol.8, PP.1291-1318.

LI, S. and PETZOLD, L. 1997 Moving Mesh Methods with Upwinding Schemes for Time-Dependent PDEs, *Journal of Computational Physics*, Vol.131, PP.368-377.

LI, W. Z. and YAN, Y. Y. 2002 An Alternating Dependent Variables (ADV) Method for Treating Slip Boundary Conditions of Free Surface Flows with Heat and Mass Transfer, *Numerical Heat Transfer B*, Vol. 41, No.2, PP. 165-189.

LI, W. Z. and YAN, Y. Y. 2002 A Direct-Predictor Method for Solving Steady Terminal Shape of A Gas Bubble Rising Through A Quiescent Liquid, *Numerical Heat Transfer B*, Vol. 42, No.1, PP.55-71.

LI, Y., ZHANG, J. and FAN, L. S. 2000 Discrete Phase Simulation of Single Bubble Rise Behaviour at Elevated Pressure in a Bubble Column, *Chemical Engineering Science*, Vol.55, PP.4597-4609.

LIU, J. and SPALDING, D.B. 1988 Numerical Simulation of Flows with Moving Interfaces, *PCH Physico-Chemical Hydrodynamics*, Vol.10, No.5/6, PP. 625-637.

LIU, J. and SHYY W. 1996 Assessment of Grid Interface Treatments for Multi-Block Incompressible Viscous Flow Computation, *Computers and Fluids*, Vol. 25, No.8, PP. 719-740.

LOTH, E., TAEIBI-RAHNI, M. and TRYGGVASON, G. 1997 Deformable Bubbles in a Free Shear Layer, *Int. J. Multiphase Flow*, Vol.23, No.5, PP. 977-1001.

LUEWISUTTICHAT, W., TSUTSUMI, A. and YOSHIDA, K. 1997 Chaotic Hydrodynamics of Continuous Single-Bubble Flow Systems, *Chemical Engineering Sciences*, Vol.52, No.21/22, PP.3685-3691.

MAGNAUDET, J., RIVERO, M. and FABRE, J. 1995. Accelerated Flows Past a Rigid Sphere or a Spherical Bubble. Part I: Steady Straining Flow, *Journal of Fluid Mechanics*, Vol.284. PP. 97-135.

MARONNIER, V., PICASSO, M. and RAPPAZ, J. 1999 Numerical Simulation of Free Surface Flows, *Journal of Computational Physics*, Vol.155, PP. 435-455.

MATSUMOTO, Y. 1986 Influence of Noncondensable Gas Bubble Motion, *Trans. Jpn. Soc. Mech. Eng.*, Vol.52, No.475, Series B, PP. 1168.

MATSUMOTO, Y. and TAKEMURA, F. 1992 Influence of Internal Phenomena on Gas Bubble Motion," 1st Report, *Trans. Jpn. Soc. Mech. Eng.*, Vol. 58, No.547, Series B, PP. 645.

MAVRIPLIS, D. and JAMESON, A. 1987 Multi-grid Solution of Two Dimensional Euler Equation on Unstructured Triangular Meshes, AIAA Paper 87-0353.

MAXWORTHY, T., GNANN, C., KURTEN, M. and DURST, F. 1996 Experiments on the Rise of Air Bubbles in Clean Viscous Liquids, *Journal of Fluid Mechanics*, Vol.321, PP. 412-441.

- McLAUGHLIN, J. B.** 1996 Numerical Simulation of Bubble Motion in Water, *Journal of Colloid and Interface Science*, Vol.184, PP. 614-625.
- MEI, R., KLAUSNER, J. F. and LAWRENCE, J.** 1994 A Note on the History Force on a Spherical Bubble at Finite Reynolds Number, *Physics of Fluids*, Vol. 6, No.1, PP. 418-420.
- MIGMATULIN, R. I, KHABEEV, N. S. and NAGIEV, F. B.** 1981 Dynamics, Heat and Mass Transfer of Vapour Gas Bubbles in Liquids, *International Journal of Heat and Mass Transfer*, Vol.24, No.6, PP. 1033-1044.
- MIKIC, B. B., ROHSENOW, W. M. and GRIFFITH, P.** 1970 On Bubble Growth Rate, *International Journal of Heat and Mass Transfer*, Vol. 13, PP.657-666.
- MIYAHARA, T. and TAKAHASHI, T.** 1985 Drag Coefficient of a Single Bubble Rising Through a Quiescent Liquid, *International Chemical Engineering*, Vol.25, No.1, PP.146-148.
- NAKAHASHI, K. and OBAYAYSHI, K.** 1987 FDM-FEM Zonal Approach for Viscous Flow Computations over Multiple-Bodies, AIAA Paper No.87-0604.
- NI, M., TAO, W. and WANG, S.** 1999 Stability Analysis for Discretised Steady Convective-Diffusion Equation, *Numerical Heat Transfer, Part B.*, Vol.35, PP. 369-388.
- NICHOLS, B.D. and HIRT, C.W.** 1975 Methods for Calculating Multidimensional, Transient Free Surface Flows Past Bodies. *Proc. of the First International Conf. On Num. Ship Hydrodynamics*, Gaithersburg, ML, Oct. 20-23.
- OSHER, S. and SETHIAN, J.A.** 1988 Fronts Propagating with Curvature Dependent Speed: Algorithm Based on Halmilton-Jacobi Formulations, *Journal of Computational Physics*, Vo.79, PP. 12-49.
- PATANKAR, S. V.** 1980, *Numerical Heat Transfer and Fluid Flow*, Hemisphere, Washington DC.
- PATANKAR, S. V. and SPALDING, D. B.** 1972 A Calculation Procedure for Heat, Mass and Momentum Transfer in Three-Dimensional Parabolic Flows, *Int. Heat and Mass Transfer*, Vol.115, PP.1787-1803.
- PEDLEY, T. J. and STEPHANOFF, K. D.** 1985 Flow Along a Channel with a

Time-Dependent Indentation in One Wall: The Generation of Vorticity Waves, *Journal of Fluid Mechanics*, Vol.160, PP. 337-367.

PERIC, M., KESSLER, R. and SCHEUERER, G. 1988 Comparison of Finite Volume Numerical Methods with Staggered and Collocated Grids, *Computers and Fluids*, Vol.16, PP. 389-403.

PLESSET, M. S. and ZWICK, S. A. 1954 The Growth of Vapour Bubbles in Superheated Liquids, *Journal of Applied Physics*, Vol.25, No.4, PP. 493-500.

PLESKO, C. and LEUTHERSSER, H. J. 1982 Dynamic Effects of Bubble Motion," *Chem. Eng. Commun.*, Vol.17, PP.195-218.

PINTO, Y. and DAVIS, 1971, *AIChE Journal*, Vol.17, PP. 1453.

PONOTH, S. S. and McLAUGHLIN, J. B. 2000 Numerical Simulation of Mass Transfer for Bubbles in Water, *Chemical Engineering Science*, Vol.55, PP.1237-1255.

PUCKETT, E.G., ALMGREN, A.S., BELL, J.B., MARCUS, D.L. and RIDER, W.J. 1997 A High-Order Projection Method for Tracking Fluid Interfaces in Variable Density Incompressible Flows, *Journal of Computational Physics*, Vol.130, PP. 269.

RAI, M. M. 1984 A Conservative Treatment of Zonal Boundaries for Euler Equation Calculations, AIAA Paper No. 84-0164.

RALPH, M. E. and PEDLEY, T. J. 1988 Flow in a Channel with a Moving Indentation, *Journal of Fluid Mechanics*, Vol.190, PP.87-112.

RAMASWAMY, B. 1990 Numerical Simulation of Unsteady Viscous Free Surface Flow, *Journal of Computational Physics*, Vol.90, PP. 396-430.

RASTOGI, A. K. 1984 Hydrodynamics in Tubes Perturbed by Curvilinear Obstructions, *ASME Journal of Fluids Engineering*, Vol.106, PP. 262-269.

RAYLEIGH, L. 1917 Pressure Due to Collapse of Bubbles," *Phil. Mag.*, Vol.34, PP. 94-98.

RAYMOND, F. and ROSSANT, J. M. 2000 A Numerical and Experimental Study of the Terminal Velocity and Shape of Bubbles in Viscous Liquids, *Chemical Engineering Science*, Vol.55, PP. 943-955.

- RHIE, C. M and CHOW, W. L.** 1983 Numerical Study of the Turbulent Flow Past an Airfoil with Trailing Edge Separation, *AIAA Journal*, Vol.21, No.11, PP. 1523-1532.
- RIDER, W.J. and KOTHE, D.B.** 1998, Reconstructing Volume Tracking, *Journal of Computational Physics*, Vol. 141, PP. 112.
- RIVKIND, V. Y. and RYSKIN, G. M.** 1976, Flow Structure in Motion of a spherical Drop in a Fluid Medium at Intermediate Reynolds Numbers, *Fluid Dynamics*, Vol. 11, PP. 5-12.
- ROSENFELD, M. and KWAK, D.** 1991 Time-Dependent Solutions of Viscous Incompressible Flows in Moving Coordinates, *International Journal for Numerical Methods in Fluids*, Vol.13, PP. 1311-1328.
- RUCKENSTEIN, E.** 1964 On Mass Transfer in the Continuous Phase from Spherical Bubbles or Drops, *Chem. Engng. Sci*, Vol.19, PP.131-146.
- RUCKENSTEIN, E. and DAVIS, E. J.** 1971 On the mechanism of drag reduction in turbulent flow of viscoelastic liquids, *Chem Eng Sci*, Vol.26, No.7, PP.1075-1079.
- RUDMAN, M.** 1997 Volume-Tracking Methods for Interfacial Flow Calculation, *International Journal for Numerical Methods in Fluids*, Vol.24, PP. 671-691.
- RYBZYNSKI, W.** 1911, Uber Die Fortschreitende Bewegung Einer Flussigen Kugel in Einem Zaben Medium, *Bull. Internat. Acad. Sci. Cracovia*, Ser A, No1A, PP. 40.
- RYSKIN, G. and LEAL, L.G.** 1984a Numerical Solution of Free-Boundary Problems in Fluid Mechanics. Part 1: The Finite-Difference Technique, *Journal of Fluid Mechanics*, Vol.148, PP.1-17.
- RYSKIN, G. and LEAL, L.G.** 1984b Numerical Solution of Free-Boundary Problems in Fluid Mechanics. Part 2: Buoyancy-Driven Motion of a Gas Bubble Through a Quiescent Liquid, *Journal of Fluid Mechanics*, Vol.148, PP. 19-35.

- RYSKIN, G.** and **LEAL, L.G.** 1984c Numerical Solution of Free-Boundary Problems in Fluid Mechanics. Part 3: Bubble Deformation in an Axisymmetric Straining Flow, *Journal of Fluid Mechanics*, Vol.148, PP.37-43.
- SAFFMAN, P. G.** 1956 On the Rise of Small Bubbles in Water, *Journal of Fluid Mechanics*, Vol.1, PP. 249-275.
- SALVADOR, Y.** 1994 Contribution to Numerical Simulation of Flow Around a Deformable Bubble, Ph.D. thesis, E.C.N.-Université de Nantes.
- SANKARANARAYANAN, K., SHAN, X., KEVREKIDIS, I.G.** and **SUNDARESAN, S.** 1999 Bubble Flow Simulation with the Lattice-Boltzmann Method, *Chemical Engineering Science*, Vol.54, PP. 4817-4823.
- SATO, T., JUNG, R.T.** and **ABE, S.** 2000 Direct Simulation of Droplet Flow with Mass Transfer at Interface, *ASME Journal of Fluids Engineering*, Vol.122, PP. 510-517.
- SCHMIDT, J., NASSAR, R.** and **LUBBERT, A.** 1992 Local Dispersion in the Liquid Phase of Gas-Liquid Reaction, *Chemical Engineering Science*, Vol.47, No.13/14, PP. 3363-3370.
- SHAH, V. L.** and **SHA, W. T.** 1978 Growth of a Sodium Vapour Bubble Rising in the Superheated Liquid, *Nuclear Engineering and Design*, Vol.45, PP. 81-91.
- SHIEH, C. F.** 1984 Three-Dimensional Grid Generation Using Elliptic Equation with Direct Grid Distribution Control, *AIAA Journal*, Vol. 22, PP. 361-364.
- SHYY, W., UDAYKUMAR, H. S., RAO, M. M.** and **SMITH, R. W.** 1996 *Computational Fluid Dynamics with Moving Boundaries*, Taylor & Francis.
- SMITH, J.M.** 1998 Impeller Performance in Boiling Agitated Reactors, EPSRC Final Report on GR/J 45640.
- SON, G.** 2001 A Numerical Method for Bubble Motion with Phase Change, *Numerical Heat Transfer, Part B*, Vol. 39, PP. 509-523.
- SON, G., DHIR, V. K.** and **RAMANUJAPU, N.** 1999 Dynamics and Heat Transfer Associated with a Single Bubble During Nucleate Boiling on a Horizontal Surface, *ASME Journal of Heat Transfer*, Vol.121, No.3, PP. 623-631.

- SOO, S. L. 1967 *Fluid Dynamics of Multiphase Systems*, Blaisdell Publishing, Waltham.
- SOU, A., TOMIYAMA, A., ZUN, I. and YABUSHITA, Y. 1997 Comparison of Two Volume Tracking Algorithms for Bubbly Flow Simulation, in *Moving Boundaries IV---Computational Modelling of Free and Moving Boundary Problems*, Edited by R. Van Keer and C.A. Brebbia, Computational Mechanics Publications, Southampton, UK, Boston, USA.
- STEGER, J. L. 1981 Thoughts on the Chimera Method of Simulation of Three-Dimensional Viscous Flow, *Proceedings Computational Fluid Dynamics on Aeropropulsion*, Cleveland, OH, NASA CP-3078. PP.1-10.
- SUSSMAN, M., ALMGREN, A.S., BELL, J.B., COLELLA, P., HOWELL, L.H. and WELCOME, M.L. 1999 An Adaptive Level Set Approach for Incompressible Two-Phase Flows, *Journal of Computational Physics*, Vol.148, PP. 81-124.
- SUSSMAN, M., SMEREKA, P. and OSHER, S. 1994 A Level Set Approach for Computing Solutions to Incompressible Two-Phase Flow, *Journal of Computational Physics*, Vol.114, PP.146-159.
- SWEBY, P. K. 1984, High Resolution Schemes Using Flux Limiter for Hyperbolic Conservation Law, *SIAM Journal of Numerical Analysis*, Vol.21, PP. 995-1011.
- TAKAGI, S. and MATSUMOTO, Y. 1993 Numerical Analysis of a Single Rising Bubble Using Body-Fitted Coordinate System, *JSME International Journal*, Series B, Vol. 40, No.1, PP. 42-50.
- TAKAGI, S. and MATSUMOTO, Y. 1995 A Rising Bubble in the Simple Shear Flow, ASME FED-Vol.210, PP.145-148.
- TAKAGI, S., MATSUMOTO, Y. and HUANG, H. 1997 Numerical Analysis of a Single Rising Bubble Using Boundary-Fitted Coordinate System, *JSME International Journal*, Series B., Vol.40, No.1, PP. 42-50.

TAKATA, Y., SHIRAKAWA, H., TANAKA, K., KUROKI, T. and ITO, T. 1996 Numerical Analysis of Bubble Growth under Electric Field, *Transactions of the Japan Society of Mechanical Engineers*, Part B, Vol. 62, 595, PP.1142-1147.

TAKEMURA, F. and MATSUMOTO, Y. 1994 Influence of Internal Phenomena on Gas Bubble Motion, *JSME International Journal*, Series B, Vol.37, No.4, PP. 736-745.

THOMAS, P. D. and LOMBARD, C. K. 1979 Geometric Conservation Law and Its Application to Flow Computations on Moving Grids, *AIAA Journal*, Vol.17, PP.1030-1037.

THOMAS, P. D. and MIDDELCOFF, J. F. 1980 Direct Control of Grid Point distribution in Meshes Generated by Elliptic Equations, *AIAA Journal*, Vol.8, PP. 652-656.

THOMPSON, J. F., THAMES, F. C. and MASTIN, C. W. 1974 Automatic Numerical Generation of Body-Fitted Curvilinear Coordinate System for Field Containing Any Number of Arbitrary Two-Dimensional Bodies, *Journal of Computational Physics*, Vol.15, PP. 299-319.

THOMPSON, J. F., WARSI, Z. U. A. and MASTIN, C. W. 1982, Body-Fitted Coordinate Systems for Numerical Solution of Partial Differential Equations- A Review, *Journal of Computational Physics*, Vol.47, PP. 1-108.

THOMPSON, J. F., WARSI, Z. U. A. and MASTIN, C. W. 1985 *Numerical Grid Generation, Fundamentals and Applications*, North-Holland, New York.

TOKUDA, N., YANG, W. J. and CLARK, J. A. 1968 Dynamics of Moving Gas Bubbles in Injection Cooling, *ASME Journal of Heat Transfer*, Vol.91, PP.371-378.

TOMIYAMA, A., SOU, A., MINAGAWA, H. and SAKAGUCHI, T. 1993 Numerical Analysis of a Single Bubble by VOF Method, *JSME International Journal*, Series B, Vol.36, No.1, PP. 51-56.

TOMIYAMA, A., SOU, A., YOSHIKAWA, H. and SAKAGUCHI, T. 1994 Three-Dimensional Detailed Numerical Simulation of Bubbly Flow in Vertical Square Duct, *Transaction of JSME*, Series B, Vol.60, No.576, PP. 2678-2685.

TONG, L. S. 1966, *Boiling Heat Transfer and Two-Phase Flow*, John Wiley & Sons, Inc., New York- London- Sydney.

TRULIO, J. G. and **TRIGGER, K. R.** 1961, Numerical Solution of the One-Dimensional Hydrodynamic Equations in an Arbitrary Time-Dependent Coordinate System, *University of California Lawrence Radiation Laboratory Report UCLR-6522*.

TSUCHIYA, K. and **FAN, L. S.** 1988 Near Wake Structure of a Single Gas Bubble in a Two-Dimensional Liquid-Solid Fluidised Bed: Vortex Shedding and Wake Size Variation, *Chem. Eng. Sci.*, Vol.43, PP.1167-1181.

UENO, K., NISHITA, T. and **KAMIYAMA, S.** 1999 Numerical Simulation of Deformed Single Bubbles Rising in Magnetic Fluid, *Journal of Magnetism and Magnetic Materials*, Vol.201, PP.281-284.

UNVERDI, S.O. and **TRYGGVASON, G.** 1992 A Front-Tracking Method for Viscous, Incompressible, Multi-Fluid Flows, *Journal of Computational Physics*, Vol.100, PP. 25-37.

Van LEER, B. 1974, Towards the Ultimate Conservative Difference Scheme. II. Monotonicity and Conservation Combined in a Second Order Scheme, *Journal of Computational Physics*, Vol.14, PP.361-370.

Van LEER, B. 1977 Towards the Ultimate Conservative Difference Scheme. IV. A New Approach to Numerical Convection, *Journal of Computational Physics*, Vol.23, PP. 276-299.

Van LEER, B. 1979 Towards the Ultimate Conservative Difference Scheme. V. a Second Order Sequel to Godunov's Method, *Journal of Computational Physics*, Vol.32, PP.101-136.

VASSALLO, P. F., SYMOLON, P. D., MOORE, W. E. and **TRABOLD, T. A.** 1995 Freon Bubble Rise Measurements in a Vertical Rectangular Duct, *ASME Journal of Fluids Engineering*, Vol.117, No.4, PP.729-732.

WANG, H. P. and **McLAY, R.T.** 1986 Automatic remeshing scheme for modelling hot forming process, *J. Fluids Engrg.*, Vol.108, PP. 465-469.

WARMING, R. F. and **BEAM, R. M.** 1981 Upwind Second Order Difference Schemes and Applications in Aerodynamics, *AIAA Journal*, Vol.14, PP.1241.

WELCH, S.W.J. 1995 Local Simulation of Two-Phase Flows Including Interface Tracking with Mass Transfer, *Journal of Computational Physics*, Vol.121, PP.142-154.

WELCH, S.W.J. 1998 Direct Simulation of Vapour Bubble Growth, *International Journal of Heat and Mass Transfer*, Vol.41, No.12, PP. 1655-1666.

WINSLOW, A. M. 1967 Numerical Solution of the Quasilinear Poisson Equation in a Nonuniform Triangle Mesh, *Journal of Computational Physics*, Vol.2, PP. 49-172.

YAN, Y. Y. and **LI, W. Z.** 2002 Numerical modelling of fluid flow with heat and mass transfer at the surface of a gas bubble, *Chemical Engineering Research and Design*, Vol.80, No.6, PP.674-680.

YAN, Y. Y. and **SMITH, J. M.** 1999 Simulation of Two-Phase Bubbly Flow—Inert Bubbles Introduced into a Hot Volatile Liquid, EPSRC Proposal, GR/M90207.

YANG, Z., DINH, T.N., NOURGALIEV, R.R. and **SEHGAL, B.R.** 2000 Numerical Investigation of Bubble Coalescence Characteristics under Nucleate Boiling Condition by a Lattice-Boltzmann Model, *International Journal of Thermal Science*, Vol.39, PP. 1-17.

YOON, H. Y., KOSHIZUKA, S. and **OKA, Y.** 2001 Direct Calculation of Bubble Growth, Departure, and Rise in Nucleate Pool Boiling, *International Journal of Multiphase Flow*, Vol.27, PP. 277-298.

YOUNG, D.F and **TASI, F. Y.** 1973 Flow characteristics in models of arterial stenoses—I. Steady flow, *J. Biomech.* Vol. 6, PP. 395-410.

YOUNGREN, G. K. and **ACRIVOS, A.** 1976 On the Shape of a Gas Bubble in a Viscous Extensional Flow, *Journal of Fluid Mechanics*, Vol.76, Part.3, PP. 433-442.

Appendix

Development of FORTRAN Codes for Solving the Inert Bubble Problem

A.1 Flow Chart for Steady Calculation

Figure A.1 is the flow chart for calculating steady heat and fluid flows in the inert bubble problem in this paper. The functions of each code-blocks are as follows:

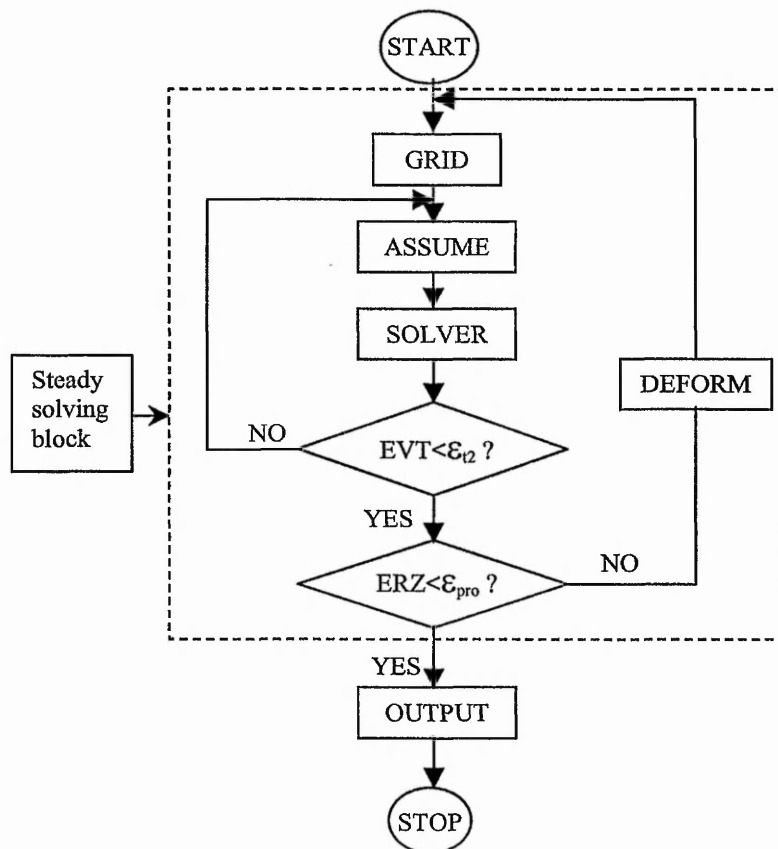


Figure A.1 Flow chart for steady calculations

GRID

Setting up computational domain and generating grids. The TTM method introduced in section 4.3.5 is employed to generate second-order smooth numerical mesh. Based on these, the geometrical parameters such J , α , β and γ are calculated. In case of unsteady problem, the space conservation law is applied to calculating J .

ASSUME

Assuming initial fields. Uniform initial fields are always imposed for spherical bubbles; for deformable bubbles, the velocity and pressure values at the last profile updating are used. Far field boundary conditions will be posed in this block.

SOLVER

Firstly, establish the solution equations for velocity and solve them using TDMA method; Secondly, calculate the coefficients of pressure correction equations and obtain corrections of pressure and velocity.

CONVERG

Check the criteria EVT and ERZ.

DEFORM

Update the bubble profile by using the modified Ryskin-Leal method presented in section 5.2.3.

A.2 Flow Chart for Time-Accurate Simulations

The flow chart for the algorithm presented in section 7.3 is shown in figure A.2. In this figure, the parameter NT is the index of time level. The basic code block is the “steady solving block” enclosed by the dashed lines in figure A.1 whose computational function has been described. It should be noticed that the “steady solving block” is employed by an external iterating loop even at a physical time level while calculation for a series of time levels must be carried out for a time-accurate simulation. Because of these, we have no doubt about the extremely time-consuming calculations in chapter 7.

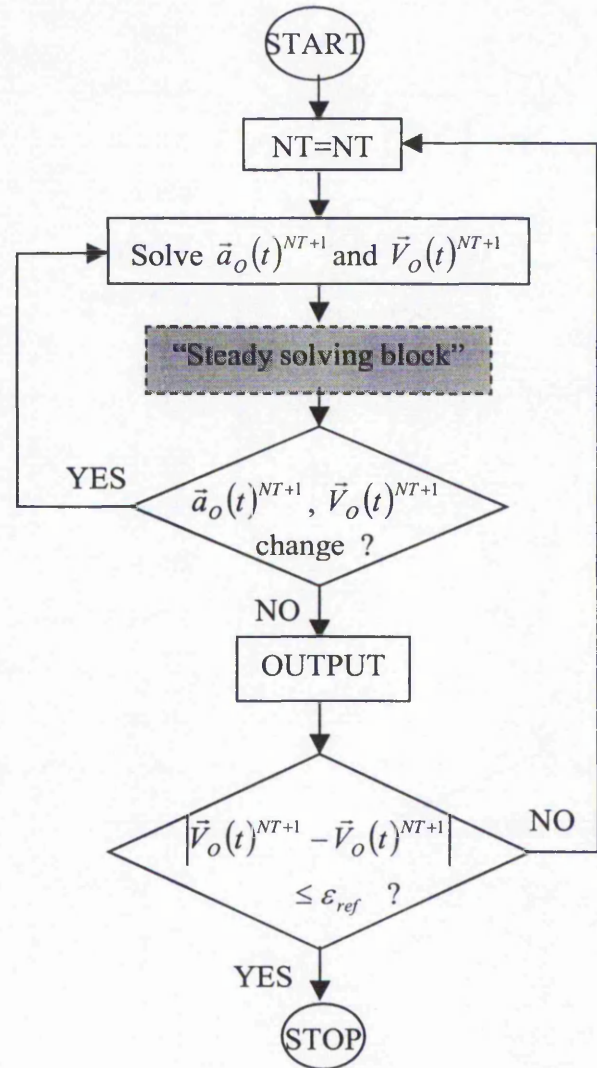


Figure A.2 Flow chart for time-accurate simulations